

Functional Nanomaterials for Optoelectronic Conversion and Energy Storage 2014

Guest Editors: Yongfeng Luo, Li Li, Sanqing Huang, Tao Chen,
and Hongmei Luo





**Functional Nanomaterials for Optoelectric
Conversion and Energy Storage 2014**

Journal of Nanomaterials

Functional Nanomaterials for Optoelectric Conversion and Energy Storage 2014

Guest Editors: Yongfeng Luo, Li Li, Sanqing Huang, Tao Chen,
and Hongmei Luo



Copyright © 2014 Hindawi Publishing Corporation. All rights reserved.

This is a special issue published in "Journal of Nanomaterials." All articles are open access articles distributed under the Creative Commons Attribution License, which permits unrestricted use, distribution, and reproduction in any medium, provided the original work is properly cited.

Editorial Board

Katerina E. Aifantis, USA
Nageh K. Allam, USA
Margarida Amaral, Portugal
Xuedong Bai, China
Lavinia Balan, France
Enrico Bergamaschi, Italy
Theodorian Borca-Tasciuc, USA
C. Jeffrey Brinker, USA
Christian Brosseau, France
Xuebo Cao, China
Shafiq Chowdhury, USA
Kwang-Leong Choy, UK
Cui ChunXiang, China
Miguel A. Correa-Duarte, Spain
Shadi A. Dayeh, USA
Ali Eftekhari, USA
Claude Estourns, France
Alan Fuchs, USA
Lian Gao, China
Russell E. Gorga, USA
Hongchen Chen Gu, China
Mustafa O. Guler, Turkey
John Z. Guo, USA
Smrati Gupta, Germany
Michael Harris, USA
Zhongkui Hong, China
Michael Z. Hu, USA
David Hui, USA
Y.-K. Jeong, Republic of Korea
Sheng-Rui Jian, Taiwan
Wanqin Jin, China
Rakesh K. Joshi, UK
Zhenhui Kang, China
Fathallah Karimzadeh, Iran
Alireza Khataee, Iran

Do Kyung Kim, Korea
Alan K. T. Lau, Hong Kong
Burtrand Lee, USA
Jun Li, Singapore
Benxia Li, China
Xing-Jie Liang, China
Shijun Liao, China
Gong-Ru Lin, Taiwan
Tianxi Liu, China
Jun Liu, USA
Songwei Lu, USA
Daniel Lu, China
Jue Lu, USA
Ed Ma, USA
Gaurav Mago, USA
Santanu K. Maiti, India
Sanjay R. Mathur, Germany
Vikas Mittal, UAE
Weihai Ni, China
Sherine Obare, USA
Atsuto Okamoto, Japan
Abdelwahab Omri, Canada
Edward A. Payzant, USA
Kui-Qing Peng, China
Anukorn Phuruangrat, Thailand
Mahendra Rai, India
Suprakas Sinha Ray, South Africa
Ugur Serincan, Turkey
Huaiyu Shao, Japan
Donglu Shi, USA
Vladimir Sivakov, Germany
Marinella Striccoli, Italy
Bohua Sun, South Africa
Saikat Talapatra, USA
Nairong Tao, China

Titipun Thongtem, Thailand
Somchai Thongtem, Thailand
Alexander Tolmachev, Ukraine
Valeri P. Tolstoy, Russia
Tsung-Yen Tsai, Taiwan
Takuya Tsuzuki, Australia
Raquel Verdejo, Spain
Mat U. Wahit, Malaysia
Zhenbo Wang, China
Ruiping Wang, Canada
Shiren Wang, USA
Cheng Wang, China
Yong Wang, USA
Jinquan Wei, China
Ching-Ping Wong, Hong Kong
Xingcai Wu, China
Guodong Xia, Hong Kong
Ping Xiao, UK
Zhi Li Xiao, USA
Yangchuan Xing, USA
Shuangxi Xing, China
Nanping Xu, China
Doron Yadlovker, Israel
Yingkui Yang, China
Khaled Youssef, USA
Kui Yu, Canada
William W. Yu, USA
Haibo Zeng, China
Tianyou Zhai, China
Bin Zhang, China
Renyun Zhang, Sweden
Yanbao Zhao, China
Lianxi Zheng, Singapore
Chunyi Zhi, Hong Kong

Contents

Functional Nanomaterials for Optoelectric Conversion and Energy Storage 2014, Yongfeng Luo, Li Li, Sanqing Huang, Tao Chen, and Hongmei Luo
Volume 2014, Article ID 210853, 2 pages

The Cellulose Nanofibers for Optoelectronic Conversion and Energy Storage, Yongfeng Luo, Jianxiong Zhang, Xi Li, Chunrong Liao, and Xianjun Li
Volume 2014, Article ID 654512, 13 pages

The Carbon Nanotube Fibers for Optoelectric Conversion and Energy Storage, Yongfeng Luo, Xi Li, Jianxiong Zhang, Chunrong Liao, and Xianjun Li
Volume 2014, Article ID 580256, 13 pages

Progress in Application of CNTs in Lithium-Ion Batteries, Li Li, Hui Yang, Dongxiang Zhou, and Yingyue Zhou
Volume 2014, Article ID 187891, 8 pages

Study on the Highly Sensitive AChE Electrode Based on Multiwalled Carbon Nanotubes, Shuping Zhang, Zhancheng Gu, Yongli Hu, Song Qu, and Ying Liu
Volume 2014, Article ID 828141, 6 pages

Synergistic Effect of Nanosilica Aerogel with Phosphorus Flame Retardants on Improving Flame Retardancy and Leaching Resistance of Wood, Xiaodan Zhu, Yiqiang Wu, Cuihua Tian, Yan Qing, and Chunhua Yao
Volume 2014, Article ID 867106, 8 pages

Synthesis of GeSe₂ Nanobelts Using Thermal Evaporation and Their Photoelectrical Properties, Lijie Zhang, Hongfei Yu, Yun Yang, Keqin Yang, Youqing Dong, Shaoming Huang, Ning Dai, and Da-Ming Zhu
Volume 2014, Article ID 310716, 9 pages

High Cycling Performance Cathode Material: Interconnected LiFePO₄/Carbon Nanoparticles Fabricated by Sol-Gel Method, Zhigao Yang and Shengping Wang
Volume 2014, Article ID 801562, 7 pages

Enhanced Performance of Dye-Sensitized Solar Cells with Graphene/ZnO Nanoparticles Bilayer Structure, Chih-Hung Hsu, Cheng-Chih Lai, Lung-Chien Chen, and Po-Shun Chan
Volume 2014, Article ID 748319, 6 pages

A New Method for Superresolution Image Reconstruction Based on Surveying Adjustment, Jianjun Zhu, Cui Zhou, Donghao Fan, and Jinghong Zhou
Volume 2014, Article ID 931616, 6 pages

The Fabrication and Properties Characterization of Wood-Based Flame Retardant Composites, Xia He, Xianjun Li, Zhu Zhong, Yongli Yan, Qunying Mou, Chunhua Yao, and Chun Wang
Volume 2014, Article ID 878357, 6 pages

Detection of Triphenylmethane Drugs in Fish Muscle by Surface-Enhanced Raman Spectroscopy Coupled with Au-Ag Core-Shell Nanoparticles, Lu Pei, Yiqun Huang, Chunying Li, Yuanyuan Zhang, Barbara A. Rasco, and Keqiang Lai
Volume 2014, Article ID 730915, 8 pages

Editorial

Functional Nanomaterials for Optoelectric Conversion and Energy Storage 2014

Yongfeng Luo,¹ Li Li,² Sanqing Huang,³ Tao Chen,⁴ and Hongmei Luo⁵

¹College of Science, Central South University of Forestry and Technology, Changsha, Hunan 410004, China

²Shanghai Engineering Research Center of Aquatic-Product Processing & Preservation, College of Food Science and Technology, Shanghai Ocean University, Shanghai 201306, China

³School of Materials and Textiles, Zhejiang Sci-Tech University, Hangzhou, Zhejiang 310018, China

⁴Department of Macromolecular Science and Engineering, Case Western Reserve University, Cleveland, OH 44106, USA

⁵Department of Chemical Engineering, New Mexico State University, Las Cruces, NM 88003, USA

Correspondence should be addressed to Yongfeng Luo; yongfengluo@csu.edu.cn

Received 23 September 2014; Accepted 23 September 2014; Published 22 December 2014

Copyright © 2014 Yongfeng Luo et al. This is an open access article distributed under the Creative Commons Attribution License, which permits unrestricted use, distribution, and reproduction in any medium, provided the original work is properly cited.

With depleting fossil fuels and growing concern on environmental protection, urgent research efforts are needed to find alternative energy resources that are efficient, economically and ecologically friendly. New nanomaterials [1] have opened up new frontiers in materials science and engineering to meet this challenge, particularly functional nanomaterials, for photovoltaic and energy storage. During the past 25 years, therefore, considerable efforts have been made to utilize the unique properties of functional nanomaterials, including carbon nanomaterial [2, 3], metallic oxide [4–6], and organic materials [7] as energy materials, and tremendous progress has been achieved in developing high-performance optoelectric conversion and energy storage devices.

Because of the rapid development of optoelectric conversion and energy storage in recent years, we would like to take the opportunity to launch this special issue focusing on advanced functional nanomaterials for optoelectric conversion and energy storage. The aim of this special issue is to highlight remarkable contributions made by the related scientists in this important research area and to cover the broad impacts of energy storage and conversion. This special issue contains 3 review articles and 8 research articles.

Solar cells are the main optoelectric conversion devices, which can efficiently convert sunlight into electricity. This special issue will provide the readers with two review articles and one paper on solar cells. The recent advancement in

carbon nanotube fibers in “*The carbon nanotube fibers for optoelectric conversion and energy storage*” and cellulose nanofibers in “*The cellulose nanofibers for optoelectronic conversion and energy storage*” for optoelectric conversion and energy storage and the current challenge including low energy conversion efficiency and low stability and future direction of the energy fiber have been finally summarized. Characteristics of dye-sensitized solar cells with graphene/ZnO nanoparticle bilayer structure were studied by C.-H. Hsu et al. in “*Enhanced performance of dye-sensitized solar cells with graphene/ZnO nanoparticles bilayer structure.*”

Lithium batteries with high safety, long cycle life, and high rate performance are very important for their applications. The applicable research progress of carbon nanotubes in lithium-ion battery is described in “*Progress in application of CNTs in lithium-ion batteries,*” and its future development is put forward from its two aspects of being not only the anodic conductive reinforcing material and the cathodic energy storage material but also the electrically conductive framework material. Interconnected LiFePO₄/carbon nanoparticles for Li-ion battery cathode have been fabricated by sol-gel method followed by a carbon coating process involving redox reactions in “*High cycling performance cathode material: interconnected LiFePO₄/carbon nanoparticles fabricated by sol-gel method.*”

Supercapacitors are another group of energy storage devices, which have the features of high power density, long cycling life, and high energy efficiency. Y. Luo et al. in “*The carbon nanotube fibers for optoelectric conversion and energy storage*” and “*The cellulose nanofibers for optoelectronic conversion and energy storage*” highlighted the most recent progress in supercapacitors based on carbon nanotube fibers and cellulose nanofibers. Carbon nanotube fibers and cellulose nanofibers have been explored as both electrode materials and electrode additives for developing high-performance supercapacitors which based on CNT fibers recently attracted more attention.

We hope this special issue with a small collection of papers can provide the readers with an overview of the recent progress achieved and the future developing directions in the optoelectric conversion and energy storage field. We sincerely hope that this special issue could provide a valuable reference and perspective for the research community working in this exciting field and inspire many more to enter it.

Acknowledgment

We would like to thank all the authors who have contributed high-quality peer-reviewed articles that advance state-of-the-art research to this special issue.

Yongfeng Luo
Li Li
Sanqing Huang
Tao Chen
Hongmei Luo

References

- [1] K. Kalyanasundaram and M. Grätzel, “Themed issue: nanomaterials for energy conversion and storage,” *Journal of Materials Chemistry*, vol. 22, no. 46, pp. 24190–24194, 2012.
- [2] L. Dai, D. W. Chang, J.-B. Baek, and W. Lu, “Carbon nanomaterials for advanced energy conversion and storage,” *Small*, vol. 8, no. 8, pp. 1130–1166, 2012.
- [3] M. Pumera, “Graphene-based nanomaterials for energy storage,” *Energy and Environmental Science*, vol. 4, no. 3, pp. 668–674, 2011.
- [4] A. S. Aricò, P. Bruce, B. Scrosati, J. M. Tarascon, and W. van Schalkwijk, “Nanostructured materials for advanced energy conversion and storage devices,” *Nature Materials*, vol. 4, no. 5, pp. 366–377, 2005.
- [5] D. Wang, R. Kou, D. Choi et al., “Ternary self-assembly of ordered metal oxide-graphene nanocomposites for electrochemical energy storage,” *ACS Nano*, vol. 4, no. 3, pp. 1587–1595, 2010.
- [6] J. Jiang, Y. Li, J. Liu, X. Huang, C. Yuan, and X. W. Lou, “Recent advances in metal oxide-based electrode architecture design for electrochemical energy storage,” *Advanced Materials*, vol. 24, no. 38, pp. 5166–5180, 2012.
- [7] H. Dong, H. Zhu, Q. Meng, X. Gong, and W. Hu, “Organic photoreponse materials and devices,” *Chemical Society Reviews*, vol. 41, no. 5, pp. 1754–1808, 2012.

Review Article

The Cellulose Nanofibers for Optoelectronic Conversion and Energy Storage

Yongfeng Luo,¹ Jianxiong Zhang,¹ Xi Li,¹ Chunrong Liao,¹ and Xianjun Li²

¹ College of Science, Central South University of Forestry and Technology, Changsha, Hunan 410004, China

² Material Science and Engineering School, Central South University of Forestry and Technology, Changsha, Hunan 410004, China

Correspondence should be addressed to Xianjun Li; lxjmu@163.com

Received 6 May 2014; Accepted 26 June 2014; Published 25 August 2014

Academic Editor: Li Li

Copyright © 2014 Yongfeng Luo et al. This is an open access article distributed under the Creative Commons Attribution License, which permits unrestricted use, distribution, and reproduction in any medium, provided the original work is properly cited.

Cellulose widely exists in plant tissues. Due to the large pores between the cellulose units, the regular paper is nontransparent that cannot be used in the optoelectronic devices. But some chemical and physical methods such as 2,2,6,6-tetramethylpiperidine-1-oxyl radical (TEMPO) oxidation can be used to improve the pores scale between the cellulose units to reach nanometer level. The cellulose nanofibers (CNFs) have good mechanical strength, flexibility, thermostability, and low thermal expansion. The paper made of these nanofibers represent a kind of novel nanostructured material with ultrahigh transparency, ultrahigh haze, conductivity, biodegradable, reproducible, low pollution, environment friendly and so on. These advantages make the novel nanostructured paper apply in the optoelectronic device possible, such as electronics energy storage devices. This kind of paper is considered most likely to replace traditional materials like plastics and glass, which is attracting widespread attention, and the related research has also been reported. The purpose of this paper is to review CNFs which are applied in optoelectronic conversion and energy storage.

1. Introduction

Cellulose mainly exists in plant cell walls; the hierarchical structure of the plant cell walls is complicated; fiber in the cell wall is a kind of nature nanostructure cellulose. CNFs are rapidly developed since Turbak found microfibril in 1983. The CNFs preparation and their application in composite materials are widely reported. Nanofibers are defined as nanosized fiber with size of less than 100 nm. Although they are thin, they have high aspect ratio and strong mechanical properties. The three-dimensional (3D) hierarchical structure is demonstrated in Figure 1. CNFs whose surface contains abundance of light base group have a kind of extremely potential reinforced material, which can replace traditional materials such as glass and plastic. Our country is rich in timber resource, which can be used to extract CNFs. CNFs extracted from tree have excellent performance such as renewability, low consumption, low density, biocompatibility, biodegradability, and being environmentally friendly. The characteristics have extremely far-reaching significance to utilize the function and high added-value of CNFs.

In addition to the characteristics described above, CNFs also have some advantages which are abundance of resource, high aspect ratio, and specific surface area. Simultaneously, nanofibers can be interwoven into mesh tangles in polymer structure. These nanofibers maintain strong mechanical strength and flexibility.

As we know, paper is made from cellulose in wood fiber. There is great difference between the traditional paper and the novel nanostructured paper. Under the same deposition conditions, traditional papers consisting of microsized pulp fibers produce very low conductivity lines with nonuniform boundaries because of their larger pore structures. Although they are both composed of lignocellulose, CNFs paper, as low-cost substrate for flexible electronics and energy devices, has gained extensive attention because of its flexibility, thermostability and low thermal expansion, highly ultrahigh transparency and ultrahigh haze, conductivity, biodegradable, reproducible and low pollution environment friendly. The novel paper application in optoelectronic devices is an emerging research area gathering significant attention. Many recent advances in application of nanofiber involve

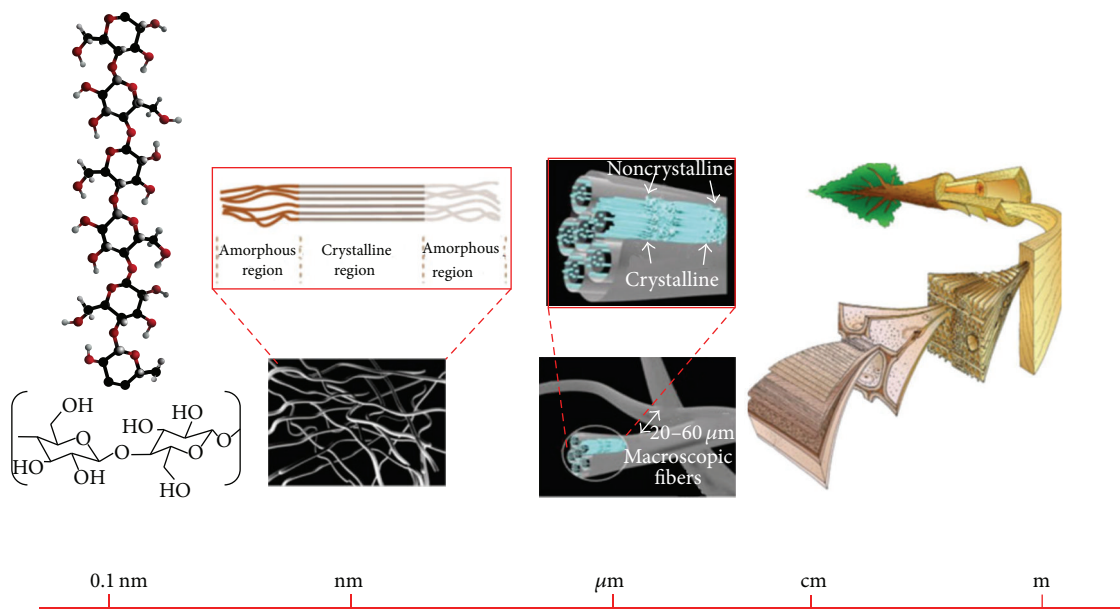


FIGURE 1: The three-dimensional (3D) hierarchical structures show the hierarchical structure of cellulose from the wood cell wall to microfibril to nanofibril to a cellulose molecule [7].

fabricating electronic devices, such as displays, transistors, batteries, sensors, and solar cells [1–4]. Paper electronics is an attractive solution for low-cost applications since it is renewable, scalable, light weight, mechanically flexible, and disposable [5, 6].

In this paper we mainly review the preparation methods of CNFs and the properties of the nanostructured paper and expound the special application in energy storage devices.

2. CNFs

Cellulose is linear polymers composed of the group D-glucose by 1,4- β -glucoside connection. The fundamental unit of cellulose is cellulose elementary fibril, and 36 cellulose molecules that link together form a cellulose elementary fibril whose length is about 30 nm. Cellulose elementary fibril is composed of cellulose microfibril with diameter of 10–20 nm and length of several hundred nanometers to a few microns. Microfibril constitutes the fiber which is the primary substance of the tree.

2.1. Preparation of CNFs

2.1.1. Chemical Preparation of CNFs. Chemical preparation method of CNFs is the enzyme hydrolysis. The amorphous area of fiber is destroyed to isolate nanocrystallite under the condition of strong acid. Morán et al. [8] treated sisal fiber with 60% H_2SO_4 about 30 minutes extract nanometer crystallite under temperature of 45°C. Martins et al. [9] found the acid hydrolysis conditions of commodity cotton pulp, which is in 45°C with 6.5 M H_2SO_4 , processing in 75 minutes to get nanometer crystallite length in 150 ± 50 nm, diameter of 14 ± 5 nm, and has good thermal stability.

2.1.2. Physical Preparation of CNFs. Mechanical grinding is often used to manufacture cellulose. Nakagaito and Yano [10] found that the pulp ground 16–30 times can completely extract the CNFs. Chakraborty et al. [11] obtained nanofibers by grinding the pulp in 125000 rpm.

High intensity ultrasonic treatment is also a kind of effective method of preparation of CNFs. Pretreatment of fibers will be diluted to 0.05% of suspension, and then using 20–25 kHz ultrasonic treatment for 30 minutes, CNFs with diameter of 30–80 nm will be obtained. The advantage of physical preparation method is a very simple operation and without impurities, but this method causes large energy consumption and it is easy to form flocculation.

2.1.3. Biological Preparation of CNFs. Cellulose enzymes are often used to prepare CNFs and cellulose enzymes are able to attack the amorphous regions of the fiber so that the fiber structure splits easier. Since, only the enzyme treatment is hard to get CNFs, mechanical treatment must be combined to get qualified CNFs. Janardhnan and Sain [12] found that the enzyme-treated fibers in the high shear grinding can obtain a smaller size microfibril. Pääkkö et al. [13] mechanically dispersed the fibers that have disposed with the enzyme getting spindle-shaped nanofibers.

Bacterial cellulose is another method to prepare nanofibers. Bacterial cellulose is firstly reported by Brown in 1886. Under the appropriate condition, *Acetobacter xylinum* can secrete cellulose microfibril in diameter of 1.78 nm by concatenating glucose with D-glycosidic bond to form poly-dextrose. Due to the effect of hydrogen bonding, bacterial cellulose microfibril will form a fiber ribbon with length and width of 30–100 nm and thickness of 3–8 nm.

2.1.4. TEMPO-Oxidized CNFs. The chemical and biological method is low yield and difficult to control, so it cannot perfectly prepare CNFs. TEMPO-oxidized CNFs have attracted widespread attention. Individualized CNFs with width of 3–4 nm and length of at least a few microns from wood were prepared completely by 2,2,6,6-tetramethylpiperidine-1-oxyl radical (TEMPO-) mediated oxidation under moderate aqueous conditions [14–16]. The process of TEMPO oxidized CNFs is as follows.

The application of TEMPO catalytic oxidation has opened up a new field of effective and selective conversion chemistry of alcoholic hydroxyl groups to ketones, aldehydes, and carboxyl groups under mild conditions. The related studies have been extensively carried out in recent years [17, 18]. Particularly, deNooy et al. first applied TEMPO-mediated oxidation to water-soluble polysaccharides such as starch, amylopectin, and pullulan for regioselective conversion of C6 primary hydroxyls to carboxylate groups. Isogai et al. [19] reviewed preparation methods and fundamental characteristics of TEMPO-oxidized CNFs. Catalytic amounts of TEMPO and NaBr were dissolved in polysaccharide solutions at pH 10–11, and oxidation was started when NaClO solution was added as a primary oxidant. The efficient conversion of primary hydroxyl groups to carboxylates via aldehydes is hypothesized to proceed according to the mechanism shown in Figure 2 [20, 21]. All kinds of TEMPO-mediated oxidation reactions of mono-, oligo-, and polysaccharides for conversion of primary hydroxyls to carboxylate groups have been reviewed.

According to the approach shown in Figure 3, the C6 primary hydroxyls of cellulose were oxidized to C6 carboxylate groups by TEMPO/NaBr/NaClO oxidation in water at pH 10–11. The oxidation process can be indicated from the pattern of aqueous NaOH consumption, which is continuously added to the reaction mixture to keep the pH at 10 during the oxidation. When TEMPO/NaBr/NaClO oxidation was applied to native cellulose even for extended reaction times or under harsh oxidation conditions, almost no or only a small number of water-soluble products were obtained [22]. On the other hand, pulp of regenerated and mercerized cellulose and ball-milled and liquid NH₃-treated native cellulose became clear solution when the oxidation proceeded; water-soluble oxidized products were obtained in this fashion. The oxidized products had almost coessential chemical structures of sodium (1/4)-b-D-poly-glucuronate or Na salt of cellouronic acid consisting of D-glucuronosyl units alone. So the C6 primary hydroxyls of cellulose can be entirely and selectively converted to C6 Na carboxylate groups by TEMPO-mediated oxidation. It was demonstrated that not only are C6-carboxylate groups formed by the oxidized TEMPO but also NaBrO and/or NaClO exist in the TEMPO/NaBr/NaClO system at pH 10 (see Figure 3).

3. Structures of Cellulose Nanopaper

The basic structure of CNFs determinates the light transmittance of paper. Wood pulp for paper is primarily comprised of cellulose, and most lignin hemicellulose is removed

during the pulping and bleaching procedure. Cellulose is polymerized by a repeating unit of glucose. There are many components of ether, hydroxyl, carbon–carbon, and carbon–hydrogen bonds in the cellulose, so it does not adsorb light in the visible wavelength, which renders the pure cellulose colorless.

Traditional paper is made of fibrous network permeated by microsized air cavities, and the different refractive indices of the cellulose and air (1.5 and 1.0, resp.) lead to the light scattering at the fiber surfaces, so traditional paper is opaque. Fang et al. [23] reported that all the fibers are arranged into a random fibrous network with lots of microsized air cavities in a traditional paper substrate (see Figure 4(a)). Due to the fact that the size of the fibers is much larger than the visible wavelength, incident light will largely scatter. This large difference between refractive indexes invokes slight scattering at the fiber surfaces and is revealed as the nontransparent paper. For paper made of bleached softwood kraft fibers, the specific mass attenuation coefficient is 200–350 cm²g⁻¹ and the specific light absorption coefficient is 1–10 cm²g⁻¹ [24].

In comparison with regular paper, CNFs with diameter of 5–30 nm are used to fill the pores within the paper and, thus, microsized pores that cause light scattering are reduced to nanosize by adding CNFs via a papermaking method. Consequently, minimal light scattering occurs due to the reduced number of open spaces and matched refractive index between the effective index of the transparent paper and air, which allow more light to pass directly through the paper rather than getting scattered (Figure 4(b)) and lead to excellent optical transparency of up to 91.5% (Figure 4(c)).

4. Properties of CNFs Paper

4.1. Mechanical Property. The mechanical properties of paper play an important role for the optoelectronic device. A SEM image of the nanopaper dried after filtration from a water suspension is shown in Figure 5(a). This SEM image shows that the nanofiber cellulose is randomly distributed in flat. Although we observe the nanopaper looks like a thin plastic film with the naked eye, in fact it has a unique porous structure in the nanoscale that makes a difference with traditional transparent substrates. The typical size of pore is 10–50 nm. The fiber porous network structure makes the nanopaper own excellent flexibility. The cross profile (Figure 5(b)) shows that the nanopaper has a layered nanoporous structure. This structure enables the nanopaper to bend the electronics devices based on the effective release of the stress in the active layers generated. Due to the tightly packed nanofibrillar network and numerous fiber-fiber hydrogen bonds, the remarkable high tensile strength, Young's modulus, and toughness become other interesting properties of the transparent nanopaper. These properties make the transparent nanopaper ten times stronger, lighter, and more flexible than traditional paper. The typical stress-strain curve for nanopaper with different porosities is shown in Figure 5(c). It demonstrates that the higher porosity has the lowest tensile strength. The nanopaper with 19% porosity has the highest tensile strength about 205 MPa. Combined

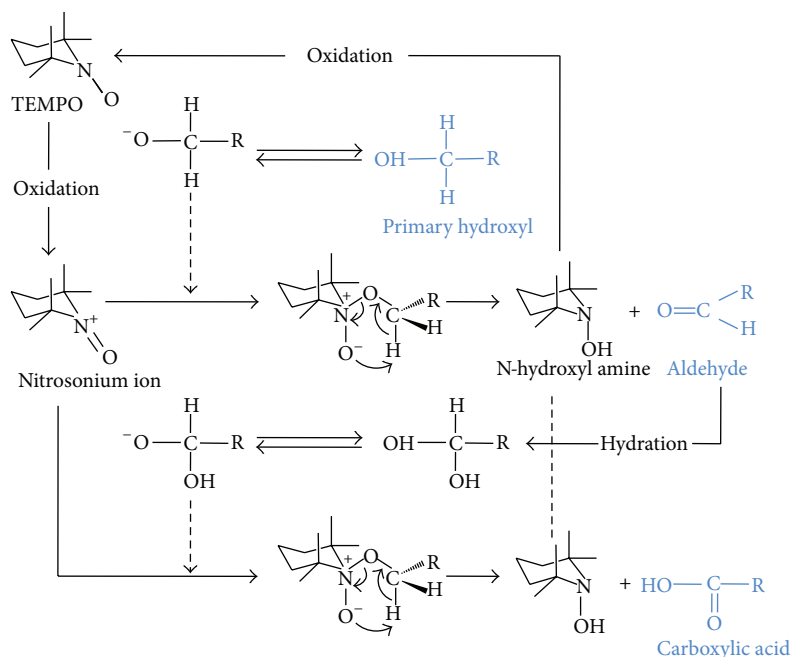


FIGURE 2: TEMPO-mediated oxidation reactions of the efficient conversion of primary hydroxyl groups to carboxylates via aldehydes [19].

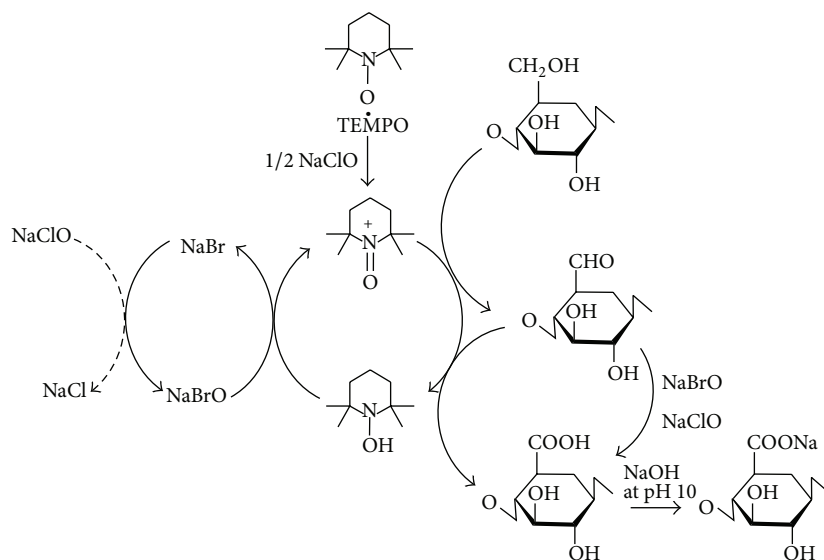


FIGURE 3: Regioselective oxidation of C6 primary hydroxyls of cellulose to C6 carboxylate groups by TEMPO/NaBr/NaClO oxidation in water at pH 10-11 [19].

with its porosity, nanopaper's tensile strength relates directly to its fabrication process [25], and the stress-strain curves for nanopaper were compared in Figure 5(d), Polyethylene terephthalate (PET) and regenerated cellulose film (RCF). The nanopaper has higher tensile stress than PET, but a lower strain-to-failure. The high mechanical strength gives nanopaper huge potential in roll-to-roll printed electronics.

4.2. Optical Properties. Other fascinating properties of CNFs paper are ultrahigh transparency and adjustable optical haze. The regular paper is nontransparent, but the CNFs paper

can be transparent when it is fabricated with nanofibers. This property makes the nanopaper become a possibility as a transparent substrate. The maximum transparency among all current reports on glass and plastic is about 90% but with a very low optical haze (<20%) [15, 26, 27]. Optical haze quantifies the percent of the transmitted light that diffusely scatters, which is preferable in solar cell applications [28, 29]. Optical transparency and haze are inversely proportional values in various papers. Plastic has transparency of about 90% but with an optical haze of less than 1% [30]. Fang et al. [31] recently investigated highly transparent and hazy paper with hybrid cellulose. They research a novel

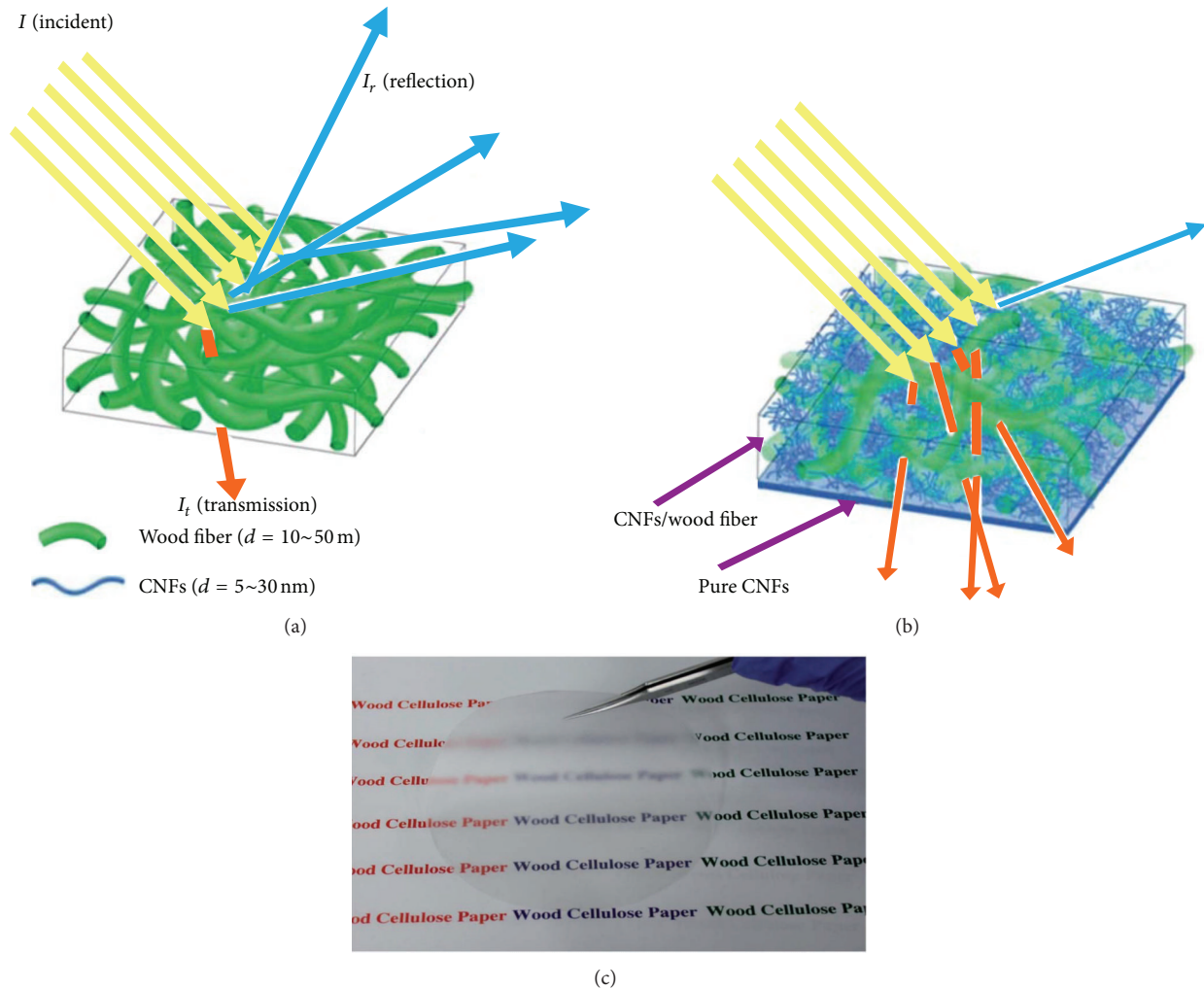


FIGURE 4: (a) Opaque cellulosic paper made of wood fibers. (b) Transparent hybrid paper consisting of two layers: the bottom layer is made of CNFs and the top layer is produced by saturating CNFs into the pores among the network of wood fibers. The width of the wood fiber and CNFs is 10–50 nm and 5–30 nm, respectively. (c) Image of the designed all-cellulose hybrid transparent paper with thickness of 70 μm [23].

transparent paper based on wood fibers, which has an ultrahigh optical transparency ($\sim 96\%$) and simultaneously an ultrahigh optical haze ($\sim 60\%$).

Nogi et al.'s experiment results [5] are shown in Figure 6(a). The dried sheet was not optically transparent but translucent and has plastic film-like appearance indicating that light scattering in the bulk sheet is significantly suppressed. In other words, the lack of transparency seemed to be caused by surface light scattering. When the sheet is polished using emery paper (4000 grit followed by 15000 grit), it becomes transparent. The regular light transmittance levels of the sheet before and after polishing are compared in Figure 6(a) (sheet thicknesses are 60 μm before and 55 μm after polishing, resp.). The light transmittance of the CNFs sheet upon polishing reached 71.6%, including surface reflection (Fresnel's reflection) at a wavelength of 600 nm. Despite the plastic-like transparency, the sheet is as foldable as conventional paper (Figure 6(b)).

The achievement of optical transparency in the CNFs paper by smoothing the surface suggests various approaches for making functional transparent cellulose sheets. Smooth surfaces can be obtained by the lamination of optically transparent plastics, such as polycarbonate films, on the nanofiber paper by exploiting the thermal softening temperature of thermoplastics while avoiding thermal deterioration of cellulose (Figure 7(a)). This would greatly contribute to the simplification of the roll-to-roll process as well. Another approach would be to deposit transparent resins on the surface (Figure 7(b)), or even transparent conductive materials, like indium tin oxide (ITO), using a spin-coater. Ink-jet printers may allow the drawing of precise transparent and functional patterns on the sheet via the addition of functional nanoelements to the ink (Figure 7(c)). As cellulose is highly hygroscopic, transparent-CNf sheets without chemical modification are liable to dimensional instability [33]. These surface-smoothing approaches would not only impart

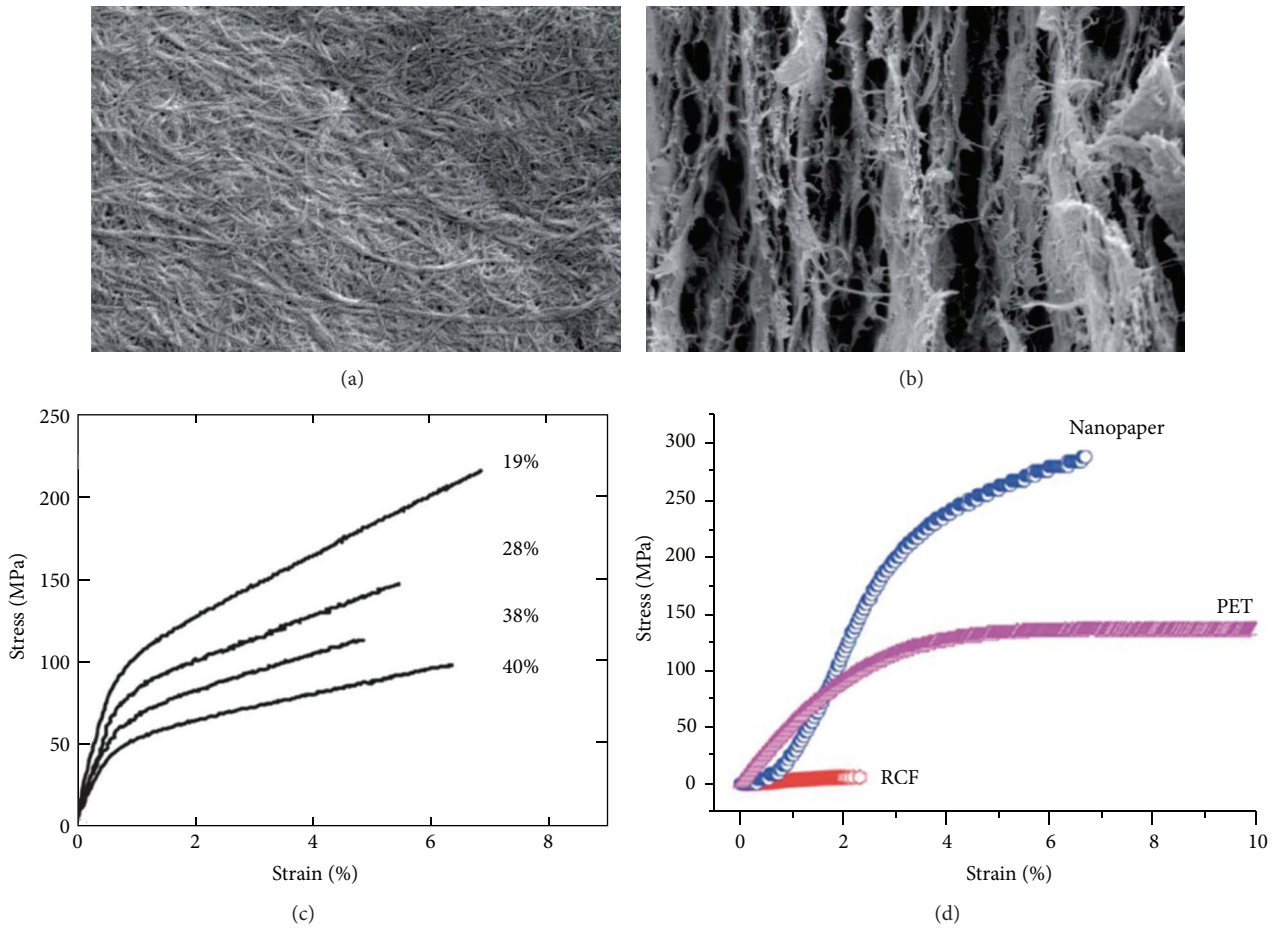


FIGURE 5: (a) SEM image of a nanopaper surface. (b) SEM image of a nanopaper cross-section. (c) Stress-strain curves for nanopaper with different porosities. Cellulose with degree of polymerization (DP) 800 was used. (d) Comparison of tensile strength for different transparent substrate, including PET, regenerated cellulose film, and nanopaper. Note that the maximum strain for PET is up to 81% [32].

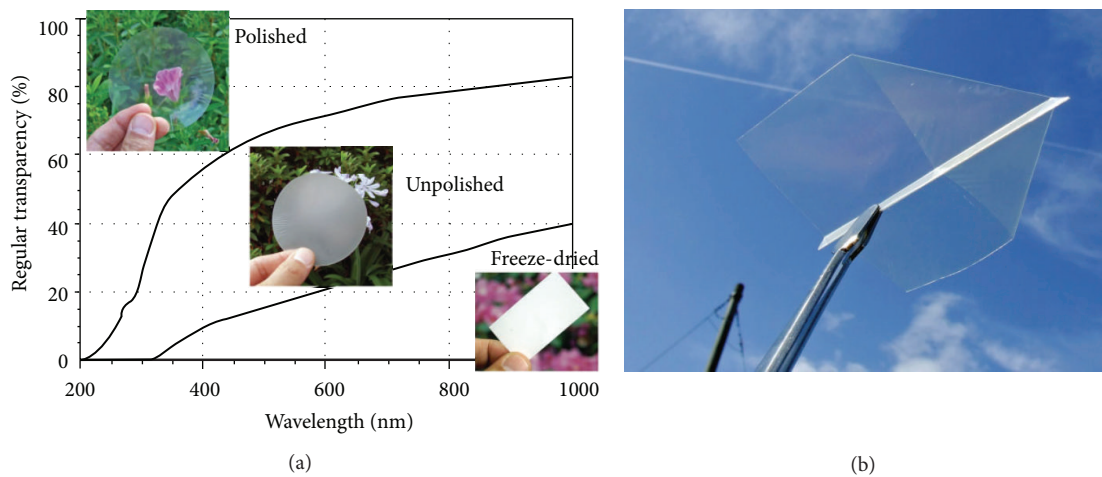


FIGURE 6: (a) Light transmittance of the CNFs sheets. The thicknesses of the oven-dried nanofiber sheet were $60\ \mu\text{m}$ before and $55\ \mu\text{m}$ after polishing. (b) The sheet is as foldable as conventional paper [5].

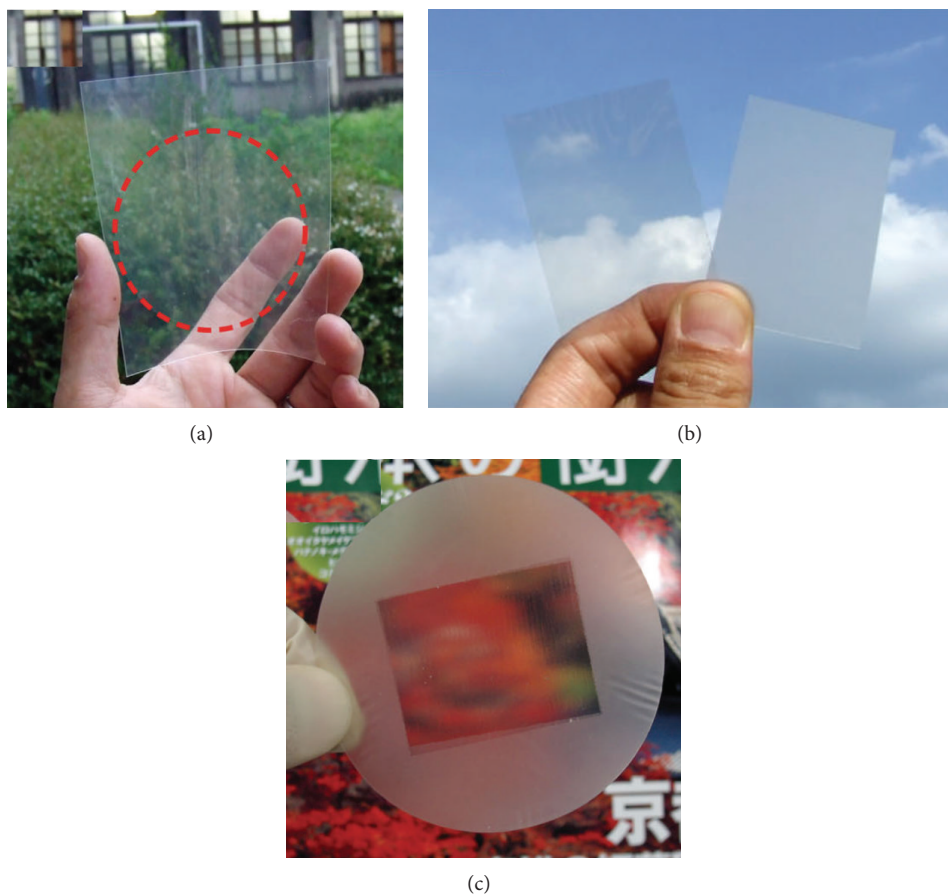


FIGURE 7: The approaches to preparing functional transparent cellulose sheets. (a) Lamination of optically transparent plastics (inside the red circle). (b) Deposition of transparent resins on the surface of cellulose sheets (left: surface-coated sheet, right: uncoated sheet). (c) Drawing of transparent patterns on the sheet using a domestic ink-jet printer [5].

high optical transparency but also act as moisture barriers to the CNFs sheets. The optical haze and transmittance of transparent paper can be tuned by the porosity and the size of CNFs. It is critical to design transparent paper with tunable optical properties with low-cost processes.

4.3. Thermal Expansion and Thermal Durability Properties.

Most electronic devices sustain a heat treatment at a temperature of approximately 300–500°C to obtain the optimal performance [32]. The devices must be fabricated on inorganic silicon or glass substrates, which have high thermal durability and low thermal expansion, so the thermal properties of CNFs paper are very important for its application in optoelectronic devices [34]. Thus CNFs paper must endure temperature during the process without wrinkling, tinting, or thermal decomposing. The DP of original cellulose begins to decrease around 250°C, and extensive degradation of cellulose occurs when the temperature is over 300°C [35]. Thermal chemical degradation and coefficient of thermal expansion (CTE) of transparent paper can be tested by thermogravimetric analysis (TGA) and thermomechanical analysis (TMA).

The CNFs paper is different from regular paper due to a change of particle type and surface modification; there is a decrease in the initial decomposed temperature of cellulose that was observed when it was tested by TGA [36]. Figure 8(a) displays the TGA curves of original cellulose. Fukuzumi et al. [37] found the thermal decomposition temperature decreased with an introduction of sodium carboxyl group into cellulose by TGA. Hsieh et al. [38] presented only a cellulose nanopaper with a high thermal stability that can be used to fabricate conductive circuits in 2013. As shown aforementioned CNFs and pulp paper were stable, but these properties were altered for photo paper when it was exposed to different processing temperatures and treatment times (Figure 8(b)). The optical transmittance of transparent paper remained unchanged, and no obvious change of the surface morphology was observed after it was treated at 150°C for different processing times (Figure 8(c)).

The CTE of crystalline cellulose in the axial direction is around 0.1 ppm K⁻¹, which is more than an order of magnitude lower than plastics, most metals, and ceramics [39, 40]. The optically transparent paper made of CNFs has a CTE of <8.5 ppm K⁻¹, which is much lower than plastic (CTE, 50 ppm K⁻¹). This is desirable for electronic devices

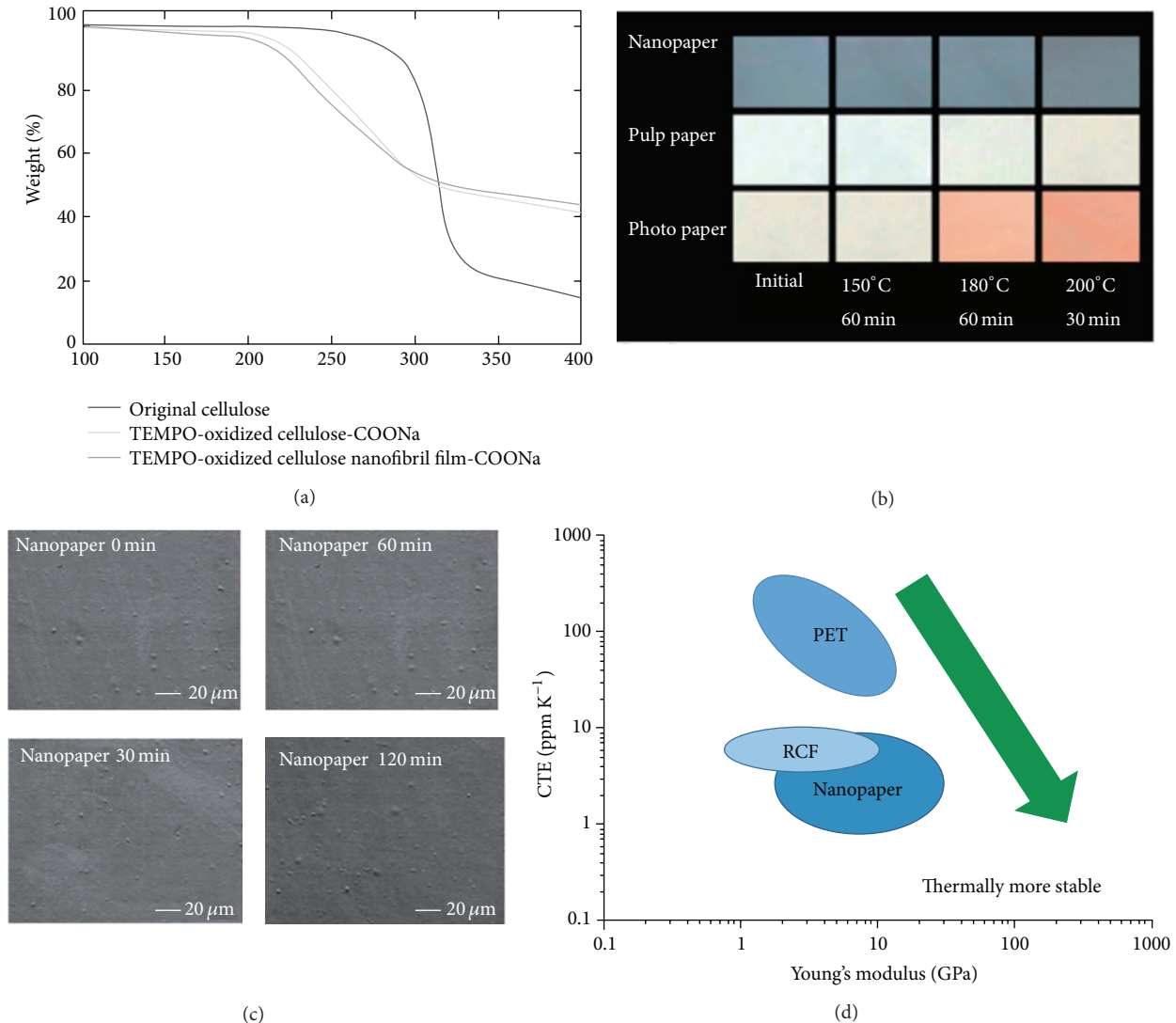


FIGURE 8: (a) TGA of original cellulose, TEMPO-oxidized cellulose with sodium carboxyl group, and TEMPO-oxidized cellulose film with sodium carboxyl group. (b) Digital image of photo paper, pulp paper, and nanopaper under the treatment of various temperatures. (c) SEM images of the surface of nanopaper when it is exposed to 150°C for different time. (d) Coefficient of thermal expansion versus Young's modulus [32].

since it can maintain the dimensional stability under thermal processing condition [5]. The Ashby plot of CTE versus Young's modulus is shown in Figure 8(d) [41]. CNFs paper shows lowest CTE compared to regenerated cellulose film (RCF) and PET, which has the potential to replace current plastic to fabricate flexible electronics.

5. The CNFs for Optoelectronic Conversion and Energy Storage

Optoelectronic devices, such as mobile phones, displays, organic light-emitting diodes lighting (OLED), and solar cells, are manufactured by process that involves extreme conditions, such as high temperatures, high vacuum, which must be fabricated on glass or inorganic silicon substrates and have high thermal durability and low thermal expansion, so

these devices are heavy and inflexible. In order to fabricate flexible, lightweight, high thermal expansion and low thermal durability, paper substrates have been attracting attention for consumer electronics applications.

5.1. Energy Storage with Conductive Paper. The energy storage system involving liquid electrolytes can utilize our CNFs paper because its interconnected porosity allows fast access of ionic species to the electrode surfaces [7]. Researchers try to render electrical conduction in CNFs paper, so the conducting materials such as graphene [42], carbon nanotubes (CNTs) [43], and conductive metal oxide [44] can be integrated. Pushparaj et al. [45] developed a method to dissolve unmodified cellulose fibers in a room-temperature ionic liquid, 1-butyl-3-methylimidazolium chloride. The cellulose solution was then coated onto vertically grown CNTs to

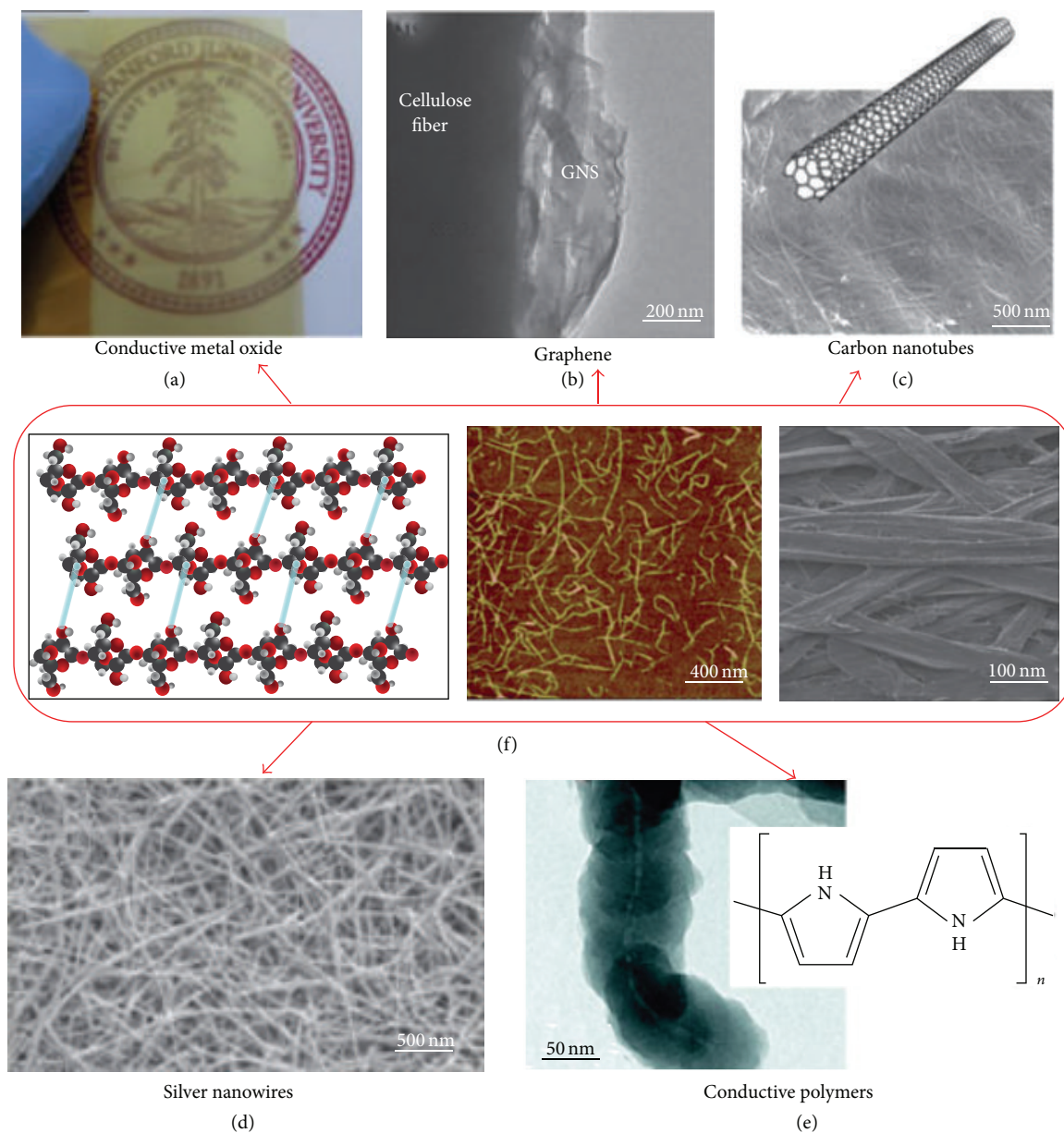


FIGURE 9: Diagram showing conductive materials, such as (a) tin doped indium oxide (ITO), (b) graphene, (c) carbon nanotubes, (d) silver nanowires, (e) and conductive polymers, (f) ranging from the molecular level to nanofibrils and the microfibril level [7].

form the conductive paper, which can be used as an electrode for super capacitors and lithium-ion batteries (Figure 9(a)).

The similarity in dimensions of the CNFs and CNTs allows uniform mixing of the two materials at the nanofibrils scale, following a highly conductive porous composite suitable for high surface area electrodes (Figure 9(b)) [46]. Conductive polymers are also widely used to coat CNFs. Polypyrrole has been found to wet cellulose very well, and polymerization of pyrroles on the surface of cellulose turned out to be conformal coatings of polypyrrole on the CNFs [47]. Coating of CNFs aerogel was demonstrated by using a polyaniline-dodecyl benzene sulfonic acid doped solution in toluene [48].

Nonunique Meyer rod coating of CNTs ink onto commercially available photocopy paper was shown to be highly effective in conductive paper with a sheet resistance of around $10 \Omega/\text{sq}$. The high conductivity was attributed to the strong solvent absorption properties of the porous paper structure and the conformal coating of flexible CNTs on the CNFs to form continuous electrical conduction pathways. Conductive paper made from CNFs also demonstrates excellent mechanical properties.

Due to the hydrophilicity of CNFs, conductive paper as electrodes has been widely used in supercapacitor. Unmodified CNTs are hydrophobic, and their applications in super capacitors have been impeded by poor electrolyte wetting.

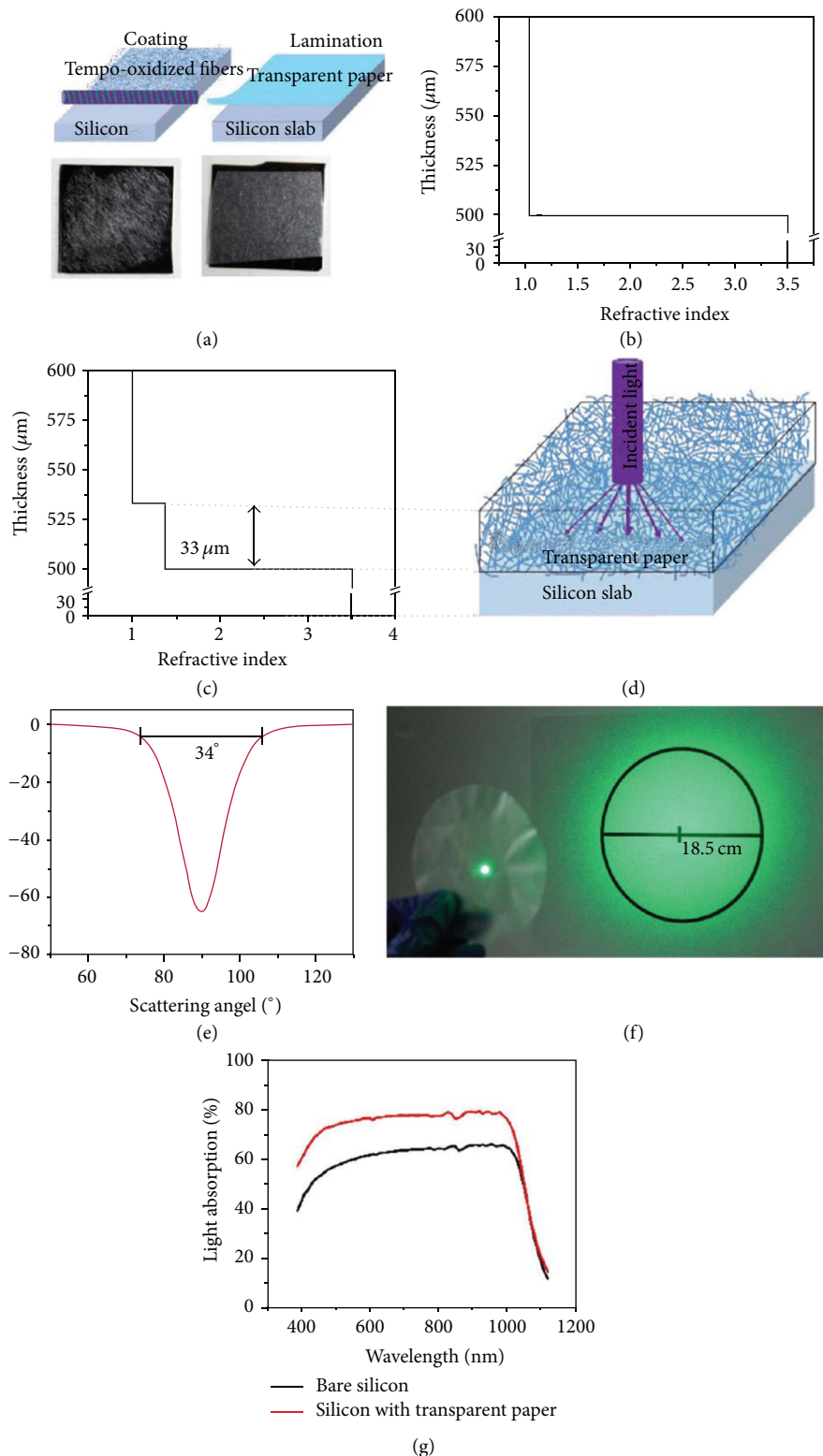


FIGURE 10: (a) Schematics and images of cellulose-deposited silicon slab. Top left: a schematic structure of wood fibers deposited on a silicon slab by Meyer rod coating. Top right: a schematic of transparent paper attached on silicon slab by lamination. Bottom left: TEMPO-oxidized wood fibers deposited on a silicon slab. Bottom right: transparent paper with a thickness of $33\ \mu\text{m}$ attached on a silicon slab. (b) The effective refractive index profiles of the interfaces between air and silicon slab. (c) The effective refractive index profiles of $33\ \mu\text{m}$ cellulose deposited on a silicon slab. (d) A schematic diagram of transparent paper and its light scattering behavior. (e) Scattering angular distribution with an arbitrary y -axis unit for transparent paper. The maximum scattering angle is 34° . (f) A photo showing the light scattering effect of transparent paper when a laser with a diameter of $0.4\ \text{cm}$ passes through transparent paper. (g) The light absorption of transparent paper laminated on a silicon slab [31].

By using CNFs as a substrate for the carbon matrix, aqueous electrolyte can be easily absorbed into the electrode, providing intimate contact between the carbon electrode and electrolyte [49]. For lithium-ion battery applications, the use of conductive nanofiber paper offers new opportunities in fabricating highly flexible electrodes.

Zheng et al. [7] studied the new development of CNFs and discuss how to combine CNFs with other nanomaterials to expand the application in supercapacitor. They utilize the regular paper with high porosity that can suck conductive ink as the substrate and then coat CNT directly on it. It is found that the paper coated with CNT as a supercapacitor electrode demonstrated excellent performance with a capacitance of 200 F/g and stable capability for more than 40000 cycles. The electrode of graphene-nanofiber paper also boasted a good capacitance of 120 F/g; 99% maintained up to 5000 cycles. They also provided another simple method to fabricate super capacitors, taking graphite pencil/nanofiber paper for electrode, water as electrolyte capacitor. The capacitance is around 2.3 mF/m² after 15000 cycles of charge/discharge, and this device maintained over 90% initial value.

CNFs can be used for energy storage base-materials, due to their porous structure promoting the diffusion of ions. Gui et al. [50] have given a strong proof for this conclusion by comparing the base-material of supercapacitor with the holes without holes. They use solution dip and electrodeposition method to prepare hybrid electrode of paper/CNTs/MnO₂ (P-CM), paper/Al₂O₃/CNTs/MnO₂ (P-ACM), and paper/CNTs/MnO₂/CNTs (P-CMC). However, for the Al₂O₃ coated CNFs paper, owing to the nonporous Al₂O₃ layer, the pores on the surface of CNFs will be blocked. Comparing the P-CM and P-ACM, the P-CM-base super capacitor has better electrochemical performance than the latter, and CNFs are very conducive to the ion diffusion. Furthermore, comparing the P-CM and P-CMC, P-CMC-based electrode has superior capacitive performance for its dual ion diffusion pathway. The nanofiber paper-based electrode demonstrates excellent cycling performance, and the retention of its capacity is 85% up to 50000 cycles. This study illustrated fully that hole cellulose fiber is very conducive to the ion diffusion and it is a great potential material of super capacitor.

5.2. CNFs for Optoelectronic Conversion. A new outcome has been reported by Fang et al. [31] novel nanostructured paper with ultrahigh transparency and ultrahigh haze for solar cells. Because it is a kind of natural materials, this CNFs paper is more environment friendly than traditional substrates such as glass and plastic [51–53]. The maximum transparency of regular substrates is high about 90%, but its optical haze is very low (<20%), while CNFs paper has not only ultrahigh optical transparency (~96%), but also ultrahigh optical haze (~60%).

The CNFs paper with ultrahigh transmittance and high transmission haze has potential applications in solar cells [31]. The light scattering effect of transparent paper can improve the path of light traveling through the active layers of thin film solar cells resulting in an enhanced light absorption. An

experiment is implemented that, as shown in Figure 10(a), TEMPO-oxidized wood fibers were directly coated onto the surface of a silicon slab and transparent paper laminated onto the surface of silicon using CNFs as a binder to analyze any resulting enhancement of light absorption in the silicon. The possible mechanisms are as follows: (1) the index of transparent paper that is between the values for the Si substrate and air, which can effectively decrease the index contrast and lower the reflection for light entering from air to Si (Figures 10(b) and 10(c)); (2) a large light forward scattering effect of transparent paper, which can increase the path length of light in the Si layer (Figure 10(d)); and (3) an ultrahigh optical transparency up to 96% of transparent paper. These effects make transparent paper fundamentally better than plastic substrates for thin film solar cells.

The direct incident light is scattered as it propagates through the transparent paper, generating a high transmission haze (Figure 10(d)). To quantitatively explain the light scattering effect of transparent paper, an optical setup consisting of a rotating light detector is applied to measure the angular distribution of transmitted light. Light passing through transparent paper exhibits high diffuse scattering with an expected inverse Gaussian-like pattern (Figure 10(e)). Transparent paper delivers a maximum scattering angle of 34°. The light scattering effect is also visualized in Figure 10(f). A laser with a wavelength of 532 nm and a beam diameter of 0.4 cm passes through transparent paper and forms a larger illuminated circular area on the surface of the target with a diameter of over 18.5 cm. The same experiment is also applied to glass and PET to illustrate the light scattering effect, and because the transmission haze of PET and glass is lower than 1%, the transmitted light is scattered only slightly as visualized by a smaller illuminated area on the target behind the transparent paper. Figure 10(g) indicates the light absorption of transparent paper laminated on a silicon slab. Compared to a bare silicon slab, there is enhanced light trapping in all the prepared samples by approximately 10–18% from 400 to 1000 nm. These results show that (1) both TEMPO-oxidized wood fibers and transparent paper can enhance the broadband absorption efficiency of the silicon slab and (2) transparent paper or TEMPO-treated wood fibers can be applied to a silicon slab with simple coating, dipping, or lamination that depends on the specific application desired.

6. Conclusions

In this paper, we mainly review the preparation structure, properties, and applications in optoelectronic devices of CNFs in latest research. CNFs paper has huge potential to replace traditional materials such as glasses and plastic. However, there are tremendous challenges [32] including (1) transparent paper nanofabrication challenges with an aim of much higher speed and much lower energy consumption; (2) substrate property improvement including the shape stability, water absorption, and barrier properties to water and oxygen; (3) printing process development and improved properties of printed materials; (4) device fabrication, reliability, and

integrations with roll-to-roll processing. We believe that these problems can be overcome sooner or later. For device applications, cellulose nanopaper will give us more flexibility to tune the substrate properties for different applications, such as display, solar cell, and energy storage.

Conflict of Interests

The authors declare that there is no conflict of interests regarding the publication of this paper.

Acknowledgments

The authors thank the support of the New-Century Training Program Foundation for the Talents by the Ministry of Education of China (NCET-11-0979), National Natural Science Foundation of China (no. 31370564), and Graduate Student Innovation Fund of Central South University of Forestry and Technology (no. CX2014B20).

References

- [1] N. Komoda, M. Nogi, K. Suganuma, H. Koga, and K. Otsuka, "Silver nanowire antenna printed on polymer and paper substrates," in *Proceedings of the 12th IEEE International Conference on Nanotechnology (NANO '12)*, pp. 1–5, IEEE, August 2012.
- [2] F. Eder, H. Klauk, M. Halik, U. Zschieschang, G. Schmid, and C. Dehm, "Organic electronics on paper," *Applied Physics Letters*, vol. 84, no. 14, pp. 2673–2675, 2004.
- [3] A. Russo, B. Y. Ahn, J. J. Adams, E. B. Duoss, J. T. Bernhard, and J. A. Lewis, "Pen-on-paper flexible electronics," *Advanced Materials*, vol. 23, no. 30, pp. 3426–3430, 2011.
- [4] Z. Weng, Y. Su, D. Wang, F. Li, J. Du, and H. Cheng, "Graphene-cellulose paper flexible supercapacitors," *Advanced Energy Materials*, vol. 1, no. 5, pp. 917–922, 2011.
- [5] M. Nogi, S. Iwamoto, A. N. Nakagaito, and H. Yano, "Optically transparent nanofiber paper," *Advanced Materials*, vol. 21, no. 16, pp. 1595–1598, 2009.
- [6] Y. Okahisa, A. Yoshida, S. Miyaguchi, and H. Yano, "Optically transparent wood-cellulose nanocomposite as a base substrate for flexible organic light-emitting diode displays," *Composites Science and Technology*, vol. 69, no. 11–12, pp. 1958–1961, 2009.
- [7] G. Zheng, Y. Cui, E. Karabulut, L. Wågberg, H. Zhu, and L. Hu, "Nanostructured paper for flexible energy and electronic devices," *MRS Bulletin*, vol. 38, no. 4, pp. 320–325, 2013.
- [8] J. I. Morán, V. A. Alvarez, V. P. Cyras, and A. Vázquez, "Extraction of cellulose and preparation of nanocellulose from sisal fibers," *Cellulose*, vol. 15, no. 1, pp. 149–159, 2008.
- [9] M. A. Martins, E. M. Teixeira, A. C. Corrêa, M. Ferreira, and L. H. C. Mattoso, "Extraction and characterization of cellulose whiskers from commercial cotton fibers," *Journal of Materials Science*, vol. 46, no. 24, pp. 7858–7864, 2011.
- [10] A. N. Nakagaito and H. Yano, "The effect of morphological changes from pulp fiber towards nano-scale fibrillated cellulose on the mechanical properties of high-strength plant fiber based composites," *Applied Physics A*, vol. 78, no. 4, pp. 547–552, 2004.
- [11] A. Chakraborty, M. Sain, and M. Kortschot, "Cellulose microfibrils: a novel method of preparation using high shear refining and cryocrushing," *Holzforschung*, vol. 59, no. 1, pp. 102–107, 2005.
- [12] S. Janardhan and M. M. Sain, "Isolation of cellulose microfibrils—an enzymatic approach," *Bioresources*, vol. 1, no. 2, pp. 176–188, 2007.
- [13] M. Pääkkö, M. Ankerfors, H. Kosonen et al., "Enzymatic hydrolysis combined with mechanical shearing and high-pressure homogenization for nanoscale cellulose fibrils and strong gels," *Biomacromolecules*, vol. 8, no. 6, pp. 1934–1941, 2007.
- [14] T. Saito, Y. Nishiyama, J. Putaux, M. Vignon, and A. Isogai, "Homogeneous suspensions of individualized microfibrils from TEMPO-catalyzed oxidation of native cellulose," *Biomacromolecules*, vol. 7, no. 6, pp. 1687–1691, 2006.
- [15] H. Fukuzumi, T. Saito, T. Iwata, Y. Kumamoto, and A. Isogai, "Transparent and high gas barrier films of cellulose nanofibers prepared by TEMPO-mediated oxidation," *Biomacromolecules*, vol. 10, no. 1, pp. 162–165, 2009.
- [16] T. Saito, M. Hirota, N. Tamura et al., "Individualization of nano-sized plant cellulose fibrils by direct surface carboxylation using TEMPO catalyst under neutral conditions," *Biomacromolecules*, vol. 10, no. 7, pp. 1992–1996, 2009.
- [17] W. Adam, C. R. Saha-Möller, and P. A. Ganeshpure, "Synthetic applications of nonmetal catalysts for homogeneous oxidations," *Chemical Reviews*, vol. 101, no. 11, pp. 3499–3548, 2001.
- [18] P. L. Bragd, A. C. Besemer, and H. van Bekkum, "Bromide-free TEMPO-mediated oxidation of primary alcohol groups in starch and methyl α -D-glucopyranoside," *Carbohydrate Research*, vol. 328, no. 3, pp. 355–363, 2000.
- [19] A. Isogai, T. Saito, and H. Fukuzumi, "TEMPO-oxidized cellulose nanofibers," *Nanoscale*, vol. 3, no. 1, pp. 71–85, 2011.
- [20] W. F. Bailey, J. M. Bobbitt, and K. B. Wiberg, "Mechanism of the oxidation of alcohols by oxoammonium cations," *Journal of Organic Chemistry*, vol. 72, no. 12, pp. 4504–4509, 2007.
- [21] S. Goldstein and A. Samuni, "Kinetics and mechanism of peroxy radical reactions with nitroxides," *The Journal of Physical Chemistry A*, vol. 111, no. 6, pp. 1066–1072, 2007.
- [22] A. Isogai and Y. Kato, "Preparation of polyuronic acid from cellulose by TEMPO-mediated oxidation," *Cellulose*, vol. 5, no. 3, pp. 153–164, 1998.
- [23] Z. Fang, H. Zhu, C. Preston et al., "Highly transparent and writable wood all-cellulose hybrid nanostructured paper," *Journal of Materials Chemistry C*, vol. 1, no. 39, pp. 6191–6197, 2013.
- [24] M. A. Hubbe, J. J. Pawlak, and A. A. Koukoulas, "Paper's appearance: a review," *Bioresources*, vol. 3, no. 2, pp. 627–665, 2008.
- [25] H. Sehaqui, M. Allais, Q. Zhou, and L. A. Berglund, "Wood cellulose biocomposites with fibrous structures at micro- and nanoscale," *Composites Science and Technology*, vol. 71, no. 3, pp. 382–387, 2011.
- [26] H. Zhu, S. Parvinian, C. Preston, O. Vaaland, Z. Ruan, and L. Hu, "Transparent nanopaper with tailored optical properties," *Nanoscale*, vol. 5, no. 9, pp. 3787–3792, 2013.
- [27] I. Siró, D. Plackett, M. Hedenqvist, M. Ankerfors, and T. Lindström, "Highly transparent films from carboxymethylated microfibrillated cellulose: the effect of multiple homogenization steps on key properties," *Journal of Applied Polymer Science*, vol. 119, no. 5, pp. 2652–2660, 2011.
- [28] Y. Chiba, A. Islam, Y. Watanabe, R. Komiya, N. Koide, and L. Han, "Dye-sensitized solar cells with conversion efficiency of 11.1%," *Japanese Journal of Applied Physics*, vol. 45, no. 24–28, part 2, pp. L638–L640, 2006.

- [29] M. Berginski, J. Hüpkes, M. Schulte et al., "The effect of front ZnO: Al surface texture and optical transparency on efficient light trapping in silicon thin-film solar cells," *Journal of Applied Physics*, vol. 101, no. 7, Article ID 074903, 2007.
- [30] W. A. MacDonald, M. K. Looney, D. Mackerron et al., "Latest advances in substrates for flexible electronics," *Journal of the Society for Information Display*, vol. 15, no. 12, pp. 1075–1083, 2007.
- [31] Z. Fang, H. Zhu, Y. Yuan et al., "Novel nanostructured paper with ultrahigh transparency and ultrahigh haze for solar cells," *Nano Letters*, vol. 14, no. 2, pp. 765–773, 2014.
- [32] H. Zhu, Z. Fang, C. Preston, Y. Li, and L. Hu, "Transparent paper: fabrications, properties, and device applications," *Energy & Environmental Science*, vol. 7, no. 1, pp. 269–287, 2014.
- [33] M. Nogi, K. Abe, K. Handa, F. Nakatsubo, S. Ifuku, and H. Yano, "Property enhancement of optically transparent bionanofiber composites by acetylation," *Applied Physics Letters*, vol. 89, no. 23, Article ID 233123, 2006.
- [34] M. Nogi, C. Kim, T. Sugahara, T. Inui, T. Takahashi, and K. Sukanuma, "High thermal stability of optical transparency in cellulose nanofiber paper," *Applied Physics Letters*, vol. 102, no. 18, Article ID 181911, 2013.
- [35] J. B. Dahiya and K. Kumar, "Flame retardant study of cotton coated with intumescent: kinetics and effect of metal ions," *Journal of Scientific and Industrial Research*, vol. 68, no. 6, pp. 548–554, 2009.
- [36] R. J. Moon, A. Martini, J. Nairn, J. Simonsen, and J. Youngblood, "Cellulose nanomaterials review: structure, properties and nanocomposites," *Chemical Society Reviews*, vol. 40, no. 7, pp. 3941–3994, 2011.
- [37] H. Fukuzumi, T. Saito, Y. Okita, and A. Isogai, "Thermal stabilization of TEMPO-oxidized cellulose," *Polymer Degradation and Stability*, vol. 95, no. 9, pp. 1502–1508, 2010.
- [38] M.-C. Hsieh, C. Kim, M. Nogi, and K. Sukanuma, "Electrically conductive lines on cellulose nanopaper for flexible electrical devices," *Nanoscale*, vol. 5, no. 19, pp. 9289–9295, 2013.
- [39] T. Nishino, I. Matsuda, and K. Hirao, "All-cellulose composite," *Macromolecules*, vol. 37, no. 20, pp. 7683–7687, 2004.
- [40] H. Yano, J. Sugiyama, A. N. Nakagaito et al., "Optically transparent composites reinforced with networks of bacterial nanofibers," *Advanced Materials*, vol. 17, no. 2, pp. 153–155, 2005.
- [41] H. Zhu, Z. Xiao, D. Liu et al., "Biodegradable transparent substrates for flexible organic-light-emitting diodes," *Energy and Environmental Science*, vol. 6, no. 7, pp. 2105–2111, 2013.
- [42] Z. Yang, H. Sun, T. Chen, L. Qiu, Y. Luo, and H. Peng, "Photovoltaic wire derived from a graphene composite fiber achieving an 8.45 % energy conversion efficiency," *Angewandte Chemie*, vol. 52, no. 29, pp. 7545–7548, 2013.
- [43] T. Chen, S. T. Wang, Z. B. Yang et al., "Flexible, light-weight, ultrastrong, and semiconductive carbon nanotube fibers for a highly efficient solar cell," *Angewandte Chemie*, vol. 50, no. 8, pp. 1815–1819, 2011.
- [44] X. Chen, L. Li, X. Sun et al., "Magnetochromatic polydiacetylene by incorporation of Fe₃O₄ nanoparticles," *Angewandte Chemie*, vol. 50, no. 24, pp. 5486–5489, 2011.
- [45] V. L. Pushparaj, M. M. Shaijumon, A. Kumar et al., "Flexible energy storage devices based on nanocomposite paper," *Proceedings of the National Academy of Sciences of the United States of America*, vol. 104, no. 34, pp. 13574–13577, 2007.
- [46] L. Hu, N. Liu, M. Eskilsson et al., "Silicon-conductive nanopaper for Li-ion batteries," *Nano Energy*, vol. 2, no. 1, pp. 138–145, 2013.
- [47] D. O. Carlsson, G. Nyström, Q. Zhou, L. A. Berglund, L. Nyholm, and M. Stromme, "Electroactive nanofibrillated cellulose aerogel composites with tunable structural and electrochemical properties," *Journal of Materials Chemistry*, vol. 22, no. 36, pp. 19014–19024, 2012.
- [48] M. Pääkkö, J. Vapaavuori, R. Silvennoinen et al., "Long and entangled native cellulose I nanofibers allow flexible aerogels and hierarchically porous templates for functionalities," *Soft Matter*, vol. 4, no. 12, pp. 2492–2499, 2008.
- [49] G. Zheng, L. Hu, H. Wu, X. Xie, and Y. Cui, "Paper supercapacitors by a solvent-free drawing method," *Energy & Environmental Science*, vol. 4, no. 9, pp. 3368–3373, 2011.
- [50] Z. Gui, H. Zhu, E. Gillette et al., "Natural cellulose fiber as substrate for supercapacitor," *ACS Nano*, vol. 7, no. 7, pp. 6037–6046, 2013.
- [51] K. Missoum, M. N. Belgacem, and J. Bras, "Nanofibrillated cellulose surface modification: a review," *Materials*, vol. 6, no. 5, pp. 1745–1766, 2013.
- [52] K. Missoum, M. N. Belgacem, J. Barnes, M. Brochier-Salon, and J. Bras, "Nanofibrillated cellulose surface grafting in ionic liquid," *Soft Matter*, vol. 8, no. 32, pp. 8338–8349, 2012.
- [53] K. Missoum, J. Bras, and M. N. Belgacem, "Organization of aliphatic chains grafted on nanofibrillated cellulose and influence on final properties," *Cellulose*, vol. 19, no. 6, pp. 1957–1973, 2012.

Review Article

The Carbon Nanotube Fibers for Optoelectric Conversion and Energy Storage

Yongfeng Luo,¹ Xi Li,¹ Jianxiong Zhang,¹ Chunrong Liao,¹ and Xianjun Li²

¹ College of Science, Central South University of Forestry and Technology, Changsha, Hunan 410004, China

² Material Science and Engineering School, Central South University of Forestry and Technology, Changsha, Hunan 410004, China

Correspondence should be addressed to Xianjun Li; lxjmu@163.com

Received 25 April 2014; Accepted 31 May 2014; Published 21 August 2014

Academic Editor: Li Li

Copyright © 2014 Yongfeng Luo et al. This is an open access article distributed under the Creative Commons Attribution License, which permits unrestricted use, distribution, and reproduction in any medium, provided the original work is properly cited.

This review summarizes recent studies on carbon nanotube (CNT) fibers for weavable device of optoelectric conversion and energy storage. The intrinsic properties of individual CNTs make the CNT fibers ideal candidates for optoelectric conversion and energy storage. Many potential applications such as solar cell, supercapacitor, and lithium ion battery have been envisaged. The recent advancement in CNT fibers for optoelectric conversion and energy storage and the current challenge including low energy conversion efficiency and low stability and future direction of the energy fiber have been finally summarized in this paper.

1. Introduction

Flexible and portable electronic devices have been extensively studied for a wide range of applications in solar cell [1–21], lithium ion battery [22, 23], supercapacitor [24–29], sensors [30], and their integrated device [31–36]. Weavable electronic devices usually require corresponding fiber materials to fabricate them. There is an increasing interest in flexible solar cells and researchers have been investigating weavable fiber solar cells based on metal wires, glass fibers, or polymer fibers [37–42]. Unfortunately, the low efficiencies of these fiber-based solar cells greatly limit their promising applications.

Carbon nanotubes have been widely introduced to fabricate high-efficiency organic solar cells because of their extremely high surface area (e.g., ca. $1600 \text{ m}^2 \text{ g}^{-1}$ for single-walled nanotubes) and superior electrical properties [43]. However, nanotubes are used in electrode materials. For example, the incorporation of nanotubes onto titania nanoparticle films has been shown to increase the roughness factor and decrease the charge recombination of electron/hole pairs [44], and the replacement of platinum with nanotubes as counter electrode catalyzed the reduction of triiodide to improve the cell performance. The distribution of nanotubes within the photoactive layer improved the short circuit current density and fill factor owing to rapid charge separation at the nanotube/electron donor interface and efficient electron

transport through nanotubes [45]. However, the degrees of improvement are far from what is expected for nanotubes, mainly because of random aggregation of nanotubes in the cells. For a random nanotube network, the electrons have to cross many more boundaries. Therefore, alignment of nanotubes will further greatly improve cell performance as charge transport is more efficient. To improve the practical application of CNTs, scientists are exploring various nanomaterials to improve charge separation and transport in these fiber-based photovoltaic devices. Researchers aligned continuous multiwalled CNT sheets and fibers to produce materials with high mechanical strength and electrical conductivity; it is critically important to extend their physical properties from the nanoscale to the macroscopic scale. The excellent mechanical and electrical performance of individual CNTs make the CNT fibers ideal candidates for optoelectric conversion and energy storage.

CNT fibers can be fabricated directly from chemical vapor deposition (CVD) [50] or can be spun from high-quality aligned CNT arrays [1, 2, 51–53]; Li and coauthors [50] spun fibers and ribbons of CNTs directly from CVD synthesis zone of a furnace using a liquid source of carbon and an iron nanocatalyst. This process was realized through the appropriate choice of reactants, control of the reaction conditions, and continuous withdrawal of the product with a rotating spindle used in various geometries. This direct

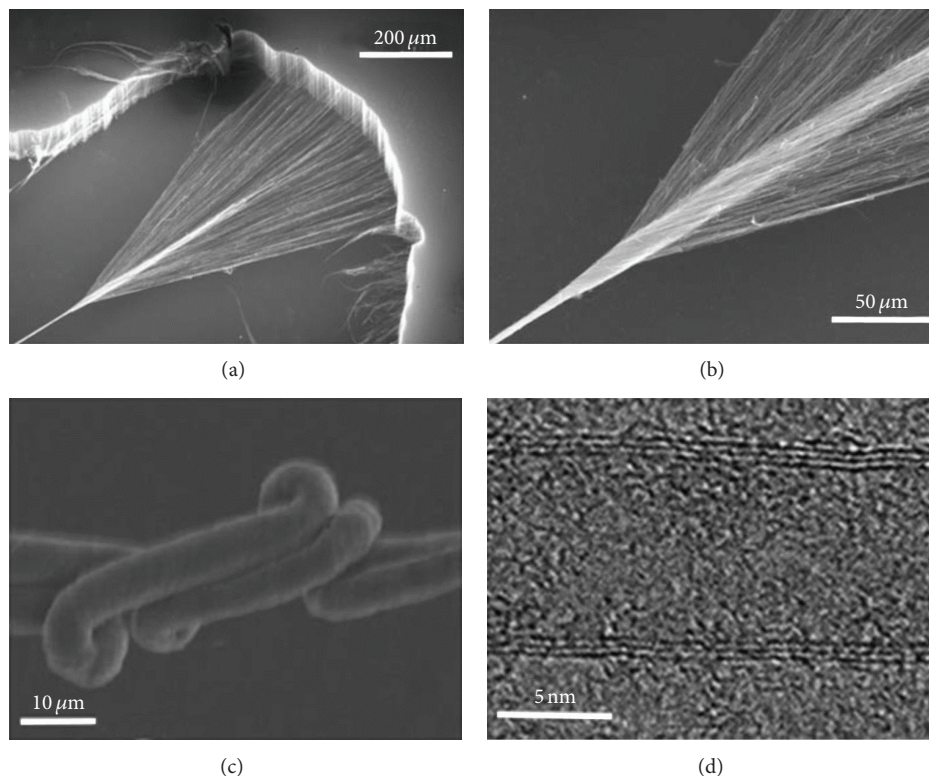


FIGURE 1: CNT fibers characterized by scanning electron microscopy (SEM) and transmission electron microscopy (TEM) [1, 2]. (a) and (b) SEM images, at two different magnifications of CNT fibers in the process of being simultaneously drawn and twisted during spinning from nanotube arrays. (c) Knots could be tied in the nanotube fibers, revealing their high flexibility and resistance to torsion. (d) High-resolution TEM image of a component nanotube.

spinning from a CVD reaction zone is extendable to other types of fiber and to the spin coating of rotating objects in general. But these CNT fibers contained 5 to 10 wt% iron and a large number of defects. To produce desired high-quality CNT fibers [1, 2], the high-quality nanotube arrays are firstly synthesized by a typical chemical vapor deposition method. This provided an important clue to the use of multiwalled CNTs at macroscopic scale, and researchers have made multiple efforts to optimize this aligned structure and improve the properties of CNT fibers [54–61] to many applications; for example, Chen et al. [2] and Luo et al. [3] use flexible, light-weight, ultrastrong, and semiconductive CNT fibers to develop a novel solar cell. The high alignment of building nanotubes in the fiber allows charges to separate and transport along the fibers efficiently, which provides a fiber solar cell with high performance.

In this review, we briefly highlight the fabrication of CNT fibers and its applications for solar cell, lithium ion battery, supercapacitor, and their integrated device.

2. Fabrication of High-Quality Carbon Nanotube Fibers

High-quality CNT fibers are obtained by dry spinning from highly aligned CNT arrays (see Figure 1). The synthetic details of the CNT arrays are summarized as follows: Fe/Al₂O₃ was used as the catalyst, ethylene served as the

carbon source, and Ar with 6% H₂ was used to carry the precursor to a tube furnace, where the growth took place. The reaction temperature was controlled at 750°C and the reaction time was typically between 10 and 20 min. CNT fibers were directly spun from the high-quality aligned CNT array, and the fiber diameter was controlled from 6 to 20 μm by varying the initial ribbon, a bunch of nanotubes pulled out from the array at the beginning of the spinning. The CNT fibers can be spun with lengths of tens of meters or even longer, and the fiber is uniform in diameter. The density of the nanotube fiber was calculated to be on the order of 1 g·cm⁻³, and its linear density was on the order of 10 μg·m⁻¹, relative to 10 mg·m⁻¹ and 20–100 mg·m⁻¹ for cotton and wool yarns, respectively [1, 62]. As shown in Figure 1(c), the CNT fibers are flexible and will not break after being bent, folded, or even tied many times. High-resolution transmission electron microscopy (see Figure 1(d)) indicates a multiwalled structure for the building nanotubes with diameter of approximately 8.5 nm in the fiber. The high degree of alignment of the component nanotubes gives the fiber excellent mechanical and electrical properties.

3. The Applications of Carbon Nanotube Fibers

3.1. Dye-Sensitized Solar Cells (DSC) Based on Carbon Nanotube Fibers. A DSC, a low-cost solar cell, is based on

a semiconductor formed between a photosensitized anode and an electrolyte, a photoelectrochemical system. The DSC can convert solar energy to electric energy, which is a promising technology to use renewable energies, and have typically been fabricated from rigid plates [63]. Solar cells are unfavorable for many applications, especially in the fields of portable and highly integrated equipment. As a result, flexible devices have become the subject of active research as a good solution [64]. In particular, weavable fiber devices are very promising and have attracted increasing attention in recent years. The CNT fibers in fiber-shaped photovoltaic devices have been widely incorporated into active layers to improve charge separation and transport or directly used as electrodes, for example, as counter electrode in replacement of conventional platinum in a planar DSC to catalyze the reduction of triiodide. For random CNT networks, the charges have to cross a lot of contacting points, so the charge transport in the random CNT networks is much slower than that in the CNT fibers. Fiber solar cells based on metal wires, glass fibers, or polymer fibers have been investigated [37–42]. Metal wires and glass fibers have bad flexibility, and conductive performance of polymer fibers is not good. So Chen et al. [2] and Luo et al. [3] developed a novel solar cell based on flexible, light-weight, ultrastrong, and semiconductive CNT fibers (Figure 2). They used CNT/N719 composite fibers to fabricate the organic solar cells on fluorine-doped tin oxide, and the power conversion efficiencies can reach 2.6%; the high alignment of CNTs arrays in the fiber allows charges to separate and transport along the fibers efficiently, which provides a fiber solar cell with high performance. The efficiency of the above fiber device may be further improved through the increase of the open-circuit photovoltage value by shifting the Fermi level of nanotubes more negatively, increasing fill factor by improving the electric contact between the fiber and the charge collector and increasing the short-circuit photocurrent value by enhancing the dye loading of the nanotube fiber. This discovery expands the scope of materials and architectures available for photovoltaic devices.

To take advantage of the CNT fibers, Cai and his coauthors [5] designed and fabricated an all CNT fibers dye-sensitized solar cell; CNT/N719 and CNT/PVDF fibers in Figure 3 were used as working and counter electrodes in replacement of metal wire electrode, respectively. The power conversion efficiency of this kind of photovoltaic wires was greatly improved through modification at the working electrode, for example, incorporation of titanium dioxide nanomaterials. But a short circuit was produced in this device. However, it remained challenging to obtain an ideal all CNT fibers dye-sensitized solar cell.

In order to overcome the above shortcomings, Chen et al. [8] fabricated a polymer fiber solar cell on the basis of spun CNT fibers as the electrode (Figures 4(a) and 4(b)), and the maximum energy conversion efficiency of this solar cell is only 0.15%. Although the cell efficiency is low, this work provides an effective route to the development of fiber-shaped polymer solar cells. More efforts will be paid to improve the photovoltaic performance by further increasing the electrical properties of the CNT fiber and tuning the morphology and structure of the titanium dioxide

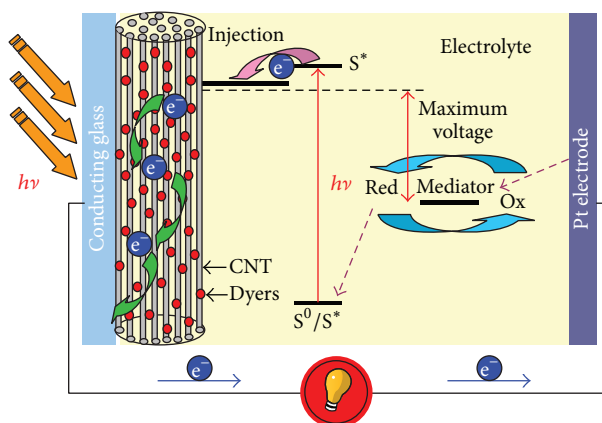


FIGURE 2: Schematic diagram of the production and transportation of photoelectron in a nanotube fiber solar cell [2].

nanotube. So the researchers [6] developed a fiber-shaped DSC based on flexible, ultralight, and ultrastrong CNT fibers as both working and counter electrodes (Figure 5), and the conversion efficiency is up to 2.94%. This fiber solar cell may be easily scaled up for a practical application, as the power conversion efficiency is independent of both the cell length and the incident light. And Chen and his coauthors [9] have studied the performance of a fiber dye-sensitized solar cell by using a CNT fiber as the counter electrode and a titanium wire modified with perpendicularly aligned TiO_2 nanotubes as the working electrode (Figure 4(c)). This novel interface design provides the photovoltaic wire with a high efficiency of 4.6%. The photovoltaic wires can be easily integrated into various flexible devices by a convenient weaving technology, which remains challenging to conventional planar solar cells.

On this basis, Yang and his coauthors [17] have developed fiber-shaped photovoltaic devices based on graphene/Pt composite fibers (Figure 6). The high flexibility, mechanical strength, and electrical conductivity of graphene fibers resulted in a certified maximum energy conversion efficiency of 8.45%, which is much higher than that of the aforementioned fiber-shaped photovoltaic devices. These flexible fiber solar cells can act as woven fabrics to make textiles by a conventional weaving technology, which enables a wide variety of applications in portable devices, for example, power regeneration for space aircraft and clothing integrated photovoltaics. These discoveries also provide a paradigm to develop new materials for high-performance solar cells.

Pan et al. [46] developed an organic thiolate/disulfide redox couple with low absorption in the visible region for use in fabricating fiber dye-sensitized solar cells (see Figure 7(a)). These flexible wire devices achieved high energy conversion efficiencies with a maximal value of 7.33%. This work also opens a new avenue in the development of highly efficient optoelectronic and electronic devices by designing matchable materials in different parts and making effective structures. At the same time, a coaxial DSC fiber [14] has been fabricated with a highly aligned multiwalled CNT sheet as the counter electrode (see Figure 7(b)), and energy conversion efficiency of 4.10% is achieved. The coaxial DSC fiber also shows a

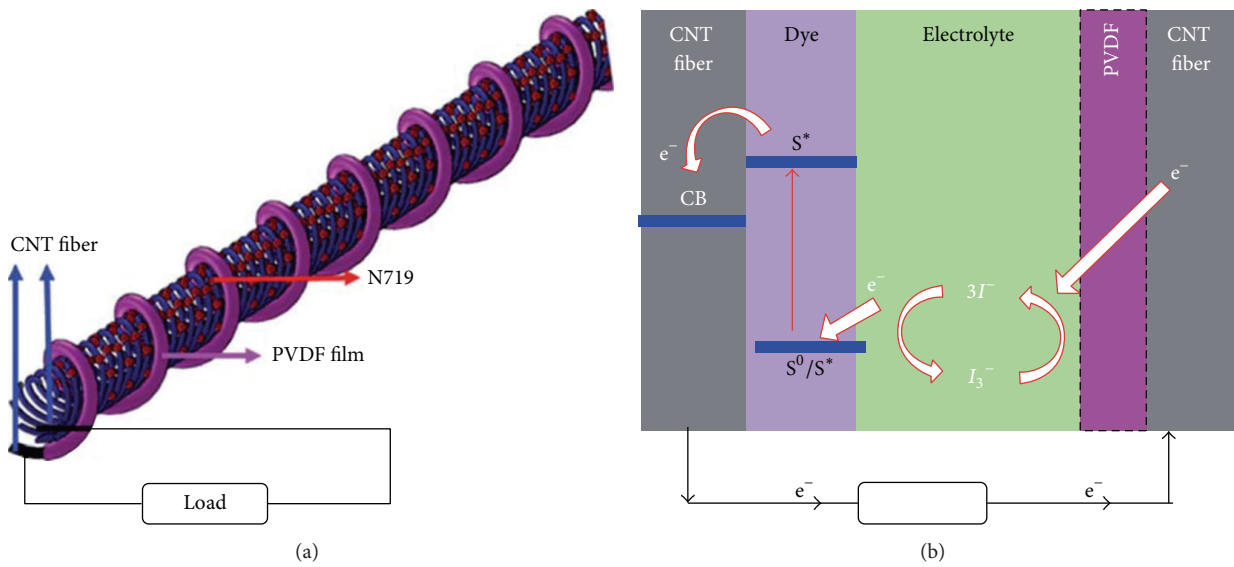


FIGURE 3: (a) Schematic illustration of a photovoltaic wire with two twined CNT fibers as working and counter electrodes, respectively. (b) The working principle of the CNT fiber-based sensitized photovoltaic wire, in which CB represents conduction band of CNT [5].

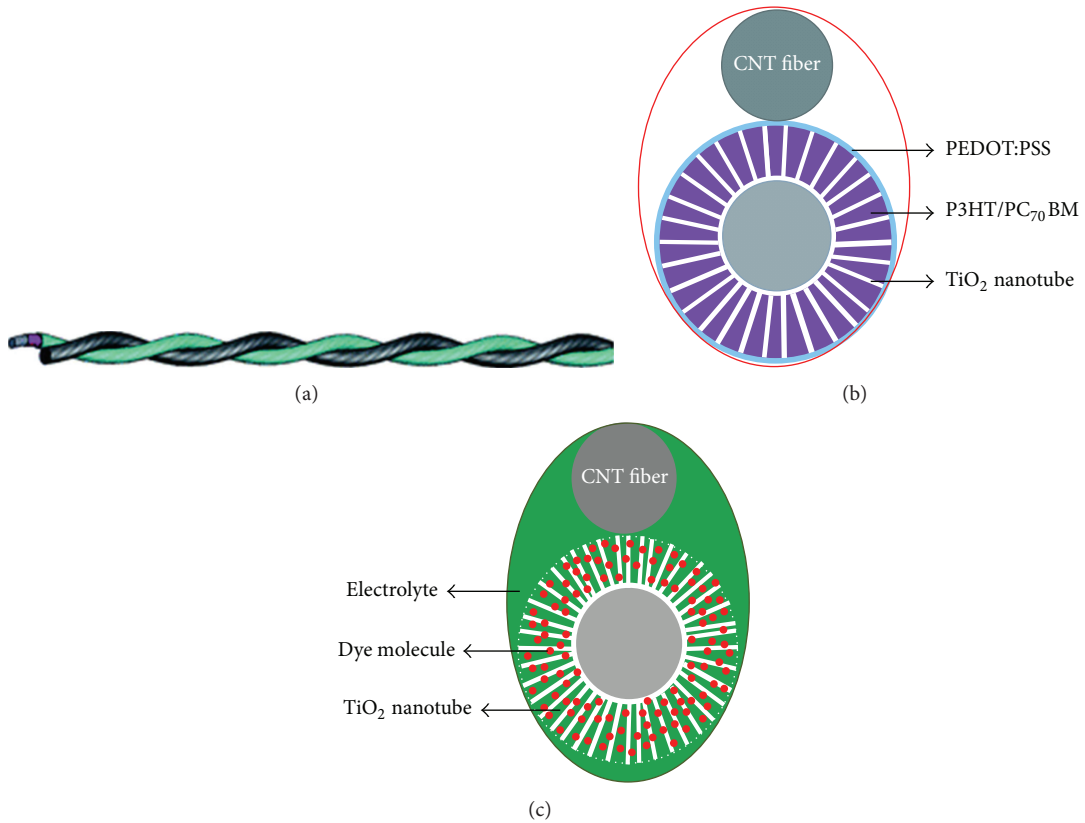


FIGURE 4: (a) Schematic illustration of side view of a fiber solar cell, (b) a polymer fiber solar cell from top view [8], and (c) a fiber-shaped dye-sensitized solar cell by top view [9]. Here an aligned TiO₂ nanotube-modified titanium wire as the working electrode is twined with one CNT fiber as the counter electrode to produce the fiber solar cell.

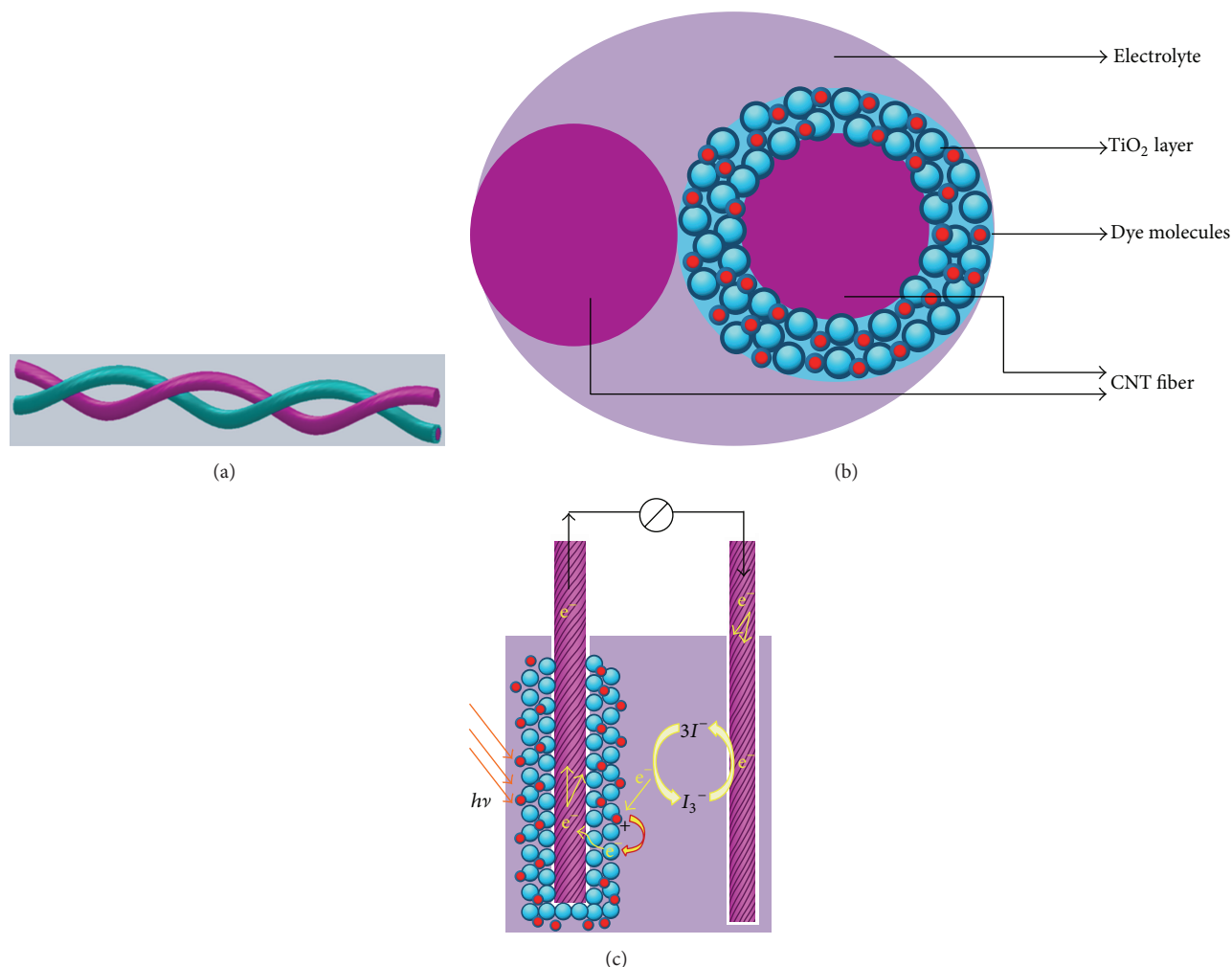


FIGURE 5: Schematic illustration of a wire-shaped DSC fabricated from two CNT fibers. (a) Two CNT fibers twined into a cell. (b) Top view of a cell. (c) Working mechanism [6].

high flexibility and stability. Although a fiber-shaped DSC has been demonstrated in this work, the aligned multiwalled CNT sheet can be also used as an electrode material to fabricate coaxial, fiber-shaped polymer solar cells and other various optoelectronic and electronic devices.

The above fiber solar cells need liquid electrolyte, which is volatile, so device performance is not stable. In order to overcome this problem, Sun et al. [19] developed a quasi-solid-state, coaxial DSC fiber (see Figure 8), which has a high performance including a high thermal stability and flexibility that offer particularly promising applications for flexible devices at high temperatures. This fiber DSC has also established some foundations for future photovoltaics and electronics with an ongoing push towards smaller and faster devices that are still confined to the planar silicon wafer.

3.2. Supercapacitor Based on Carbon Nanotube Fibers. Supercapacitor, formerly electric double-layer capacitor or pseudocapacitor, is one important electrochemical energy storage device that has been extensively developed for many

applications. The energy storage capability, power delivery capability, and cycle life of supercapacitor are highly desired to satisfy the increasing performance demands. CNT fibers have been explored as both electrode materials and electrode additives for developing high-performance supercapacitors which based on CNT fibers recently attracted more attention. Cai et al. [24] synthesized highly aligned multiwalled CNT-polyaniline composite fibers with excellent mechanical, electrical, and electrochemical properties through an easy electrodeposition process. They were further twisted to fabricate a fiber-shaped supercapacitor (see Figure 9) with high specific capacitances up to 263 mF cm^{-1} . The light weight, high flexibility, high strength, and good weavability provide them with promising applications in various fields. This work also presents a fabrication paradigm for the development of high performance energy storage devices based on the use of new electrode nanomaterials. A flexible and wearable electric double-layer capacitor wire by twisting two aligned multiwalled CNT/ordered mesoporous carbon composite fibers as electrodes has been developed.

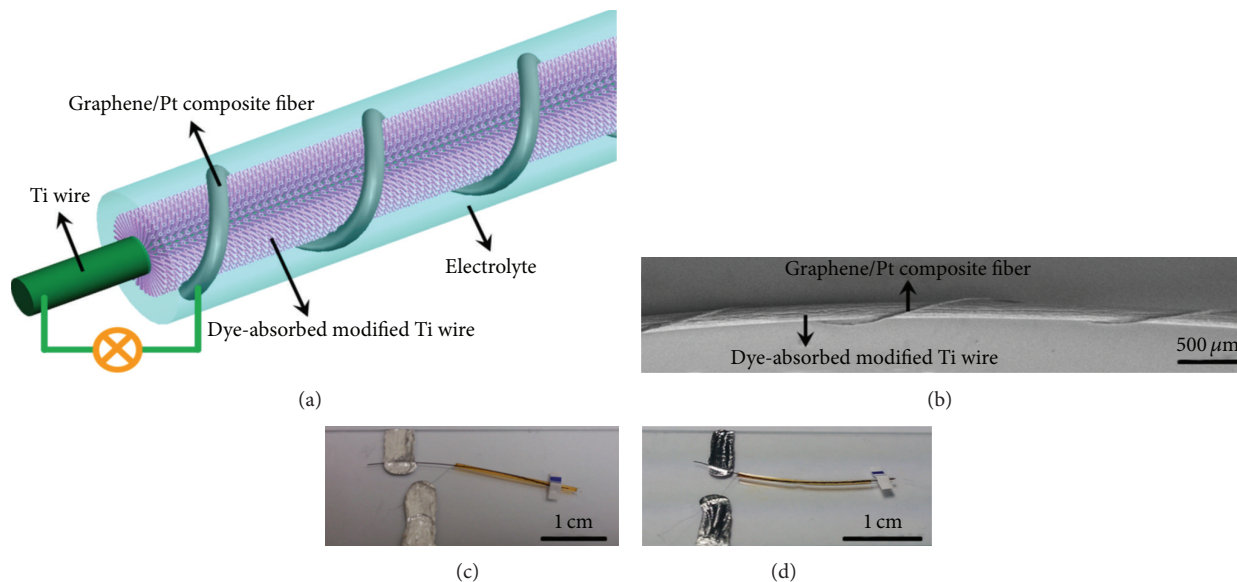


FIGURE 6: Dye-sensitized photovoltaic wire prepared by using a graphene/Pt composite fiber as the counter electrode and a Ti wire impregnated with TiO_2 nanotubes as the working electrode. (a) Schematic illustration. (b) SEM image. (c) and (d) Photographs of photovoltaic wires sealed in a capillary glass tube and flexible fluorinated ethylene propylene tube, respectively [17].

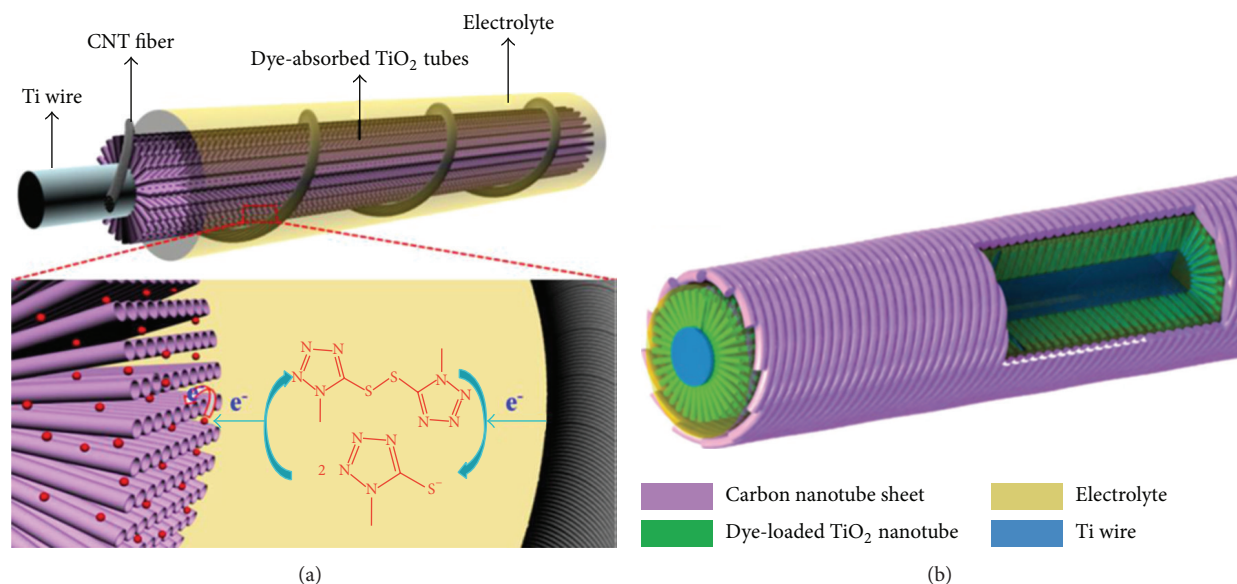


FIGURE 7: (a) Schematic illustration of a photovoltaic wire with a CNT fiber as the counter electrode, a Ti wire impregnated with titania nanotubes as the working electrode, and the thiolate/disulfide redox couple as the electrolyte [46]. (b) Schematic illustration of the coaxial DSC fiber [14].

As the ordered mesoporous carbon is incorporated into the axially aligned multiwalled CNT skeleton to combine the structure and property advantages of the two components in the composite fiber electrode, the electric double-layer capacitor wire exhibits high specific capacitance and long life stability. Compared with the conventional planar structure, the capacitor wire is also lightweight and can be integrated into various textile structures that are particularly promising for portable and wearable electronic devices.

And then Chen et al. [25] developed coaxial electric double-layer capacitor fibers from the CNT fibers (see Figure 10), which functioned as two electrodes with a polymer gel sandwiched between them. The unique coaxial structure had decreased the contact resistance between the two electrodes with a maximum discharge capacitance of 59 F g^{-1} (32.09 F cm^{-3} or $29 \mu\text{F cm}^{-1}$ or 8.66 mF cm^{-2}), much higher than 4.5 F g^{-1} of the electric double-layer capacitor by twisting two CNT fibers together. These electric double-layer

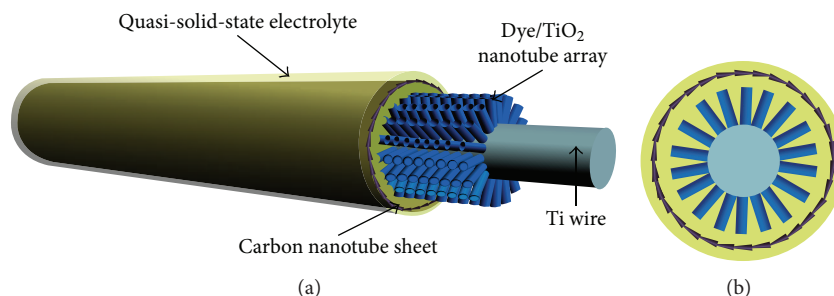


FIGURE 8: Schematic illustration of the quasi-solid-state, coaxial, fiber-shaped DSC. (a) Side view. (b) Cross-sectional view [19].

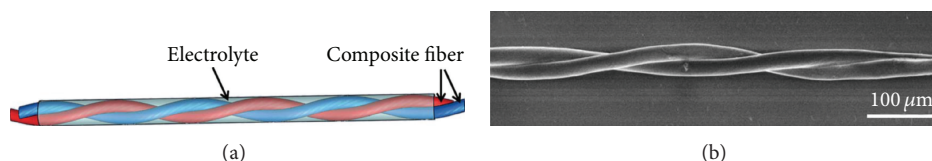


FIGURE 9: Two aligned multiwalled CNT-polyaniline composite fibers twisted into a supercapacitor wire. (a) Schematic illustration. (b) Typical scanning electron microscopy image [24, 28].

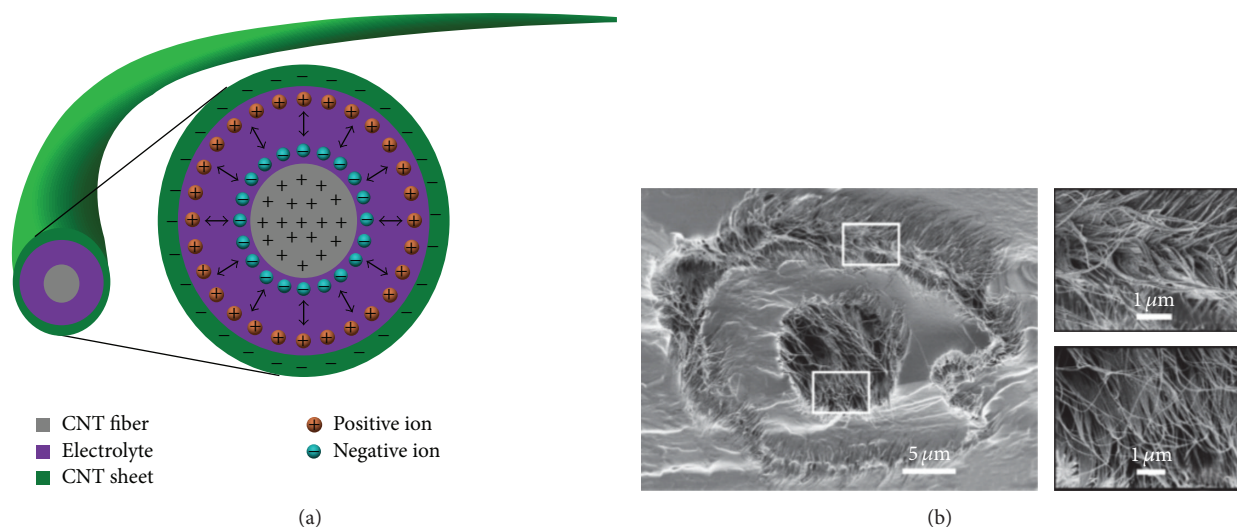


FIGURE 10: Schematic illustration to both the cross-sectional structure and mechanism for the high electrochemical property of the coaxial electric double-layer capacitor fiber. (a) The electropositive CNT fiber and electronegative CNT sheet functioned as the positive and negative electrodes, respectively; (b) SEM images at low (left image) and high (right images) magnifications for a cross section. The right images correspond to the left rectangle-labeled areas [25].

capacitor fibers exhibit energy densities up to 1.88 Wh kg^{-1} and power densities up to 755.9 W kg^{-1} . In addition, they are flexible and stretchable and can be easily scaled up with high efficiency and low cost. These electric double-layer capacitor fibers also represent the first demonstration of stretchable energy devices in a fiber format, which is critically important for the practical application in the flexible equipment such as various electronic textiles. This work further provides a general and effective strategy in the development of highly efficient electronic devices.

Yang et al. [47] and Xu et al. [65] developed highly stretchable, fiber-shaped, high-performance supercapacitors

(see Figure 11). Aligned CNT sheets that are sequentially wrapped on an elastic fiber serve as two electrodes (see Figure 11(a)). The use of aligned CNT sheets offers combined remarkable properties including high flexibility, tensile strength, electrical conductivity, and mechanical and thermal stability. As a result, the fiber-shaped supercapacitor maintains a high specific capacitance of approximately 18 F/g after stretch by 75% for 100 cycles. The high stretchability and specific capacitance have been simultaneously achieved by designing a coaxial structure that favors high contact areas between the electrode and electrolyte besides the combined remarkable properties enabled by the aligned CNTs.

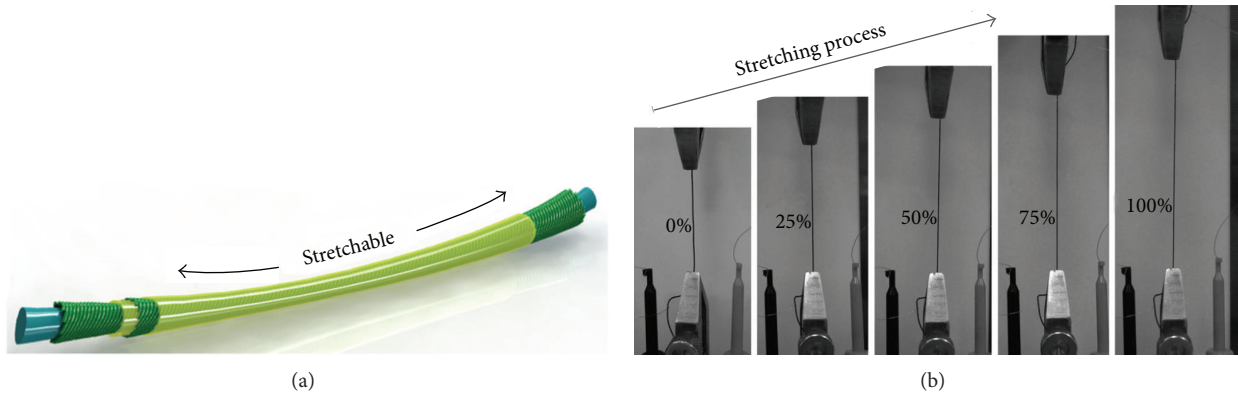


FIGURE 11: (a) A highly stretchable, fiber-shaped supercapacitor with a coaxial structure. (b) Photograph of the fiber-shaped supercapacitor with different strains of 0%, 25%, 50%, 75%, and 100% [47].

3.3. Lithium Ion Battery Based on Carbon Nanotube Fibers.

Lithium ion batteries are receiving considerable attention in applications, ranging from portable electronics to electric vehicles, due to their superior energy density over other rechargeable battery technologies. However, lighter, thinner, and higher capacity lithium ion batteries necessitate ongoing research for novel materials with improved properties. Researchers require a concerted development of both electrodes and electrolyte to improve battery capacity, cycle life, and charge-discharge rates while maintaining the highest degree of safety available. CNT fibers are a candidate material for use in lithium ion batteries. A fiber device can be easily woven into textiles or other structures to exhibit unique and promising applications. CNT fibers as a conductive additive at a lower weight loading than conventional carbons, like carbon black and graphite, present a more effective strategy to establish an electrical percolation network. Ren et al. [22] used twisted CNT fibers and composite fibers to produce both fiber-shaped lithium ion batteries with high capacitive performances (see Figure 12). The microsupercapacitor fiber was fabricated by twisting two CNT fibers and showed a mass specific capacitance of 13.31 F/g, area specific capacitance of 3.01 mF/cm², or length specific capacitance of 0.015 mF/cm at 2×10^{-3} mA (1.67 A/g). The fiber-shaped battery was produced by twisting a CNT fiber and a lithium wire which functioned as positive and negative electrodes, respectively. The specific capacity was calculated as 94.37 mAh/cm³ or 174.40 mAh/g at 2×10^{-3} mA. The energy and power densities in both supercapacitors and batteries could be further greatly improved by incorporation of MnO₂ nanoparticles into CNT fibers. For instance, the charge and discharge energy densities achieved 92.84 and 35.74 mWh/cm³ while the charge and discharge power densities were 3.87 and 2.43 W/cm³ at 2×10^{-3} mA in the fiber-shaped microbattery. The combined flexible fiber structure and high tensile strength also enable promising applications in various fields; for example, these fibers can be easily integrated into electronic textiles by a conventional weaving technique. This work further presented a fabrication paradigm in the development of novel storage devices by using strong and conductive nanostructured fibers as effective electrodes.

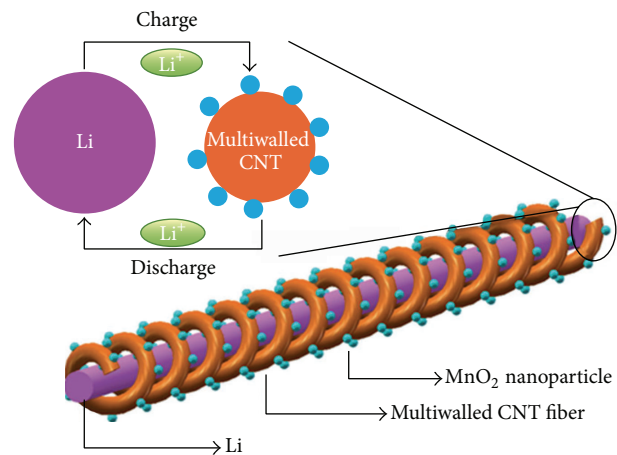


FIGURE 12: Fiber-shaped lithium ion battery fabricated by twisting an aligned multiwalled CNTs/MnO₂ composite fiber and Li wire as positive and negative electrodes, respectively. The inserted top left image shows the charge-discharge process [22].

And then Lin et al. [23] reported the development of twisted, aligned multi-walled CNT/Si composite fiber anodes for flexible, fiber-shaped lithium ion batteries (Figure 13). A thin layer of silicon was coated on the outer surface of the aligned multiwalled CNTs to form a core-sheath structure that can effectively and simultaneously exploit the high specific capacity of the silicon and high electrical conductivity of the multiwalled CNTs, while the designed space with sizes of tens to hundreds of nanometers among the aligned composite nanotubes can effectively counterbalance the volume change of the silicon component. As a result, the aligned multiwalled CNTs/Si fiber electrode shows a combined high specific capacity and cyclic stability. And this fiber electrode offers unique advantages, such as being lightweight and weavable compared with the conventional planar structure. This core-sheath architecture and aligned structure of the multiwalled CNTs/Si composite nanotubes display a remarkable electrochemical performance, including high specific capacity and cyclic stability.

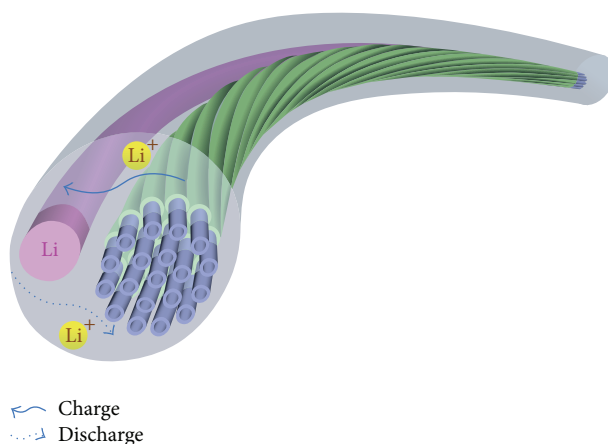


FIGURE 13: Schematic illustration of a half lithium-ion battery based on the aligned multiwalled CNT/Si composite fiber as a working electrode with a lithium wire as both counter and reference electrodes [23].

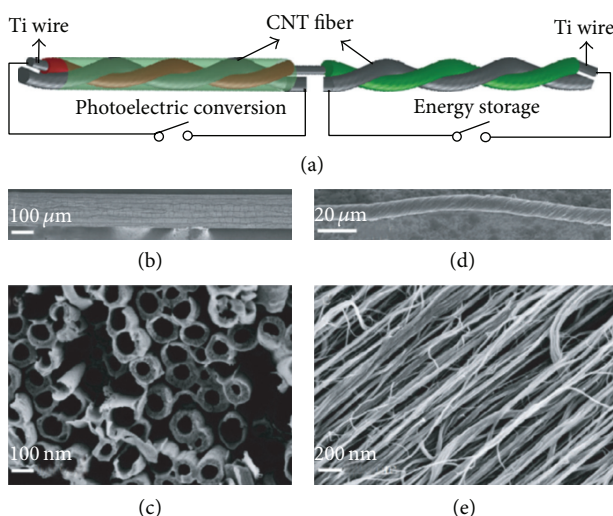


FIGURE 14: (a) The integrated wire-shaped device for photoelectric conversion and energy storage. (b), (c) Scanning electron microscopy images of aligned titania nanotubes grown on a Ti wire by electrochemical anodization for 2 h at low and high magnifications, respectively. (d) and (e) SEM images of a CNT fiber at low and high magnifications, respectively [48].

3.4. The Integrated Wire-Shaped Device Based on Carbon Nanotube Fibers. The solar energy is converted into electric energy which is transferred through external electric wires to electrochemical devices, such as lithium ion batteries and supercapacitors. To further improve the energy conversion and storage efficiency, it is important to simultaneously realize the two functions, photoelectric conversion (PC) and energy storage (ES), in one device. Recently, attempts have been made to directly stack a photovoltaic cell and a supercapacitor into one device which can absorb and store solar energy. Chen et al. [48] developed an integrated energy fiber to simultaneously realize PC and ES with high efficiency (see Figure 14). A titanium wire was modified in sections with aligned titania nanotubes on the surface. Active materials for PC and ES were then coated onto the modified parts within titania nanotubes. CNT fibers were twisted with the modified Ti wire to produce the desired device. The Ti wire and CNT

fiber had been used as electrodes. Figure 14(a) schematically shows a wire in which one part is capable of PC and one part is capable of ES. This integrated fiber device exhibits an overall photoelectric conversion and storage efficiency of 1.5%. The fiber structure also enables unique and promising applications; for example, it is envisaged that it can be easily integrated into electronic textiles by a well-defined weaving technique and serve as a self-powering system for portable microelectronic devices and equipment.

Zhang et al. [33] have developed an all solid-state, coaxial, and self-powered “energy fiber” which simultaneously converts solar energy to electric energy and stores it (Figure 15). The design of a coaxial structure in the “energy fiber” enables promising advantages for both PC and ES. For the PC part, it is similar to the efficient planar polymer solar cell in the radial direction, so the generated charges can be rapidly separated and transported to produce high photocurrents. For the ES

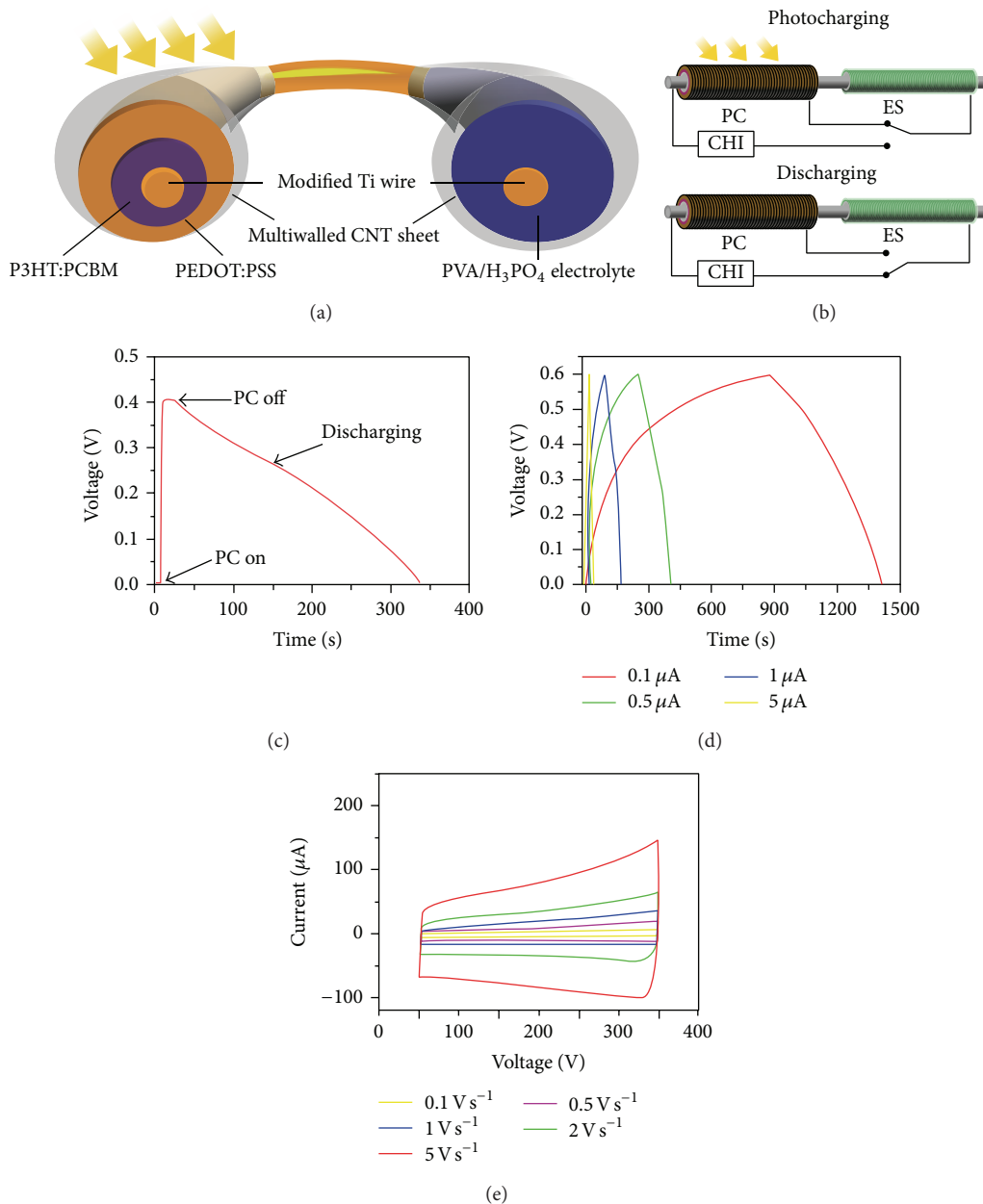


FIGURE 15: (a) Schematic illustration to the structure of all-solid-state, coaxial, and integrated fiber device. The left and right sections correspond to the PC and ES parts, respectively. (b) Schematic diagram shows the circuit connection state in the process of charging and discharging. (c) Charging-discharging curve with a current of 0.1 μA during the discharging process. (d) Galvanostatic charging-discharging curve of the self-charging fiber at different current from 0.1, 0.5, and 1 to 5 μA. (e) Cyclic voltammograms at increasing scan rates from 0.1 to 5 V s⁻¹ [33].

part, different from the explored twisted structure of two fiber electrodes with high electrical resistances, the coaxial structure with much higher effective contact area also favors a rapid charge transport. In addition, the use of flexible, transparent, strong, and conductive multiwalled CNT sheets can also greatly improve the photoelectric conversion and energy storage. The “energy fiber” is flexible and can be scaled up for the practical application by the well-developed textile technology and may open a new avenue to future photoelectronics and electronics.

And then Chen et al. [49] have developed an energy fiber which can simultaneously realize energy conversion and storage by integrating dye-sensitized solar cell and electrochemical capacitor (see Figure 16). A Ti wire substrate modified with perpendicularly aligned titania nanotubes on the surface and horizontally aligned CNT sheets serves as two electrodes in the integrated “energy fiber” device. The maximal photoelectric conversion efficiency achieved 2.73%, while the energy storage efficiency reached 75.7% with specific capacitances up to 0.156 mFcm⁻¹ or 3.32 mFcm⁻² and

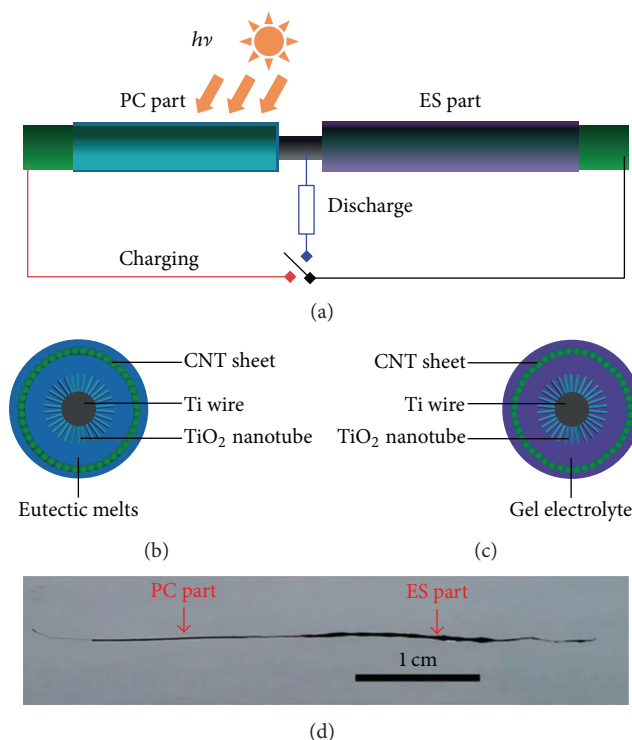


FIGURE 16: (a) Schematic illustration of the structure of the coaxially integrated dye-sensitized solar cell and electrochemical capacitor into an “energy fiber.” (b) and (c) Cross-sectional views of the PC and ES parts of the “energy fiber,” respectively. (d) Photograph of an “energy fiber” [49].

power densities up to 0.013 mW cm^{-1} or 0.27 mW cm^{-2} at a current of 50 mA. The “energy fiber” is flexible and stable and shows promising applications for various portable electronic devices that require lightweight and weavable materials.

4. Conclusions

The recent studies of the CNT fibers for optoelectric conversion and energy storage are summarized. The CNT has been extensively applied to fiber-shaped dye-sensitized solar cell, lithium ion battery, supercapacitor, and their integrated device. These “energy fibers” are flexible, stable, and stretchable and show promising applications to be integrated into electronic textiles by a well-defined weaving technique and serve as a self-powering system for portable microelectronic devices and equipment.

Conflict of Interests

The authors declare that there is no conflict of interests regarding the publication of this paper.

Acknowledgments

The authors thank the support of the New-Century Training Program Foundation for the Talents by the Ministry of

Education of China (NCET-11-0979) and Introducing High-level Talent Research Start Fund of Central South University of Forestry and Technology (no. 1040281).

References

- [1] M. Zhang, K. R. Atkinson, and R. H. Baughman, “Multifunctional carbon nanotube yarns by downsizing an ancient technology,” *Science*, vol. 306, no. 5700, pp. 1358–1361, 2004.
- [2] T. Chen, S. T. Wang, Z. B. Yang et al., “Flexible, light-weight, ultrastrong, and semiconductive carbon nanotube fibers for a highly efficient solar cell,” *Angewandte Chemie: International Edition*, vol. 50, no. 8, pp. 1815–1819, 2011.
- [3] Y. F. Luo, Z. Q. Gong, M. D. He, X. J. Wang, Z. H. Tang, and H. Chen, “Fabrication of high-quality carbon nanotube fibers for optoelectronic applications,” *Solar Energy Materials and Solar Cells*, vol. 97, pp. 78–82, 2012.
- [4] Z. Yang, T. Chen, R. He et al., “Aligned carbon nanotube sheets for the electrodes of organic solar cells,” *Advanced Materials*, vol. 23, no. 45, pp. 5436–5439, 2011.
- [5] F. Cai, T. Chen, and H. Peng, “All carbon nanotube fiber electrode-based dye-sensitized photovoltaic wire,” *Journal of Materials Chemistry*, vol. 22, no. 30, pp. 14856–14860, 2012.
- [6] T. Chen, L. Qiu, Z. Cai et al., “Intertwined aligned carbon nanotube fiber based dye-sensitized solar cells,” *Nano Letters*, vol. 12, no. 5, pp. 2568–2572, 2012.
- [7] T. Chen, L. Qiu, H. G. Kia, Z. Yang, and H. Peng, “Designing aligned inorganic nanotubes at the electrode interface: towards highly efficient photovoltaic wires,” *Advanced Materials*, vol. 24, no. 34, pp. 4623–4628, 2012.

- [8] T. Chen, L. Qiu, H. Li, and H. Peng, "Polymer photovoltaic wires based on aligned carbon nanotube fibers," *Journal of Materials Chemistry*, vol. 22, no. 44, pp. 23655–23658, 2012.
- [9] T. Chen, L. B. Qiu, H. G. Kia, Z. B. Yang, and H. S. Peng, "Designing aligned inorganic nanotubes at the electrode interface: towards highly efficient photovoltaic wires," *Advanced Materials*, vol. 24, no. 34, pp. 4623–4628, 2012.
- [10] S. Q. Huang, Z. B. Yang, L. L. Zhang et al., "A novel fabrication of a well distributed and aligned carbon nanotube film electrode for dye-sensitized solar cells," *Journal of Materials Chemistry*, vol. 22, no. 33, pp. 16833–16838, 2012.
- [11] Z. Yang, L. Li, H. Lin et al., "Penetrated and aligned carbon nanotubes for counter electrodes of highly efficient dye-sensitized solar cells," *Chemical Physics Letters*, vol. 549, pp. 82–85, 2012.
- [12] X. Fang, Z. Yang, L. Qiu et al., "Core-sheath carbon nanostructured fibers for efficient wire-shaped dye-sensitized solar cells," *Advanced Materials*, vol. 26, no. 11, pp. 1694–1698, 2013.
- [13] G. Guan, Z. Yang, L. Qiu et al., "Oriented PEDOT:PSS on aligned carbon nanotubes for efficient dye-sensitized solar cells," *Journal of Materials Chemistry A*, vol. 1, no. 42, pp. 13268–13273, 2013.
- [14] H. Sun, X. You, Z. Yang, J. Deng, and H. Peng, "Winding ultrathin, transparent, and electrically conductive carbon nanotube sheets into high-performance fiber-shaped dye-sensitized solar cells," *Journal of Materials Chemistry A*, vol. 1, no. 40, pp. 12422–12425, 2013.
- [15] Z. Yang, T. Chen, R. He et al., "A novel carbon nanotube/polymer composite film for counter electrodes of dye-sensitized solar cells," *Polymer Chemistry*, vol. 4, no. 5, pp. 1680–1684, 2013.
- [16] Z. Yang, M. Liu, C. Zhang, W. W. Tjiu, T. Liu, and H. Peng, "Carbon nanotubes bridged with graphene nanoribbons and their use in high-efficiency dye-sensitized solar cells," *Angewandte Chemie-International Edition*, vol. 52, no. 14, pp. 3996–3999, 2013.
- [17] Z. Yang, H. Sun, T. Chen, L. Qiu, Y. Luo, and H. Peng, "Photovoltaic wire derived from a graphene composite fiber achieving an 8.45 % energy conversion efficiency," *Angewandte Chemie—International Edition*, vol. 52, no. 29, pp. 7545–7548, 2013.
- [18] H. Li, Z. Yang, L. Qiu et al., "Stable wire-shaped dye-sensitized solar cells based on eutectic melts," *Journal of Materials Chemistry A*, vol. 2, no. 11, pp. 3841–3846, 2014.
- [19] H. Sun, H. Li, X. You et al., "Quasi-solid-state, coaxial, fiber-shaped dye-sensitized solar cells," *Journal of Materials Chemistry A*, vol. 2, no. 2, pp. 345–349, 2014.
- [20] H. Sun, Z. Yang, X. Chen et al., "Photovoltaic wire with high efficiency attached onto and detached from a substrate using a magnetic field," *Angewandte Chemie*, vol. 52, no. 32, pp. 8276–8280, 2013.
- [21] X. Fang, Z. Yang, L. Qiu et al., "Core-sheath carbon nanostructured fibers for efficient wire-shaped dye-sensitized solar cells," *Advanced Materials*, vol. 26, no. 11, pp. 1694–1698, 2014.
- [22] J. Ren, L. Li, C. Chen et al., "Twisting carbon nanotube fibers for both wire-shaped micro-supercapacitor and micro-battery," *Advanced Materials*, vol. 25, no. 8, pp. 1155–1159, 2013.
- [23] H. Lin, W. Weng, J. Ren et al., "Twisted aligned carbon nanotube/silicon composite fiber anode for flexible wire-shaped lithium-ion battery," *Advanced Materials*, vol. 26, no. 8, pp. 1217–1222, 2014.
- [24] Z. Cai, L. Li, J. Ren, L. Qiu, H. Lin, and H. Peng, "Flexible, weavable and efficient microsupercapacitor wires based on polyaniline composite fibers incorporated with aligned carbon nanotubes," *Journal of Materials Chemistry A*, vol. 1, no. 2, pp. 258–261, 2013.
- [25] X. Chen, L. Qiu, J. Ren et al., "Novel electric double-layer capacitor with a coaxial fiber structure," *Advanced Materials*, vol. 25, no. 44, pp. 6436–6441, 2013.
- [26] H. Lin, L. Li, J. Ren et al., "Conducting polymer composite film incorporated with aligned carbon nanotubes for transparent, flexible and efficient supercapacitor," *Scientific Reports*, vol. 3, article 1353, 2013.
- [27] M. K. Liu, Y. E. Miao, C. Zhang et al., "Hierarchical composites of polyaniline-graphene nanoribbons-carbon nanotubes as electrode materials in all-solid-state supercapacitors," *Nanoscale*, vol. 5, no. 16, pp. 7312–7320, 2013.
- [28] J. Ren, W. Bai, G. Guan, Y. Zhang, and H. Peng, "Flexible and weavable capacitor wire based on a carbon nanocomposite fiber," *Advanced Materials*, vol. 25, no. 41, pp. 5965–5970, 2013.
- [29] Z. Yang, J. Deng, X. Chen, J. Ren, and H. Peng, "A highly stretchable, fiber-shaped supercapacitor," *Angewandte Chemie International Edition*, vol. 52, no. 50, pp. 13453–13457, 2013.
- [30] L. Li, Z. Yang, H. J. Gao et al., "Vertically aligned and penetrated carbon nanotube/polymer composite film and promising electronic applications," *Advanced Materials*, vol. 23, no. 32, pp. 3730–3735, 2011.
- [31] T. Chen, L. Qiu, Z. Yang et al., "An integrated "energy wire" for both photoelectric conversion and energy storage," *Angewandte Chemie—International Edition*, vol. 51, no. 48, pp. 11977–11980, 2012.
- [32] Z. Yang, L. Li, Y. Luo et al., "An integrated device for both photoelectric conversion and energy storage based on free-standing and aligned carbon nanotube film," *Journal of Materials Chemistry A*, vol. 1, no. 3, pp. 954–958, 2013.
- [33] Z. Zhang, X. Chen, P. Chen et al., "Integrated polymer solar cell and electrochemical supercapacitor in a flexible and stable fiber format," *Advanced Materials*, vol. 26, no. 3, pp. 466–470, 2014.
- [34] X. Chen, H. Sun, Z. Yang et al., "A novel "energy fiber" by coaxially integrating dye-sensitized solar cell and electrochemical capacitor," *Journal of Materials Chemistry A*, vol. 2, no. 6, pp. 1897–1902, 2014.
- [35] H. Sun, X. You, J. Deng et al., "Novel graphene/carbon nanotube composite fibers for efficient wire-shaped miniature energy devices," *Advanced Materials*, vol. 26, no. 18, pp. 2868–2873, 2014.
- [36] Y. Luo, L. Li, S. Huang, T. Chen, and H. Luo, "Functional nanomaterials for optoelectric conversion and energy storage," *Journal of Nanomaterials*, vol. 2013, Article ID 414193, 2 pages, 2013.
- [37] J. Liu, M. A. Namboothiry, and D. L. Carroll, "Optical geometries for fiber-based organic photovoltaics," *Applied Physics Letters*, vol. 90, no. 13, Article ID 133515, 2007.
- [38] J. Ramier, C. J. G. Plummer, Y. Leterrier, J.-E. Månson, B. Eckert, and R. Gaudiana, "Mechanical integrity of dye-sensitized photovoltaic fibers," *Renewable Energy*, vol. 33, no. 2, pp. 314–319, 2008.
- [39] B. O'Connor, K. P. Pipe, and M. Shtein, "Fiber based organic photovoltaic devices," *Applied Physics Letters*, vol. 92, no. 19, Article ID 193306, 2008.
- [40] X. Fan, Z. Chu, F. Wang et al., "Wire-shaped flexible dye-sensitized solar cells," *Advanced Materials*, vol. 20, no. 3, pp. 592–595, 2008.
- [41] B. Weintraub, Y. Wei, and Z. L. Wang, "Optical fiber/nanowire hybrid structures for efficient three-dimensional dye-sensitized

- solar cells," *Angewandte Chemie—International Edition*, vol. 48, no. 47, pp. 8981–8985, 2009.
- [42] M. R. Lee, R. D. Eckert, K. Forberich, G. Dennler, C. J. Brabec, and R. A. Gaudiana, "Solar power wires based on organic photovoltaic materials," *Science*, vol. 324, no. 5924, pp. 232–235, 2009.
- [43] Q. Li, Y. Li, X. Zhang et al., "Structure-dependent electrical properties of carbon nanotube fibers," *Advanced Materials*, vol. 19, no. 20, pp. 3358–3363, 2007.
- [44] C. Yen, Y. Lin, S. Liao et al., "Preparation and properties of a carbon nanotube-based nanocomposite photoanode for dye-sensitized solar cells," *Nanotechnology*, vol. 19, no. 37, Article ID 375305, 2008.
- [45] S. Berson, R. de Bettignies, S. Bailly, S. Guillerez, and B. Jousselme, "Elaboration of P3HT/CNT/PCBM composites for organic photovoltaic cells," *Advanced Functional Materials*, vol. 17, no. 16, pp. 3363–3370, 2007.
- [46] S. Pan, Z. Yang, H. Li, L. Qiu, H. Sun, and H. Peng, "Efficient dye-sensitized photovoltaic wires based on an organic redox electrolyte," *Journal of the American Chemical Society*, vol. 135, no. 29, pp. 10622–10625, 2013.
- [47] Z. B. Yang, J. Deng, X. L. Chen, J. Ren, and H. S. Peng, "A highly stretchable, fiber-shaped supercapacitor," *Angewandte Chemie—International Edition*, vol. 52, no. 50, pp. 13453–13457, 2013.
- [48] T. Chen, L. Qiu, Z. Yang et al., "An integrated "energy wire" for both photoelectric conversion and energy storage," *Angewandte Chemie*, vol. 51, no. 48, pp. 11977–11980, 2012.
- [49] X. Chen, H. Sun, Z. Yang et al., "A novel "energy fiber" by coaxially integrating dye-sensitized solar cell and electrochemical capacitor," *Journal of Materials Chemistry A*, vol. 2, no. 6, pp. 1897–1902, 2014.
- [50] Y.-L. Li, I. A. Kinloch, and A. H. Windle, "Direct spinning of carbon nanotube fibers from chemical vapor deposition synthesis," *Science*, vol. 304, no. 5668, pp. 276–278, 2004.
- [51] X. Zhang, Q. Li, T. G. Holesinger et al., "Ultrastrong, stiff, and lightweight carbon-nanotube fibers," *Advanced Materials*, vol. 19, no. 23, pp. 4198–4201, 2007.
- [52] X. Zhang, Q. Li, Y. Tu et al., "Strong carbon-nanotube fibers spun from long carbon-nanotube arrays," *Small*, vol. 3, no. 2, pp. 244–248, 2007.
- [53] K. Koziol, J. Vilatela, A. Moisala et al., "High-performance carbon nanotube fiber," *Science*, vol. 318, no. 5858, pp. 1892–1895, 2007.
- [54] H. Peng, "Aligned carbon nanotube/polymer composite films with robust flexibility, high transparency, and excellent conductivity," *Journal of the American Chemical Society*, vol. 130, no. 1, pp. 42–43, 2008.
- [55] H. Peng, M. Jain, Q. Li, D. E. Peterson, Y. Zhu, and Q. Jia, "Vertically aligned pearl-like carbon nanotube arrays for fiber spinning," *Journal of the American Chemical Society*, vol. 130, no. 4, pp. 1130–1131, 2008.
- [56] H. Peng, M. Jain, D. E. Peterson, Y. Zhu, and Q. Jia, "Composite carbon nanotube/silica fibers with improved mechanical strengths and electrical conductivities," *Small*, vol. 4, no. 11, pp. 1964–1967, 2008.
- [57] H. Peng, X. Sun, F. Cai et al., "Electrochromatic carbon nanotube/polydiacetylene nanocomposite fibres," *Nature Nanotechnology*, vol. 4, no. 11, pp. 738–741, 2009.
- [58] T. Chen, Z. Cai, Z. Yang et al., "Nitrogen-doped carbon nanotube composite fiber with a core-sheath structure for novel electrodes," *Advanced Materials*, vol. 23, no. 40, pp. 4620–4625, 2011.
- [59] Z. B. Yang, X. M. Sun, X. L. Chen et al., "Dependence of structures and properties of carbon nanotube fibers on heating treatment," *Journal of Materials Chemistry*, vol. 21, no. 36, pp. 13772–13775, 2011.
- [60] W. Guo, C. Liu, X. Sun, Z. Yang, H. G. Kia, and H. Peng, "Aligned carbon nanotube/polymer composite fibers with improved mechanical strength and electrical conductivity," *Journal of Materials Chemistry*, vol. 22, no. 3, pp. 903–908, 2012.
- [61] L. Qiu, X. Sun, Z. Yang, W. Guo, and H. Peng, "Preparation and application of aligned carbon nanotube/polymer composite material," *Acta Chimica Sinica*, vol. 70, no. 14, pp. 1523–1532, 2012.
- [62] Y. F. Luo, X. L. Wang, M. D. He, X. Li, and H. Chen, "Synthesis of high-quality carbon nanotube arrays without the assistance of water," *Journal of Nanomaterials*, vol. 2012, Article ID 542582, 5 pages, 2012.
- [63] H. Qin, S. Wenger, M. Xu et al., "An organic sensitizer with a fused dithienothiophene unit for efficient and stable dye-sensitized solar cells," *Journal of the American Chemical Society*, vol. 130, no. 29, pp. 9202–9203, 2008.
- [64] M. B. Schubert and J. H. Werner, "Flexible solar cells for clothing," *Materials Today*, vol. 9, no. 6, pp. 42–50, 2006.
- [65] P. Xu, T. Gu, Z. Cao et al., "Carbon nanotube fiber based stretchable wire-shaped supercapacitors," *Advanced Energy Materials*, vol. 4, no. 3, 2014.

Review Article

Progress in Application of CNTs in Lithium-Ion Batteries

Li Li, Hui Yang, Dongxiang Zhou, and Yingyue Zhou

The Department of Chemistry, College of Food Science and Technology, Shanghai Ocean University, Shanghai 201306, China

Correspondence should be addressed to Li Li; l-li@shou.edu.cn

Received 15 April 2014; Revised 31 May 2014; Accepted 31 May 2014; Published 10 August 2014

Academic Editor: Yongfeng Luo

Copyright © 2014 Li Li et al. This is an open access article distributed under the Creative Commons Attribution License, which permits unrestricted use, distribution, and reproduction in any medium, provided the original work is properly cited.

The lithium-ion battery is widely used in the fields of portable devices and electric cars with its superior performance and promising energy storage applications. The unique one-dimensional structure formed by the graphene layer makes carbon nanotubes possess excellent mechanical, electrical, and electrochemical properties and becomes a hot material in the research of lithium-ion battery. In this paper, the applicable research progress of carbon nanotubes in lithium-ion battery is described, and its future development is put forward from its two aspects of being not only the anodic conductive reinforcing material and the cathodic energy storage material but also the electrically conductive framework material.

1. Introduction

New energy technology is of great importance for the sustainable development of human society. Li-ion batteries (LIBs) have been developing robustly due to their advantages such as high energy density, long cycle life, low self-discharge, nonmemory effect, and environmental friendliness since they were developed by SONY corp. in 1990. And they have been widely applied in many fields including mobile phone, laptop, and auto power batteries. Meanwhile, it is anticipated that they can be used on a large scale in the storage of clean electric energy that is produced by solar energy and wind energy [1, 2]. Carbon nanotubes (CNTs) can serve as one-dimensional nanomaterials and they can be made into two kinds of CNTs—single-walled carbon nanotube (SWCNT) rolled up by one-layer graphene and multiwalled carbon nanotube (MWCNT) rolled up by multilayer graphene. CNTs have excellent mechanical, electrical, and chemical properties due to their light weight and perfect connection in their hexagon structure. In recent years, with the progress in the research on CNTs and nano materials, the prospect of wide application of CNTs is emerging [3–6], because of its excellent electrochemical properties, (10^6 Sm^{-1} at 300 K for single-walled CNTs (SWCNTs) and $>10^5 \text{ Sm}^{-1}$ for multiwalled nanotubes (MWCNTs)), low density, high rigidity, and high tensile strength [7]. CNTs are widely used in lithium-ion batteries, both as the anode material and the conductive additive in the composite electrodes. In this paper, the

progress of latest research on the application of CNTs in anode and cathode materials is discussed.

2. Application of CNTs in Anode Materials

CNTs have the typical hollow structure of multilayer and are the coaxial circular tube mainly composed of a dozen of layers of carbon atoms arrayed in hexagon. There is a certain distance, 0.34 nm, between two neighboring layers with the diameter ranging from 2 nm to 20 nm. The low density of carbon atom and the typical structure of CNTs allow the imbedding of Li-ion. Thanks to the structure defect on the surface and edge of CNTs, as well as the nanoscale slit between walls, Li-ion can be imbedded not only anywhere on CNTs wall, but also between layers [8]. Udomvech et al. [9] have found out that it is easy for Li/Li⁺ to spread along the wall inside; however, it is easier for Li/Li⁺ to be imbedded on the location of C6 on the surface outside; thus, an effective opening on the end or adding more defects will help Li/Li⁺ to spread inside. Nishidate and Hasegawa [10] have discovered after calculating that the defect on the surface of SWNT facilitates the entrance of Li⁺ and the entrance of Li⁺ can add more defects in turn, which deepens the imbedding of Li⁺ and shortens the process; as a result, Li⁺ can be imbedded not only anywhere inside the tube, but also in the gap. Studies on electron density have revealed that complete charge transfer happens between Li⁺ and CNTs after Li⁺ is imbedded in

the tube. Meanwhile, the imbedding causes slight structural deformations in the CNTs. And inside CNTs, the gap between layers allow Li^+ to enter [11]. Wu et al. [12] found that the structures of the CNT played major roles in both specific capacity and cycle life. Slightly graphitized CNT showed a specific capacity of 640 mAh g^{-1} during the first charge and after 20 charge/discharge cycles the charge capacity of the slightly graphitized samples degraded to 65.3%, whereas well-graphitized carbon nanotubes showed a specific capacity of 282 mAh g^{-1} during the first charge and 91.5% of their original charge capacities after 20 charge/discharge cycles.

2.1. Raw CNTs as Anode Materials. The graphite structure of CNTs allows that CNTs can be used as the electrode material in the place of graphite. As is often the case, the specific capacity of SWCNT is $400\text{--}460 \text{ mAh g}^{-1}$, but it can reach above 1000 mAh g^{-1} after introducing defects on the surface. The solid electrolyte interface (SEI) can be formed at around 0.9 V, which can remarkably reduce the specific capacity during the first electrochemical cycle. Landi et al. [13] discover that although the melting point of propene carbonate (PC) is quite low, the graphitic layer can be peeled off when graphite is used as the anode material, and if SWCNT is used as the anode material, when PC is added to the system consisting of ethylene carbonate (EC) and dimethyl carbonate (DMC), the reversible specific capacity can be improved effectively, retaining 95% with the specific capacity of 520 mAh g^{-1} at the 10th cycle. A layer of 3,4-ethylenedioxythiophene (PEDOT) with good conductivity and electrochemical activity has been polymerized on the top of MWCNT array by Chen et al. [14] to improve the conductivity between the CNTs. A layer of polymer as thick as $0.5 \mu\text{m}$ can be formed by painting 10% PVDF in acetonitrile solvent on the layer of PEDOT, and the intensity can peel the array completely off the silicon substrate. As the anode material, a specific capacity of 265 mAh g^{-1} could be reached without noticeable fading of capacity after 50 cycles. Pushparaj et al. [15] have built a multilayer nanocomposite serving as the thin power storage device with electrode, separator, current collector, and electrolyte in a way similar to that of building blocks. An even interface that can be peeled off can be formed after the mixture of cellulose and 1-butyl 3-methyl imidazole chloride which is a PTIL permeating into the CNTs array. The interface can be used as the electrode to assemble supercapacitors or lithium-ion batteries or to assemble the double-layer device by capacitors and lithium batteries. As the lithium-ion battery, the working voltage is 2.1 V, and the specific capacity of CNTs is 430 mAh g^{-1} after the first charge and discharge while that will drop to 110 mAh g^{-1} after 10 cycles. The specific capacity of 373 mAh g^{-1} and good cyclability have been realized by Zhang et al. [16] through using the CNTs array as the electrode. He also discusses the lithium storage mechanism of carbon tube. It is believed that the graphite in the inner layer provides better conducting passages so as to avoid the loss of active material in the process of charge and discharge. Therefore, the performance of cycle is good. There are many defects on the graphene layer on the surface of carbon tube. During the process of charging,

Li^+ can insert between graphite layers through these defects, which will deform the graphene layer close to these defects, especially on the top of CNTs, as shown in Figure 1 where the deformation is quite obvious. More defects on the top will be produced in the period of nucleation growth of carbon tube. The reversible specific capacity of 279 mAh g^{-1} is lower than that of graphene (372 mAh g^{-1}), corresponding to a chemical composition of about $\text{Li}_{0.75}\text{C}_6$. The diffusion distance of Li^+ inside the wall of carbon tube is very short, less than 10 nm, which avoids the damages to the inner layer and the section far from defects. This frame with high mechanical strength can avoid the damage on materials in the process of charge and discharge, guaranteeing its cyclability.

The resistance of CNTs array is $1\text{--}5 \text{ k}\Omega/\text{cm}^2$, which hinders the electron transportation and generates heat. Therefore, the CNTs growing directly on the current collector have attracted people's concern. The CNTs can grow on the carbon layer which is loaded on metal foil by Chen et al. [17]. The resistance between carbon and copper foil is only $1\text{--}2 \Omega$; this resistance of carbon tube is similar to that of carbon, which can be ignored. After 100 cycles, the specific capacity is 572 mAh g^{-1} and the compound between Li and graphite layer is $\text{Li}_{1.6}\text{C}_6$. Carbon sheet CNTs composite electrode material is produced by Chen et al. [18] through chemical vapor deposition (CVD) on carbon fiber sheet. There is good contact between CNTs and carbon fiber sheet and the CNTs have put their advantage of large specific surface, so it has good low-temperature stability and chemical stability. Its specific capacity was retained at 546 mAh g^{-1} after 50 cycles. The catalyst of Ti-Ni thin layer ($20\text{--}25 \text{ nm}$) on copper foil has been loaded by Lahiri et al. [19] through magnetron sputtering and thus carbon tubes can directly grow on the copper foil through CVD method, which produces the electrode free of adhesive. The carbon tube is tightly connected to the copper foil which is used as the substrate and current collector with good conductivity, which makes the specific capacity of electrode (900 mAh g^{-1} , 1C) three times as that of graphite. Even at high charge/discharge current densities of 3C rate, the electrode still keeps good curve. It shows negligible capacity decay with capacity retention of 99% after 50 cycles.

As a flexible electrode, CNT fiber or CNT paper can be used as active material and current collector, which can effectively reduce the contact resistance and electrode weight. With the development of wearable electrode application, the material of thread binding energy storage has attracted researchers' attention [20, 21]. The self-supporting CNT paper has some strength and stability without any adhesion, so it can be used as the electrode material of flexible device and helps improve the specific capacity of electrode. Ng et al. [22] have produced SWNT agents through the ultrasound of SWNT and Triton X-100 in water; the unsupported SWNT paper serving as the electrode of lithium-ion batteries has also been produced through pressure filtration method in which poly (vinylidene fluoride) (PVDF) membrane with the aperture of $0.22 \mu\text{m}$ is used as filter membrane. The electrolyte is 1 mol/L LiPF_6 in ethylene carbonate (EC) and dimethyl carbonate (DMC) (1:1), and its specific capacity

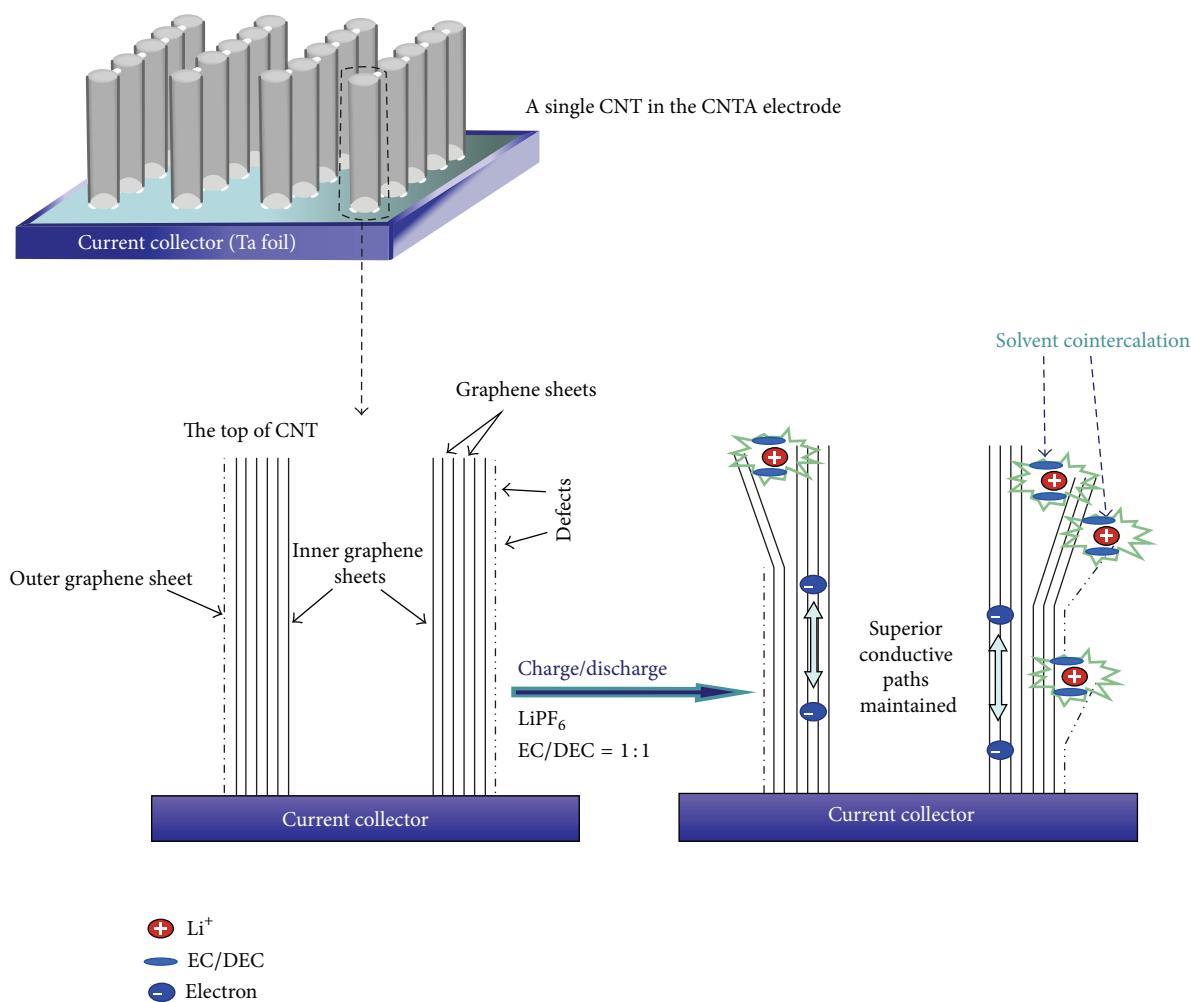


FIGURE 1: Schematic representation of the microstructure and energy storage characteristics of the CNTA anodes.

is 180 mAh g^{-1} which will be raised to about 230 mAh g^{-1} with good cyclicality when loaded on Ni layer. Chew et al. [23] have produced self-supported CNT film with this method and the performances of SWCNTs, DWCNTs, and MWCNTs are compared. In the study on oxidation process, MWCNTs display good reversibility and the Li/Li^+ redox peaks appear at about the potential of 0.15 V. As for graphite material, the peaks correspond to lithium insertion and extraction. In particular, the 10–20 nm hollow MWCNTs facilitate the spread of Li^+ . Oxidation peak of Li/Li^+ appears at the position of 1.2 V in SWCNTs and DWCNTs, which means Li^+ has reacted with the oxygen-containing functional groups on the surface to produce COO^-Li^+ or Li^+ has reacted with hydrogen in the CNTs. Li^+ can mainly penetrate the place between the external walls of SWCNTs and DWCNTs and their inner walls. Comparatively speaking, MWCNT is more suitable for lithium-ion batteries.

2.2. Composite of CNTs as the Anode Material. In the past decades, to improve the performance of CNT electrode, materials with high specific capacity such as metallic oxide and Si are combined with CNTs in many studies, which

play its advantage of huge specific surface area and the role of supporting and conducting as the frame. Ren et al. [24] have produced flexible fibrous lithium-ion batteries through spinning CNTs into fibers on which MnO_2 was deposited, which is shown in Figure 2. As an N-type wide-band-gap semiconductor (300 k , $E_g = 3.6 \text{ eV}$), SnO_2 is one kind of anode material of great application potential [25]. However large volume change during lithiation/delithiation process makes the electrochemical active particles crack and lose the electrical contact, which results in fast decline of reversible capacity. MWCNTs composite material coated by a layer of even SnO_2 is produced by Wang et al. [26] through thioglycolic acid assisted hydrothermal method and the thickness of SnO_2 can be controlled by reaction conditions. After the SEI interface is formed in the first cycle, the specific capacity is improved and the stability is quite good. After 50 cycles of complete charge and discharge of 0.2 C rate, the specific capacity stays at 435 mAh g^{-1} which is higher than that of graphite. $\text{SnCl}_{0.5}$ and Sb nanoparticles are produced on the external wall of CNTs through reduction reaction by Chen et al. [27]. When the weight ratio of Sb is 36 wt%, the specific capacity is 462 mAh g^{-1} while when the weight ratio of SnSb

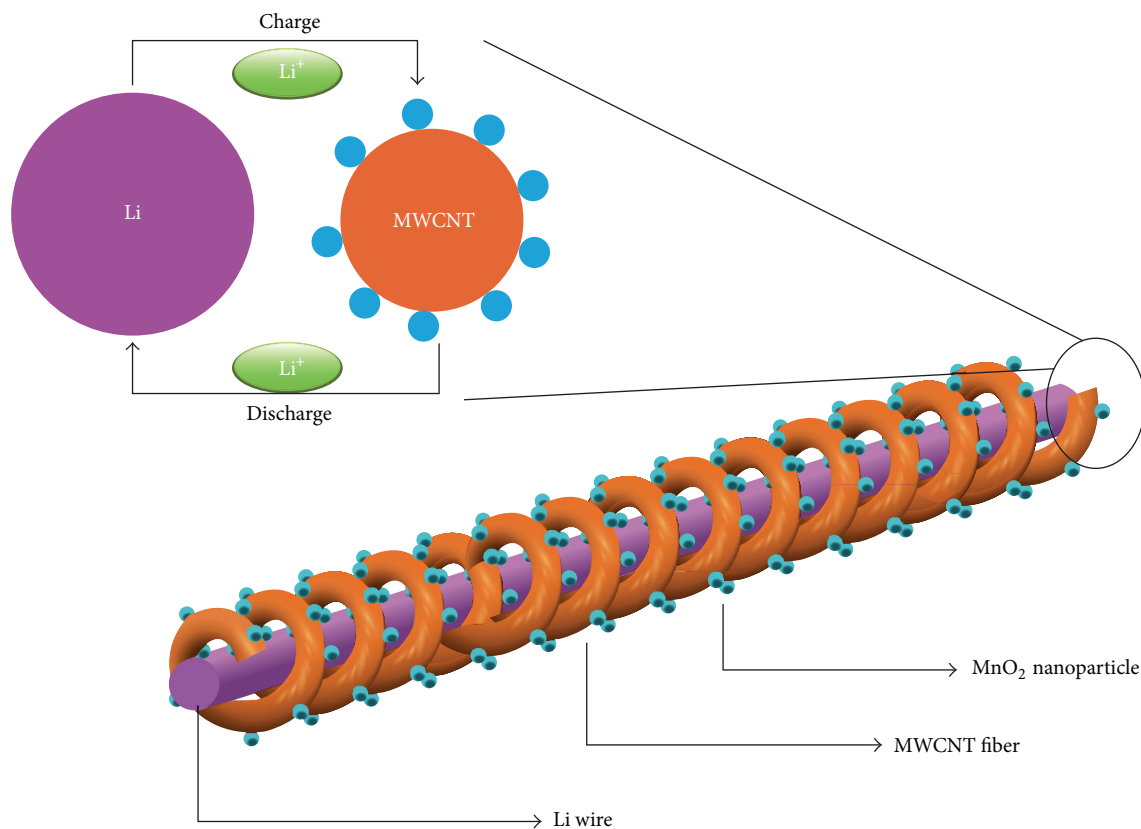


FIGURE 2: Schematic illustration to the wire-shaped lithium-ion battery fabricated by twisting an aligned MWCNT/MnO₂ composite fiber and Li wire as positive and negative electrodes, respectively.

is 56 wt%, the specific capacity is 518 mAh g⁻¹. After 30 cycles, the capacity retention is 62.1% and 67.2%, respectively. As a buffer, CNTs reduce the damage on nanoparticles during lithiation/delithiation. Zhang et al. [28] have produced the CNTs array with CVD before drawing the array into a CNT film on which nano SnO₂ is produced. The specific capacity is as high as 850 mAh g⁻¹, and it retains 100% after 65 cycles at 0.01–3 V voltage range. The Co₃O₄ was reported to show a high theoretic reversible specific capacity of 890 mAh g⁻¹ [29]. Park et al. [30] fabricated vertically aligned mesoporous carbon nanotubes (MCTs) by a dual template method: a hard template-assisted sol-gel process. And this kind of carbon nanotubes was filled with Co₃O₄ nanoparticles (NPs). As an anode material, it shows a high reversible capacity of about 627 mAh g⁻¹ after the 50th discharge. The small-size of Co₃O₄ NPs improved electrochemical performance of Co₃O₄/MCT and the rapid diffusion of Li-ions was induced by the three-dimensional structure of the MCT. Therefore, the 3D nanostructure can be widely applied to other promising 11 conversion reaction electrodes to improve LIB performance.

Si and Lithium can produce Si-Li alloy phase of Li₂Si₅ whose specific capacity can reach 4200 mAh g⁻¹, having great potential of replacing graphite; thus, the study on silicon nanowire, porous silicon, and carbon fiber covering amorphous silicon has been accelerated. One-dimensional composite material has been produced by Wang and Kumta [31] through depositing nanocrystalline silicon on CNTs

array with simple two-step pouring liquor into chemical vapor deposition. Nano silicon clusters connect tightly with CNTs, which minimize the loss when the silicon connects with and desorbs from Li⁺. This novel structure has good rate capability, high reversible capacity (2050 mAh g⁻¹), and good stability (after 25 cycles, only 20% has been reduced). The capacity loss results mainly from the damage on the boundary between the silicon and CNTs as well as the hindering of Li⁺ transport by SEI's weakening. Rong et al. [32] proposed a kind of anode material—a layer of silicon formed on SWNTs. This method can effectively improve the performance of silicon electrode easily. A rough surface can be formed on SWNT which produces a layer of buffer between copper foil current collector and silicon layer. At 0.1 C rate, the specific capacity is 2221 mAh g⁻¹ after 40 cycles, which is 3.6 times as that of silicon layer directly covering the copper foil and 11 times as that of SWNT. And after 40 cycles, a stable porous structure can be formed. Kawasaki et al. [33] add 9,10-Dihydroanthracene, β -carotene and hexabenzobenzene to form pod structure which obtained high irreversible specific capacity (>900 mAh g⁻¹). Compared with that of pure CNTs, the specific capacity of CNTs added with organics can be improved 2.5 times. Wang et al. [34] reported that super-aligned CNT films could be used as current collectors for LIBs. The CNT current collectors are with excellent flexibility, extremely low density, stronger adhesion, lower contact resistance, and higher energy density than those with metal

current collectors. Fu et al. [35] used the super-aligned CNT sheet as the current collector on which the silicon active material is deposited. The aligned CNT structure provides significant uniform deposition of silicon coatings. The charge capacity was 1494 mAh g^{-1} after 45 cycles with a capacity retention of over 94%. The CE for each cycle was stabilized above 98%. Lin et al. [36] reported the development of novel wire-shaped lithium-ion batteries fabricated by twisted, aligned multiwalled MWCNT/Si composite fiber anodes for flexibility. The Si exhibited a high capacity and remained at 1648 mAh g^{-1} in 30 cycles at 0.6 C (1 A g^{-1}). Weng et al. [37] used a new type anode which was fabricated by three-dimensionally aligned CNT/Si hybrid to develop for LIB. The LIBs have high specific capacity and cyclic stability which were retained at 1055 mAh g^{-1} after 1000 13 cycles at 5 A g^{-1} .

3. Application of CNTs in Cathode Material

Cathode material is the provider of Li^+ . Currently, the materials in lithium-ion batteries are mainly inorganic salts including LiCoO_2 of hexagonal layered structure, LiMn_2O_4 of spinel structure, and LiFePO_4 of olivine structure. In the circle of research, the conducting polymer used as the cathode material of lithium-ion batteries has got more and more attention. The cathode materials determine the safety performance of batteries and a major technical bottleneck of improving the specific capacity of batteries as well.

LiFePO_4 is a kind of cathode material which has been widely studied and applied because of its low price, environmental compatibility, high theory specific capacity (170 mAh g^{-1}), proper working voltage (3.42 V versus Li^+/Li), and secure safety. However, in the structure of LiFePO_4 , the PO_4 tetrahedral between the octahedron limits the change in the capacity of crystal lattice, influencing the intercalation of Li-atom and de-Li atom, which slows down the spread of ions of LiFePO_4 . Meanwhile, since there is no a continuous network of octahedron, electric conductor cannot be formed, which lowers the electronic conductivity of LiFePO_4 . Therefore, studies on the modification of LiFePO_4 all focus on how to improve the conductivity. $\text{LiFePO}_4/\text{MWCNTs}$ have been produced through hydrothermal by Jin et al. [38] who have explored the electrical property of batteries at room temperature. The conductivity of composite material at RT is $1.08 \times 10^{-1} \text{ S/cm}$, 8 times as that of pure LiFePO_4 . The CNTs added can not only improve the electronical conductivity, but also improve the Li^+ diffusion coefficient, reducing the crystallite size and transportation resistance. For the diffusion of Li^+ into LiFePO_4 , it has to pass a 1-dimensional passage in which the defect of LiFePO_4 will hinder the diffusion of Li^+ . As a result, how to reduce the defects is an important direction in the study on LiFePO_4 . On one hand, it is admitted that defects of amorphous substances such as FePO_4 cannot affect the diffusion of Li^+ , but the speed of Li^+ intercalation and deintercalation can be influenced by the low conductivity of FePO_4 . Core-shell nanowire has been produced from CNT-amorphous FePO_4 and been used in making anode by Kim et al. [39]. At 3.4 V, a smooth discharge voltage plateau appears and the specific capacity is

149 mAh g^{-1} , so it is of good stability. Similarly, Hosono et al. [40] has produced spinning LiFePO_4 whose core is MWCNTs and complex shell of LiFePO_4 and amorphous carbon, and this nanowire is used as cathode of lithium-ion batteries through electrostatic spinning. CNTs play a leading role in the electron transportation and inhibition the oxidation of Fe^{2+} . At 0.1 A g^{-1} , the specific capacity is 130 mAh g^{-1} , and the rate capability and cycle properties are excellent. LiMn_2O_4 -MWCNTs composite material has been produced by Liu et al. [41] with sol-gel method. As the 1-dimensional conductor in nanocomposite material, CNTs facilitate the transport of electron; the resistance of composite material is far lower than that of LiMn_2O_4 of spinel structure and displays high cycle stability after 20 cycles; the capacity retention is 99% while that of pure LiMn_2O_4 is only 9%. Xia et al. [42] synthesized ultrafine $\text{LiMn}_2\text{O}_4/\text{carbon nanotube (CNT)}$ nanocomposite by a one-step hydrothermal treatment. In the nanocomposite, the CNTs not only provide a conductive matrix, but also effectively reduce agglomeration of LiMn_2O_4 nanoparticles which between 10–20 nm in diameters are well crystallized and uniformly distributed in the CNT matrix. The nanocomposite with unique structural and morphological features exhibits superior high-rate capability and long term cycling stability, delivering discharge capacities of 116 mAh g^{-1} (92% retention) after 500 cycles at 1 C rate and 77 mAh g^{-1} (77% retention) even after 1000 cycles at 10 C. Porous material provides channels for a rapid diffusion of Li^+ and the scattered conductive network can effectively guarantee the supply of electron (Figure 3), which improves the diffusion speed of Li^+ . Porous LiFePO_4 -CNT composite material has been synthesized by Zhou et al. with sol-gel method [43]. The oxidation peak and reduction peak appear at 3.51 V and 3.38 V, respectively, and the potential difference is 0.13 V which improves the irreversibility and reaction activity.

Due to the innovative work of Tarascon which revealed a new strategy for high capacity electrodes by exhibiting that metal oxides can store more than one Li ion per transition metal atom, many researchers have investigated various conversion reaction compounds, such as metal nitrides, sulfides, fluorides, and oxides [44–46]. As a kind of novel cathode material, Vanadium pentoxide (V_2O_5) obtains the characteristics of low cost and being earth-rich and shows much higher energy density than traditional LiMn_2O_4 , LiCoO_2 , and LiFePO_4 materials [47]. But the multiphase transitions of V_2O_5 in the charge/discharge process correspond to the multiple voltage plateaus, which caused repeated damages to the structure of V_2O_5 . To improve the structural stability of V_2O_5 , Zhou et al. [48] synthesized vanadium oxide nanosheet-MWCNT composite via sol-gel method and subsequent hydrothermal treatment process. This nanosheet-MWCNT composite with distinct single phase transition feature displays high specific capacity and good cycling stability owing to its sheet-like nanostructure and uniform adding of MWCNTs, which makes this novel composite quite suitable. Cao and Wei [49] prepared $\text{V}_2\text{O}_5/\text{SWNT}$ hybrid films with mesoporous structure by a simple floating CVD method. Li^+ diffusivity can be promoted by 2 to 4 orders due to SWNTs. The hybrid films as cathodes for lithium-ion

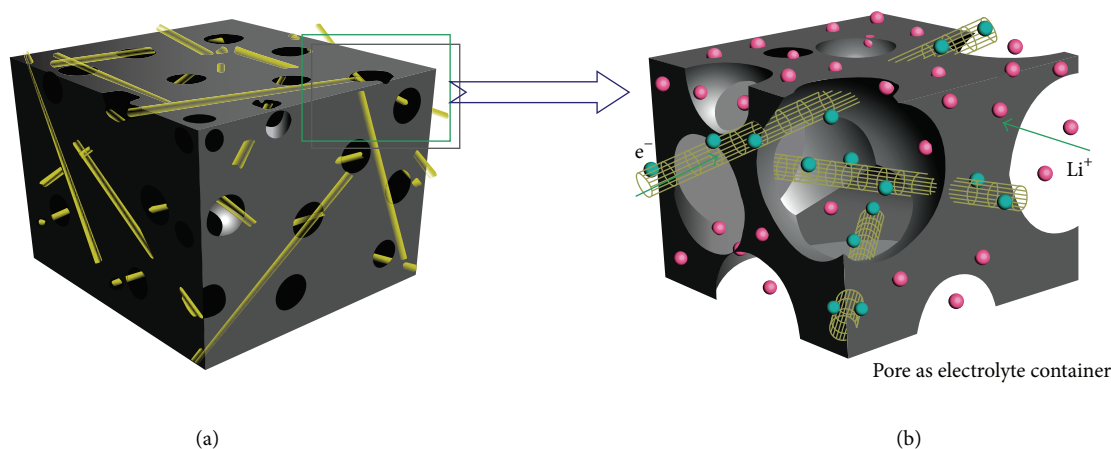


FIGURE 3: Schematic illustrations of the porous LiFePO_4 -CNT composite. (b) is an enlarged zone from (a), showing the corresponding electron transport and ion diffusion mechanisms.

batteries demonstrate a high rate capacity of 548 mAh g^{-1} at the discharge rate of 1C. Kim et al. [46] fabricated nanoarchitectures composed of FeF_3 nanoflowers on CNT branches by functionalizing the surfaces of CNT with FeF_3 . Electron transport made the nanostructured cathode deliver more than 210 mAh g^{-1} at a current rate of 20 mA g^{-1} with the specific energy about 650 Wh kg^{-1} under these conditions of average discharge voltage of about 3.1V in the voltage range 2.0–4.5 V, which was higher than conventional cathode materials.

In recent years, researchers have made a wide range of investigation on rechargeable lithium-sulfur (Li-S) batteries due to theoretically high specific capacity (1675 mAh g^{-1}), low cost, and environmentally benign sulfur. The rechargeable Li-S cell works through reducing S at the cathode on discharge to form various polysulphides combining with Li to finally produce Li_2S [50, 51]. The commercialization of lithium-sulfur batteries is hindered by inadequate electrode rechargeability and limited rate capability induced by sulfur active material loss and polysulfide shuttle reaction through dissolution into electrolyte. Wang et al. [51] synthesized three-dimensional carbon nanotube frameworks with bipyramidal sulfur particles by simple mixing of multiwalled carbon nanotubes (MWCNTs), sulfur powder, and capping agents in water/tetrahydrofuran. The Li-S cells deliver a specific discharge capacity of $\approx 1600 \text{ mAh g}^{-1}$ at 0.05 C on the first cycle. Guo et al. [52] fabricated disordered carbon nanotubes (DCNTs) due to a template wetting technique which means impregnating sulfur into DCNTs as cathode material for Li-S batteries. The superior cyclability (showed better stability of 72.9% retention after 100 cycles except the first one,) and Coulombic efficiency (at 0.25 C rate were averagely at 89% and 96% during 100 cycles) were demonstrated in the obtained sulfur-carbon tube cathodes.

As the cathode material of lithium batteries, conducting polymer has many characteristics such as being safe and easy to use. The conducting polymer such as polyacetylene and polypyrrole has great application potential. However, compared with inorganic cathode material, there

is a problem of low working voltage. Poly-PMT has drawn wide attention with its high oxidative potential (3.6 V versus Li/Li^+). With in situ polymerization, Kim et al. [53] have synthesized poly(PMT)/MCNT; PMT/CNT is used as the cathode while incombustible 1-Ethyl-3-methylimidazolium Tetrafluoroborate (EMIBF_4) and LiBF_4 make up the ionic liquid electrolyte. Polymer lithium-ion batteries of high safety and high voltage have been produced with the porous membrane of P (VdF-co-HFP) and the specific capacity at 1.0 C is 80 mAh g^{-1} . The specific capacity can be reduced dramatically by the degradation of or damage on polymer because of the contraction and swelling of polyaniline during the charge and discharge process. With the method of in situ polymerization, Sivakkumar and Kim [54] have produced PAN/CNT composite electrode material. The charge voltage remains at 3.7 V after 250 cycles; in the potential range of 2.0–3.9 V, the cell delivered a maximum discharge capacity of 86 mAh g^{-1} at the 80th cycle with an average Coulombic efficiency of 98%.

After carboxylation and amination, CNTs have been assembled as the cathode of lithium batteries by Horn with layer-by-layer method [55], and the thickness ranges from 20 nm to $30 \mu\text{m}$ or even more thicker. The output power, 10 times as that of ordinary lithium batteries, can reach 100 kW Kg^{-1} and the specific capacity preserves at the original one—about 200 mAh g^{-1} after 1000 cycles. This is the first report in which CNTs have been used as the cathode of lithium-ion batteries, and the reaction mechanism of $\text{C} = \text{O}_{\text{LBL-MWNT}} + \text{Li}^+ \leftrightarrow \text{C-O-Li}_{\text{LBL-MWNT}}$ is different from Li_xC formed by graphite material and Li^+ . This has widened and deepened the application of CNTs in lithium-ion batteries.

4. Prospect

As an electrode material for lithium-ion batteries, CNTs have promising prospect of application. Although the study on CNTs has made much progress, there is great potential. In future studies and researches, more efforts and energy should be invested in the following aspects. Firstly, it is necessary

to further the study on the lithium storage mechanism of CNTs. The influence of the tubes' length, diameter, number of walls, and defects on the wall on the performance of lithium storage should be analyzed and tested both theoretically and empirically in order to minimize the loss of specific capacity after the formation of SEI and to improve the stability and cycle performance. Secondly, the study on composite material of CNTs as electrode should be expanded. As the surface template and conductive frame with high specific capacity, CNTs can give greater play. Thirdly, the cost should be cut down, technology be simplified, and performance be stabilized in the real application of CNTs in electrode material.

Conflict of Interests

The authors declare that there is no conflict of interests regarding the publication of this paper.

Acknowledgments

This work was supported by Innovation Program of Shanghai Municipal Education Commission (14YZ120), the Shanghai Engineering Research Center of Aquatic-Product Processing & Preservation (11DZ2280300), and the National High Technology Research and Development Program of China (863 Program, 2012AA092301).

References

- [1] J.-M. Tarascon and M. Armand, "Issues and challenges facing rechargeable lithium batteries," *Nature*, vol. 414, no. 6861, pp. 359–367, 2001.
- [2] B. J. Landi, M. J. Ganter, C. D. Cress, R. A. DiLeo, and R. P. Raffaele, "Carbon nanotubes for lithium ion batteries," *Energy and Environmental Science*, vol. 2, no. 6, pp. 638–654, 2009.
- [3] L. Li, Z. Yang, H. Gao et al., "Vertically aligned and penetrated carbon nanotube/polymer composite film and promising electronic applications," *Advanced Materials*, vol. 23, no. 32, pp. 3730–3735, 2011.
- [4] G. Centi and S. Perathoner, "Problems and perspectives in nanostructured carbon-based electrodes for clean and sustainable energy," *Catalysis Today*, vol. 150, no. 1-2, pp. 151–162, 2010.
- [5] H. Peng and X. Sun, "Highly aligned carbon nanotube/polymer composites with much improved electrical conductivities," *Chemical Physics Letters*, vol. 471, no. 1-3, pp. 103–105, 2009.
- [6] H. Peng, M. Jain, Q. Li, D. E. Peterson, Y. Zhu, and Q. Jia, "Vertically aligned pearl-like carbon nanotube arrays for fiber spinning," *Journal of the American Chemical Society*, vol. 130, no. 4, pp. 1130–1131, 2008.
- [7] C. Casas and W. Li, "A review of application of carbon nanotubes for lithium ion battery anode material," *Journal of Power Sources*, vol. 208, no. 1, pp. 74–85, 2012.
- [8] X. Han, G. Qing, J. Sun, and T. Sun, "How many lithium ions can be inserted onto fused C₆ aromatic ring systems?" *Angewandte Chemie—International Edition*, vol. 51, no. 21, pp. 5147–5151, 2012.
- [9] A. Udomvech, T. Kerdcharoen, and T. Osotchan, "First principles study of Li and Li⁺ adsorbed on carbon nanotube: variation of tubule diameter and length," *Chemical Physics Letters*, vol. 406, no. 1-3, pp. 161–166, 2005.
- [10] K. Nishidate and M. Hasegawa, "Energetics of lithium ion adsorption on defective carbon nanotubes," *Physical Review B: Condensed Matter and Materials Physics*, vol. 71, no. 24, Article ID 245418, 2005.
- [11] R. S. Morris, B. G. Dixon, T. Gennett, R. Raffaele, and M. J. Heben, "High-energy, rechargeable Li-ion battery based on carbon nanotube technology," *Journal of Power Sources*, vol. 138, no. 1-2, pp. 277–280, 2004.
- [12] G. T. Wu, C. S. Wang, X. B. Zhang et al., "Structure and lithium insertion properties of carbon nanotubes," *Journal of the Electrochemical Society*, vol. 146, no. 5, pp. 1696–1701, 1999.
- [13] B. J. Landi, M. J. Ganter, C. M. Schauerman, C. D. Cress, and R. P. Raffaele, "Lithium ion capacity of single wall carbon nanotube paper electrodes," *The Journal of Physical Chemistry C*, vol. 112, no. 19, pp. 7509–7515, 2008.
- [14] J. Chen, Y. Liu, A. I. Minett, C. Lynam, J. Wang, and G. G. Wallace, "Flexible, aligned carbon nanotube/conducting polymer electrodes for a lithium-ion battery," *Chemistry of Materials*, vol. 19, no. 15, pp. 3595–3597, 2007.
- [15] V. L. Pushparaj, M. M. Shaijumon, A. Kumar et al., "Flexible energy storage devices based on nanocomposite paper," *Proceedings of the National Academy of Sciences of the United States of America*, vol. 104, no. 34, pp. 13574–13577, 2007.
- [16] H. Zhang, G. Cao, Z. Wang, Y. Yang, Z. Shi, and Z. Gu, "Carbon nanotube array anodes for high-rate Li-ion batteries," *Electrochimica Acta*, vol. 55, no. 8, pp. 2873–2877, 2010.
- [17] J. Chen, A. I. Minett, Y. Liu et al., "Direct growth of flexible carbon nanotube electrodes," *Advanced Materials*, vol. 20, no. 3, pp. 566–570, 2008.
- [18] J. Chen, J. Z. Wang, A. I. Minett et al., "Carbon nanotube network modified carbon fibre paper for Li-ion batteries," *Energy and Environmental Science*, vol. 2, no. 4, pp. 393–396, 2009.
- [19] I. Lahiri, S. Oh, J. Y. Hwang et al., "High capacity and excellent stability of lithium ion battery anode using interface-controlled binder-free multiwall carbon nanotubes grown on copper," *ACS Nano*, vol. 4, no. 6, pp. 3440–3446, 2010.
- [20] Z. Cai, L. Li, J. Ren, L. Qiu, H. Lin, and H. Peng, "Flexible, weavable and efficient micro-supercapacitor wires based on polyaniline composite fibers incorporated with aligned carbon nanotubes," *Journal of Materials Chemistry A*, vol. 1, no. 2, pp. 258–261, 2013.
- [21] L. Li, C. Chen, J. Xie, Z. Shao, and F. Yang, "The preparation of carbon nanotube/MnO₂ composite fiber and its application to flexible micro-supercapacitor," *Journal of Nanomaterials*, vol. 2013, Article ID 821071, 5 pages, 2013.
- [22] S. H. Ng, J. Wang, Z. P. Guo, J. Chen, G. X. Wang, and H. K. Liu, "Single wall carbon nanotube paper as anode for lithium-ion battery," *Electrochimica Acta*, vol. 51, no. 1, pp. 23–28, 2005.
- [23] S. Y. Chew, S. H. Ng, J. Wang et al., "Flexible free-standing carbon nanotube films for model lithium-ion batteries," *Carbon*, vol. 47, no. 13, pp. 2976–2983, 2009.
- [24] J. Ren, L. Li, C. Chen et al., "Twisting carbon nanotube fibers for both wire-shaped micro-supercapacitor and micro-battery," *Advanced Materials*, vol. 25, no. 8, pp. 1155–1159, 2013.
- [25] N. Du, H. Zhang, B. Chen et al., "Synthesis of polycrystalline SnO₂ nanotubes on carbon nanotube template for anode material of lithium-ion battery," *Materials Research Bulletin*, vol. 44, no. 1, pp. 211–215, 2009.

- [26] Z. Wang, G. Chen, and D. Xia, "Coating of multi-walled carbon nanotube with SnO_2 films of controlled thickness and its application for Li-ion battery," *Journal of Power Sources*, vol. 184, no. 2, pp. 432–436, 2008.
- [27] W. X. Chen, J. Y. Lee, and Z. Liu, "The nanocomposites of carbon nanotube with Sb and $\text{SnSb}_{0.5}$ as Li-ion battery anodes," *Carbon*, vol. 41, no. 5, pp. 959–966, 2003.
- [28] H. Zhang, C. Feng, Y. Zhai, K. Jiang, Q. Li, and S. Fan, "Cross-stacked carbon nanotube sheets uniformly loaded with SnO_2 nanoparticles: a novel binder-free and high-capacity anode material for lithium-ion batteries," *Advanced Materials*, vol. 21, no. 22, pp. 2299–2304, 2009.
- [29] J. Cabana, L. Monconduit, D. Larcher, and M. R. Palacín, "Beyond intercalation-based Li-ion batteries: the state of the art and challenges of electrode materials reacting through conversion reactions," *Advanced Materials*, vol. 22, no. 35, pp. E170–E192, 2010.
- [30] J. Park, W. G. Moon, G. P. Kim et al., "Three-dimensional aligned mesoporous carbon nanotubes filled with Co_3O_4 nanoparticles for Li-ion battery anode applications," *Electrochimica Acta*, vol. 105, pp. 110–114, 2013.
- [31] W. Wang and P. N. Kumta, "Nanostructured hybrid silicon/carbon nanotube heterostructures: reversible high-capacity lithium-ion anodes," *ACS Nano*, vol. 4, no. 4, pp. 2233–2241, 2010.
- [32] J. Rong, C. Masarapu, J. Ni, Z. Zhang, and B. Wei, "Tandem structure of porous silicon film on single-walled carbon nanotube macrofilms for lithium-ion battery applications," *ACS Nano*, vol. 4, no. 8, pp. 4683–4690, 2010.
- [33] S. Kawasaki, Y. Iwai, and M. Hirose, "Electrochemical lithium ion storage properties of single-walled carbon nanotubes containing organic molecules," *Carbon*, vol. 47, no. 4, pp. 1081–1086, 2009.
- [34] K. Wang, S. Luo, Y. Wu et al., "Super-aligned carbon nanotube films as current collectors for lightweight and flexible lithium ion batteries," *Advanced Functional Materials*, vol. 23, no. 7, pp. 846–853, 2013.
- [35] K. Fu, O. Yildiz, H. Bhanushali et al., "Aligned carbon nanotube-silicon sheets: a novel nano-architecture for flexible lithium ion battery electrodes," *Advanced Materials*, vol. 25, no. 36, pp. 5109–5114, 2013.
- [36] H. Lin, W. Weng, J. Ren et al., "Twisted aligned carbon nanotube/silicon composite fiber anode for flexible wire-shaped lithium-ion battery," *Advanced Materials*, vol. 26, no. 8, pp. 1217–1222, 2014.
- [37] W. Weng, H. Lin, X. Chen et al., "Flexible and stable lithium ion batteries based on three-dimensional aligned carbon nanotube/silicon hybrid electrodes," *Journal of Materials Chemistry A*, vol. 2, pp. 9306–9312, 2014.
- [38] B. Jin, E. M. Jin, K. Park, and H. Gu, "Electrochemical properties of LiFePO_4 -multiwalled carbon nanotubes composite cathode materials for lithium polymer battery," *Electrochemistry Communications*, vol. 10, no. 10, pp. 1537–1540, 2008.
- [39] S. Kim, J. Ryu, C. B. Park, and K. Kang, "Carbon nanotube-amorphous FePO_4 core-shell nanowires as cathode material for Li ion batteries," *Chemical Communications*, vol. 46, no. 39, pp. 7409–7411, 2010.
- [40] E. Hosono, Y. Wang, N. Kida et al., "Synthesis of triaxial LiFePO_4 nanowire with a VGCF core column and a carbon shell through the electrospinning method," *ACS Applied Materials and Interfaces*, vol. 2, no. 1, pp. 212–218, 2010.
- [41] X. Liu, Z. Huang, S. Oh et al., "Sol-gel synthesis of multiwalled carbon nanotube- LiMn_2O_4 nanocomposites as cathode materials for Li-ion batteries," *Journal of Power Sources*, vol. 195, no. 13, pp. 4290–4296, 2010.
- [42] H. Xia, K. R. Ragavendran, J. Xie, and L. Lu, "Ultrafine LiMn_2O_4 /carbon nanotube nanocomposite with excellent rate capability and cycling stability for lithium-ion batteries," *Journal of Power Sources*, vol. 212, no. 1, pp. 28–34, 2012.
- [43] Y. Zhou, J. Wang, Y. Hu, R. O'Hayre, and Z. Shao, "A porous LiFePO_4 and carbon nanotube composite," *Chemical Communications*, vol. 46, no. 38, pp. 7151–7153, 2010.
- [44] N. Yamakawa, M. Jiang, B. Key, and C. P. Grey, "Identifying the local structures formed during lithiation of the conversion material, iron fluoride, in a Li ion battery: a solid-state NMR, X-ray diffraction, and pair distribution function analysis study," *Journal of the American Chemical Society*, vol. 131, no. 30, pp. 10525–10536, 2009.
- [45] P. L. Taberna, S. Mitra, P. Poizot, P. Simon, and J. M. Tarascon, "High rate capabilities Fe_3O_4 -based Cu nano-architected electrodes for lithium-ion battery applications," *Nature Materials*, vol. 5, no. 7, pp. 567–573, 2006.
- [46] S. W. Kim, D. H. Seo, H. Gwon, J. Kim, and K. Kang, "Fabrication of FeF_3 nanoflowers on CNT branches and their application to high power lithium rechargeable batteries," *Advanced Materials*, vol. 22, no. 46, pp. 5260–5264, 2010.
- [47] M. Winter, J. O. Besenhard, M. E. Spahr, and P. Novák, "Insertion electrode materials for rechargeable lithium batteries," *Advanced Materials*, vol. 10, no. 10, pp. 725–763, 1998.
- [48] X. W. Zhou, G. G. Wu, G. H. Gao et al., "The synthesis, characterization and electrochemical properties of multi-wall carbon nanotube-induced vanadium oxide nanosheet composite as a novel cathode material for lithium ion batteries," *Electrochimica Acta*, vol. 74, pp. 32–38, 2012.
- [49] Z. Y. Cao and B. Q. Wei, " V_2O_5 /single-walled carbon nanotube hybrid mesoporous films as cathodes with high-rate capacities for rechargeable lithium ion batteries," *Nano Energy*, vol. 2, no. 4, pp. 481–490, 2013.
- [50] X. Ji and L. F. Nazar, "Advances in Li-S batteries," *Journal of Materials Chemistry*, vol. 20, no. 44, pp. 9821–9826, 2010.
- [51] L. N. Wang, Y. Zhao, M. L. Thomas, and H. R. Byon, "In situ synthesis of bipyramidal sulfur with 3D carbon nanotube framework for lithium-sulfur batteries," *Advanced Functional Materials*, vol. 24, no. 15, pp. 2248–2252, 2013.
- [52] J. Guo, Y. Xu, and C. Wang, "Sulfur-impregnated disordered carbon nanotubes cathode for lithium-sulfur batteries," *Nano Letters*, vol. 11, no. 10, pp. 4288–4294, 2011.
- [53] D. Kim, S. R. Sivakkumar, D. R. MacFarlane, M. Forsyth, and Y. Sun, "Cycling performance of lithium metal polymer cells assembled with ionic liquid and poly(3-methyl thiophene)/carbon nanotube composite cathode," *Journal of Power Sources*, vol. 180, no. 1, pp. 591–596, 2008.
- [54] S. R. Sivakkumar and D. Kim, "Polyaniline/carbon nanotube composite cathode for rechargeable lithium polymer batteries assembled with gel polymer electrolyte," *Journal of the Electrochemical Society*, vol. 154, no. 2, pp. A134–A139, 2007.
- [55] S. W. Lee, N. Yabuuchi, B. M. Gallant et al., "High-power lithium batteries from functionalized carbon-nanotube electrodes," *Nature Nanotechnology*, vol. 5, no. 7, pp. 531–537, 2010.

Research Article

Study on the Highly Sensitive AChE Electrode Based on Multiwalled Carbon Nanotubes

Shuping Zhang, Zhancheng Gu, Yongli Hu, Song Qu, and Ying Liu

College of Science, University of Shanghai for Science and Technology, Shanghai 200093, China

Correspondence should be addressed to Shuping Zhang; zhang_lucy9999@vip.126.com and Song Qu; qsong2004@163.com

Received 8 April 2014; Accepted 5 June 2014; Published 13 July 2014

Academic Editor: Sanqing Huang

Copyright © 2014 Shuping Zhang et al. This is an open access article distributed under the Creative Commons Attribution License, which permits unrestricted use, distribution, and reproduction in any medium, provided the original work is properly cited.

Using chitosan (CS) as carrier, the method named layer-by-layer (LBL) self-assembly modification to modify the glassy carbon electrode (GCE) with multiwalled carbon nanotubes (MWNTs) and acetylcholine esterase (AChE) was proposed to prepare the acetylcholine esterase electrode with high sensitivity and stability. The modified electrode was used to detect pesticide of aldicarb, and the enzyme inhibition rate of the electrode showed good linearity with pesticide concentrations in the range of 10^{-10} g·L⁻¹ to 10^{-3} g·L⁻¹. The detection limit was 10^{-11} g·L⁻¹. The modified electrode was also used to detect the actual sample, and the recovery rate range was from 97.72% to 107.15%, which could meet the rapid testing need of the aldicarb residue. After being stored in the phosphate buffer solution (PBS) in 4°C for 30 days, the modified electrode showed good stability with the response current that was 80% of the original current.

1. Introduction

At present carbamate pesticide residue detecting technology mainly includes such following types: enzyme inhibition based on biological detection techniques [1], immunoassay [2], chromatographic detection [3–5], and GC-MS&LC-MS [6]. Carbamate pesticide residue in vegetables is usually determined by HPLC, but it has a long test cycle, high price of derivative reagents, and poor stability. Biosensor, through preparing enzyme electrode, has aroused worldwide researchers' interest in its advantages, such as good specificity, no sample pretreatment, and fast analysis. Cai and Du [7], and so forth, adopted drop-coating by dispensing mixed processing objects of CS and MWNTs on prepared screen printing glassy carbon electrode, then coating AChE on the surface to make enzyme electrodes for rapid detection of carbaryl. The detection limit reached 10^{-6} g·L⁻¹. Due to potential mechanical, thermal, electrical, and electrochemical properties, graphene is usually regarded as a competitive candidate for new electronic and electrochemical applications, such as batteries [8, 9], catalysts [10, 11], fuel cells [12, 13], biosensors [14, 15], solar cells [16, 17], sensors [18, 19], and super-capacitors [20, 21]. Upadhyay et al. [22], and so forth, modified mixed nanoparticles of gold and platinum

in glassy carbon electrode surface at first and then modified AChE on electrode surface to make enzyme electrode for organophosphate and carbamate pesticide detection. The detection limit reached 10^{-9} g·L⁻¹. In China, the research of this aspect was generally focused on the preparation of AChE membrane [23–25] and conducted by adopting screen printing electrode technology [26]. Indeed, the inhibition of acetylcholinesterase (AChE) activity by pesticides can result in a disturbance of normal neuronal function and possibly death [27, 28]. At present AChE electrode's immobilized enzyme technology is typically to use the crosslinking methods with glutaraldehyde as crosslinking agent [29–31]. The immobilized enzyme was firm, but violent reaction, poor mechanical performance, and low enzyme activity greatly affected the sensitivity and stability of obtained AChE. To improve the sensitivity and stability of obtained AChE, this paper adopted CS and MWNTs as modified materials to fix MWNTs and AChE by LBL technique and made highly efficient and stable AChE electrodes for the detection of pesticide aldicarb. The existence of CS can provide both very good sensitivity and stability of the biosensor and good precision of measurements. The principle of layer self-assembly method was to use the mutual attraction between positive and negative charge to realize material modification and enzyme

immobilization. It hardly destroys the enzyme molecule, and at the same time through multilayer modification it can prevent loss of enzyme and improve the activity of electrode. In recent years, biosensors based on AChE have become a promising technique for environmental monitoring, toxicity analysis, military investigations, and foodstuff quality [32, 33].

2. Materials and Methods

2.1. Main Reagent and Instrument. AChE (317 U/mg, Sigma Company), ATChCl (Sigma Company), DTNB (Shanghai Junchuang Biological Technology Co. Ltd), CS (Molecular weight is 15000, Deacetylation was about 95%, Zhejiang Aoxing Biological Technology Co. Ltd.), MWNTs (Diameter was 40–60 nm, length was 1–10 μm , purity > 95%, Shenzhen Namigang Co. Ltd.), CH_3OH (AR, Guoyao Group Chemistry Reagent Co. Ltd.), aldicarb ($10^{-3} \text{ g}\cdot\text{L}^{-1}$, Shanghai Pesticide Research Institute), other reagents were AR.

CHI800 Electrochemical analyzer (Three electrode systems: Glassy carbon electrode was working electrode; Saturated calomel electrode was reference electrode; Platinum electrode as the counter electrode, current sensitivity range: 10^{-3} – 10^{-11} A, Shanghai Chenhua Instrument Company), Electronic analytical balance (AB104-N, Mettler-Toledo Instr Ltd.), Ultrasonic Cleaner (KQ218CQ-250, Kunshan Ultrasonic Instruments Co. Ltd.), Collection hot type constant temperature magnetic blender (DF-101S, Gongyi Yingyu Yuhua Instrument factory); pH meter (PHB-3BW, Shanghai Lida Instrument factory).

2.2. MWNTs Modified Glassy Carbon Electrode. We polished carefully the glassy carbon electrode using Al_2O_3 turbid liquid with particle size of 0.3 and 0.05 μm successively on the shammy for 3 min until we got a bright mirror. Then we cleaned the electrode surface with deionized water to remove Al_2O_3 . Afterwards, the electrode was ultrasonic-cleaned in acetone, ethanol, and deionized water for 3 min, respectively, in order to further clear the electrode surface dirt. Then we dried the electrode under the infrared lamp.

6 mL of deionized water dispersion of MWNTs with concentration of $10 \text{ g}\cdot\text{L}^{-1}$ was put into reaction pool, and the pretreated glassy carbon electrode and platinum electrode were combined into two-electrode system with electrical deposition (ED) in 1.7 V voltage for 2 hours. In order to disperse it evenly, we set the magnetic stirring speed at 300 rpm (rev/sec) and the electricity deposition temperature was controlled for 30°C in water.

In order to make more MWNTs modified to the surface of electrodes, we dipped the probe into sodium borate solution of pH 9.18 for 15 min, carefully washed it with deionized water, and then immersed it into 0.5% concentration of CS solution (to adjust the PH value of chitosan solution with NaOH solution to 5.0) for 15 min. Then we rinsed the electrode surface with deionized water to get rid of redundant CS. Then it was immersed in $10 \text{ g}\cdot\text{L}^{-1}$ of the MWNTs dispersion of sodium borate and removed after 15 min, after which the electrode surface was rinsed again with deionized water and

nature-aided. Thus a layer of the electrostatic self-assembly had been completed. The steps above were repeated until the ideal number of modified layers was gained.

2.3. Layer Self-Assembly Method Modified AChE on the Electrode Surface. We carefully rinsed MWNTs/CS electrode which was well modified before with deionized water and immersed the electrode into 0.5% concentration of CS solution for 15 min. The electrode surface was rinsed with deionized water to get rid of redundant CS and then immersed in the enzyme liquid of 100 U (the isoelectric point of acetylcholinesterase $\text{I}_p = 4.5$, so when liquid $\text{pH} > \text{I}_p$, AChE was with a negative charge; the experiment was prepared for the AChE solution with the 7.4 pH PBS) for 15 min and then taken out and rinsed carefully with deionized water. Thus a layer of the AChE assembly was completed. Afterwards, this series of steps were repeated until the specified number of modified AChE electrodes was gotten.

2.4. AChE Electrode Detection of Aldicarb. $10^{-2} \text{ g}\cdot\text{L}^{-1}$ (100 ppm) of aldicarb standard samples progressively diluted to $10^{-2} \text{ g}\cdot\text{L}^{-1}$ was prepared, and the enzyme electrode was immersed in the pesticide solution for 10 min. Then enzyme inhibition rate could be determined.

We weighed 5 g cabbage which was planted by the group and cut it into pieces properly. They were placed in a 25 mL centrifuge tube adding 1 mL concentration of $10^{-2} \text{ g}\cdot\text{L}^{-1}$ of the standard sample aldicarb and then blended and sealed. 10 min later, 9 mL of methanol was added and shocked for 10 minutes. Then we poured out the extract and diluted it to $10^{-6} \text{ g}\cdot\text{L}^{-1}$. Sample solution was obtained. Recovery rate should be detected with obtained acetylcholinesterase electrode.

2.5. Determination of Electrode Life. In order to validate the stability of the immobilized enzyme electrode, we saved prepared acetylcholinesterase electrode in the PBS at 4°C . We left it in the PBS of $0.10 \text{ mol}\cdot\text{L}^{-1}$ to determine its current response to 80 μL of ATChCl with concentration of $0.10 \text{ mol}\cdot\text{L}^{-1}$ every 5 days during 30 days.

3. Results and Discussion

3.1. {MWNTs/CS} Modified Layer Selection. After electrodeposition it can be known that, with different {CS/MWNTs} layers, the background currents of the income of PBS scanning are different. As {CS/MWNTs} layer increased, the background currents of the modified electrodes' CV scanning for PBS and the characteristic redox peaks of MWNTs also increased. When the number of layers was more than 5, the linear relationship began to become poor. The reason may be when the thickness of the modified layer became too large, it hindered the electron transfer between modified layer surface and electrodes. Thus, the number of this experiment's {CS/MWNTs} self-assembly layer was five. At this time, the resulting modified layers were relatively dense and even. So far we obtained {MWNTs/CS}₅/ED/GCE.

3.2. Determination of the Effect of Activated Electrodes. The value of O/C on the surface of the electrode went up significantly after being activated by diluted sulphuric acid, which illustrated the great increase of oxygen-containing groups. Relevant research showed that those oxygen-containing groups, including carboxy groups, carbonyl groups, phenols and quinones, and so forth, played a crucial role in improving the electrochemical properties.

Figure 1 is GCE's cyclic voltammograms scanogram with 10 cycles in diluted sulphuric acid. We can see that the electrochemical windows gradually decrease due to the small changes on the surface in the activation process, and it explains that GCE's properties tend to be steady.

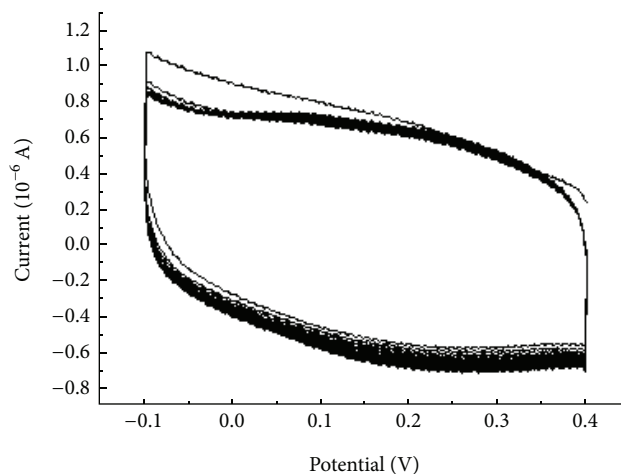


FIGURE 1: The CV scanogram of activated GCE.

3.3. Cysteine's Electrochemical Behavior on {MWNTs/CS}₅/ED/GCE. Acetylthiocholine chloride generated thiocholine through the catalysis of acetylcholinesterase electrodes. It had the electrochemical activity because of the existence of sulfhydryl. Under a certain potential difference it can produce significant oxidation current. But too high peak potential would bring negative effect to determination, such as interference of a large background current or other impurities [34]. So reducing the peak potential of thiocholine and increasing the peak current would be effective ways to improve the sensitivity of acetylcholinesterase electrodes. It was easier to get cysteine and it also had thiol. So this experiment used cysteine instead of thiocholine to detect its electrochemical behavior on {MWNTs/CS}₅/ED/GCE. For current configuration cysteine solution of 5 mmol·L⁻¹, cyclic voltammetry with polished bare glassy carbon electrode and modified {MWNTs/CS}₅/ED/GCE, scan rate was 0.1 V·S⁻¹. According to Figure 2, it can be seen that, through the modification of MWNTs, the peak potential of cysteine reduced and the peak current obviously improved. The expected purpose was achieved.

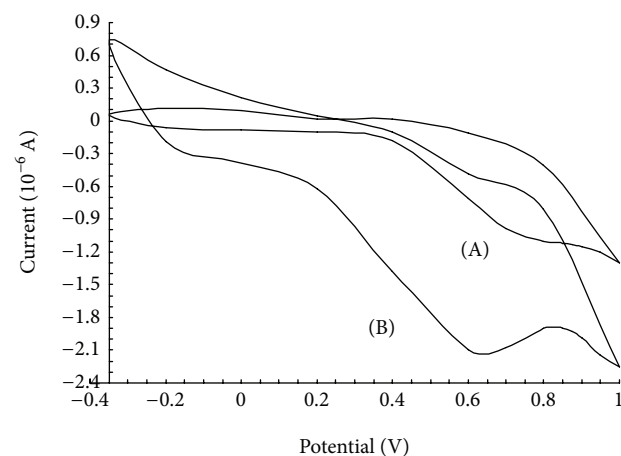
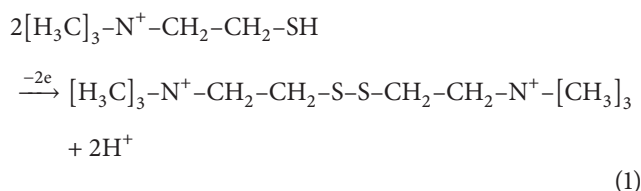


FIGURE 2: The electrochemical behavior of cysteine on the (A) GCE and (B) {MWNTs/CS}₅/ED/GCE.

3.4. {AChE/CS} Modified Layer Selection. To modify the different layers of {AChE/CS}_n/ {MWNTs/CS}₅/ED/GCE as the working electrode, the time-current method with the +0.3 V conditions was used. Add 60 μL, 0.1 mol·L⁻¹ of ATChCl into PBS of pH 7.40 to get response current.

It can be seen from Figure 3 that when the number of self-assembled layers was less than 4, the immobilized enzyme activity improved rapidly with the number of layers increased. When the number of layers was more than or equal to 4, the enzyme activity no longer increased but had a downward trend. The reason may be that when there were too many layers of immobilized enzyme, enzyme molecule congestion would be caused by excessive supply of the enzyme, steric hindrance enhanced, and the substrate and the products spread too late. That is why the enzyme activity was no longer even greater [35]. In order to obtain the most significant experimental results, we chose immobilized layers for 4. At this time the response of the enzyme electrode to the substrate choline chloride acetyl sulfur generation was the biggest.

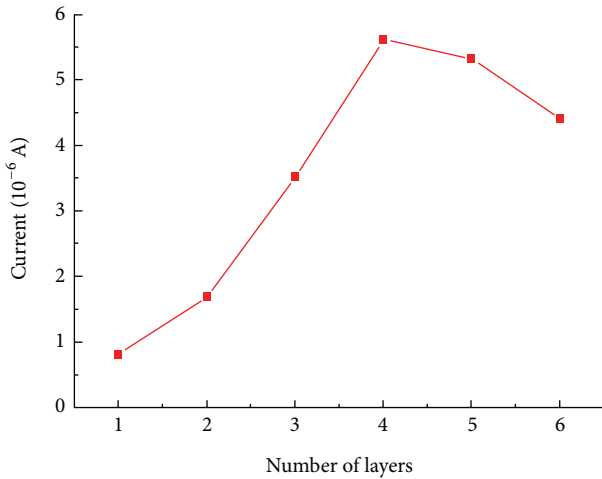
3.5. Thiocholine's Electrochemical Behavior on Modified Electrodes. Due to the sulfhydryl structure, thiocholine (TCh) can react in a specific voltage as the following:



As shown in Figure 4, TCh would be oxidized on both bare electrode and modified electrode and formed anodic peak. On the surface of bare electrode, as the concentration of TCh came to 5 mmol·L⁻¹, $I_{\text{pa}} = -27 \mu\text{A}$, $E_{\text{pa}} = 0.65 \text{ V}$. On the surface of modified electrode, as the concentration of TCh came to 5 mmol·L⁻¹, $I_{\text{pa}} = -54 \mu\text{A}$, $E_{\text{pa}} = 0.35 \text{ V}$. It demonstrated that the electrocatalysis properties of modified electrode were improved apparently.

TABLE 1: The recovery rate of detecting aldicarb by $\{AChE/CS\}_4/\{MWNTs/CS\}_5/ED/GCE$.

Sample	Practical sample concentration ($g \cdot L^{-1}$)	Test sample concentration ($g \cdot L^{-1}$)	Yield (%)	Average yield (%)	Standard deviation
0	0	0	—		
1	$10^{-6.00}$	$10^{-5.98}$	104.71	103.19	6.92
2	$10^{-6.00}$	$10^{-6.01}$	97.72		
3	$10^{-6.00}$	$10^{-5.97}$	107.15		

FIGURE 3: The response currents of the $0.1 \text{ mol} \cdot \text{L}^{-1}$ ATChCl by different number of $\{AChE/CS\}$ layers.

3.6. For the Detection of Pesticide Aldicarb by $\{AChE/CS\}_4/\{MWNTs/CS\}_5/ED/GCE$. With the increasing of the concentration of pesticides, the inhibition rate of the enzyme electrode also increased accordingly. The inhibition rate should be calculated according to the following formula:

$$\text{Inhibition rate (\%)} = I_0 - \frac{I_1}{I_0} \times 100\%. \quad (2)$$

In the formula, I_0 was the steady current caused by acetylcholinesterase sensor which acted on a certain concentration of thio acetylcholine. I_1 was the steady current caused by acetylcholinesterase sensor which acted on the same concentration of thio acetylcholine after an inhibition by pesticides.

In the experiment, the enzyme electrode was put into pesticide solution for 10 min, and then we could determine the inhibition rate of enzyme.

It can be seen in Figures 5 and 6 that, in 10^{-4} – $10^{-11} \text{ g} \cdot \text{L}^{-1}$ range of the aldicarb concentration, inhibition rate of the enzyme electrode had a good linear relationship with the negative logarithm of its concentration. The detection limit can achieve $10^{-11} \text{ g} \cdot \text{L}^{-1}$. Figure 6 showed the standard curve of aldicarb concentration detected by $\{AChE/CS\}_4/\{MWNTs/CS\}_5/ED/GCE$.

We detected the sample solution with three acetylcholinesterase electrodes which were prepared, respectively, and the determination results were showed as in Table 1. When the concentration of the sample solution was

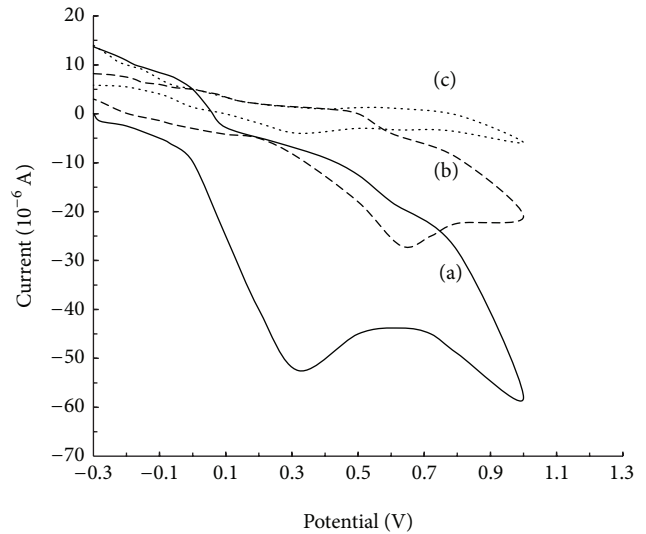
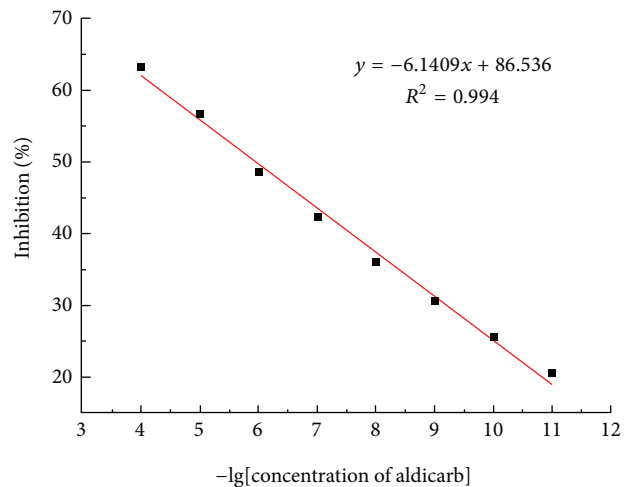
FIGURE 4: Electrochemical behavior of TCh. (a) $\{CS/MWNTs\}_5/ED/GCE$; (b) bare electrode; (c) based current of bare electrode, $0.10 \text{ mol} \cdot \text{L}^{-1}$ of phosphate buffer with $\text{pH} = 7.40$ and scanning rate of $100 \text{ mV} \cdot \text{s}^{-1}$.

FIGURE 5: The curvilinear relation between the enzyme inhibition and the negative logarithm of aldicarb concentration.

$10^{-6} \text{ g} \cdot \text{L}^{-1}$, the recovery rate was in the range of 97.72–107.15%, the average recovery rate was 103.19, and the standard deviation was 6.92. Considering the error of electrochemical detection method and the difference between the electrodes obtained, this result can be almost accurate.

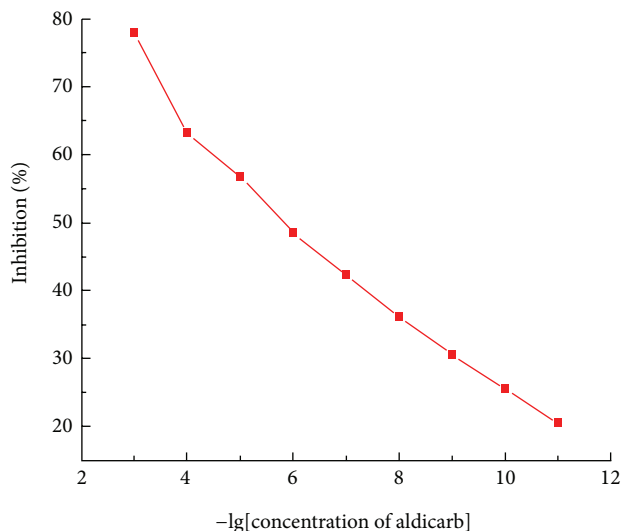


FIGURE 6: The standard curve of acetylcholinesterase electrode to detect the aldicarb.

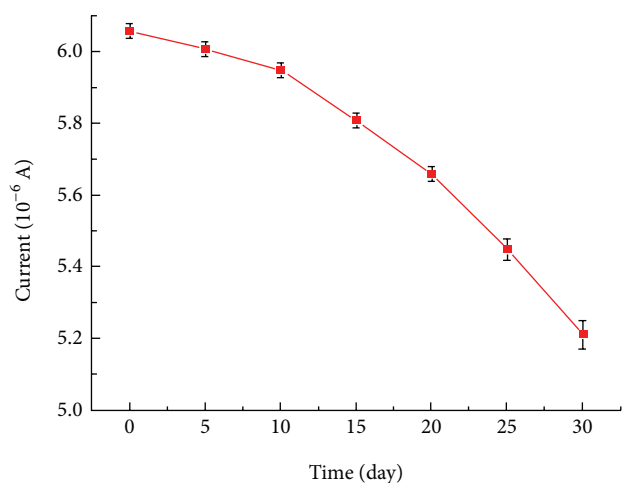


FIGURE 7: The stability of the $\{AChE/CS\}_4/\{MWNTs/CS\}_5/ED/GCE$.

3.7. Determination Result of $\{AChE/CS\}_4/\{MWNTs/CS\}_5/ED/GCE$'s Age. According to Figure 7, the response current value of enzyme electrode was still 72% of the initial current after 30 days. This showed that acetylcholinesterase activity could be well preserved with chitosan and MWNTs as modified materials and layers self-assembly method used to immobilize acetylcholinesterase. The immobilized enzyme electrode may have longer life expectancy and provided the basis for its practical application of pesticide detection.

4. Conclusion and Outlook

The current-acetylcholinesterase electrode was prepared with layer self-assembly method and modified materials of carbon nanotubes and chitosan. Carbon nanotubes can effectively promote electronic relay and chitosan has good biological compatibility [36] that can fix acetylcholinesterase well.

Experiments showed that modified cholinesterase sensor had speedy response, high sensitivity, and good stability. To take advantage of organophosphorus pesticide's inhibitory effect on acetylcholinesterase, with (ATChCl) as substrate, the limit of detection of organophosphorus pesticide parathion reached $10^{-11} \text{ g}\cdot\text{L}^{-1}$. The detection result of practical samples was favorable, so there would be a broad prospect for this method applied to detecting the organophosphorus pesticide residues.

Conflict of Interests

The authors declare that there is no conflict of interests regarding the publication of this paper.

References

- [1] Y. Wang and Y. Wang, "Pesticide residues in vegetables-speed measurement method—enzyme inhibition method," *Shandong Vegetables*, vol. 3, pp. 39–40, 2006.
- [2] Y. Zhang and Y. Liu, "ELISA and rapid detection of food safety," *Food Science*, vol. 24, no. 8, pp. 200–204, 2003.
- [3] X. Chen, X. Zhang, H. Yang et al., "To determine the 24 organophosphate and carbamate pesticide residues of vegetables with gel permeation chromatography-gas chromatography," *Chinese Journal of Health Laboratory*, vol. 19, no. 1, pp. 75–76, 2009.
- [4] W. Gong, H. Liu, J. Shi et al., "Analysis of carbamate pesticide residues in tobacco by LC-MS-MS," *Tobacco technology*, vol. 8, pp. 45–48, 2008.
- [5] J. Zhou, W. Long, and J. Peng, "Salting-phase microextraction or Liquid chromatography (HPLC) determined carbamate pesticides in water," *Chinese Water Supply and Drainage*, vol. 8, pp. 98–100, 2010.
- [6] J. Gong, Y. Li, Y. Hong et al., "Optimization method of high-performance liquid chromatography to determine Vegetables carbamate pesticide residues," *Southwest Agricultural Journal*, vol. 22, no. 5, pp. 1332–1335, 2009.
- [7] J. Cai and D. Du, "A disposable sensor based on immobilization of acetylcholinesterase to multiwall carbon nanotube modified screen-printed electrode for determination of carbaryl," *Journal of Applied Electrochemistry*, vol. 38, no. 9, pp. 1217–1222, 2008.
- [8] E. J. Yoo, J. Kim, E. Hosono, H. Zhou, T. Kudo, and I. Honma, "Large reversible Li storage of graphene nanosheet families for use in rechargeable lithium ion batteries," *Nano Letters*, vol. 8, no. 8, pp. 2277–2282, 2008.
- [9] J. Xiao, D. Mei, X. Li et al., "Hierarchically porous graphene as a lithium-air battery electrode," *Nano Letters*, vol. 11, no. 11, pp. 5071–5078, 2011.
- [10] S. Guo and S. Dong, "Graphene and its derivative-based sensing materials for analytical devices," *Journal of Materials Chemistry*, vol. 21, no. 46, pp. 18503–18516, 2011.
- [11] X. Y. Yang, X. Y. Zhang, Y. F. Ma, Y. Huang, Y. S. Wang, and Y. S. Chen, "Superparamagnetic graphene oxide- Fe_3O_4 nanoparticles hybrid for controlled targeted drug carriers," *Journal of Materials Chemistry*, vol. 19, no. 18, pp. 2710–2714, 2009.
- [12] B. Seger and P. V. Kamat, "Electrocatalytically active graphene-platinum nanocomposites. role of 2-D carbon support in pem fuel cells," *Journal of Physical Chemistry C*, vol. 113, no. 19, pp. 7990–7995, 2009.

- [13] R. Kou, Y. Y. Shao, D. H. Wang et al., "Enhanced activity and stability of Pt catalysts on functionalized graphene sheets for electrocatalytic oxygen reduction," *Electrochemistry Communications*, vol. 11, no. 5, pp. 954–957, 2009.
- [14] S. S. Han, H. Kim, and N. Park, "Effect of shuttling catalyst on the migration of hydrogen adatoms: A strategy for the facile hydrogenation of graphene," *The Journal of Physical Chemistry C*, vol. 115, no. 50, pp. 24696–24701, 2011.
- [15] R. Nie, J. Wang, L. Wang, Y. Qin, P. Chen, and Z. Hou, "Platinum supported on reduced graphene oxide as a catalyst for hydrogenation of nitroarenes," *Carbon*, vol. 50, no. 2, pp. 586–596, 2012.
- [16] X. Wang, L. J. Zhi, N. Tsao, Z. Tomovic, J. L. Li, and K. Mullen, "Transparent carbon films as electrodes in organic solar cells," *Angewandte Chemie International Edition*, vol. 47, pp. 2990–2992, 2008.
- [17] J. B. Wu, H. A. Becerril, Z. N. Bao, Z. F. Liu, Y. S. Chen, and P. Peumans, "Organic solar cells with solution-processed graphene transparent electrodes," *Applied Physics Letters*, vol. 92, no. 26, pp. 263302–263303, 2008.
- [18] X. Yang, X. Zhang, Y. Ma, Y. Huang, Y. Wang, and Y. Chen, "Superparamagnetic graphene oxide-Fe₃O₄ nanoparticles hybrid for controlled targeted drug carriers," *Journal of Materials Chemistry*, vol. 19, no. 18, pp. 2710–2714, 2009.
- [19] J. D. Qiu, J. Huang, and R. P. Liang, "Nanocomposite film based on graphene oxide for high performance flexible glucose biosensor," *Sensors and Actuators B: Chemical*, vol. 160, no. 1, pp. 287–294, 2011.
- [20] M. D. Stoller, S. J. Park, Z. Yanwu, J. H. An, and R. S. Ruoff, "Graphene-based ultracapacitors," *Nano Letters*, vol. 8, no. 10, pp. 3498–3502, 2008.
- [21] A. K. Mishra and S. Ramaprabhu, "Functionalized graphene-based nanocomposites for supercapacitor application," *Journal of Physical Chemistry C*, vol. 115, no. 29, pp. 14006–14013, 2011.
- [22] S. Upadhyay, G. R. Rao, M. K. Sharma, B. K. Bhattacharya, V. K. Rao, and R. Vijayaraghavan, "Immobilization of acetylcholinesterase-choline oxidase on a gold-platinum bimetallic nanoparticles modified glassy carbon electrode for the sensitive detection of organophosphate pesticides, carbamates and nerve agents," *Biosensors and Bioelectronics*, vol. 25, no. 4, pp. 832–838, 2009.
- [23] Y. Wang, Y. Peng, S. Zhao, and F. Xu, "Preparation research of Acetylcholinesterase chitosan membrane," *Guangxi Academy of Sciences Journal*, vol. 23, no. 2, pp. 85–88, 2007.
- [24] Y. Wang, L. Zheng, S. Zhao, Y. Peng, and F. Xu, "Research of homemade AChE membrane detecting organic phosphorus pesticide residues," *Guangxi Light Industry*, vol. 23, no. 10, pp. 13–14, 2007.
- [25] Y. Wang, Y. Peng, S. Zhao, and F. Xu, "Enzymatic properties of AChE membrane and the detection results of organophosphorus pesticides," *Guangxi Academy of Sciences Journal*, vol. 23, no. 3, pp. 160–162, 2007.
- [26] J. Zhang, Y. Wang, and Z. Yuan, "Screen printing enzyme electrode that can detect organophosphorus pesticide residues," *Journal of Chemical*, vol. 64, no. 5, pp. 428–434, 2006.
- [27] F. Saez, C. Pozo, M. A. Gomez, M. V. Martinez-Toledo, B. Rodelas, and J. Gonzalez-Lopez, "Growth and denitrifying activity of *Xanthobacter autotrophicus* CECT 7064 in the presence of selected pesticides," *Applied Microbiology and Biotechnology*, vol. 71, no. 4, pp. 563–567, 2006.
- [28] R. A. Videira, M. C. Antunes-Madeira, V. I. C. F. Lopes, and V. M. C. Madeira, "Changes induced by malathion, methylparathion and parathion on membrane lipid physicochemical properties correlate with their toxicity," *Biochimica et Biophysica Acta—Biomembranes*, vol. 1511, no. 2, pp. 360–368, 2001.
- [29] F. Meng, X. Tang, G. Li, L. Cao, and Y. Li, "Use of Ache sensor monitoring seawater monocrotophos," *Marine Environmental Science*, vol. 22, no. 4, pp. 63–67, 2003.
- [30] H. Zhou, H. Wang, D. Liu, Q. Luo, and X. Jiang, "Carbon nanotubes-based modified enzyme biosensor detects organophosphorus pesticide," *Sensor World*, vol. 14, no. 8, pp. 23–27, 2008.
- [31] J. Yuan and C. Wang, "Modification of materials of acetylcholinesterase biosensor surface," *Functional Materials*, vol. 38, no. A05, pp. 2002–2004, 2007.
- [32] N. A. Hosea, H. A. Berman, and P. Taylor, "Specificity and orientation of trigonal carboxyl esters and tetrahedral alkylphosphonyl esters in cholinesterases," *Biochemistry*, vol. 34, no. 36, pp. 11528–11536, 1995.
- [33] S. Andreescu and J.-L. Marty, "Twenty years research in cholinesterase biosensors: from basic research to practical applications," *Biomolecular Engineering*, vol. 23, no. 1, pp. 1–15, 2006.
- [34] G. Liu, S. L. Riechers, M. C. Mellen, and Y. Lin, "Sensitive electrochemical detection of enzymatically generated thiocholine at carbon nanotube modified glassy carbon electrode," *Electrochemistry Communications*, vol. 7, no. 11, pp. 1163–1169, 2005.
- [35] R. Xia, X. Liu, and C. Ma, "With chitosan as the carrier to fix acetylcholinesterase," *Huazhong University of Science and Technology Journal (Medical Sciences Version)*, vol. 35, no. 6, pp. 721–724, 2006.
- [36] X. Chen, C. Zeng, Y. Mi, and L. Deng, "Application of Chitosan on the immobilized enzyme carrier," *Guangxi Light Industry*, vol. 23, no. 8, pp. 18–19, 2007.

Research Article

Synergistic Effect of Nanosilica Aerogel with Phosphorus Flame Retardants on Improving Flame Retardancy and Leaching Resistance of Wood

Xiaodan Zhu, Yiqiang Wu, Cuihua Tian, Yan Qing, and Chunhua Yao

Material Science and Engineering College, Central South University of Forestry and Technology, Changsha, Hunan 410004, China

Correspondence should be addressed to Yiqiang Wu; wuyq0506@126.com

Received 25 April 2014; Accepted 18 June 2014; Published 6 July 2014

Academic Editor: Sanqing Huang

Copyright © 2014 Xiaodan Zhu et al. This is an open access article distributed under the Creative Commons Attribution License, which permits unrestricted use, distribution, and reproduction in any medium, provided the original work is properly cited.

Nanosilica (Nano-SiO₂) sol fabricated by a sol-gel process was introduced into wood modification with phosphorus flame retardants to improve the flame retardancy and leaching resistance of wood. The obtained materials were characterized by scanning electron microscopy and energy dispersive spectrometer (SEM-EDS), thermogravimetric analysis (TGA), cone calorimetric (CONE), and infrared spectroscopy (FT-IR). The residual rate of flame retardants before and after leaching was determined by a leaching resistance. The results showed that the phosphorus flame retardants and SiO₂ sol could reside in the poplar wood and are widely distributed in the vessels, pits, wood timber, and the spaces between wood cells of poplar substrate. TGA and CONE results indicated that the introduction of nano-SiO₂ aerogel with phosphorus flame retardants had a significantly synergistic effect on improving the flame retardancy and inhibiting the release of smoke and toxic gases. In addition, the leaching resistance test, combined with infrared analysis and EDS analysis, confirmed that the phosphorus flame retardants were able to be fixed by SiO₂ aerogel in the wood.

1. Introduction

Wood is the only truly sustainable resource. Its unique advantages such as good visual characteristics, tactile properties, nontoxicity have made it one of the most important materials in the furniture, building, and construction industries. However, wood is combustible due to its organic constitution, which may not only lead to the spread of fire but also produce a large number of smoke and toxic gases like CO, the leading cause of casualties. Therefore, in order to gain safe and environmentally friendly wood materials, the wood products with fire retardation and smoke suppression are needed urgently.

Inorganic chemicals are attracting more and more attention among common fire retardants due to their high flame retardant efficiency, low cost, and environmental friendliness [1–4]. Specifically, phosphorus flame retardants like ammonium polyphosphate (APP) and ammonium monohydrate phosphate (DAP) are effective fire retardants and have been widely used for fire retardation treatment of wood and

other cellulosic combustible materials [5–8]. However, the inorganic salts of the flame retardants are water-soluble, resulting in a gradual loss during using terms, which directly affect the durability of fire-retardant properties, thus limiting its use in contact with water or humidity. What is more, with the use of phosphorus flame retardants, more gases like CO are produced which result in the suffocation of people [9]. Therefore, nontoxic, leach resistance smoke suppression will be a trend in the development of flame retardants for wood.

The inorganic nano-SiO₂ aerogel plays a certain role in the adsorption and blocking action, which shows a porous structure when it is resided in interior materials. Meanwhile, the Si element existed in SiO₂ aerogel, combined with P or N presented in phosphorus flame retardants, exert a certain synergistic flame retardant and smoke suppression effect [10, 11]. What is more, nano-SiO₂ aerogel has large specific surface area and strong adsorbability, which may help to prevent the phosphate flame retardant from running off [12]. Hence, in this work, nano-SiO₂ aerogel, obtained by sol-gel method, was used to combine with three different phosphate

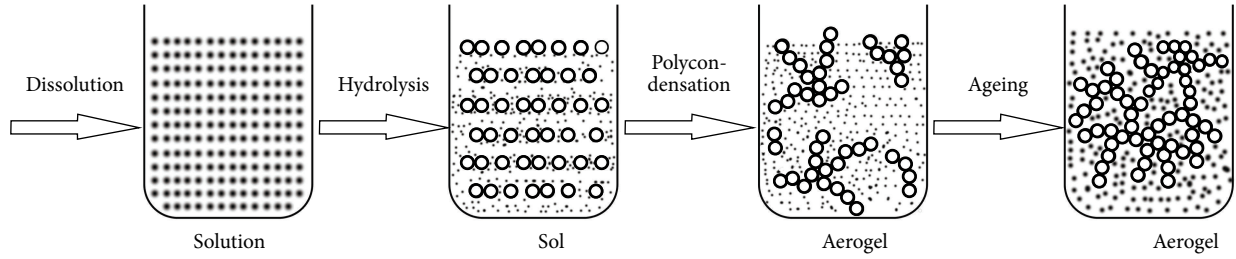


FIGURE 1: Basic schematic diagram of sol-gel process.

flame retardants to treat wood in order to improve the flame retardancy and smoke suppression and leaching resistance of wood.

2. Materials and Methods

2.1. Materials. Poplar wood (*Populus deltoides* cv. I-69/55) was obtained from Yiyang Forest, Hunan. Wood specimens were cut from untreated poplar sapwood into wood blocks with dimensions of 100 mm × 10 mm × 100 mm and 20 mm × 20 mm × 20 mm (T × R × L), whose moisture content was 8–12%. Tetraethyl orthosilicate (TEOS, C (SiO₂) ≥ 98%), ethanol (ET), and hydrochloric acid (HCl, 36–38%) which were all analytically pure were purchased from XiLong Chemical Co., Ltd., while distilled water (H₂O) was prepared in the laboratory. Phosphorus flame retardants including ammonium polyphosphate (APP), ammonium monohydrate phosphate (DAP), and ammonium phosphate (AP) were supported by Shanghai Luzhong Chemical Product Co., Ltd. APP, DAP, and AP were dissolved in water, respectively, to prepare three kinds of solutions of 10% mass fraction.

2.2. Preparation of Nano-SiO₂ Aerogel. The SiO₂ aerogel with nanoporous network structure was made by sol-gel method. The preparation was shown in Figure 1. The TEOS/ET/H₂O with a molar ratio of 1:5:8 were poured into the reaction system. To promote the hydrolysis process, HCl was added until the pH value was 3. The mixture solution was stirred at 50°C for 60 min until the solution was clear.

2.3. Preparation of Nanosilica Aerogel with Phosphorus Flame Retardants Treated Wood. The poplar wood specimens were treated with flame retardants by impregnation method. The prepared solutions of APP, DAP, and AP were impregnated into poplar wood specimens at room temperature under a high pressure (0.5 MPa) for 40 min, respectively, while H₂O was impregnated into wood at the same condition as control group. The impregnated specimens were then placed in an oven controlled to be 60°C for 24 h. In addition, half of the impregnated samples again with the silica sol solution were treated under the same process condition as mentioned above. After that, they were placed in an oven controlled at 60°C for 24 h and at 105°C for another 24 h to age the gels until SiO₂ aerogel formed in the cell of wood. The specific formula

TABLE 1: Formula of impregnation experiment for untreated and treated wood.

Samples	H ₂ O	APP	DAP	AP	SiO ₂ sol
S0	Y	N	N	N	N
S1	N	Y	N	N	N
S2	N	N	Y	N	N
S3	N	N	N	Y	N
S4	N	Y	N	N	Y
S5	N	N	Y	N	Y
S6	N	N	N	Y	Y

Note. Y is short for Yes. N is short for No.

of impregnation experiment of every group could be seen in Table 1.

2.4. Evaluation and Characterization

2.4.1. Weight Percent Gain (WPG). The WPG of the samples (20 mm × 20 mm × 20 mm (T × R × L)) was determined on an oven-dried weight basis as shown in (1), by measuring the oven-dried weights of untreated specimens (M_0) and the composite specimens (M_1):

$$\text{WPG} = \frac{M_1 - M_0}{M_0} \times 100\%. \quad (1)$$

2.4.2. Leaching Resistance. The prepared wood blocks including untreated and treated ones (20 mm × 20 mm × 20 mm (T × R × L)) were subject to a leaching test in a certain flow rate of water for 24 h. After the test, the specimens were removed out to dry in an air atmosphere for 24 h. After which, they should be placed in an oven controlled to be 60°C for another 24 h and then set to be 103°C until the weight was almost the same.

2.4.3. Microstructure Observation. Small samples with dimensions of 10 mm × 20 mm × 3 mm (T × R × L) were cut from the untreated and treated poplar wood, which were located 3 mm from each radial, tangential, and transverse surface of the wood. Before observing the samples with a scanning electron microscope (SEM, FEI Quanta 450) at an accelerating voltage of 20 kV, each sample surface should be sputter-coated with a thin layer of gold. The element composition was determined by regional analysis using an

TABLE 2: Mass variety of different stage for untreated and treated poplar wood.

Samples	W_0^a (g)	W_1^a (g)	W_2^a (g)	WPG ^b (%)	RL ^c (%)	ERL ^d (%)	RSFR ^e (%)	LRV ^f (%)
S0	2.8811	2.8811	2.8673	0		0.48		
S1	3.3466	3.795	3.4283	13.40	9.66		4.22	31.46
S2	3.2395	3.6746	3.2906	13.43	10.45		2.98	22.19
S3	3.3678	3.8283	3.4149	13.67	10.80		2.88	21.03
S4	3.2961	3.9796	3.6510	20.73	8.26		12.48	60.18
S5	3.4955	4.1337	3.8157	18.26	7.69		10.56	57.87
S6	3.1912	3.7708	3.4628	18.16	8.17		9.99	55.03

^a W_0 : weight of untreated wood. W_1 : weight of treated wood after impregnation experiment. W_2 : weight of treated wood after leaching test. ^bWPG (weight percent gain) = $(W - W_0)/W_0$. ^cRL (average turnover rate) = $(W_1 - W_2)/W_1$. ^dERL was the average turnover rate of untreated wood. ^eRSFR (rest loading efficiency) = $WPG - RL + ERL$. ^fLRV (leaching resistance value) = $RSFR/WPG$.

energy dispersive spectrometer (EDS) combined with the SEM.

2.4.4. Thermogravimetric Analysis (TGA). TG data of the untreated and treated wood powder were obtained using a Pyris-6 thermal analyzer. Each sample powder of about 8 mg was placed in a platinum crucible and heated at the rate of 10°C/min from ambient temperature to 700°C. The flow of dynamic carrier nitrogen gas was set at a rate of 40 mL/min.

2.4.5. Cone Calorimetric (CONE) Test. The CONE tests of the untreated and treated wood were performed on Stanton Redcroft Inc. (Fire Testing Technology) following ISO5660-1. For each test, the specimen (100 mm × 10 mm × 100 mm (T × R × L)) covered with aluminum foil except the upper surface was placed into a specific steel frame, and the steel frame was mounted horizontally on the loader and exposed to the heat radiation of 50 kW·m⁻². This heat radiation corresponded to a temperature of 780°C on the upper surface of test sample.

2.4.6. Fourier Transform Infrared Spectrometer (FTIR) Analysis. For testing the change of chemical bonds and the combination mode between functional components and poplar wood, the method of tableting with KBr was used with FTIR (IRAffinity-1). The powder of untreated and treated specimens was oven-dried, and the KBr was dried at 200°C in a muffle oven for 24 h. Subsequently, the testing sample was obtained by mixing about 1-2 mg oven dried samples with 100-200 mg KBr. The FTIR curves of samples were obtained at the test scanning range of 4000-400 cm⁻¹.

3. Results and Discussion

3.1. Weight Percent Gain (WPG) and Leaching Resistance. The impregnation experiment and leaching resistance test are evaluated by weight percent gain (WPG) and leaching resistance value (LRV), respectively. Every group has been prepared with ten samples to calculate the average weight. As we know, the mass of fire-retardant treated wood decreases after the extraction with water, which means the fire retardant is lost during the process of extraction. The LRV is the percentage of residue loading efficiency after extraction (RSFR) to the WPG. The larger the LRV is, the better the performance

of leach resistance will be [13]. The results of mass variety of different stages for untreated and treated wood are shown in Table 2.

It can be seen from Table 2 that the WPG of phosphate flame retardant treated wood blocks is 13-14%, while that of wood treated with phosphate flame retardant and SiO₂ sol reaches 18-21%. This illustrates that the effect of impregnation results is prominent. The mass of untreated wood after extraction is lost with average turnover rate (RL) of 0.48%, which means there is almost nothing lost of wood itself. The mass loss of wood treated with phosphate flame retardants is obvious. It is reflected in that the RL reaches by 9-11% while WPG is 13-14%, meaning a big loss of phosphate flame retardants. Besides, the LRV is only 20-32%. That is to say, its performance of leach resistance is poor. The LRV of wood treated with the combination of phosphate flame retardants and SiO₂ sol reaches 55-61%, which is much bigger than that of wood treated with phosphate flame retardants. This means the wood treated with the combination of two materials have the better performance of leaching resistance. It can be explained that SiO₂ sol has large specific surface area and strong absorbability, which helps to prevent the phosphate flame retardant from running off.

3.2. SEM-EDS. Figure 2 shows the SEM images of the surface of both transverse section and tangential section for untreated wood (S0) and treated wood samples (S1, S3, S4, and S6). It is clear that the vessel, wood fiber, and pit of poplar wood are interconnected. The porous structure of poplar wood is the main channels for phosphorus flame retardants and SiO₂ sol into the poplar wood. It is obvious that no compound was detected in any part of the untreated wood blocks. When the samples were treated with phosphorus flame retardant (S1, S3), there are just white particles in the vessel, wood fiber, and wood ray. While the samples were treated with the mixture of phosphorus flame retardant and SiO₂ sol (S4, S6), many agglomerates can be found in the vessel, wood fiber, wood ray, and pit. This is because the fluid can diffuse, resulting in the impregnation of agents into the wood.

To confirm the presence of flame retardants and SiO₂ sol inside the cell of poplar wood, SEM-EDS mapping was carried out. Figure 3 shows the SEM-EDS map for the

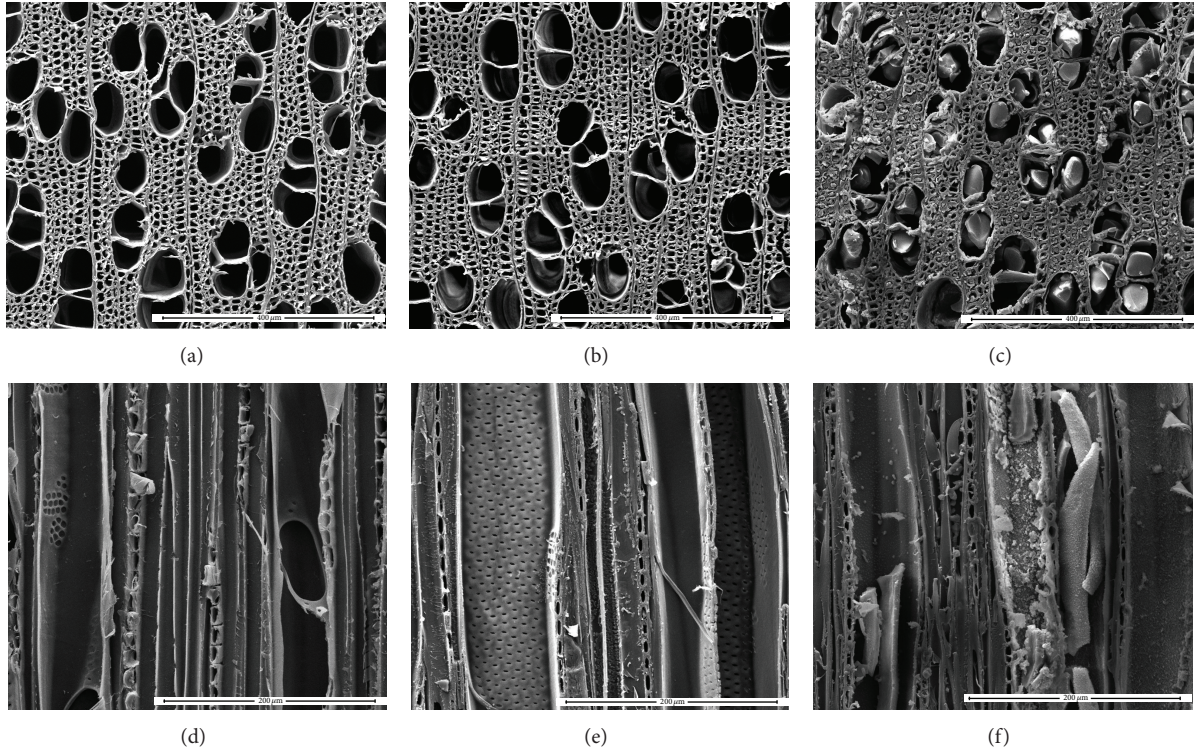


FIGURE 2: SEM images of the surface of transverse section of (a) S0, (b) S1, and (c) S4 and the tangential section of (d) S0, (e) S3, and (f) S6, respectively.

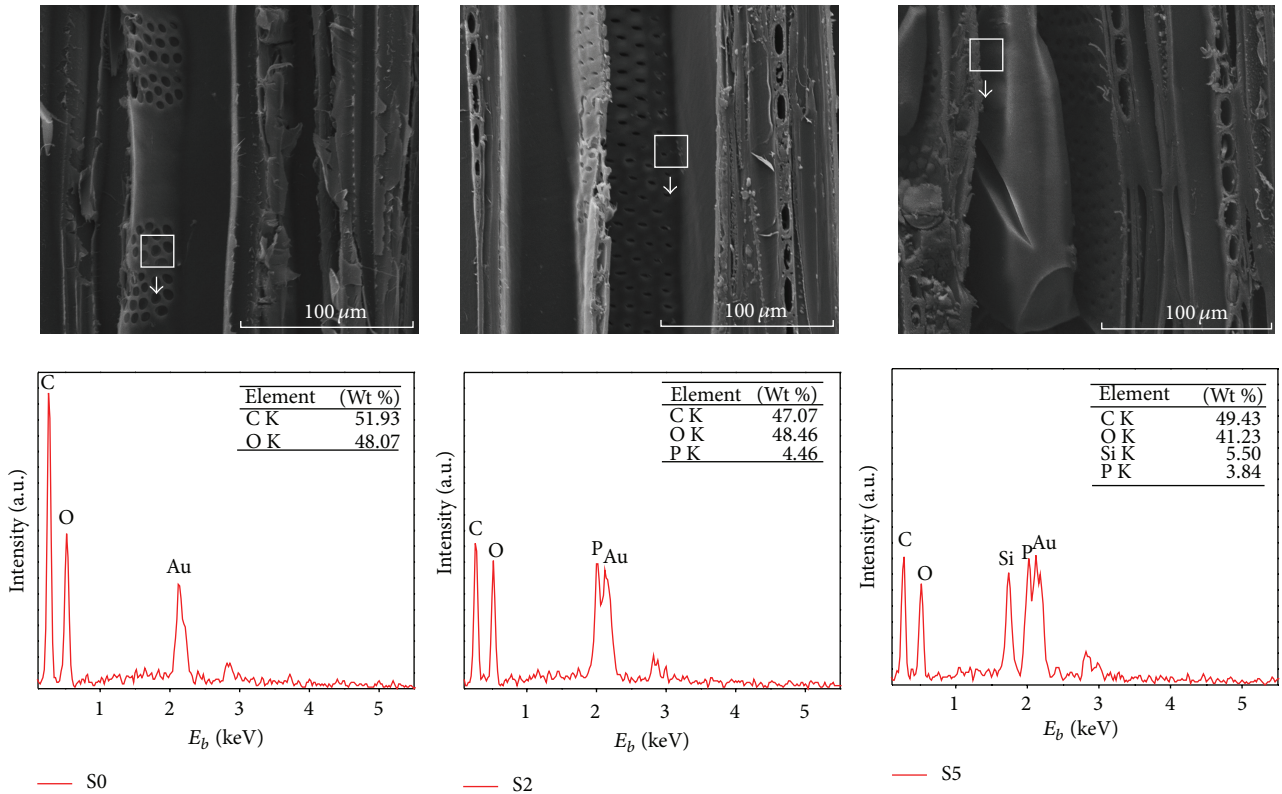


FIGURE 3: EDS spectral profiles of untreated (S0) and treated wood (S2, S5).

TABLE 3: Values of combustion parameters for untreated and treated poplar wood.

Samples	THR (MJ/m ²)	TSR (m ² /m ²)	Mean COY (kg/kg)	Mean CO ₂ Y (kg/kg)
S0	56.24	142.76	0.032	1.08
S1	36.72	55.63	0.065	0.69
S2	34.46	56.52	0.057	0.75
S3	38.19	68.53	0.062	0.72
S4	29.25	21.42	0.035	0.79
S5	29.03	23.83	0.037	0.78
S6	31.35	22.48	0.044	0.76

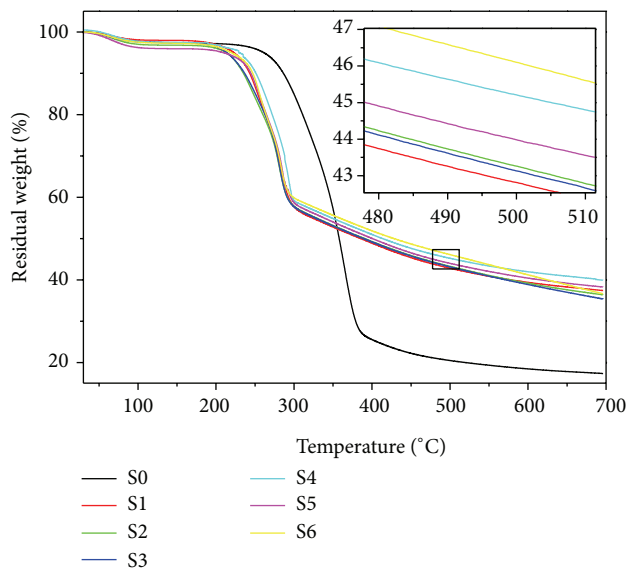


FIGURE 4: TGA data for untreated and treated wood.

untreated and treated blocks and indicates that there is no functional element except the basic elements of wood such as C and O. When samples were treated with only phosphorus based flame retardant (S2), it was verified that the functional element P distribute inside porous structure of wood from the SEM-EDS analysis, although there was no obvious agglomerate block found in the vessel, wood fiber, and pit of wood. Additionally, the SEM-EDS images of the samples treated with both phosphorus flame retardants and SiO₂ sol (S5) indicate that the P and Si elements exist concurrently in the wood cell. This means that phosphorus based flame retardants and SiO₂ sol can reside in the poplar wood since poplar wood itself does not have P and Si elements. As the samples were obtained 3 mm from each radial, tangential, and transverse surface of the wood, it can be concluded that phosphorus flame retardants and SiO₂ sol are easy to be brought by water into the poplar wood. Similarly, because the phosphorus flame retardants are water-soluble, this is why the phosphorus flame retardants are easy to be washed away by water.

3.3. Thermal Degradation. The TGA curves of untreated and treated poplar wood are shown in Figure 4. All the materials show three stages of decomposition. The first decomposition

stage of all materials starts at 30°C and ends at 120°C, which mainly is the evaporation of moisture resulting in about 1.5–3% of weight loss. In the range of 200°C–420°C, the weight of untreated wood decreases significantly up to 76.01% due to the decomposition or dehydration of hemicellulose and the decomposition of cellulose [7]. Whereas the second decomposition stage of treated wood starts at 200°C and ends at 330°C, the range of decomposition temperature is shorter than untreated wood, and the weight loss is only 42%–45%, which is less than untreated wood. And the rate of weight loss of treated wood is faster than untreated wood during this temperature range. After that there is a gradual loss in both cases.

The thermal degradation of treated wood ends earlier than that of untreated wood, while the qualities of carbon residue of treated wood are higher than those of untreated group. All these indicate that flame retardants catalyze the decomposition of treated wood and advance the decomposition of wood. Simultaneously, flame retardants change the reaction mechanism and direction of decomposition of treated wood which can generate more carbon and water when the treated wood decompose [7, 8]. What is more, the weight loss of the compound wood material treated with both phosphorus-containing flame retardants and SiO₂ sol is even less than the wood treated with only phosphorus-containing flame retardants. The weight loss of S4, S5, and S6 is 60.28%, 61.72%, and 63.36%, while the weight loss of S1, S2, and S3 is 62.59%, 63.65%, and 64.63%, respectively, indicating that SiO₂ sol can further improve the flame retardation of wood, because the presence of SiO₂ sol can enhance char formation of the matrix material and form a protective surface barrier to prevent the immediate damage of substrate materials [14].

3.4. Flame-Retardation and Smoke-Suppression Characteristics. The results of cone calorimeter tests for untreated and treated poplar wood are displayed in Figure 5 and Table 3. It is observed from Figure 5(a) and Table 3 that untreated wood burns very fast after ignition and a sharp heat release rate (HRR) peak appearing with a pk-HRR as high as 309.40 kW/m², whose total heat release (THR) values are 56.24 MJ/m². After treatment with phosphorus flame retardant, the HRR values all decrease by over 45%. The THR values of treated wood are lowered by 30% to 40%, which suggested that the addition of phosphorus flame retardant alone can improve the flame retardancy of wood. Besides, when the combination of phosphorus flame

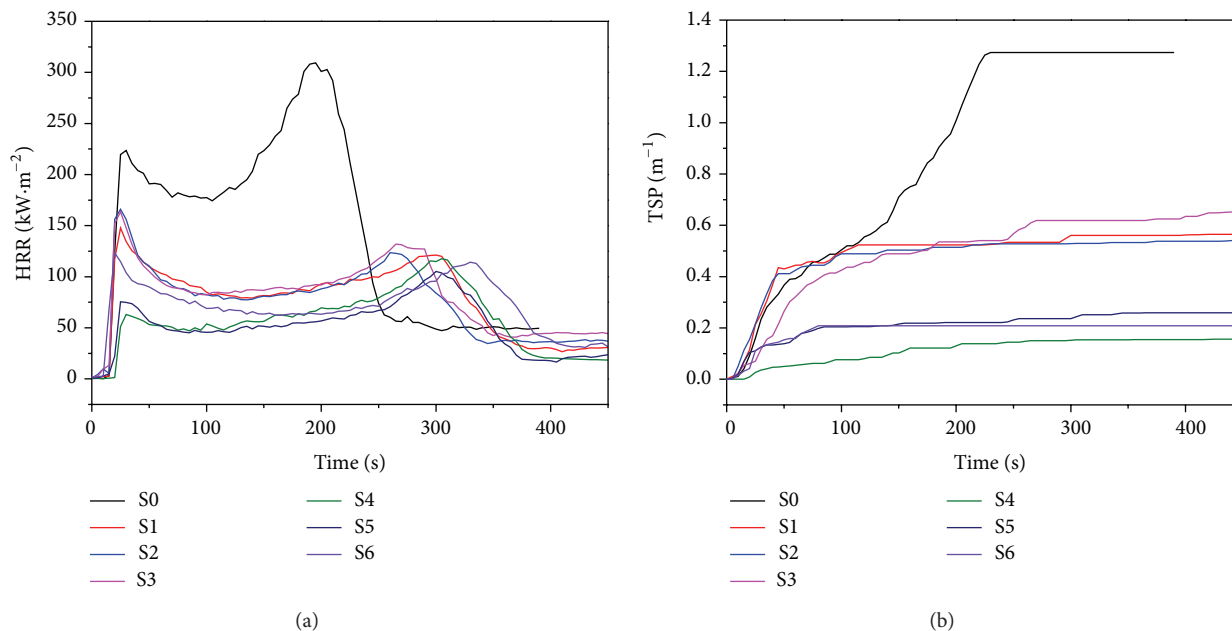


FIGURE 5: HRR (a) and TSP (b) as a function of time for untreated and treated poplar wood.

retardant and SiO_2 aerogel is applied for wood, the HRR, pk-HRR, and THR values show an obvious reduction compared with that of untreated wood, while present more reduction compared with that of wood treated with phosphorus flame retardant alone. For example, the poplar wood treated with APP and SiO_2 aerogel whose THR values are 29.25 MJ/m^2 reduces by 48% and 20%, respectively, compared to that of untreated wood whose THR values are 56.24 MJ/m^2 and that of APP treated wood whose THR values are 36.72 MJ/m^2 . These results demonstrated a synergistic effect of phosphorus flame retardant and SiO_2 aerogel on improving the flame retardancy of wood. It can be illustrated that phosphorus flame retardants decompose at low temperature to form char residue layer on the surface of the sample, which acts as a barrier to prevent heat to underlying materials and flammable gases into flame zone. On the other hand, SiO_2 aerogel significantly enhances the thermal stability of carbon, thus forming a defending charring layer of Si-O-C and Si-C bonds, which protect the poplar wood from burning.

Figure 5(b) shows the total smoke production (TSP) curves of wood at a flux of 50 kW/m^2 in the cone calorimeter test. The total smoke release (TSR), mean CO yield (COY), and CO_2 yield (CO_2Y) parameters can be seen in Table 3. As is portrayed in Figure 5(b), the distinction between pure wood and the flame retarded samples is apparent. Furthermore, the TSP values of wood significantly decrease with the addition of SiO_2 aerogel. According to Table 3, the TSR of wood that was treated with phosphorus flame retardants alone and the combination of phosphorus flame retardants and SiO_2 aerogel was reduced by 51–62% and 83–85%, respectively, compared to untreated wood. However, the mean COY of wood treated with phosphorus flame retardants is much higher than that of untreated wood. While SiO_2 aerogel is incorporated into the system, the mean COY

can reduce almost the same to that of untreated wood. Besides, the CO_2Y of treated wood is all lower than that of untreated wood, while the SiO_2 aerogel can inhibit the release of smoke and toxic gases, which are the leading cause of fire casualties. The phosphorus flame retardants act by the condensed phase mechanism, during which dehydration of the substrates leads to form more char, and protective coating of polyphosphoric acid, phosphorus oxynitride structures or polyphosphoramidic structures on the surface of burning material is formed, resulting in the fact that less smoke and gas were generated from wood [15]. The reason for good smoke suppression of nano- SiO_2 aerogel is attributed to the SiO_2 with highly adsorptive capacity and catalytic conversion effect on the release of smoke and gas.

3.5. FT-IR Spectroscopy. The FTIR spectra of wood treated with phosphorus and silicon-phosphorus flame retardant are shown in Figure 6. It can be seen that most of the characteristic peaks of treated wood are similar to those of untreated one. The FTIR spectrum of wood treated with phosphorus flame retardant (S1, S2, S3) shows an absorption band at $1250\text{--}1253 \text{ cm}^{-1}$, attributed to the stretching vibration of P=O. The FTIR spectrum of wood treated with silicon-phosphorus flame retardant (S4, S5, S6) indicated that the composite not only has the peaks of phosphorus-oxygen bond which can prove that the phosphorus flame retardant exists in the poplar wood, but also shows new intensities of peak which is proof that silica aerogel is present in the wood. The FT-IR peaks of $1080\text{--}1110 \text{ cm}^{-1}$ and $450\text{--}460 \text{ cm}^{-1}$ corresponded to the asymmetric stretching of linear Si-O-Si and bending vibration Si-O-Si [16, 17]. The absorption band located between 1020 and 1040 cm^{-1} ascribes to Si-OH groups [18]. What is more, the peak of $3000\text{--}3500 \text{ cm}^{-1}$ which correspond to the stretching vibration of OH of treated

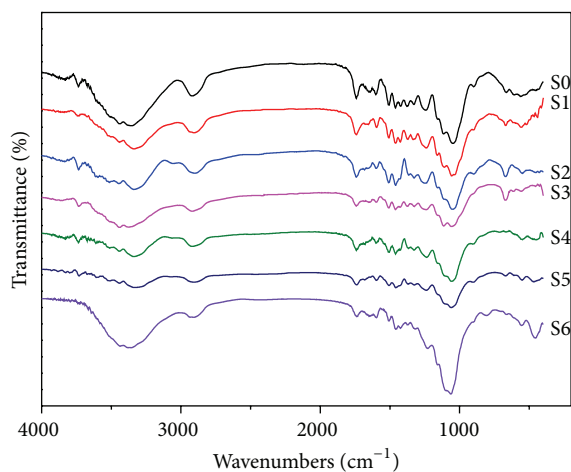


FIGURE 6: FTIR spectra of untreated and treated wood.

wood is different than that of untreated group; that is to say, the phosphorus flame retardants or SiO_2 aerogel may bond with wood cellulose by hydrogen bonds.

4. Conclusion

The nano- SiO_2 sol, obtained by sol-gel method, combined with three different phosphate flame retardants to treat wood in order to improve the flame retardancy and leaching resistance of wood. The SEM and SEM-EDS results showed that phosphorus flame retardants and SiO_2 sol resided in the poplar wood and widely distributed in the vessels, pits, wood timber, and the spaces between wood cells of poplar substrate. TGA indicated that phosphorus flame retardants could significantly improve the thermal stability of wood, while the SiO_2 sol could further enhance the thermal stability of the system. It was found that phosphorus flame retardant and nano- SiO_2 aerogel have a synergistic effect on improving the flame retardation of wood by CONE test. Besides, the combination of phosphorus flame retardants and nano- SiO_2 aerogel exerts a significant influence on inhibiting the release of smoke and toxic gases in the combustion processes, while the phosphorus flame retardants alone would lead to more smoke and toxic gases than untreated wood. In addition, the average LRV of composite could reach 55–61%, while that of untreated wood was 20–32% by a leaching resistance test, which means the phosphorus flame retardants were able to be fixed in the wood by nano- SiO_2 aerogel.

Conflict of Interests

The authors declare that there is no conflict of interests regarding the publication of this paper.

Acknowledgments

This work was financially supported by the National Science and Technology Pillar Program during the Twelfth Five-year Plan Period (2012BAD24B03), National Natural and Science

Foundation of China (31070496), the financial support from Significant Program of Forestry Industry Special Funds for Public Welfare of China (201204704), and Hunan Provincial Innovation Foundation For Postgraduate (CX2013B346).

References

- [1] T. R. Hull, A. Witkowski, and L. Hollingbery, "Fire retardant action of mineral fillers," *Polymer Degradation and Stability*, vol. 96, no. 8, pp. 1462–1469, 2011.
- [2] Y. Fang, Q. Wang, C. Guo, Y. Song, and P. A. Cooper, "Effect of zinc borate and wood flour on thermal degradation and fire retardancy of Polyvinyl chloride (PVC) composites," *Journal of Analytical and Applied Pyrolysis*, vol. 100, pp. 230–236, 2013.
- [3] Y. Yen, H. Wang, and W. J. Guo, "Synergistic effect of aluminum hydroxide and nanoclay on flame retardancy and mechanical properties of EPDM composites," *Journal of Applied Polymer Science*, vol. 130, no. 3, pp. 2042–2048, 2013.
- [4] Y. Q. Wu, C. H. Yao, Y. C. Hu, S. L. Yang, Y. Qing, and Q. L. Wu, "Flame retardancy and thermal degradation behavior of red gum wood treated with hydrate magnesium chloride," *Journal of Industrial and Engineering Chemistry*, vol. 20, no. 5, pp. 3536–3542, 2014.
- [5] J. X. Jiang, J. Z. Li, J. Hu, and D. Fan, "Effect of nitrogen phosphorus flame retardants on thermal degradation of wood," *Construction and Building Materials*, vol. 24, no. 12, pp. 2633–2637, 2010.
- [6] F. Shukor, A. Hassan, I. M. Saiful et al., "Effect of ammonium polyphosphate on flame retardancy, thermal stability and mechanical properties of alkali treated kenaf fiber filled PLA biocomposites," *Materials & Design*, vol. 54, pp. 425–429, 2014.
- [7] M. Gao, C. Y. Sun, and C. X. Wang, "Thermal degradation of wood treated with flame retardants," *Journal of Thermal Analysis and Calorimetry*, vol. 85, no. 3, pp. 765–769, 2006.
- [8] Z. X. Zhang, J. Zhang, B.-X. Lu, Z. X. Xin, C. K. Kang, and J. K. Kim, "Effect of flame retardants on mechanical properties, flammability and foamability of PP/wood-fiber composites," *Composites B: Engineering*, vol. 43, no. 2, pp. 150–158, 2012.
- [9] A. Gentilhomme, M. Cochez, M. Ferriol, N. Oget, and J. L. Mieloszynski, "Thermal degradation of methyl methacrylate polymers functionalized by phosphorus-containing molecules. III: cone calorimeter experiments and investigation of residues," *Polymer Degradation and Stability*, vol. 88, no. 1, pp. 92–97, 2005.
- [10] Y. C. Chiu, F. Y. Liu, C. M. Ma et al., "Syntheses and characterization of novel P/Si polysilsesquioxanes/epoxy nanocomposites," *Thermochimica Acta*, vol. 473, no. 1-2, pp. 7–13, 2008.
- [11] J. Alongi, M. Ciobanu, and G. Malucelli, "Novel flame retardant finishing systems for cotton fabrics based on phosphorus-containing compounds and silica derived from sol-gel processes," *Carbohydrate Polymers*, vol. 85, no. 3, pp. 599–608, 2011.
- [12] S. Palanti, G. Predieri, F. Vignali, E. Feci, A. Casoli, and E. Conti, "Copper complexes grafted to functionalized silica gel as wood preservatives against the brown rot fungus *Coniophora puteana*," *Wood Science and Technology*, vol. 45, no. 4, pp. 707–718, 2011.
- [13] H. Miyafuji, S. Saka, and A. Yamamoto, " SiO_2 - P_2O_5 - B_2O_3 wood-inorganic composites prepared by metal alkoxide oligomers and their fire-resisting properties," *Holzforschung*, vol. 52, no. 4, pp. 410–416, 1998.
- [14] F. Yang and G. L. Nelson, "Polymer/silica nanocomposites prepared via extrusion," *Polymers for Advanced Technologies*, vol. 17, no. 4, pp. 320–326, 2006.

- [15] H. Getto and S. Ishihara, "Functionally graded wood in fire endurance with basic nitrogen compounds and phosphoric acid," *Fire and Materials*, vol. 22, no. 2, pp. 77–83, 1998.
- [16] A. Kioul and L. Mascia, "Compatibility of polyimide-silicate ceramers induced by alkoxy silane coupling agents," *Journal of Non-Crystalline Solids*, vol. 175, no. 2-3, pp. 169–186, 1994.
- [17] T.-C. Mo, H.-W. Wang, S.-Y. Chen, R.-X. Dong, C.-H. Kuo, and Y.-C. Yeh, "Synthesis and characterization of polyimide-silica nanocomposites using novel fluorine-modified silica nanoparticles," *Journal of Applied Polymer Science*, vol. 104, no. 2, pp. 882–890, 2007.
- [18] C. J. Cornelius and E. Marand, "Hybrid inorganic-organic materials based on a 6FDA-6FpDA-DABA polyimide and silica: physical characterization studies," *Polymer*, vol. 43, no. 8, pp. 2385–2400, 2002.

Research Article

Synthesis of GeSe₂ Nanobelts Using Thermal Evaporation and Their Photoelectrical Properties

Lijie Zhang,^{1,2} Hongfei Yu,² Yun Yang,² Keqin Yang,² Youqing Dong,² Shaoming Huang,² Ning Dai,¹ and Da-Ming Zhu^{1,3}

¹ National Laboratory for Infrared Physics, Shanghai Institute of Technical Physics, Chinese Academy of Sciences, Shanghai 200083, China

² Nanomaterials and Chemistry Key Laboratory, Wenzhou University, Wenzhou 325027, China

³ University of Missouri-Kansas City, Kansas City, MO 64110, USA

Correspondence should be addressed to Da-Ming Zhu; zhud@umkc.edu

Received 12 March 2014; Accepted 14 April 2014; Published 17 June 2014

Academic Editor: Li Li

Copyright © 2014 Lijie Zhang et al. This is an open access article distributed under the Creative Commons Attribution License, which permits unrestricted use, distribution, and reproduction in any medium, provided the original work is properly cited.

GeSe₂ nanobelts were synthesized via a simple thermal-evaporation process by using gold particles as catalyst and GeSe₂ flakes as starting materials. The morphology, crystal structure, and composition were characterized with scanning electron microscopy (SEM), high-resolution transmission electron microscopy (TEM), X-ray diffraction spectroscopy (XRD), X-ray photoelectron spectroscopy (XPS), and energy-dispersive X-ray spectroscopy (EDS). SEM micrographs show that most of GeSe₂ nanobelts have distinct segmented structures (wide belt, zigzag belt, and narrow belt). A possible mechanism was proposed for the growth of segmented nanobelts. It is possible that the growth of the segmented nanobelts is dominated by both vapor-liquid-solid and vapor-solid mechanisms. Devices made of single GeSe₂ nanobelt have been fabricated and their photoelectrical property has been investigated. Results indicate that these nanobelt devices are potential building blocks for optoelectronic applications.

1. Introduction

Recently, one-dimensional semiconductor nanostructures, such as nanowires and nanobelts or nanoribbons, have attracted much attention because of their excellent physical properties and their unique structure for device applications [1]. They are considered to be excellent building blocks for devices such as field effect transistors [2], field emitters [3–5], photodetectors [6–8], solar cells [9–11], nanolasers [12], and chemical [13] and biological sensors [14]. These devices demonstrate improved features in comparison to those using bulk materials. For instance, photodetectors fabricated using nanowire or nanobelt always exhibit high sensitivity to light because of their high ratio of surface to volume [8].

IV–VI chalcogenides with layered crystal structure have been widely employed in construction of devices used in optics, thermoelectrics, and optoelectronics [15–17]. As an important member of IV–VI semiconductors, GeSe₂ with

a wide band gap (~2.7 eV) was found to have promising applications in electronics, optoelectronics, and renewable energy devices [18]. Therefore, much attention has been drawn towards the preparation and the study of property of GeSe₂ nanostructures (nanowires, nanobelts, etc.). For instance, three-dimensional GeSe₂ nanostructures composed of nanobelts were synthesized with chemical vapor deposition (CVD) and have demonstrated very impressive performance in supercapacitor applications [15, 18]. GeSe₂ nanowires also could be synthesized through decomposing organic ammonium precursor [19]. Stepped-surfaced GeSe₂ nanobelts were obtained via CVD process and showed high photoresponsivity and gain [20]. Single GeSe₂ nanobelt two-terminal device exhibited high electronic transport properties, photoconductive characteristics, and temperature-dependent electronic characteristics [21].

In most cases, one-dimensional GeSe₂ nanostructures were synthesized via a wet-chemical routine or CVD process

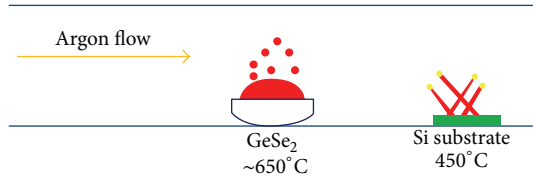


FIGURE 1: Schematic diagram of the synthesis of GeSe₂ nanobelts.

by using Ge and Se powders as starting materials [15, 18–20]. It is also known that both GeSe and GeSe₂ have high stability [17, 18]. As a result, both GeSe and GeSe₂ phases probably form simultaneously in the CVD process when Se and Ge are used as precursors. Besides, the melting point of Ge (938.25°C) is much higher than that of Se (217°C), resulting in different evaporation rate of the precursors and a complex process of the growth.

We synthesized GeSe₂ nanobelts via a simple thermal evaporation method by using GeSe₂ as starting materials and gold films as catalysts. XRD and TEM results demonstrate that the products are pure phase GeSe₂. Besides, vapor-solid (VS) mechanism might contribute to the formation of GeSe₂ nanobelts. Devices made of a single GeSe₂ nanobelt were fabricated and their photoelectrical property was investigated. Results indicate that these prepared nanobelts have good photoelectrical properties and potential application in optoelectronic devices. The detailed results and the discussion about the synthesized nanobelts and their photoelectrical properties are given in the following sections.

2. Experimental Section

The experimental setup used for nanobelt synthesis consists of a horizontal tube furnace, a quartz tube, a gas supply, and a control system (Figure 1). Commercial GeSe₂ flakes (20 mg, purity 99.99%, J&K Scientific Ltd.) used as source materials were positioned in the center of the furnace. The Au-coated (~20 nm) Si substrates were placed at the downstream zone to collect products. After the furnace was fully flushed with high-purity argon gas for 30 min, the system was heated up to 650°C at a rate of 30°C/min. The Ar flux was kept at 100 standard cubic centimeters per minute (sccm) and the deposition temperature was ~450°C. After 1 h of growth, the system was cooled to room temperature. The yellow products on the substrates were GeSe₂ nanobelts.

The morphology, crystal structure, and composition of as-synthesized products were characterized using SEM (FEI Nova NanoSEM200), XRD (Bruker D8 Advanced X-ray diffractometer, Cu K α radiation with $\lambda = 0.15418$ nm), TEM (JEOL 2100F, 200 kV), and EDS. The binding energy of the samples was examined by XPS (Kratos AXIS Ultra DLD).

To evaluate the photoelectrical properties of the nanobelts, two-terminal device made of a single nanobelt was fabricated. The as-synthesized nanobelts were dispersed on p⁺-Si wafer with marks and then treated with electron beam lithography (30 kV, 110 pA, Nanometer Pattern Generation System installed in the SEM), metallization, and lift-off process to define the Cr (10 nm)/Au (100 nm)

contacts with the nanobelt. The electrodes were used for interconnecting and the marks were used for aligning in the following electron beam lithography. The current-voltage (*I*-*V*) characteristics of the device were investigated in air and at room temperature with a semiconductor characterization system (4200 SCS, Keithley Instruments Inc., USA). The power density of the incident light was calibrated by using a standard silicon photodetectors.

3. Results and Discussion

Figure 2 shows the SEM images of the as-prepared nanobelts. As can be seen from the SEM images, most of the nanobelts have segmented A-B-C structure (A = wide belt, B = zigzag belt, and C = narrow belt). The length of the A-B-C structured nanobelts varies from hundreds of micrometers to millimeters (Figures 2(a) and 2(b)). Sections A and C are commonly seen belt-like structure (Figures 2(c)–2(e)). The thickness of most segmented nanobelts ranged from 60 to 200 nm (Figure 2(e)). Besides, section C is narrower than section A. In Figure 2(d), particle (catalyst) can be clearly observed due to contrast difference, indicating that VLS mechanism probably dominates the growth of the A-B-C structured nanobelts. Interestingly, section B has zigzag structure. Figure 2(f) clearly reveals that the zigzag structure (indicated by arrows) serves as a transition region connecting sections A and C. Figures 2(g) and 2(h) show the enlarged views of section B and the zigzag structure is clearly observed. It is well known that there is a good correlation between the nanobelt diameter and the catalyst size during VLS growth [22]. Although the size of section C and particle on the tip match well, section B has different shape and size. Therefore, VLS mechanism only partly makes contribution to the growth of nanobelt possibly. As can be seen from Figures 2(g) and 2(h), the growth of flake-like branch on the backbone might be governed by vapor solid (VS) rather than VLS mechanism. Besides, some small branches were also observed possibly due to different growth stages. As a layer-structured chalcogenides, GeSe₂ consists of Se-Ge-Se layers stacked together via van der Waals interaction [20]. The branches with different thickness are found (e.g., indicated by arrows 3 and 4 in Figure 2(h)), implying that each layer has different growth speed. The segmented nanobelts have uniform thickness at section A. Besides, the growth direction is from section A to C according to the top growth mechanism. Therefore, it is reasonable to conclude that the zigzag structures are not an ultimate state and they would grow into nanobelt with the same structure as section A if growth continues.

XPS was employed to derive composition information of the as-synthesized nanobelts. The binding energy of all the survey and finely scanned spectrums was calibrated by the standard reference of the C 1s (284.8 eV) signal. Typical XPS survey spectrum (Figure 3(a)) indicates the presence of Ge and Se. Figure 3(b) shows that the peaks of Se 3d_{3/2} and Se 3d_{5/2} core level are at 55.1 and 54.4 eV, respectively. The peak position of Ge 3d core level is at 31.1 eV which is consistent with the literature [20]. The Ge 3d core level

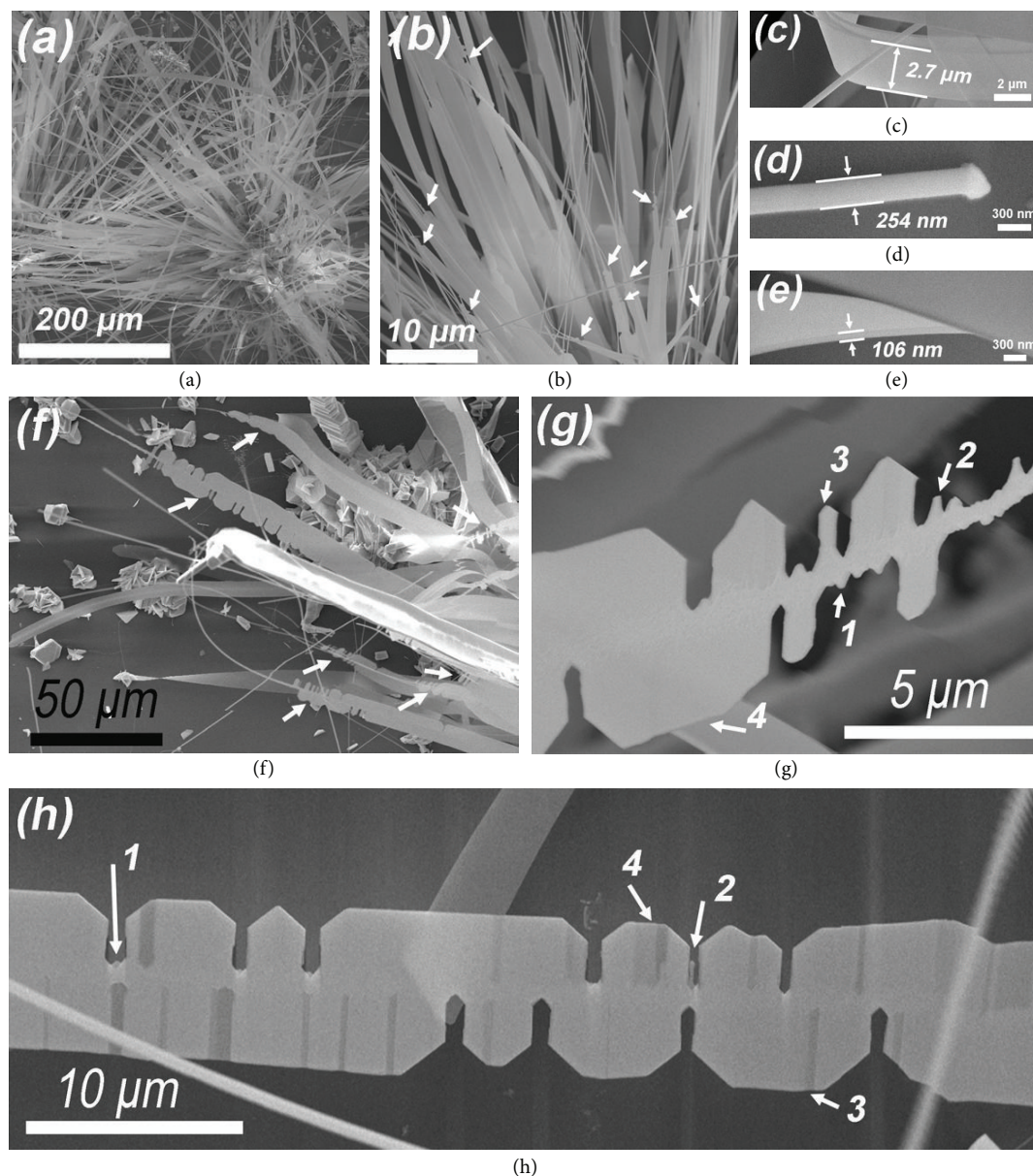


FIGURE 2: SEM images of the segmented nanobelts with A-B-C structure (A = wide belt, B = zigzag belt, and C = narrow belt). (a) A low magnification image of the segmented nanobelts. (b) An enlarged view. (c–e) SEM images taken from section A, section B, and side of section A, respectively. (f–h) SEM images taken from section B.

spectrum is asymmetric and a small shoulder on the high energy side is found (Figure 3(c)). This is caused by the Ge–O states (corresponding to 33 eV) on the surfaces [23]. No signals from Ge–Ge (29.1 eV) and Se–Se (55.4 eV) [20] were detected in the as-synthesized nanobelts, demonstrating that the products are pure phase GeSe₂.

Figure 4(a) shows a typical XRD pattern of the as-synthesized nanobelts. All the diffraction peaks can be indexed to single-crystalline monoclinic GeSe₂ (JCPDS file: 71-0117). A representative TEM image (Figure 4(b)) further confirms the belt-like morphology. Figure 4(c) shows the high-resolution TEM (HRTEM) image of the nanobelt edge, confirming that the nanobelt is a single crystal and defect-free. Two d-spacings of 1.68 and 0.70 nm match well with

the (010) and (100) planes of monoclinic GeSe₂, respectively. The reciprocal lattice peaks (Figure 4(d)) which were given by fast Fourier transform (FFT) can be indexed to a monoclinic structure of GeSe₂. The indexed FFT pattern demonstrates that the growth direction of nanobelt is along [010] direction, which is inconsistent with the [112] growth direction of stepped-surfaced GeSe₂ nanobelts synthesized via VLS mode [20]. The top and bottom surfaces of the nanobelts are {001} facets, and the side surfaces are {100} facets.

Figure 4(e) shows the scanning transmission electron microscope (STEM) image of a GeSe₂ nanobelt with catalyst droplet on the tip. Figures 4(f)–4(h) show elemental distribution of Au, Ge, and Se, respectively. Au was detected only at the catalyst droplet, whereas Ge and Se were observed in the

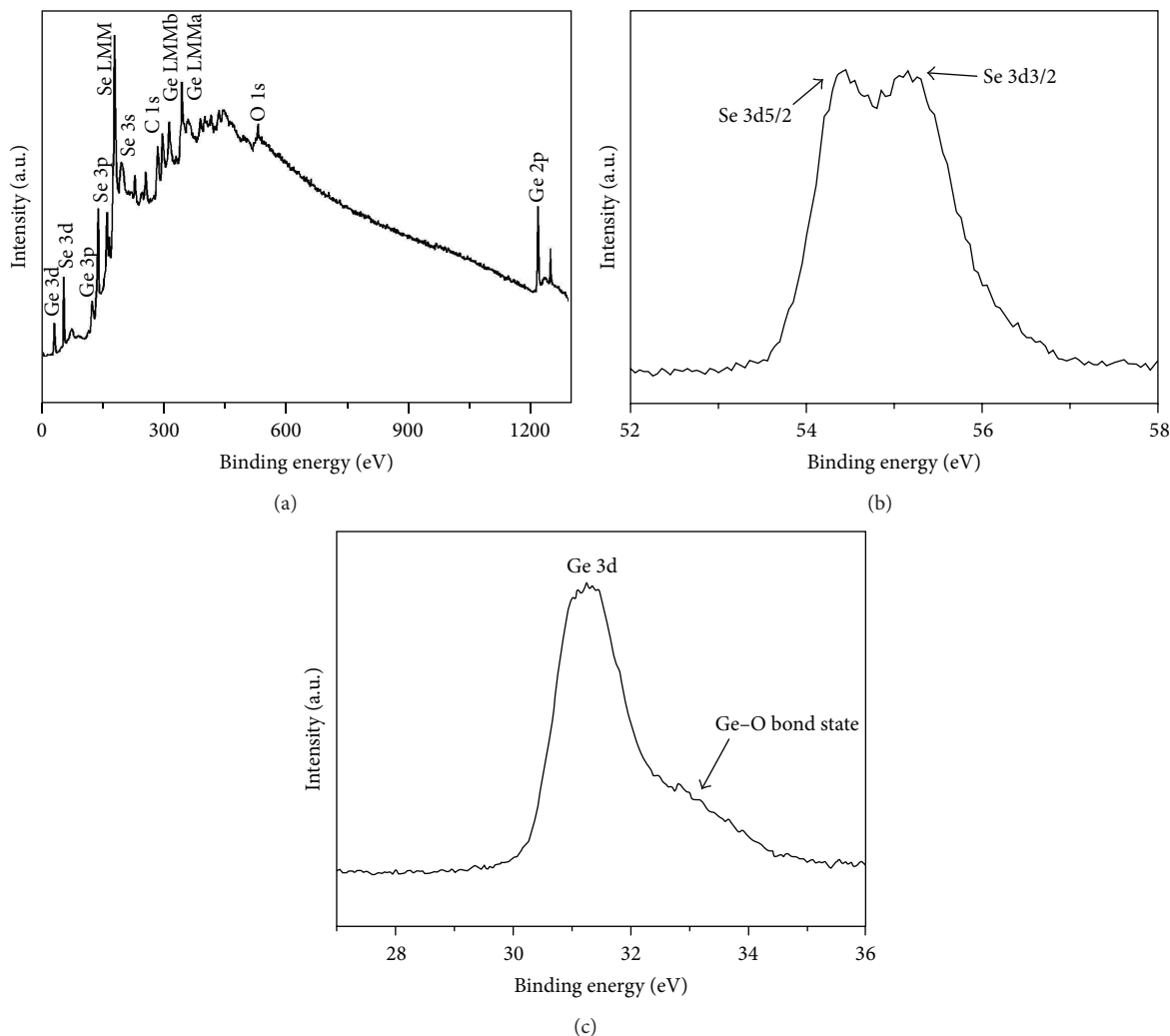


FIGURE 3: XPS analysis of the nanobelts. (a) XPS survey spectrum of the as-synthesized nanobelts. (b) High-resolution XPS spectrum of Se 3d_{3/2} and 3d_{5/2} core level. (c) High-resolution XPS spectrum of Ge 3d and Ge–O bond state.

nanobelt as well as the catalyst droplet. This further confirms the VLS growth of the nanobelts. Under high temperature, Au film changes into liquid droplet. Meanwhile, high temperature causes the formation of GeSe₂ vapor which enters the Au particles to produce Au–Ge–Se alloy particles. When GeSe₂ is oversaturated, it recrystallizes out of alloy particles, nucleates, and further grows to nanobelt. Figure 4(i) is the STEM image of single nanobelt. Figures 4(j) and 4(k) display EDS profiles along the red and green arrows in Figure 4(i), respectively. The STEM-EDS results confirm the uniform distribution of Ge and Se in the nanobelt. The atomic ratio between Se and Ge is close to stoichiometric ratio (2:1).

HRTEM was employed to investigate the structure of section B. Figure 5(a) shows a representative TEM image of a zigzag structure. Figure 5(b) is the HRTEM image of selected region marked by rectangle 1 in Figure 5(a) and the inset shows the corresponding FFT pattern. It can be found that the crystal structure of branch is identical to that of the backbone, further confirming that the growth of branches is from the backbone. Figures 5(c)–5(f), respectively, show the HRTEM

images of position marked by rectangles 2–5 in Figure 5(a). Figure 5(g) gives an enlarged view of the region marked by rectangular area in Figure 5(f) and the corresponding FFT pattern is shown in Figure 5(h). These results indicate that the GeSe₂ nanobelt grows along [010] direction. The VS growth direction of section B is along [100] and [−100] directions. The layered structure of the GeSe₂ is clearly observed in Figures 5(b) and 5(f), which is consistent with previous report [15] that Se–Ge–Se layers are assembled along [001] direction. As a result, the VS growth is parallel to (001) plane rather than perpendicular to (001). The HRTEM results also suggest that the VS growth speed of each layer is not equal and this result is in agreement with the SEM observation (Figure 2(h)). With the VS growth continuing, the side surfaces are changed from {−110} and {−1−10} facets (Figures 5(f) and 5(g)) to {−120}, {−1−20}, and {010} facets (Figures 5(c) and 5(d)).

Based on the above analysis, a possible growth mechanism is proposed for the formation of the segmented nanobelts. Firstly, Au–Ge–Se alloy particles act as catalyst and induce the growth along [010] direction via VLS mode

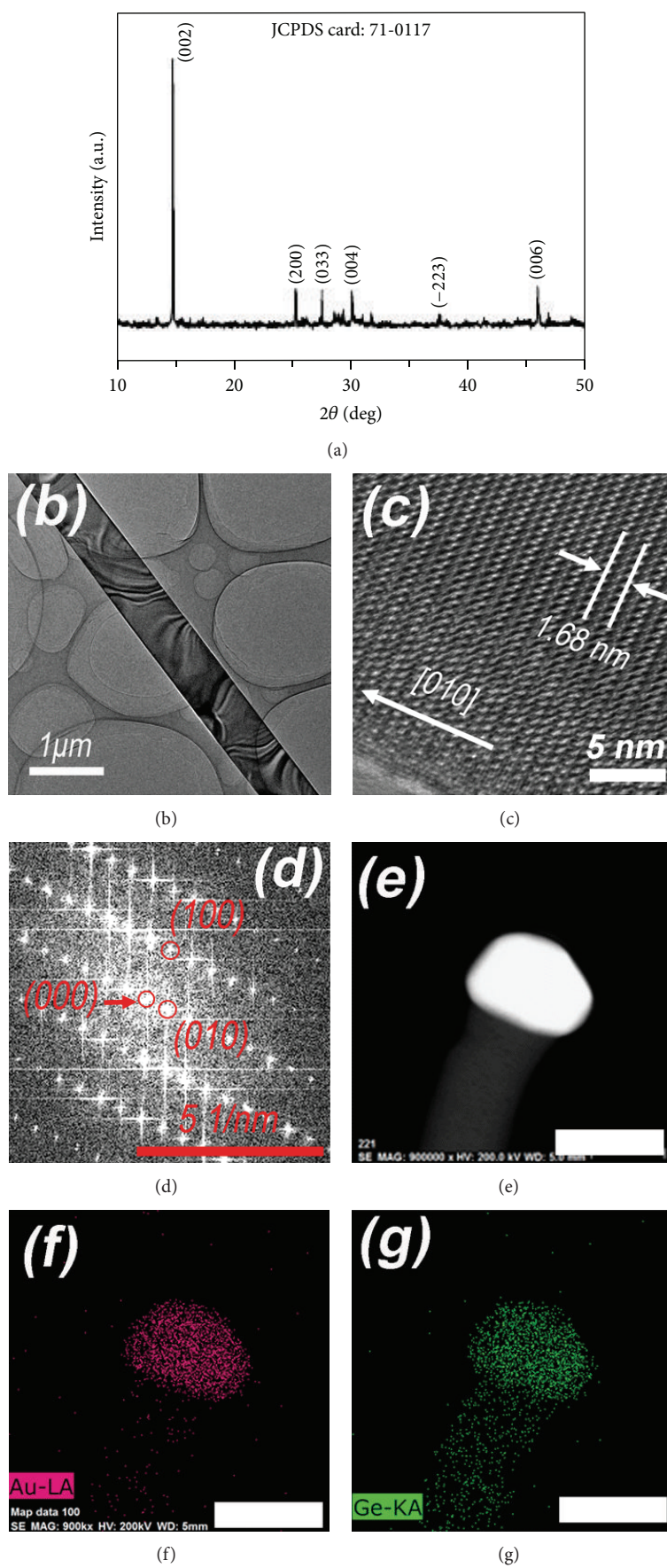


FIGURE 4: Continued.

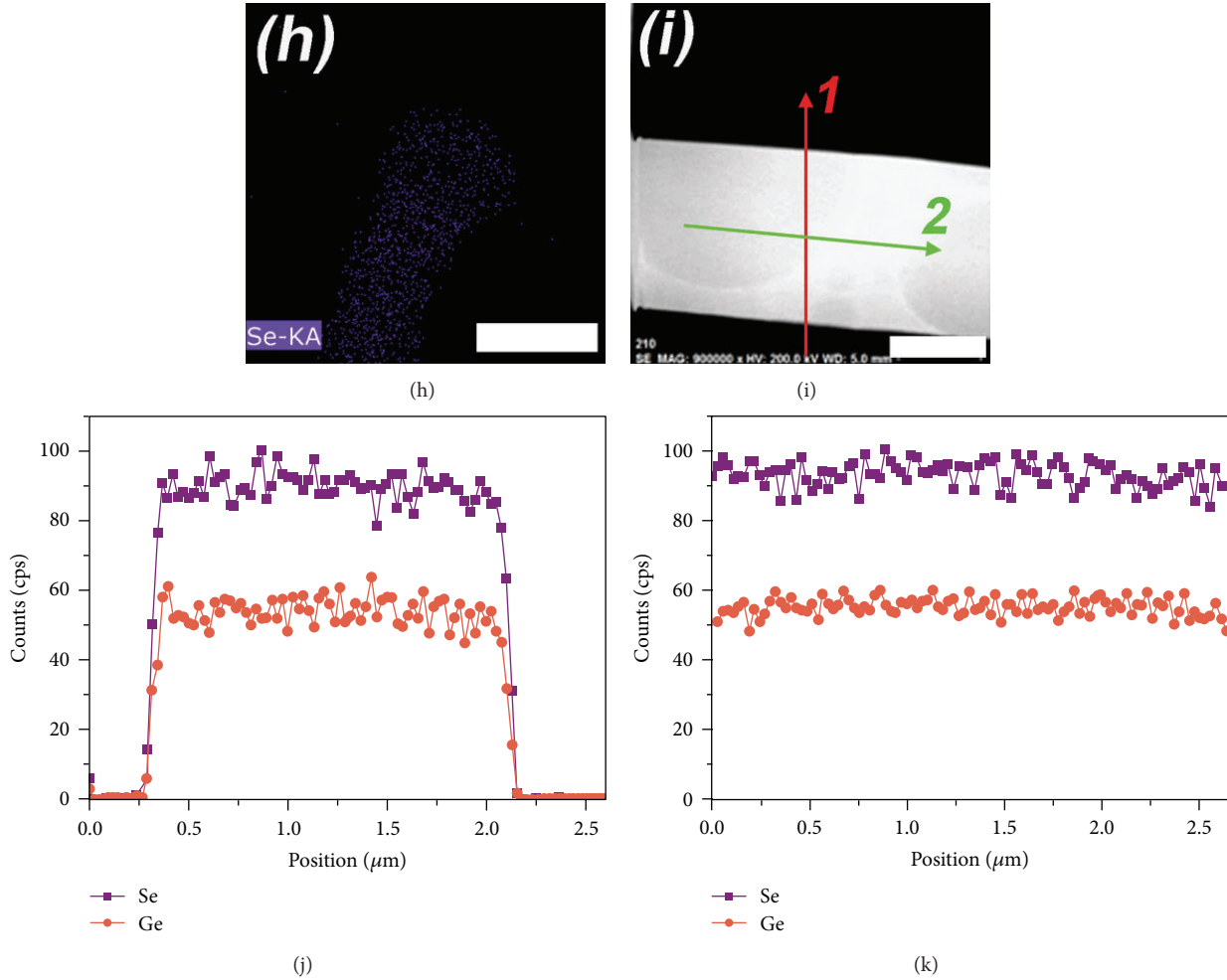


FIGURE 4: (a) XRD pattern of the nanobelts. (b) A TEM image of a nanobelt. (c, d) A HRTEM taken from the edge of the nanobelt and corresponding FFT pattern. (e) A STEM image taken from the tip of a nanobelt. (f–h) EDS maps for Au, Ge and Se, respectively. Scale bar: 100 nm. (i) A STEM image of the nanobelt. Scale bar: 1 μm . (j, k) EDS profiles taken along the red and green arrows in (i), respectively.

(Figure 6(a)). The two side surfaces of a nanobelt in this growth stage are parallel to (100) plane. Once the narrow nanobelt is formed, its side surfaces become nucleation sites which direct the VS growth along [100] and $[-100]$ directions (Figure 6(b)). However, because the growth speed of the VLS mode is faster than that of VS mode, zigzag structure forms (Figure 6(b)). With the VLS and VS growth proceeding simultaneously, the zigzag product evolves to nanobelt with the structure of section A and the length of the section C further increase (Figure 6(c)), resulting in the formation of A-B-C structured products.

Compared with bulk materials, nanostructured semiconductors have large surface-to-volume ratio and dangling bonds on the material surfaces. Therefore, there are numerous oxygen molecules absorbed on their surface which attract the electron of photoexcited carriers ($\text{O}^2 + e^- \rightarrow \text{O}_2^-$). This can improve the separation of photoexcited carriers and increase photocurrent [24]. To evaluate the photoelectrical properties of the as-synthesized nanobelts, two-terminal device was fabricated through using a single GeSe_2 nanobelt.

Figure 7(a) shows the schematic illustration of experimental setup for photoelectrical measurements. A white light with power density of $\sim 0.7 \text{ mW/mm}^2$ was used as the incident light. Figure 7(b) gives the current-voltage (I - V) characteristics of the device under incident light illumination or without illumination. The asymmetry and nonlinearity of I - V curves indicate the formation of Schottky contact between the nanobelt and the metal electrodes. Compared with the dark current at a bias of 1 V, the photocurrent increases by ~ 52 times. This indicates that the as-synthesized nanobelts have good photoelectrical properties.

4. Conclusion

In summary, we demonstrated that a simple thermal evaporation method could be used to synthesize GeSe_2 nanobelts through using gold particles as catalyst and GeSe_2 flakes as starting materials. Most of nanobelts have wide belt, zigzag belt, or narrow belt structures which are mostly single

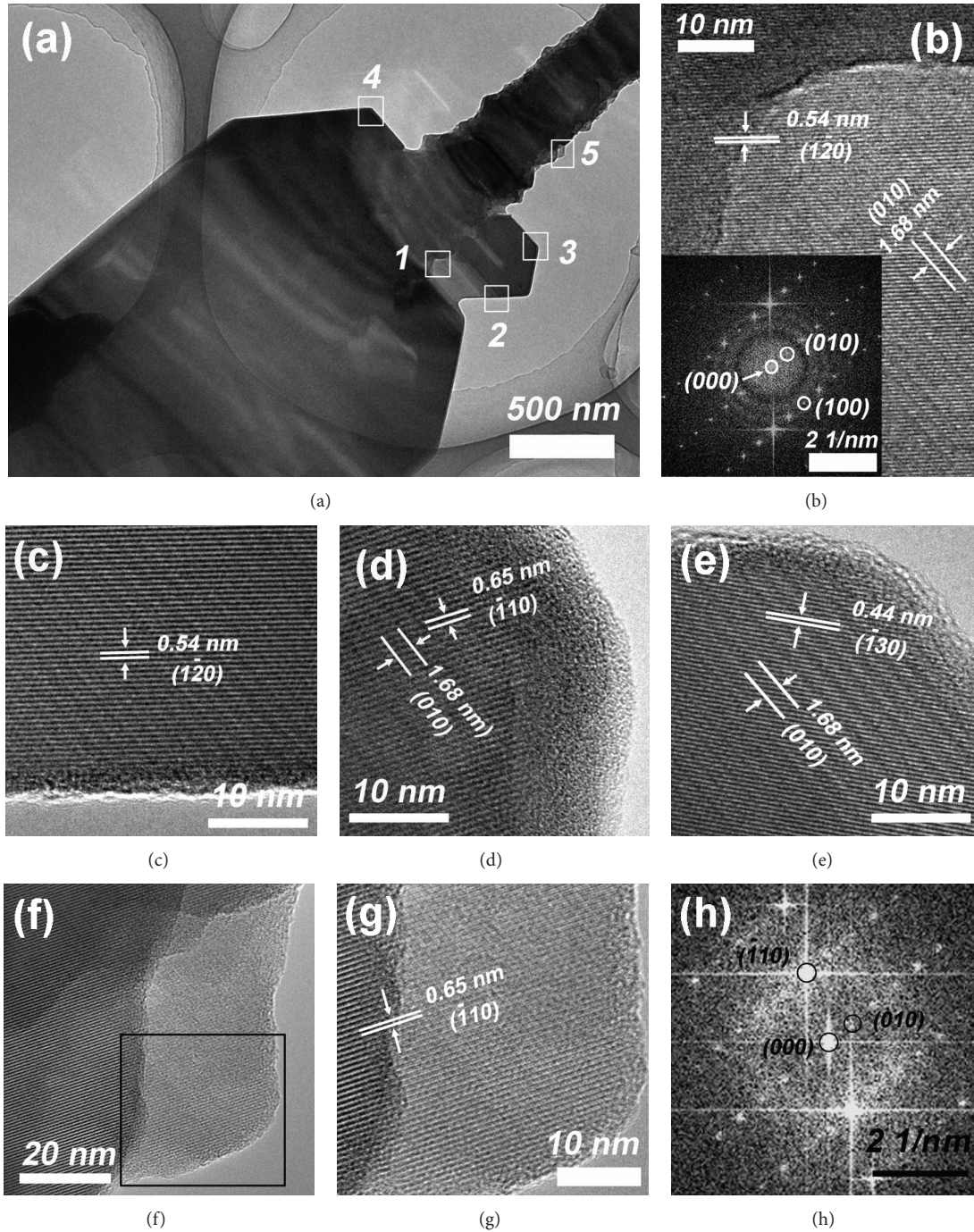


FIGURE 5: (a) A TEM image of the zigzag structure. (b–f) The corresponding HRTEM taken from the rectangular area 1–5, respectively. The inset in (b) shows its corresponding FFT pattern. (g, h) Enlarged views of the rectangular area in (f) and corresponding FFT pattern.

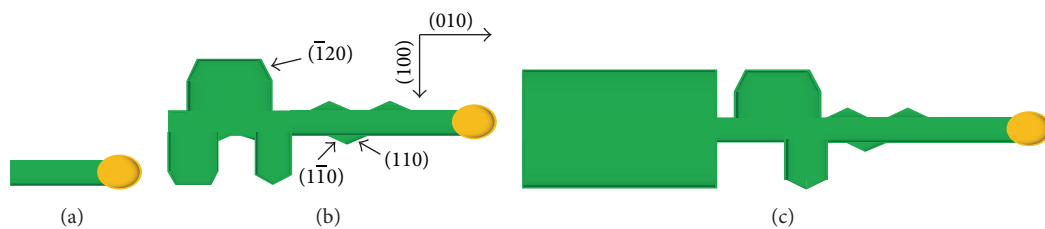


FIGURE 6: Schematic illustration of the growth process.

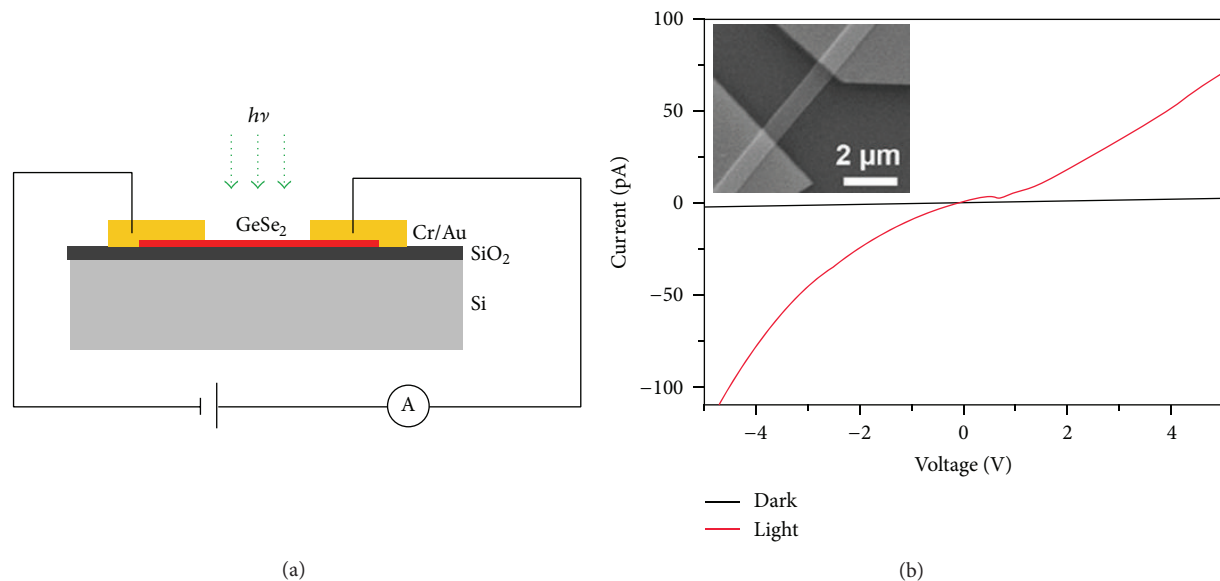


FIGURE 7: (a) Schematic illustration of the experimental setup for photoelectrical measurements. (b) I - V curves of the two-terminal device under white-light illumination or in dark condition.

crystals. A possible mechanism was proposed for explaining the growth of segmented nanobelts. The growth occurs first along [010] direction via VLS mode and then VS mode starts along [100] and $[-100]$ directions. These two growth modes result in the formation of segmented nanobelts. The as-synthesized GeSe_2 nanobelts exhibit excellent photoelectrical property.

Conflict of Interests

The authors declare that there is no conflict of interests regarding the publication of this paper.

Acknowledgments

This work was supported by NSFC (nos. 61001005 and 11375174), National 973 Project of China (nos. 2012CB934300 and 2012CB619200), and NSFZJ (Y1110734).

References

- [1] W. Wu, X. Wen, and Z. L. Wang, "Taxel-addressable matrix of vertical-nanowire piezotronic transistors for active and adaptive tactile imaging," *Science*, vol. 340, no. 6135, pp. 952–957, 2013.
- [2] A. M. Ionescu and H. Riel, "Tunnel field-effect transistors as energy-efficient electronic switches," *Nature*, vol. 479, no. 7373, pp. 329–337, 2011.
- [3] X. Zhang, Y. Chen, Z. Xie, and W. Yang, "Shape and doping enhanced field emission properties of quasisaligned 3C-SiC nanowires," *Journal of Physical Chemistry C*, vol. 114, no. 18, pp. 8251–8255, 2010.
- [4] S. Chen, P. Ying, L. Wang et al., "Growth of flexible N-doped SiC quasisaligned nanoarrays and their field emission properties," *Journal of Materials Chemistry C*, vol. 1, no. 31, pp. 4779–4784, 2013.
- [5] S. Chen, P. Ying, L. Wang et al., "Controlled growth of SiC flexible field emitters with clear and sharp tips," *RSC Advances*, vol. 4, no. 16, pp. 8376–8382, 2014.
- [6] T. Zhai, L. Li, X. Wang, X. Fang, Y. Bando, and D. Golberg, "Recent developments in one-dimensional inorganic nanostructures for photodetectors," *Advanced Functional Materials*, vol. 20, no. 24, pp. 4233–4248, 2010.
- [7] L. Zhang, H. Yu, W. Cao, C. Zou, Y. Dong, and D. M. Zhu, "Enhanced electrical and optoelectrical properties of cadmium selenide nanobelts by chlorine doping," *Micro & Nano Letters*, vol. 9, no. 1, pp. 55–59, 2014.
- [8] L. Hu, J. Yan, M. Liao, L. Wu, and X. Fang, "Ultrahigh external quantum efficiency from thin SnO_2 nanowire ultraviolet photodetectors," *Small*, vol. 7, no. 8, pp. 1012–1017, 2011.
- [9] Q. Li, L. Zhai, C. Zou et al., "Wurtzite CuInS_2 and $\text{CuIn}_x\text{Ga}_{1-x}\text{S}_2$ nanoribbons: synthesis, optical and photoelectrical properties," *Nanoscale*, vol. 5, no. 4, pp. 1638–1648, 2013.
- [10] E. Garnett and P. Yang, "Light trapping in silicon nanowire solar cells," *Nano Letters*, vol. 10, no. 3, pp. 1082–1087, 2010.
- [11] J. Heo, W. Guo, and P. Bhattacharya, "Monolithic single GaN nanowire laser with photonic crystal microcavity on silicon," *Applied Physics Letters*, vol. 98, no. 2, Article ID 021110, 2011.
- [12] D. Cammi and C. Ronning, "Persistent photoconductivity in ZnO nanowires in different atmospheres," *Journal of Nanomaterials*, vol. 2014, Article ID 184120, 5 pages, 2014.
- [13] X. Li, X. Li, N. Chen et al., "CuO- In_2O_3 core-shell nanowire based chemical gas sensors," *Journal of Nanomaterials*, vol. 2014, Article ID 973156, 7 pages, 2014.
- [14] Y. Niu, A. Qin, W. Song et al., "Biocompatible single-crystal selenium nanobelt based nanodevice as a temperature-tunable photosensor," *Journal of Nanomaterials*, vol. 2012, Article ID 384671, 6 pages, 2012.

- [15] X. Wang, B. Liu, Q. Wang et al., "Three-dimensional hierarchical GeSe₂ nanostructures for high performance flexible all-solid-state supercapacitors," *Advanced Materials*, vol. 25, no. 10, pp. 1479–1486, 2013.
- [16] P. D. Antunez, J. J. Buckley, and R. L. Brutchey, "Tin and germanium monochalcogenide IV-VI semiconductor nanocrystals for use in solar cells," *Nanoscale*, vol. 3, no. 6, pp. 2399–2411, 2011.
- [17] B. Mukherjee, Y. Cai, H. R. Tan, Y. P. Feng, E. S. Tok, and C. H. Sow, "NIR Schottky photodetectors based on individual single-crystalline GeSe nanosheet," *ACS Applied Materials & Interfaces*, vol. 5, no. 19, pp. 9594–9604, 2013.
- [18] Y. Zhang, H. Li, L. Jiang et al., "Field emission from GeSe₂ nanowalls," *Applied Physics Letters*, vol. 98, no. 11, Article ID 113118, 2011.
- [19] M. Nath, A. Choudhury, and C. N. R. Rao, "Chemical routes to GeS₂ and GeSe₂ nanowires," *Chemical Communications*, no. 23, pp. 2698–2699, 2004.
- [20] B. Mukherjee, Z. Hu, M. Zheng et al., "Stepped-surfaced GeSe₂ nanobelts with high-gain photoconductivity," *Journal of Materials Chemistry*, vol. 22, no. 47, pp. 24882–24888, 2012.
- [21] B. Mukherjee, E. S. Tok, and C. H. Sow, "Photocurrent characteristics of individual GeSe₂ nanobelt with Schottky effects," *Journal of Applied Physics*, vol. 114, no. 13, Article ID 134302, 2013.
- [22] J. Zhu, H. Peng, C. K. Chan, K. Jarausch, X. F. Zhang, and Y. Cui, "Hyperbranched lead selenide nanowire networks," *Nano Letters*, vol. 7, no. 4, pp. 1095–1099, 2007.
- [23] A. Kovalskiy, A. C. Miller, H. Jain, and M. Mitkova, "In situ measurements of X-ray-induced silver diffusion into a Ge₃₀Se₇₀ thin film," *Journal of the American Ceramic Society*, vol. 91, no. 3, pp. 760–765, 2008.
- [24] J. D. Prades, F. Hernandez-Ramirez, R. Jimenez-Diaz et al., "The effects of electron-hole separation on the photoconductivity of individual metal oxide nanowires," *Nanotechnology*, vol. 19, no. 46, Article ID 465501, 2008.

Research Article

High Cycling Performance Cathode Material: Interconnected LiFePO₄/Carbon Nanoparticles Fabricated by Sol-Gel Method

Zhigao Yang and Shengping Wang

Faculty of Material Science and Chemistry, China University of Geosciences, Wuhan 430074, China

Correspondence should be addressed to Shengping Wang; spwang@cug.edu.cn

Received 8 April 2014; Accepted 22 May 2014; Published 12 June 2014

Academic Editor: Hongmei Luo

Copyright © 2014 Z. Yang and S. Wang. This is an open access article distributed under the Creative Commons Attribution License, which permits unrestricted use, distribution, and reproduction in any medium, provided the original work is properly cited.

Interconnected LiFePO₄/carbon nanoparticles for Li-ion battery cathode have been fabricated by sol-gel method followed by a carbon coating process involving redox reactions. The carbon layers coated on the LiFePO₄ nanoparticles not only served as a protection layer but also supplied fast electrons by building a 3D conductive network. As a cooperation, LiFePO₄ nanoparticles encapsulated in interconnected conductive carbon layers provided the electrode reactions with fast lithium ions by offering the lithium ions shortening and unobstructed pathways. Field emission scanning electron microscopy (FESEM) and X-ray diffraction (XRD) tests showed optimized morphology. Electrochemical characterizations including galvanostatic charge/discharge, cyclic voltammetry (CV), and electrochemical impedance spectroscopy (EIS) tests, together with impedance parameters calculated, all indicated better electrochemical performance and excellent cycling performance at high rate (with less than 9.5% discharge capacity loss over 2000 cycles, the coulombic efficiency maintained about 100%).

1. Introduction

Reported by Goodenough and coworkers for the first time in 1997, the phosphate polyanionic compound of LiFePO₄ shows superior performance including a high theoretical capacity (170 mAh g⁻¹) and an acceptable operating voltage (3.45 V versus Li⁺/Li) [1, 2]. However, the slow diffusivity of Li⁺ in LiFePO₄ (ca. 10⁻¹⁴ cm² s⁻¹) and the low electronic conductivity (ca. 10⁻⁹ S cm⁻¹) [3] restrict the high rate performance of LiFePO₄. Generally, carbon coating, nanocrystallization, and doping are main techniques to modify LiFePO₄. Although doping improved the performance of LiFePO₄ in some researches, the mechanism had not been clearly explained yet. Furthermore, there are some problems about the balance of charge and energy raising after doping to be taken into further consideration [4, 5]. Carbon coating can significantly improve the electrical conductivity [6–8] and reduce particle size as well as avoiding particle aggregation [9], nanocrystallization shortening the pathway of Li⁺ [10], and mitigating the problem of slow Li⁺ transport in the solid state. Thus, aiming at improving the low conductivity and slow diffusivity of Li⁺ at the same time, many modification researches are conducted based on the combination of carbon

coating (or carbon-decorating) and nanocrystallization [6, 11, 12]. However, the high surface energy of nanosized materials causes the problem of agglomeration, making the efforts of fabricating nanomaterials in vain [13]. This warns us that the carbon coating process should better take place accompanying the formation of nanoparticles or their precursors. Heterogeneous distribution of carbon and LiFePO₄ results in limited utilization of the LiFePO₄ active material [14], which emphasizes the importance of the quality of carbon layer (including the integrity, uniformity, and thickness). In order to make full use of the synergistic effect of carbon coating and nanocrystallization, structure of complete and uniform carbon layer coated on every single LiFePO₄ nanoparticle is highly desirable [15, 16]. For us, that means only a carbon coating process which happens during the formation of LiFePO₄ (or LiFePO₄ precursor) nanoparticles and resulting uniform, compact, and intact carbon layers can notably enhance the electrochemical performance of LiFePO₄ nanoparticles (especially the cycling and rate performances).

The interconnected LiFePO₄/carbon nanoparticles reported here possess the target structure (structure of complete and uniform carbon layer coated on every single

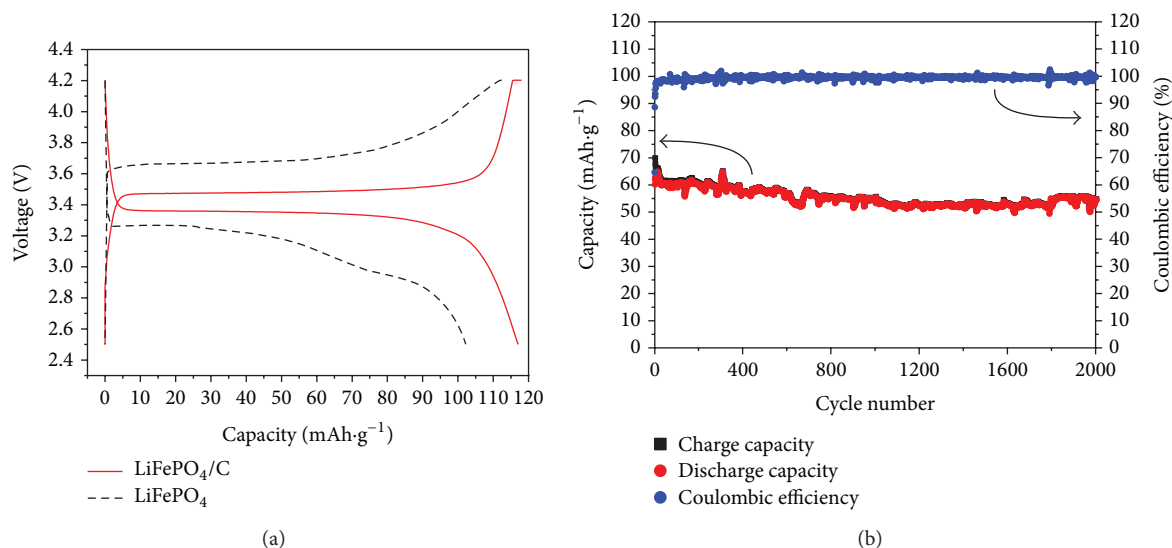


FIGURE 1: (a) Discharge/charge voltage profiles cycled at the 2nd cycle of LiFePO₄ and LiFePO₄/C at a current density of 34 mA g⁻¹ (0.2 C). (b) Cycling performance of interconnected LiFePO₄/C nanoparticles at a current density of 850 mA g⁻¹ (5 C).

LiFePO₄ nanoparticle) and exhibit commendable cycling performance at high rate.

2. Experimental

2.1. Fabrication of Bare LiFePO₄. The raw materials (all the chemical reagents used were obtained from Sinopharm Chemical Reagent Co., Ltd, China) for synthesizing the LiFePO₄ are P₂O₅, LiCl, and FeSO₄·7H₂O. With continuous stirring, 7.0970 g (0.05 mol) of P₂O₅ was dissolved into 50 mL absolute ethyl alcohol to form solution A, and 4.4621 g (0.1 mol) of LiCl was dissolved into 100 mL absolute ethyl alcohol to form solution B. After 27.8020 g (0.1 mol) of FeSO₄·7H₂O was added into 100 mL absolute ethyl alcohol, solution A and solution B were added into it with the volume ratio of 1 : 2 while stirring. Then the solution was covered with plastic film and stirred for 3 hours to form a uniform sol. After stirring in the 65°C water bath without plastic film for several hours, the gel was formed. Finally, sucrose (A reducing atmosphere was created by thermal decomposition of the sucrose at the upstream) and as-prepared gel were put in a magnetic boat with the mass ratio of 1:10 to undergo the calcining process at 700°C in argon atmosphere for 8 hours. The heat rate was 10°C min⁻¹ before 400°C and then 2°C min⁻¹ to 700°C.

2.2. Fabrication of LiFePO₄/Carbon Composite (LiFePO₄/C). All the experimental procedures did not change until the formation of a uniform sol. After forming the sol, 4.4 mL of aniline was added into the sol, followed by another stirring and reaction process for 3 hours. During this process, the redox reaction for coating polyaniline took place. The parameters of the solvent evaporation and heat treatment processes did not change either.

2.3. Characterizations. The phase structure of the products was determined by powder X-ray diffraction on a Bruker AXS D8-FOCUS diffractometer with Cu K α radiation. The morphology and particle sizes were observed by field emission scanning electron microscopy (FDAC SU8010). Thermogravimetry/differential scanning calorimetry curves were obtained using STA 449F3 analyzer (NETZSCH) in the temperature range of 30~1000°C, using alumina crucible under nitrogen atmosphere and heating rate of 10°C min⁻¹.

2.4. Electrochemical Measurements. Test cells were fabricated utilizing active materials (LiFePO₄ and LiFePO₄/C) with acetylene black and polyvinylidene difluoride (PVDF) as the working electrode. Active material (85 wt.%), acetylene black (10 wt.%), and PVDF binder (5 wt.%) were dispersed in N-methyl-2-pyrrolidinone (NMP) solvent and ground thoroughly to form a slurry. Then the slurry was spread onto aluminum foil and maintained at 65°C in oven overnight. Metallic lithium plate was used as the counter electrode. The long-term galvanostatic charge/discharge was evaluated with an Arbin BT2000 multichannel galvanostat in the potential range of 2.5~4.2 V (versus Li/Li⁺) at current densities of 34 mA g⁻¹ and 850 mA g⁻¹ (0.2 C and 5 C). CV and EIS were conducted on a Vmp3 (Biologic) electrochemical workstation. CV tests were done between 2.5 and 4.2 V (versus Li/Li⁺) at the scan rate of 0.5 mV s⁻¹. EIS measurements were carried out over a frequency range of 10⁵ ~10⁻² Hz using a sine wave of 5 mV.

3. Results and Discussion

Figure 1(a) shows the 2nd cycle of galvanostatic charge/discharge curves of LiFePO₄ and LiFePO₄/C at 0.2 C. The LiFePO₄ delivered a capacity of 102.2 mAh g⁻¹, while the

LiFePO₄/C delivered a capacity as high as 117.1 mAh g⁻¹ with a coulombic efficiency of 99.2%. The relative low specific capacity was calculated based on the composite of LiFePO₄ and carbon and could be explained by the high carbon content (~18.6%) of LiFePO₄/C obtained from the comparison of TG/DSC curves of LiFePO₄ and LiFePO₄/C shown in Figure 2 (the carbon content of our LiFePO₄/C was calculated from weight loss of the composite and this method was also reported by Lee et al. [17]). It is obviously showed that, comparing to LiFePO₄, the longer platforms of charge/discharge curves of LiFePO₄/C are almost parallel to each other from the beginning to the end, and the difference between the voltages of platforms is also much smaller, which represented better reversible performance, indicating decreased polarization. Electrochemical polarization was decreased because of fast electrons provided by carbon layers of high quality. Controlled particle size offered short diffusion distance for Li⁺ in the solid state and large specific surface areas with abundant active sites for Li⁺ to intercalate or deintercalate and concentration polarization was decreased in this way. With better reversible performance, the cycling performance of LiFePO₄/C is also notable even at high rate (5 C). As shown in Figure 1(b), with less than 9.5% discharge capacity loss over 2000 cycles, the coulombic efficiency maintained about 100%. The excellent cycling performance of our LiFePO₄/C is comparable with many other reports [15, 18, 19] and is closely associated with the structure produced by the carbon coating step involving redox reactions during the sol-gel process. The carbon coating process took place when the sol formed, as shown in Figure 3. After all the raw materials except aniline were mixed together and stirred for several hours, a uniform sol was formed. As there is O₂ in the air, amounts of ferrous ions were oxidized to ferric ions inevitably. The ferric ions were adsorbed to the surface of sol molecules due to the adsorption nature (the adsorption of charge particles) of sol. As a result of electrostatic interaction, all the ferric ions adsorbed distributed on the surface of the sol molecules uniformly and densely (state A). The polymerization of aniline is an oxidation process and ferric ions on the surface of sol molecules act as active sites for this oxidation reaction because the reduction process of ferric ions can coordinate with the oxidation process. That is to say the active sites for polymerization of aniline distributed on the surface of the sol molecules uniformly and densely. Aniline molecules have equal possibility to polymerize at anywhere on the surface of the sol molecules (state B). Thus, uniform, compact and intact polyaniline layers can be obtained by the cooperation between the polymerization of aniline (the oxidation process) and the reduction of ferric ions (state C). Finally, the same uniform, compact, and intact carbon layers coated on every single LiFePO₄ particle can be obtained after the calcining process (state D), instead of carbon layer with several agglomerated LiFePO₄ particles inside (state E) due to agglomeration caused by the high surface energy of the nanosized particles [13] or LiFePO₄ particles partially coated by carbon.

The FESEM picture shows irregular morphology of LiFePO₄ particles (Figure 4(a)). Although there are some

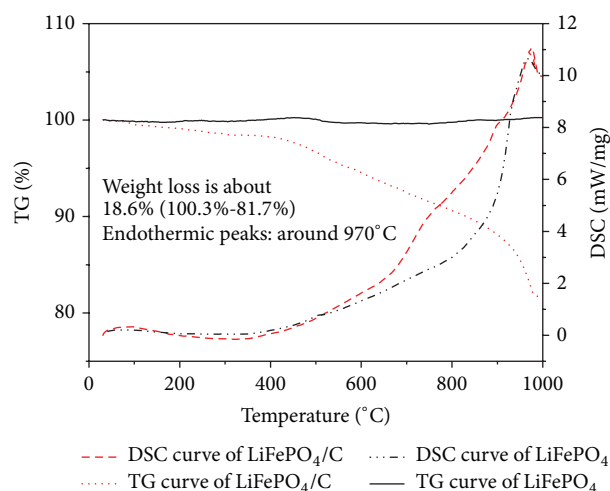


FIGURE 2: TG/DSC curves of LiFePO₄ and LiFePO₄/C.

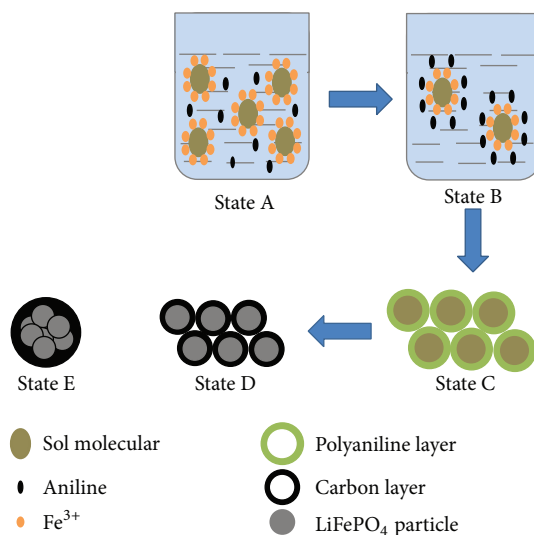


FIGURE 3: Scheme of formation process of interconnected LiFePO₄/C particles.

particles with the size of ~50 nm, these particles are not independent, but parts of much larger clusters and truly independent particles are not smaller than 500 nm. Comparing with LiFePO₄, the particles of LiFePO₄/C composite become much smaller and this huge change of morphology is mainly caused by the obtained carbon layers of high quality, which restrict the growth of LiFePO₄ and avoid the agglomeration of bare LiFePO₄ nanoparticles. As shown in Figure 4(b), with the size of ~50 nm, LiFePO₄/C nanoparticles interconnect with each other compactly, forming 3D continuous conductive structure. This is the very structure desired, which is shown as state D in Figure 3. In this optimized structure, electrons from multidimension can reach the LiFePO₄ particles immediately. The sluggish diffusion of Li⁺ in the solid state accelerated as a result of the shortened diffusion distance in smaller particles.

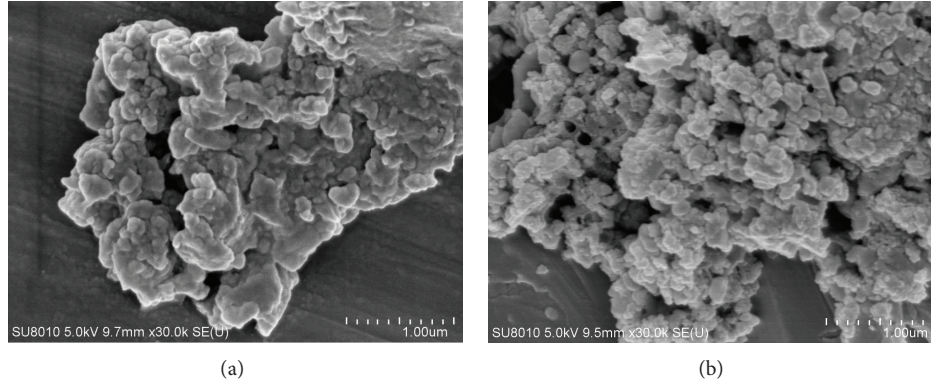


FIGURE 4: FESEM micrographs of samples: (a) SEM micrographs of LiFePO_4 and (b) SEM micrographs of LiFePO_4/C .

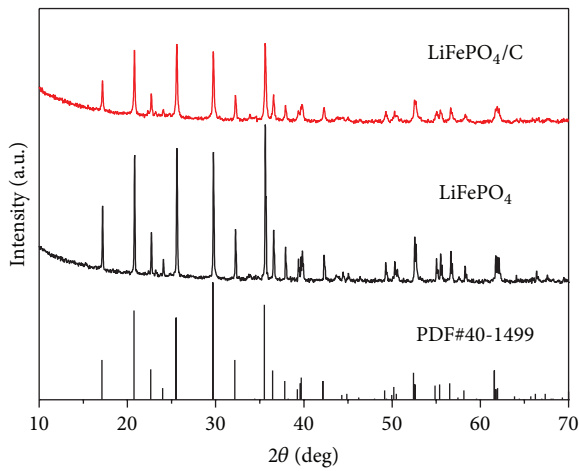


FIGURE 5: XRD patterns of LiFePO_4 and interconnected LiFePO_4/C particles.

The crystallographic structure determined by XRD further confirmed the smaller particle size after carbon coating. As shown in Figure 5, the widths of the major diffraction peaks turn to be bigger after carbon coating, indicating smaller particle size of LiFePO_4/C (according to Scherrer's formula). This phenomenon which is consistent with FESEM observations affirmed the main functions of the carbon layers, namely, the function of controlling particle size and avoiding agglomeration. From XRD patterns of the obtained LiFePO_4 and LiFePO_4/C , we can also see that all dominant diffraction peaks of LiFePO_4 and LiFePO_4/C samples can be indexed to orthorhombic LiFePO_4 (JCPDS card number 40-1499), indicating a perfect crystallinity of the as-synthesized samples. Besides, there is no evidence for the formation of amorphous carbons for the LiFePO_4/C .

As shown in Figure 6(a), a couple of redox peaks were observed for both LiFePO_4 and LiFePO_4/C in the CV curves obtained at a scan rate of 0.5 mV s^{-1} . Compared to LiFePO_4 , the smaller peak potential difference of LiFePO_4/C indicates better reversibility, which is brought about by the decreased polarizations just mentioned (Figure 1(a)). Much higher peak currents are also shown, indicating faster reaction rate of LiFePO_4/C , and further confirmed the advantage of the

interconnected structure, which provided electrode reactions of fast electrons and Li^+ . Figure 6(b) presents the typical EIS responses of LiFePO_4 and LiFePO_4/C . Both of the Nyquist plots are composed of a depressed semicircle in the high-frequency region followed by a slanted line in the low-frequency region.

Referring to reported methods [20] and based on our EIS measurements, impedance parameters were calculated and listed in Table 1. The equivalent circuit diagram is shown in Figure 7.

The Warburg coefficient σ_ω can be obtained by

$$Z_{re} = R_e + R_{ct} + \sigma_\omega \omega^{-0.5}, \quad (1)$$

where R_e is the resistance of the electrolyte, R_{ct} is the charge transfer resistance, and ω is the angular frequency in the low-frequency region. Both R_e and R_{ct} are kinetic parameters independent of frequency. So σ_ω is the slope for the plot of Z_{re} versus the reciprocal root square of the lower angular frequencies ($\omega^{-0.5}$); as shown in Figure 8, the slope of the fitted line is the Warburg coefficient σ_ω .

The diffusion coefficient values of the lithium ions (D) can be obtained from

$$D = \frac{R^2 T^2}{2A^2 n^4 F^4 C^2 \sigma^2}, \quad (2)$$

where R is the gas constant ($8.314 \text{ J mol}^{-1} \text{ K}^{-1}$), T is the temperature (298.5 K), A is the area of the electrode surface (2.0106 cm^2), F is Faraday's constant ($96,500 \text{ C mol}^{-1}$), C is the molar concentration of Li^+ (1.09 mol L^{-1}), and n is the number of electrons transferred in the electrode reactions (for LiFePO_4 , $n = 1$).

The conductivity values (σ) are calculated from

$$\sigma = \frac{1}{R_{ct}} \cdot \frac{t}{A}, \quad (3)$$

where t is the thickness of the cathode ($250 \mu\text{m}$).

The values of the exchange current density (i^0) are calculated from

$$i^0 = \frac{RT}{nFR_{ct}}. \quad (4)$$

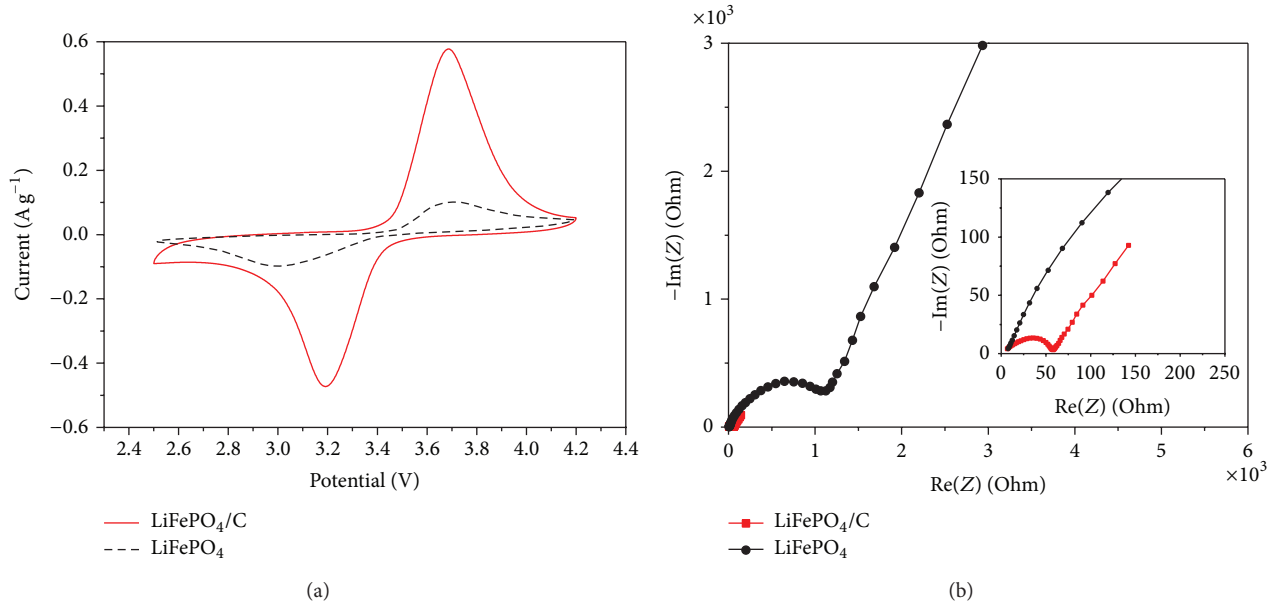


FIGURE 6: Electrochemical measurements of prepared samples: (a) CV curves of LiFePO₄ and the interconnected LiFePO₄/C nanoparticles in a voltage range of 2.5~4.2 V at a scanning rate of 0.5 mV s⁻¹. (b) Comparison of impedance spectra of LiFePO₄ and LiFePO₄/C.

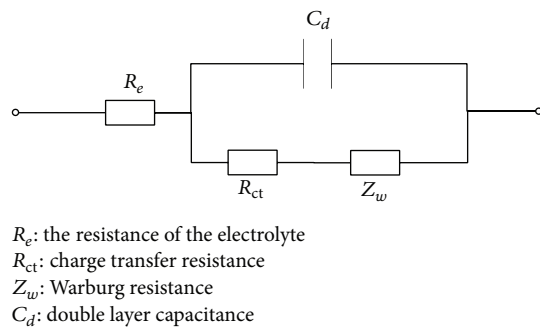


FIGURE 7: Equivalent circuit diagram used in the calculation of impedance parameters.

The double layer capacitance C_d is determined by

$$C_d = \frac{1}{\omega R_{ct}}. \quad (5)$$

Comparing all the impedance parameters of LiFePO₄/C and LiFePO₄, we can see there is no big difference of R_e between the two samples, because the whole system and operation conditions were kept the same. While the values of R_{ct} and σ_w changed dramatically, several orders of magnitude increases of D , σ , and i^0 were observed for LiFePO₄/C. All the changes reflected from the parameters listed in Table 1 can be explained from the aspect of structure. With uniform carbon layers on every single nanoparticle, all the nanoparticles interconnected with each other, forming 3D conductive network. The value of conductivity increases because electrons can diffuse from all directions. Diffusion of Li⁺ in the solid state becomes much faster in nanoparticles with controlled size, leading to the increase of the diffusion coefficient

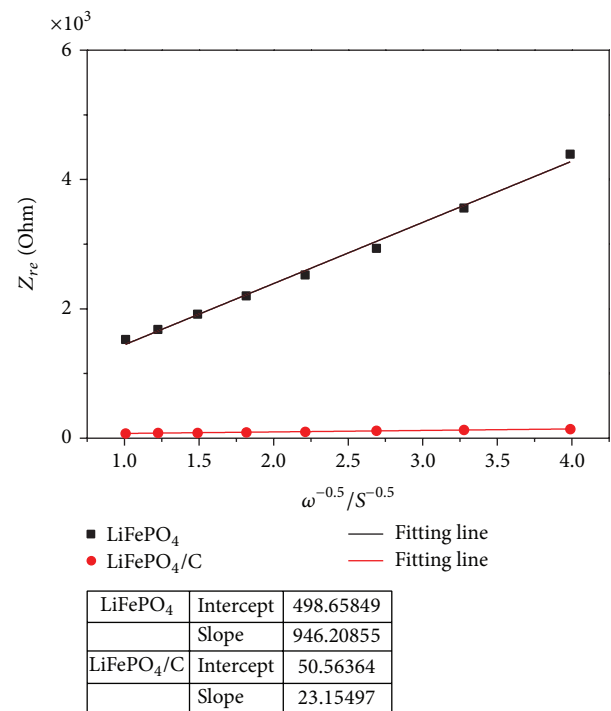


FIGURE 8: The relationship between Z_{re} and $\omega^{-0.5}$ at low frequencies for LiFePO₄ and LiFePO₄/C samples.

value of Li⁺ and reduction of Warburg impedance. Both electrons and Li⁺ can respond to the electrode reactions immediately, minimizing the electrochemical polarization and concentration polarization. What is more, according to some research, polyaniline contains element N, which can also

TABLE I: Impedance parameters of the samples.

Samples	R_e/Ω	R_{ct}/Ω	C_d/F	$\sigma_\omega/\Omega \text{ cm}^2 \text{ s}^{-0.5}$	$D/\text{cm}^2 \text{ s}^{-1}$	$\sigma/S \text{ cm}^{-1}$	$i^0/\text{mA cm}^{-2}$
LiFePO ₄ /C	9.3	41.3	2.2×10^{-4}	23.2	1.4×10^{-11}	3.0×10^{-4}	6.2×10^{-4}
LiFePO ₄	10.5	488.2	3.7×10^{-7}	946.2	8.3×10^{-15}	2.5×10^{-5}	5.3×10^{-5}

affect the electrochemical performance [21]. That is why the values of exchange current density increased and the charge transfer resistance decreased and our LiFePO₄/C sample exhibited notable cycling performance even at high rate.

Analysis based on all the parameters confirmed the results of CV and galvanostatic charge/discharge tests, which suggests that our carbon coating method is ingenious, efficient, and preferred and can result in ideal structure with carbon layers of high quality.

In addition to shortening the diffusion distance of Li⁺, the controlled particle size can also improve the utilization of active materials. In the lattice of LiFePO₄, Li⁺ migrates through one-dimensional channels [5, 22–24]. Cross-channel diffusion of Li-ion happens with the help of antisite defects [25, 26], but, with several immobile point defects (such as Fe_{Li}^{*}, a kind of defects: one ferrous ion occupies the lattice position of lithium ion) in a single channel, Li⁺ sites situated between immobile point defects cannot be reached, which causes “blocked” capacity. In very large particles most sites will be blocked by defects in this way, while the total channel length between surfaces in nanoparticles is small, resulting in channels containing very few or even zero defects. For instance, for particles smaller than 60 nm, 1% Fe_{Li}^{*} population leads to on average fewer than two defects residing in each channel and therefore no “blocked” Li⁺ sites [26]. For our interconnected LiFePO₄/C nanoparticles with an average diameter around 50 nm, there are less immobile point defects, which minimized the “blocked” capacity and improved the utilization of active materials.

Our carbon coating process is based on a couple of redox reactions following the formation of LiFePO₄ sol. Owing to the redox reactions, the position of carbon layer was fixed, the thickness of the carbon layer was limited, and the uniformity of the carbon layer was guaranteed. Finally, the target structure formed. With high quality carbon layers and controlled particle size, the electronic conductivity (σ), the diffusion coefficient of Li⁺ (D), and the exchange current density (i^0) all increased. Obviously, for the same purpose of ensuring the homogeneous distribution of carbon, our method turns to be more convenient, more efficient, and more ingenious. Because no surfactant is used, no complex experiments operations are needed and high cycling performance mentioned above is presented.

4. Conclusions

In conclusion, interconnected LiFePO₄/carbon nanoparticles were synthesized successfully in our work. By an ingenious, efficient, and convenient method involving a couple of redox reactions, the structure of uniform, compact, and intact carbon layer on every single LiFePO₄ nanoparticle was obtained. The high quality carbon layers coated on every LiFePO₄

particle not only acted as protection layers but also provided fast electrons for electrode reactions by forming 3D conductive network. The proper particle size controlled offered Li⁺ shorter diffusion distance, accelerating the diffusion of Li⁺ in the solid state. And the large specific surface area ensured the sufficient contact between the electrode material and electrolyte. Considering the existence of immobile point defects, the utilization of active materials was also improved. The synergistic effect of high quality carbon layers and controlled particle size decreased the electrochemical polarization and concentration polarization, making the reaction rate fast enough to exhibit dramatically improved electrochemical performance including remarkable cycling performance at high rate.

Conflict of Interests

The authors declare that there is no conflict of interests regarding the publication of this paper.

Acknowledgments

This work was supported by the National Natural Science Foundation of China (21173198) and the Science and Technology Support Program of Hubei Province, China (2013BHE014).

References

- [1] A. K. Padhi, K. S. Nanjundaswamy, and J. B. Goodenough, “Phospho-olivines as positive-electrode materials for rechargeable lithium batteries,” *Journal of the Electrochemical Society*, vol. 144, no. 4, pp. 1188–1194, 1997.
- [2] A. Padhi, K. Nanjundaswamy, C. Masquelier, S. Okada, and J. B. Goodenough, “Effect of structure on the Fe³⁺/Fe²⁺ redox couple in iron phosphates,” *Journal of the Electrochemical Society*, vol. 144, no. 5, pp. 1609–1613, 1997.
- [3] F. Yu, S. Ge, B. Li, G. Sun, R. Mei, and L. Zheng, “Three-dimensional porous LiFePO₄: design, architectures and high performance for lithium-ion batteries,” *Current Inorganic Chemistry*, vol. 2, no. 2, pp. 194–212, 2012.
- [4] M. Wagemaker, B. L. Ellis, D. Lützenkirchen-Hecht, F. M. Mulder, and L. F. Nazar, “Proof of supervalent doping in olivine LiFePO₄,” *Chemistry of Materials*, vol. 20, no. 20, pp. 6313–6315, 2008.
- [5] C. A. Fisher, V. M. Prieto, and M. S. Islam, “Lithium battery materials LiMPO₄ (M = Mn, Fe, Co, and Ni): insights into defect association, transport mechanisms, and doping behavior,” *Chemistry of Materials*, vol. 20, no. 18, pp. 5907–5915, 2008.
- [6] X.-L. Wu, Y.-G. Guo, J. Su, J.-W. Xiong, Y.-L. Zhang, and L.-J. Wan, “Carbon-nanotube-decorated nano-LiFePO₄@C cathode

- material with superior high-rate and low-temperature performances for lithium-ion batteries,” *Advanced Energy Materials*, vol. 3, no. 9, pp. 1155–1160, 2013.
- [7] J. Yang, J. Wang, Y. Tang et al., “In situ self-catalyzed formation of core-shell LiFePO_4 @CNTs nanowires for high rate performance lithium-ion batteries,” *Journal of Materials Chemistry A*, vol. 1, no. 25, pp. 7306–7311, 2013.
- [8] L. Fei, Y. Xu, X. Wu et al., “Instant gelation synthesis of 3D porous MoS_2 @C nanocomposites for lithium ion batteries,” *Nanoscale*, vol. 6, pp. 3664–3669, 2014.
- [9] L. Fei, Q. Lin, B. Yuan et al., “Reduced graphene oxide wrapped fcs nanocomposite for lithium-ion battery anode with improved performance,” *ACS Applied Materials and Interfaces*, vol. 5, no. 11, pp. 5330–5335, 2013.
- [10] R. Dominko, M. Bele, M. Gaberscek et al., “Porous olivine composites synthesized by sol-gel technique,” *Journal of Power Sources*, vol. 153, no. 2, pp. 274–280, 2006.
- [11] S. Wang, H. Yang, L. Feng et al., “A simple and inexpensive synthesis route for LiFePO_4 /C nanoparticles by co-precipitation,” *Journal of Power Sources*, vol. 233, pp. 43–46, 2013.
- [12] R. Yi, F. Dai, M. L. Gordin, S. Chen, and D. Wang, “Micro-sized si-c composite with interconnected nanoscale building blocks as high-performance anodes for practical application in lithium-ion batteries,” *Advanced Energy Materials*, vol. 3, no. 3, pp. 295–300, 2013.
- [13] H. Li and H. Zhou, “Enhancing the performances of li-ion batteries by carbon-coating: present and future,” *Chemical Communications*, vol. 48, no. 9, pp. 1201–1217, 2012.
- [14] J. Yang, J. Wang, Y. Tang et al., “ LiFePO_4 -graphene as a superior cathode material for rechargeable lithium batteries: impact of stacked graphene and unfolded graphene,” *Energy and Environmental Science*, vol. 6, no. 5, pp. 1521–1528, 2013.
- [15] Y. Wang, Y. Wang, E. Hosono, K. Wang, and H. Zhou, “The design of a LiFePO_4 /carbon nanocomposite with a core-shell structure and its synthesis by an in situ polymerization restriction method,” *Angewandte Chemie*, vol. 47, no. 39, pp. 7461–7465, 2008.
- [16] J. Wang and X. Sun, “Understanding and recent development of carbon coating on LiFePO_4 cathode materials for lithium-ion batteries,” *Energy and Environmental Science*, vol. 5, no. 1, pp. 5163–5185, 2012.
- [17] S.-H. Lee, M.-J. Jung, J.-S. Im, K.-Y. Sheem, and Y.-S. Lee, “Preparation and characterization of electrospun LiFePO_4 /carbon complex improving rate performance at high C-rate,” *Research on Chemical Intermediates*, vol. 36, no. 6-7, pp. 591–602, 2010.
- [18] X. Yan, G. Yang, J. Liu et al., “An effective and simple way to synthesize LiFePO_4 /C composite,” *Electrochimica Acta*, vol. 54, no. 24, pp. 5770–5774, 2009.
- [19] J. Liu, J. Wang, X. Yan et al., “Long-term cyclability of LiFePO_4 /carbon composite cathode material for lithium-ion battery applications,” *Electrochimica Acta*, vol. 54, no. 24, pp. 5656–5659, 2009.
- [20] Y. Cui, X. Zhao, and R. Guo, “Improved electrochemical performance of $\text{La}_{0.7}\text{Sr}_{0.3}\text{MnO}_3$ and carbon co-coated LiFePO_4 synthesized by freeze-drying process,” *Electrochimica Acta*, vol. 55, no. 3, pp. 922–926, 2010.
- [21] G. Ćirić-Marjanovic, I. Pašti, N. Gavrilov, A. Janošević, and S. Mentus, “Carbonised polyaniline and polypyrrole: towards advanced nitrogen-containing carbon materials,” *Chemical Papers*, vol. 67, no. 8, pp. 781–813, 2013.
- [22] J. Yang and J. S. Tse, “Li ion diffusion mechanisms in LiFePO_4 : an ab initio molecular dynamics study,” *Journal of Physical Chemistry A*, vol. 115, no. 45, pp. 13045–13049, 2011.
- [23] P. Zhang, Y. Wu, D. Zhang et al., “Molecular dynamics study on ion diffusion in LiFePO_4 olivine materials,” *Journal of Physical Chemistry A*, vol. 112, no. 24, pp. 5406–5410, 2008.
- [24] J. Hong, X. Wang, Q. Wang et al., “Structure and electrochemistry of vanadium-modified LiFePO_4 ,” *Journal of Physical Chemistry C*, vol. 116, no. 39, pp. 20787–20793, 2012.
- [25] G. K. P. Dathar, D. Sheppard, K. J. Stevenson, and G. Henkelman, “Calculations of Li-ion diffusion in olivine phosphates,” *Chemistry of Materials*, vol. 23, no. 17, pp. 4032–4037, 2011.
- [26] R. Malik, D. Burch, M. Bazant, and G. Ceder, “Particle size dependence of the ionic diffusivity,” *Nano Letters*, vol. 10, no. 10, pp. 4123–4127, 2010.

Research Article

Enhanced Performance of Dye-Sensitized Solar Cells with Graphene/ZnO Nanoparticles Bilayer Structure

Chih-Hung Hsu,^{1,2} Cheng-Chih Lai,² Lung-Chien Chen,¹ and Po-Shun Chan¹

¹ Department of Electro-Optical Engineering, National Taipei University of Technology, No. 1, Section 3, Chung-Hsiao E. Road, Taipei 106, Taiwan

² Bichen Technology Co., Ltd., 18F-3, No. 77, Section 1, Xintai 5th Road, Xizhi District, New Taipei City 22101, Taiwan

Correspondence should be addressed to Lung-Chien Chen; ocean@ntut.edu.tw

Received 27 March 2014; Accepted 19 May 2014; Published 9 June 2014

Academic Editor: Hongmei Luo

Copyright © 2014 Chih-Hung Hsu et al. This is an open access article distributed under the Creative Commons Attribution License, which permits unrestricted use, distribution, and reproduction in any medium, provided the original work is properly cited.

This study reports characteristics of dye-sensitized solar cells (DSSCs) with graphene/ZnO nanoparticle bilayer structure. The enhancement of the performance of DSSCs achieved using graphene/ZnO nanoparticle films is attributable to the introduction of an electron-extraction layer and absorption of light in the visible range and especially in the range 300–420 nm. DSSC that was fabricated with graphene/ZnO nanoparticle film composite photoanodes exhibited a V_{oc} of 0.5 V, a J_{sc} of 17.5 mA/cm², an FF of 0.456, and a calculated η of 3.98%.

1. Introduction

Graphene has attracted much interest because of its unique properties and potential applications. As the thinnest 2D material, graphene has a high carrier mobility [1] and an excellent optical transparency [2]. Graphene and its derivatives have been used in transparent conductive films [3], as a new class of efficient hole- and electron-extraction materials [4–6], and in organic photovoltaic (PV) cells [7, 8]. Graphene films can be prepared using various techniques, including the micromechanical exfoliation of graphite [9], chemical vapor deposition (CVD) [10–14], the solution-based chemical reduction of graphene oxide to graphene [15–19], and magnetron sputtering, which has many advantages such as low cost, large scale, and ease of control.

The nanostructures of ZnO films can easily be tuned by modifying the growth solution and the use of ultrasonic spraying [20]. ZnO can also be tailored to various nanostructures, such as nanorods/nanowires [21–25], nanotubes [24–27], nanoflowers [28], and nanosheets [29, 30], which have high electrical conductivity and enhanced photon absorption, supporting improved short-circuit current density and overall light conversion efficiency [31].

In this work, a graphene film with high electron mobility is incorporated into a ZnO nanoparticle film to form

a compact layer for use in dye-sensitized solar cells. This investigation studies the optical, structural, and surface properties of a graphene film that is grown on ITO electrodes by radiofrequency magnetron sputtering, as functions of thickness, in high-performance DSSCs. The introduction of the sputtered graphene film (electron-extraction layer) with optimal thickness enhances the efficiency of conversion of the DSSCs.

2. Experimental Setup

In this study, a graphene film was prepared on ITO glass using a radio frequency magnetron sputtering system. Table 1 lists the typical deposition conditions for the graphene film. The resistivity of the graphene film is around 2.2×10^3 ohm-cm. The ZnO nanoparticle film was deposited by ultrasonic spray pyrolysis at atmospheric pressure on ITO/graphene glass. Three aqueous solutions, $Zn(CH_3COO)_2 \cdot 2H_2O$ (0.5 mol/l), CH_3COONH_4 (2.5 mol/l), and $In(NO_3)_3$ (0.5 mol/l), were used as sources of zinc, nitrogen, and indium, respectively. The atomic ratio of Zn/N in the N-doped film was 1:2 and that of Zn/N/In in the N-In codoped film was 1:2:0.15 [20]. An aerosol of the precursor solution was produced using a commercial ultrasonic nebulizer. Colloidal TiO_2 was

TABLE 1: Typical deposition conditions for graphene film.

Target	Graphite
Target diameter	5 cm
Substrate-to-target distance	4 cm
RF power	90 W
Sputtering ambient	Ar
Gas flow rate	90 sccm
Residual pressure	$<5 \times 10^{-6}$ Torr
Sputtering pressure	3.1 mTorr
Deposition time	40 min

prepared from 6 g nanocrystalline powder (Degussa, P25 titanium oxide, Japan) and both 0.1 mL of Triton X-100 and 0.2 mL of acetylacetone, which were stirred together for 24 hrs. Subsequently, the mixture was spin-coated on ITO glass and ITO/graphene/ZnO substrate to a thickness of approximately $15 \mu\text{m}$, and a $3 \times 3 \text{ mm}^2$ active area was defined. Thereafter, the prepared thin film photoelectrode was immersed in a 3×10^{-4} M Ru-metal complex dye, D719 ($[\text{RuL}_2(\text{NCS})_2] : 2 \text{ TBA}$), at room temperature for 24 hrs, before it was sintered at 450 or 500°C for 30 min, to increase its anatase content (anatase : rutile = 85 : 15) [32]. The electrolyte included 0.05 M iodide, 0.5 M lithium iodide, and 0.5 M 4-tert-butylpyridine (TBP) in propylene carbonate. A 100 nm thick layer of platinum was sputtered onto the ITO substrate to form a counter electrode. Cells were fabricated by placing sealing films between the two electrodes, leaving only two via-holes for injection of the electrolyte. The sealing process was performed on a hot plate at 100°C for 3 min. Then, the electrolyte was injected into the space between the two electrodes through the via-holes. Finally, the via-holes were sealed using epoxy at a low vapor transmission rate. Figure 1 schematically depicts the complete structure.

A field emission scanning electron microscope (FESEM) (LEO 1530) was adopted to examine the cross-section and surface morphology of the cells. Additionally, the current density-voltage (J - V) characteristics were measured using a Keithley 2420 programmable source meter under irradiation by a 1000 W xenon lamp. Finally, the irradiation power density on the surface of the sample was calibrated as 1000 W/m^2 .

3. Results and Discussion

Figures 2(a) and 2(b) present the surface and cross-sectional FESEM images of the ZnO nanoparticle films on glass substrate. The surface images clearly reveal that ZnO nanoparticle films are highly dense and grown vertically on glass substrates, as shown in Figures 2(a) and 2(b). The high-resolution image reveals that the obtained ZnO nanoparticle films exhibited hexagonal morphology with an average nanoparticle diameter of 300~330 nm. Figure 2(c) shows a typical X-ray diffraction (XRD) pattern of ZnO film. Three dominant diffraction peaks, ZnO(100) ($2\theta = 31.76^\circ$), ZnO(002) ($2\theta = 34.46^\circ$), and ZnO(101) ($2\theta = 36.27^\circ$), are

observed. That demonstrates a typical ZnO polycrystalline structure.

Figure 3 presents the absorption spectra of the TiO_2 , ZnO nanoparticle, and graphene/ZnO nanoparticle/ TiO_2 films. The ZnO nanoparticle thin film yields a strong absorption peak at $\sim 380 \text{ nm}$, revealing the existence of crystalline wurtzite hexagonal ZnO. The DSSC with the graphene film clearly has higher absorption intensity than the DSSC without the graphene film in the visible range, and especially in the range 300–420 nm.

Figure 4 shows the XRD plots of the TiO_2 film electrodes before and after annealing. The TiO_2 films were dried in air at room temperature for 10 min and then annealing at 450°C for 30 min. Two dominant anatase diffraction peaks, (101) ($2\theta = 25.28^\circ$) and (004) ($2\theta = 37.73^\circ$), are observed. Following annealing, the sample was highly crystalline and all of the diffraction peaks could be indexed to anatase TiO_2 .

In optoelectronic devices, proper contact between the electrode and the transporter (recombination and back transfer) is crucial for charge collection. Figure 5 presents the schematic energy level diagram of the DSSCs with the graphene and ZnO nanoparticle film. Graphene has a work function (-4.42 eV versus vacuum) similar to that of the ITO (-4.8 eV versus vacuum) electrode. The graphene does not prevent the flow of injected electrons down to the ITO electrode because its work function exceeds that of the ITO electrode [33–35]. Therefore, the implanted graphene collects electrons and acts as a transporter in the effective separation of charge and rapid transport of the photogenerated electrons.

Based on the above discussion, the incorporation of graphene into ZnO nanoparticle film enables DSSC devices to operate more efficiently. Figure 6 plots photocurrent J - V curves of the DSSCs obtained under 100 mW/cm^2 illumination and the AM 1.5 G condition without and with the graphene and ZnO nanoparticle film, fabricated on an ITO glass substrate. The cell has an active area of $3 \times 3 \text{ mm}^2$ and no antireflective coating. Table 2 presents the measured cell parameters—open-circuit voltage (V_{oc}), short-circuit current (J_{sc}), fill factor (FF), and energy conversion efficiency (η). The DSSC that was fabricated with graphene/ZnO nanoparticle film composite photoanodes exhibited a V_{oc} of 0.5 V, a J_{sc} of 17.5 mA/cm^2 , an FF of 0.456, and a calculated η of 3.98%. Incorporating graphene oxide into the graphene film effectively decreases the internal resistance within the photoanodes and prolonged the electron lifetime. Therefore, the improved photovoltaic properties of DSSC with the graphene/ZnO nanoparticle film photoanode are attributable to the strong absorption of dye and the high light harvesting efficiency, which reduce electron recombination loss.

4. Conclusion

This work discusses the improvement that is made by the introduction of a sputtered graphene/ZnO nanoparticle film into DSSCs. The enhancement of the performance of DSSCs by the introduction of graphene/ZnO nanoparticle films may be attributed to the introduction of an electron-extraction

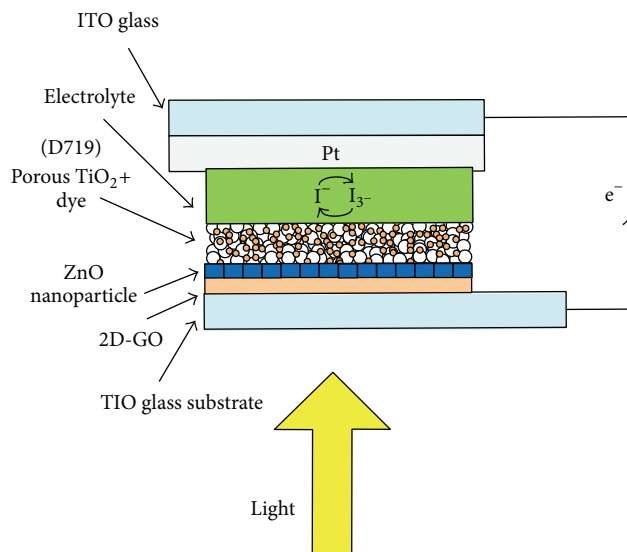


FIGURE 1: Schematic of DSSCs with graphene/ZnO nanoparticle film.

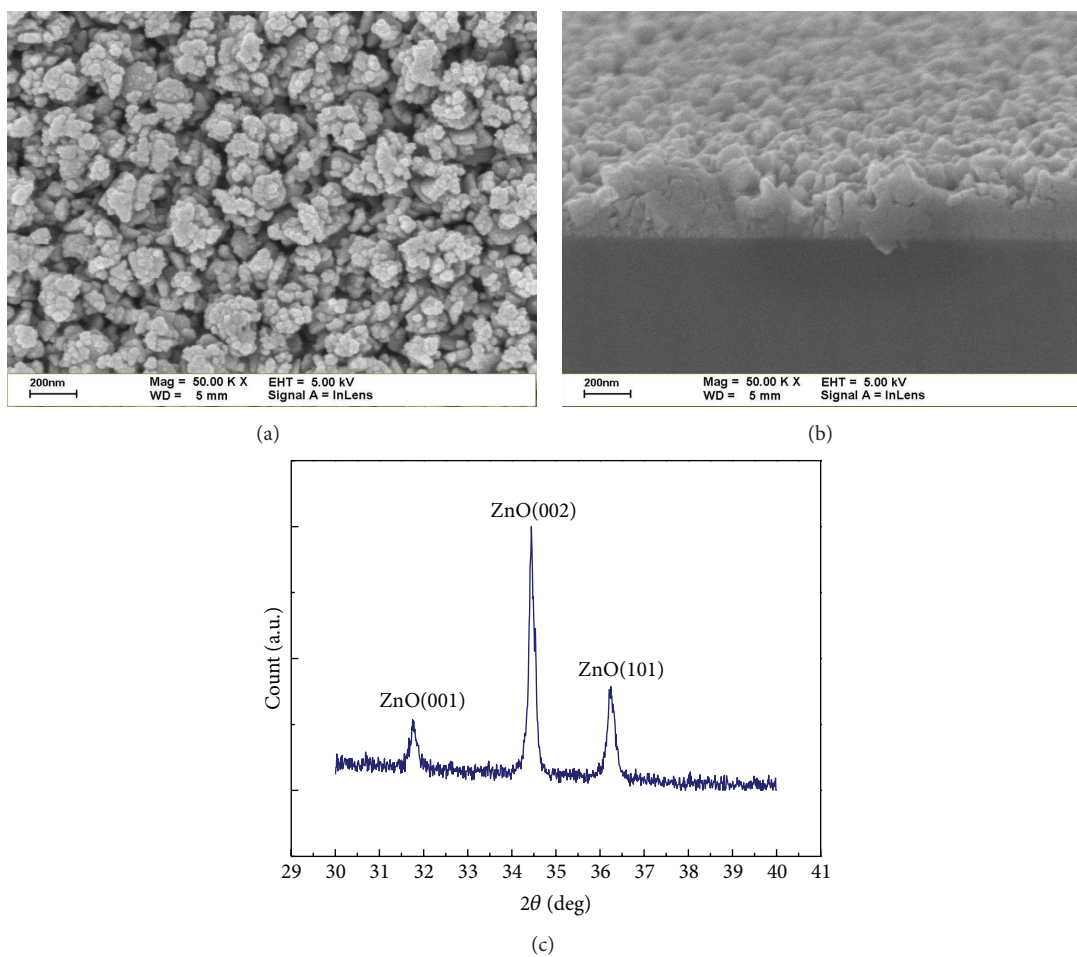
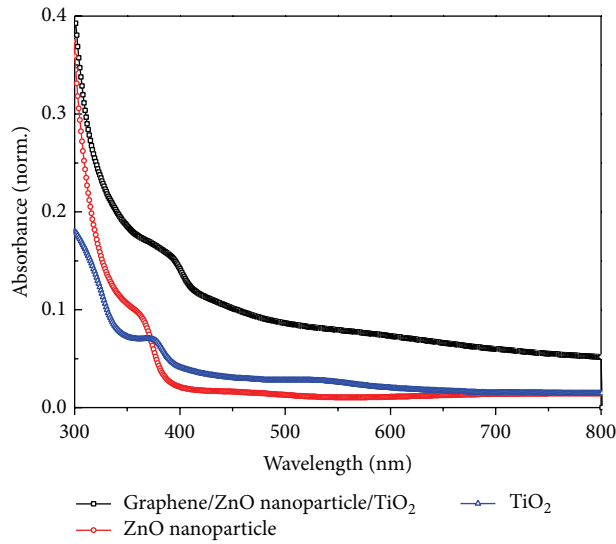
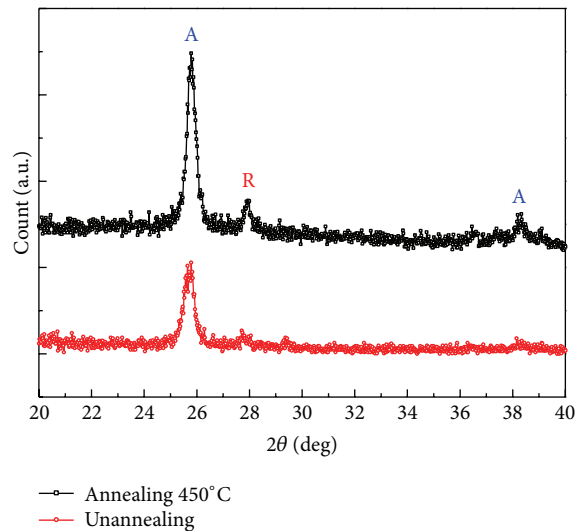


FIGURE 2: (a) FESEM surface image of photoanode with ZnO nanoparticle film. (b) FESEM cross-section image of ZnO nanoparticle film. (c) XRD pattern of ZnO nanoparticles film.

TABLE 2: Parameters of TiO₂ DSSCs with and without the graphene and ZnO nanoparticle film, fabricated on bare ITO glass substrate.

	ITO/TiO ₂	ITO/ZnO nanoparticle/TiO ₂	ITO/graphene/ZnO nanoparticle/TiO ₂
J_{sc} (mA/cm ²)	6.9	11.3	17.5
V_{oc} (V)	0.5	0.45	0.5
F.F.	0.419	0.473	0.456
Efficiency	1.45	2.4	3.98

FIGURE 3: Absorbance spectra of TiO₂, ZnO nanoparticle, and graphene/ZnO nanoparticle/TiO₂ film.FIGURE 4: XRD pattern of TiO₂ on glass substrate (A: anatase, R: rutile).

layer and the absorption of light in the visible range, especially in the range 300–420 nm. A DSSC that was fabricated with graphene/ZnO nanoparticle film composite photoanodes had a V_{oc} of 0.5 V, a J_{sc} of 17.5 mA/cm², an FF of 0.456, and a calculated η of 3.98%. Accordingly, the improvement

of photovoltaic properties of DSSC by the introduction of the graphene/ZnO nanoparticle film photoanode is attributable to the strong absorption of dye and the high light harvesting efficiency, which can reduce the electron recombination loss. The above results demonstrate the potential application of

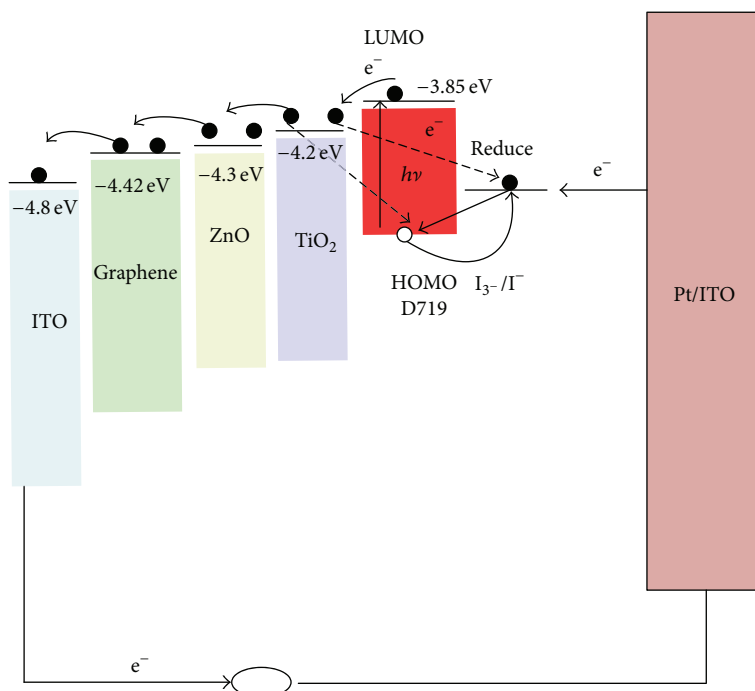


FIGURE 5: Energy level diagram and mechanism of photocurrent generation in DSSCs with GO and ZnO nanoparticles.

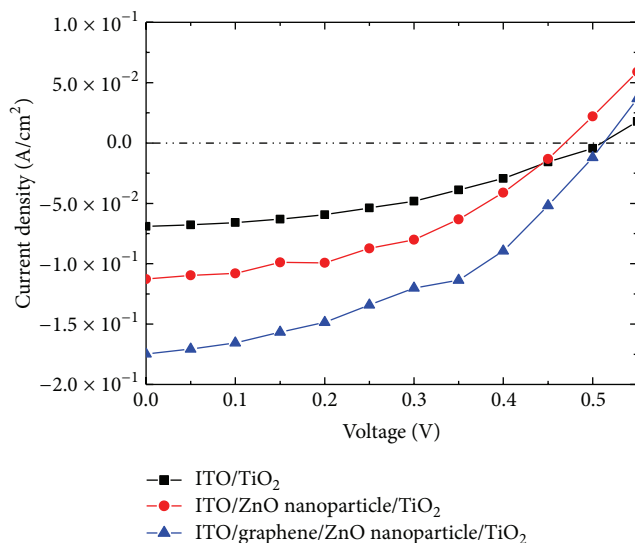


FIGURE 6: Current-voltage (J - V) characteristics of DSSCs fabricated with ITO/graphene/ZnO nanoparticle/TiO₂ photoanodes under simulated illumination by a light intensity of 100 mW/cm² (AM 1.5).

graphene oxide to improve for enhancing the performance of ZnO nanoparticle-based DSSCs, which can be produced on a large scale at low cost.

Conflict of Interests

The authors declare that there is no conflict of interests regarding the publication of this paper.

Acknowledgment

Financial support of this paper was provided by the National Science Council of the Republic of China under Contract no. NSC 102-2622-E-027-021-CC3.

References

- [1] X. Du, I. Skachko, A. Barker, and E. Y. Andrei, "Approaching ballistic transport in suspended graphene," *Nature Nanotechnology*, vol. 3, no. 8, pp. 491–495, 2008.
- [2] R. R. Nair, P. Blake, A. N. Grigorenko et al., "Fine structure constant defines visual transparency of graphene," *Science*, vol. 320, no. 5881, p. 1308, 2008.
- [3] S. Bae, H. Kim, Y. Lee et al., "Roll-to-roll production of 30-inch graphene films for transparent electrodes," *Nature Nanotechnology*, vol. 5, no. 8, pp. 574–578, 2010.
- [4] J. Liu, Y. Xue, Y. Gao, D. Yu, M. Durstock, and L. Dai, "Hole and electron extraction layers based on graphene oxide derivatives for high-performance bulk heterojunction solar cells," *Advanced Materials*, vol. 24, no. 17, pp. 2228–2233, 2012.
- [5] J. Liu, Y. Xue, and L. Dai, "Sulfated graphene oxide as a hole-extraction layer in high-performance polymer solar cells," *Journal of Physical Chemistry Letters*, vol. 3, no. 14, pp. 1928–1933, 2012.
- [6] X. Wang, L. Zhi, N. Tsao, Ž. Tomović, J. Li, and K. Müllen, "Transparent carbon films as electrodes in organic solar cells," *Angewandte Chemie—International Edition*, vol. 47, no. 16, pp. 2990–2992, 2008.
- [7] X. Wang, L. Zhi, and K. Müllen, "Transparent conductive graphene electrodes for dye-sensitized solar cells," *Nano Letters*, vol. 8, no. 1, pp. 323–327, 2007.

- [8] K. S. Novoselov, A. K. Geim, S. V. Morozov et al., "Electric field in atomically thin carbon films," *Science*, vol. 306, no. 5696, pp. 666–669, 2004.
- [9] C. Berger, Z. Song, T. Li et al., "Ultrathin epitaxial graphite: 2D electron gas properties and a route toward graphene-based nanoelectronics," *Journal of Physical Chemistry B*, vol. 108, no. 52, pp. 19912–19916, 2004.
- [10] A. Dato, V. Radmilovic, Z. Lee, J. Phillips, and M. Frenklach, "Substrate-free gas-phase synthesis of graphene sheets," *Nano Letters*, vol. 8, no. 7, pp. 2012–2016, 2008.
- [11] K. S. Kim, Y. Zhao, H. Jang et al., "Large-scale pattern growth of graphene films for stretchable transparent electrodes," *Nature*, vol. 457, no. 7230, pp. 706–710, 2009.
- [12] A. Reina, X. Jia, J. Ho et al., "Large area, few-layer graphene films on arbitrary substrates by chemical vapor deposition," *Nano Letters*, vol. 9, no. 1, pp. 30–35, 2009.
- [13] P. W. Sutter, J.-I. Flege, and E. A. Sutter, "Epitaxial graphene on ruthenium," *Nature Materials*, vol. 7, no. 5, pp. 406–411, 2008.
- [14] D. Li, M. B. Müller, S. Gilje, R. B. Kaner, and G. G. Wallace, "Processable aqueous dispersions of graphene nanosheets," *Nature Nanotechnology*, vol. 3, no. 2, pp. 101–105, 2008.
- [15] S. Park and R. S. Ruoff, "Chemical methods for the production of graphenes," *Nature Nanotechnology*, vol. 4, no. 4, pp. 217–224, 2009.
- [16] S. Stankovich, D. A. Dikin, R. D. Piner et al., "Synthesis of graphene-based nanosheets via chemical reduction of exfoliated graphite oxide," *Carbon*, vol. 45, no. 7, pp. 1558–1565, 2007.
- [17] V. C. Tung, M. J. Allen, Y. Yang, and R. B. Kaner, "High-throughput solution processing of large-scale graphene," *Nature Nanotechnology*, vol. 4, no. 1, pp. 25–29, 2009.
- [18] J. Zhang, H. Yang, G. Shen, P. Cheng, J. Zhang, and S. Guo, "Reduction of graphene oxide vial-ascorbic acid," *Chemical Communications*, vol. 46, no. 7, pp. 1112–1114, 2010.
- [19] L. C. Chen, C. H. Tien, and C. S. Fu, "Magneto-optical characteristics of Mn-doped ZnO films deposited by ultrasonic spray pyrolysis," *Materials Science in Semiconductor Processing*, vol. 15, pp. 80–85, 2012.
- [20] M. Law, L. E. Greene, J. C. Johnson, R. Saykally, and P. Yang, "Nanowire dye-sensitized solar cells," *Nature Materials*, vol. 4, no. 6, pp. 455–459, 2005.
- [21] J. B. Baxter and E. S. Aydil, "Nanowire-based dye-sensitized solar cells," *Applied Physics Letters*, vol. 86, no. 5, Article ID 053114, 2005.
- [22] A. Du Pasquier, H. Chen, and Y. Lu, "Dye sensitized solar cells using well-aligned zinc oxide nanotip arrays," *Applied Physics Letters*, vol. 89, no. 25, Article ID 253513, 2006.
- [23] H.-M. Cheng, W.-H. Chiu, C.-H. Lee, S.-Y. Tsai, and W.-F. Hsieh, "Formation of branched ZnO nanowires from solvothermal method and dye-sensitized solar cells applications," *Journal of Physical Chemistry C*, vol. 112, no. 42, pp. 16359–16364, 2008.
- [24] I. Gonzalez-Valls and M. Lira-Cantu, "Vertically-aligned nanostructures of ZnO for excitonic solar cells: a review," *Energy and Environmental Science*, vol. 2, no. 1, pp. 19–34, 2009.
- [25] A. B. F. Martinson, J. W. Elam, J. T. Hupp, and M. J. Pellin, "ZnO nanotube based dye-sensitized solar cells," *Nano Letters*, vol. 7, no. 8, pp. 2183–2187, 2007.
- [26] A. B. F. Martinson, M. S. Goes, F. Fabregat-Santiago, J. Bisquert, M. J. Pellin, and J. T. Hupp, "Electron transport in dye-sensitized solar cells based on zno nanotubes: evidence for highly efficient charge collection and exceptionally rapid dynamics," *Journal of Physical Chemistry A*, vol. 113, no. 16, pp. 4015–4021, 2009.
- [27] C. Y. Jiang, X. W. Sun, G. Q. Lo, D. L. Kwong, and J. X. Wang, "Improved dye-sensitized solar cells with a ZnO-nanoflower photoanode," *Applied Physics Letters*, vol. 90, no. 26, Article ID 263501, 2007.
- [28] E. Hosono, S. Fujihara, I. Honma, and H. Zhou, "The fabrication of an upright-standing zinc oxide nanosheet for use in dye-sensitized solar cells," *Advanced Materials*, vol. 17, no. 17, pp. 2091–2094, 2005.
- [29] E. Hosono, Y. Mitsui, and H. Zhou, "Metal-free organic dye sensitized solar cell based on perpendicular zinc oxide nanosheet thick films with high conversion efficiency," *Dalton Transactions*, vol. 28, no. 40, pp. 5439–5441, 2008.
- [30] E. M. Kaidashev, M. Lorenz, H. von Wenckstern et al., "High electron mobility of epitaxial ZnO thin films on c-plane sapphire grown by multistep pulsed-laser deposition," *Applied Physics Letters*, vol. 82, no. 22, pp. 3901–3903, 2003.
- [31] C.-C. Wang and J. Y. Ying, "Sol-gel synthesis and hydrothermal processing of anatase and rutile titania nanocrystals," *Chemistry of Materials*, vol. 11, no. 11, pp. 3113–3120, 1999.
- [32] R. Czerw, B. Foley, D. Tekleab, A. Rubio, P. M. Ajayan, and D. L. Carroll, "Substrate-interface interactions between carbon nanotubes and the supporting substrate," *Physical Review B*, vol. 66, no. 15, Article ID 033408, pp. 334081–334084, 2002.
- [33] A. Andersson, N. Johansson, P. Bröms, N. Yu, D. Lupo, and W. R. Salaneck, "Fluorine tin oxide as an alternate to indium tin oxide in polymer LEDs," *Advanced Materials*, vol. 10, no. 11, pp. 859–863, 1998.
- [34] A. Kongkanand, R. M. Dominguez, and P. V. Kamat, "Single wall carbon nanotube scaffolds for photoelectrochemical solar cells. Capture and transport of photogenerated electrons," *Nano Letters*, vol. 7, no. 3, pp. 676–680, 2007.
- [35] F. Xu, J. Chen, X. Wu et al., "Graphene scaffolds enhanced photogenerated electron transport in ZnO photoanodes for high-efficiency dye-sensitized solar cells," *Journal of Physical Chemistry C*, vol. 117, no. 17, pp. 8619–8627, 2013.

Research Article

A New Method for Superresolution Image Reconstruction Based on Surveying Adjustment

Jianjun Zhu,¹ Cui Zhou,^{1,2} Donghao Fan,¹ and Jinghong Zhou¹

¹ School of Geosciences and Info-Physics, Central South University, Changsha 410083, China

² College of Traffic Information, Hunan Communication Polytechnic, Changsha, Hunan 410132, China

Correspondence should be addressed to Jianjun Zhu; zjj@csu.edu.cn and Cui Zhou; cuizhou@163.com

Received 24 April 2014; Accepted 24 May 2014; Published 9 June 2014

Academic Editor: Yongfeng Luo

Copyright © 2014 Jianjun Zhu et al. This is an open access article distributed under the Creative Commons Attribution License, which permits unrestricted use, distribution, and reproduction in any medium, provided the original work is properly cited.

A new method for superresolution image reconstruction based on surveying adjustment method is described in this paper. The main idea of such new method is that a sequence of low-resolution images are taken firstly as observations, and then observation equations are established for the superresolution image reconstruction. The gray function of the object surface can be found by using surveying adjustment method from the observation equations. High-resolution pixel value of the corresponding area can be calculated by using the gray function. The results show that the proposed algorithm converges much faster than that of conventional superresolution image reconstruction method. By using the new method, the visual feeling of reconstructed image can be greatly improved compared to that of iterative back projection algorithm, and its peak signal-to-noise ratio can also be improved by nearly 1 dB higher than the projection onto convex sets algorithm. Furthermore, this method can successfully avoid the ill-posed problems in reconstruction process.

1. Introduction

Obtaining images is a process from ideal high-resolution (HR) image to observation image. Superresolution image reconstruction (SRIR) is a reverse process of obtaining images, which uses many low-resolution (LR) images obtained by multiple observations on the same target to calculate the real image of the target. SRIR was firstly proposed by Harris [1] and Goodman [2]. It is similar to the process of surveying adjustment, which gets optimal value by multiobservations on the same object in field of surveying. SRIR can obtain one or more HR images from multiple low-resolution images with complementary information. It can overcome the limitation of hardware and correspondingly increase the image resolution. Nowadays, SRIR techniques play an important role in remote sensing, video security monitoring, military aerial reconnaissance, medical digital image processing, and video standard conversion. One of the most typical applications of SRIR technology is in SPOT5 satellite of France. The satellite takes two images with resolution of 5 m, but with mutual dislocation of 0.5 pixel. Images with

resolution of 2.5 m are obtained by SRIR and provided to the whole world.

Up to now, a lot of algorithms have been proposed [3–16]. These algorithms can be roughly divided into two categories: one is frequency-domain algorithm [17–19] and the other is spatial-domain algorithm [4, 13]. In frequency-domain algorithms, images are transformed onto frequency domain and SRIR is carried in frequency domain. In spatial-domain algorithm, image gray value are computed directly in the process of SRIR. Frequency-domain algorithms are usually based on idealistic assumptions, so their application is very limited and cannot be effectively applied in most cases. While spatial-domain algorithm [20–25], such as nonuniform spatial interpolation, iterative back projection (IBP), has difficulty to make use of a priori information, hence the quality of SRIR will be severely limited [26]. Even the projection onto convex sets (POCS) algorithm, a real popular method, sometimes is unstable in computation and heavily depends on the initial estimation of SRIR, and its solution is often not unique and so on. Actually, most of the above two kinds of algorithms are proposed according to some specific

situations; the performance of SRIR from multiple images usually depends on the imaging system and the accurate degradation model. The algorithm universality of SRIR is rarely dealt with. In surveying and mapping field, if the same object is observed multiple times, the optimum value of the object can be obtained by using surveying adjustment. SRIR is similar to this process. If a real image can be represented by a gray function, any pixel value will be the integration of its gray function in the pixel, and hence the relationship between observation images (namely, LR images in SRIR) and real image (namely, HR image in SRIR) can be described by an integration relationship. Based on this principle, a general surveying adjustment model containing integration is established in this paper. And, on this model, a new method for SRIR is proposed. The main idea of this new method for SRIR is that a sequence of low-resolution images are taken firstly as observations, and then observation equations are established by using survey adjustment method. The gray function of the real image is estimated on the observation equations. After that, the estimated gray function is used to calculate HR pixel value of the corresponding area. Finally, HR image can be obtained.

In order to evaluate quantitatively reconstruction image, peak signal-to-noise ratio (PSNR) and structural similarity index (SSIM) are usually used as two evaluation indicators. PSNR describe gray similarity between two images, and SSIM describe structural similarity of two images. PSNR and SSIM are simultaneously used to get a comprehensive evaluation for reconstruction images in this paper [6].

2. The Principle of SRIR Based on the Surveying Adjustment

Pixel value of any image can be regarded as integration of its gray function within the scope of the pixel; namely,

$$g_i = \int_{v_i} f(x, y) ds, \quad (1)$$

where g_i is pixel value, x and y are pixel coordinates, v_i is pixel scope, and $f(x, y)$ is the gray function of object surface. If $f(x, y)$ of the real image is known, superresolution image with any resolution can be calculated by (1). Conversely, if gray values of pixels are known, we can estimate $f(x, y)$ on these gray values of pixels. Basic idea is to take pixel gray values of LR images as observations and real value of gray function as unknowns and then use surveying adjustment method to estimate $\hat{f}(x, y)$, which will be the closest to the real value of gray function, and then pixel values of SR can be calculated by gray function $\hat{f}(x, y)$.

For one or more LR images coexist within the same area, it can be regarded as multiple observation for the real gray function in such area. Considering the errors which possibly existing in the different pixel gray values, the observation equations can be approximately expressed as follows:

$$\begin{aligned} g_1 + V_1 &= \int_{v_1} f(x, y) ds, \\ g_2 + V_2 &= \int_{v_2} f(x, y) ds, \end{aligned}$$

$$\begin{aligned} &\vdots \\ g_n + V_n &= \int_{v_n} f(x, y) ds, \end{aligned} \quad (2)$$

where

$$\begin{aligned} L &= (g_1 \ g_2 \ \cdots \ g_n)^T, \quad V = (V_1 \ V_2 \ \cdots \ V_n)^T, \\ &\int_{v_i} f(x, y) ds \\ &= \left(\int_{v_1} f(x, y) ds \ \int_{v_2} f(x, y) ds \ \cdots \ \int_{v_n} f(x, y) ds \right)^T. \end{aligned} \quad (3)$$

The above observation equations can also be expressed as a matrix:

$$L + V = \int_{v_i} f(x, y) ds, \quad (4)$$

where L is the vector of observation, V is correction vector of observations, gray function $f(x, y)$ is unknown, and n is the number of pixels of LR images related to the same small region. It is an integral relationship between observations and unknowns in the above observation equations; thus we call (4) as ‘‘adjustment model with integration.’’ Different from traditional adjustment model, the functions here must be determined rather than parameters. However, how to find the solution of (4) needs to be further studied. For images, gray function $f(x, y)$ can be denoted by Fourier series or by wavelet function. Here, we use polynomial to substitute the gray function $f(x, y)$ and transform (4) into a model of parameters estimation. If gray function is replaced by quadratic polynomial within a sufficiently small region, such as

$$f(x, y) = a_0 + a_1x + a_2y + a_3x^2 + a_4y^2 + a_5xy. \quad (5)$$

Substituting (5) into (2), the following is obtained:

$$\begin{aligned} g_i + V_i &= \int_{v_i} (a_0 + a_1x + a_2y + a_3x^2 + a_4y^2 + a_5xy) ds \\ &= B_i X, \end{aligned} \quad (6)$$

where

$$\begin{aligned} X &= (a_0 \ a_1 \ a_2 \ a_3 \ a_4 \ a_5)^T; \\ B_i &= \left[\int_{v_i} ds \ \int_{v_i} x ds \ \int_{v_i} y ds \ \int_{v_i} x^2 ds \ \int_{v_i} y^2 ds \ \int_{v_i} xy ds \right]. \end{aligned} \quad (7)$$

Equation (4) can be written again as follows:

$$L + V = BX. \quad (8)$$

According to the least square adjustment method, the solution X can be found as follows:

$$X = (B^T PB)^{-1} B^T PL, \quad (9)$$

where P is the weight of observations. Estimation $\hat{f}(x, y)$ of real gray function can be calculated by putting X into (5), and then (10) is obtained by putting $\hat{f}(x, y)$ into (1):

$$\begin{aligned} \hat{g}_i &= \int_{v_i} \hat{f}(x, y) ds \\ &= \int_v (\hat{a}_0 + \hat{a}_1 x + \hat{a}_2 y + \hat{a}_3 x^2 + \hat{a}_4 y^2 + \hat{a}_5 xy) ds. \end{aligned} \quad (10)$$

According to (10), we can calculate pixel values of HR image in SRIR.

3. The Application of SRIR Based on Surveying Adjustment

When using (4) or (8) for SRIR, one key is to determine the region that the gray function will deal with, namely, how to select pixel values as observations. Generally, real gray function of object surface is very complicated; if we use a quadratic function to substitute the real gray function, it must be in a small region. In this paper, we determine the region according to the following method: for any pixel (i, j) of the reference image, one can get its surrounding 8 pixels, and then total of 9 pixels can be taken as observations. For the second image after registration, one should select the pixel closest to pixel (i, j) in reference image and its surrounding 8 pixels as observations, and so on. For every LR image, 9 pixels can be selected as observations. Based on these observations, an estimate of real gray function can be obtained according to (9). And then pixel value of coordinate (i, j) and the surrounding 8 pixel values of SR image can be calculated by (10). Obviously, the computation of this method will converge and can successfully avoid the ill-posed problems.

When (9) is used, it is necessary to determine the weight P of observations. In fact, pixel value L above contains two kinds of noise: one is the noise of image itself and the other is the model error brought in by the substitution of quadratic polynomial. The model errors will depend on the distance to the center of the region using quadratic polynomial. Accordingly, the scheme of weighting observations is taken as follows: for any pixel $L(i, j)$ of the reference image, one can calculate the distances between $L(i, j)$ and the surrounding 8 pixels and the distances between $L(i, j)$ and the corresponding 9 pixels of the second image. Then, the weight values of 17 observations are defined by inverse distances square; that is,

$$P_i = \frac{1}{d_{i,j}^2}, \quad (11)$$

where $d_{i,j}$ denotes the distance between the concerned pixel and pixel $L(i, j)$ and P_i denotes the weight of the observation corresponding to the concerned pixel. The weight value of pixel $L(i, j)$ itself will use

$$P_i = \frac{1}{xscale^2}, \quad (12)$$

where $xscale$ is half pixel width.

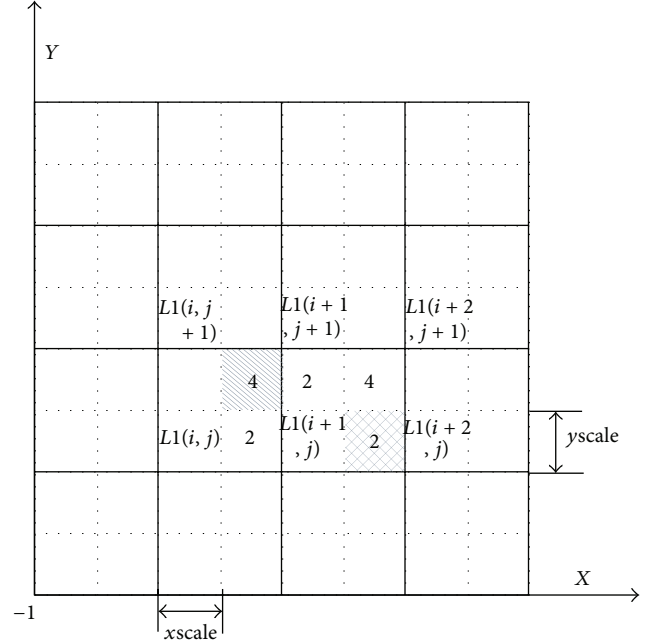


FIGURE 1: Schematic diagram of overlapping of HR pixels.

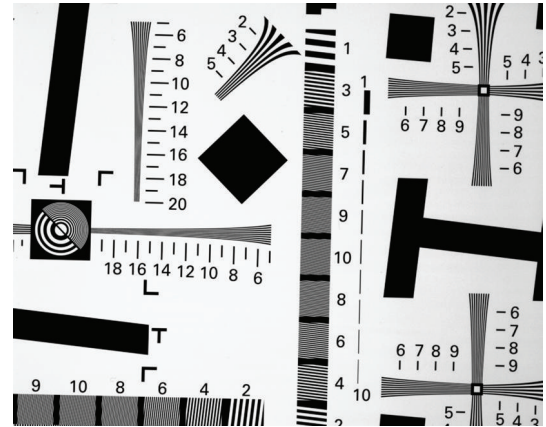


FIGURE 2: The desired HR image.

Pixel values of HR image exist overlapping area according to (10); overlapping area can be shown in Figure 1. For the overlapping region, we use the average value as the last HR pixel value.

4. Testing and Results Analysis

In order to check the feasibility of the suggested method, we design tests according to the following idea: we add some noise to a HR image and then take samples from the HR image to obtain a series of LR images. By using these LR images, we try to reconstruct the HR image. Comparing with the original image, we can know the feasibility of the suggested method. The whole process can be divided into the following four steps: obtaining LR images, image registration, fuzzy estimation, and image reconstruction.

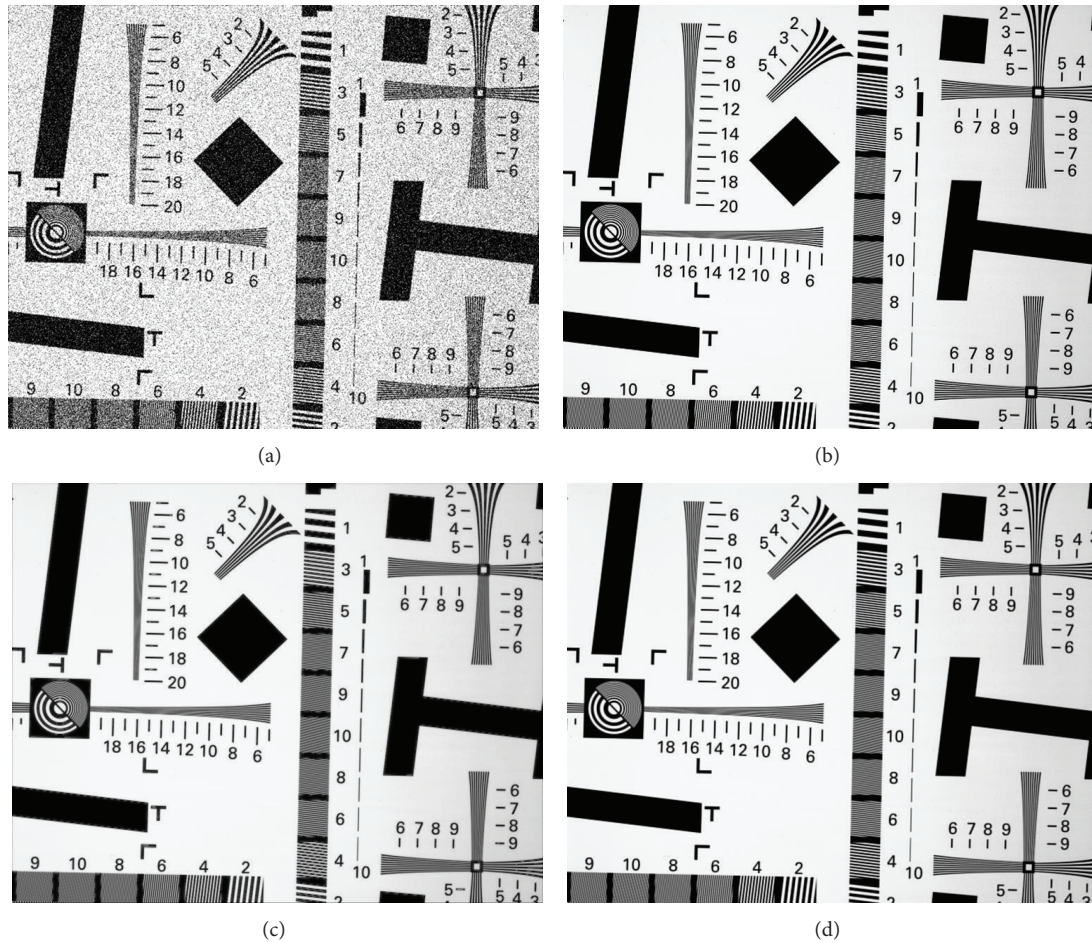


FIGURE 3: The results of image reconstruction. (a) LR image, (b) image of IBP reconstruction, (c) image of POCS reconstruction, and (d) image of our algorithm reconstruction.

4.1. Obtaining LR Images. We can firstly select a HR image, and then we transform the HR image into a sequence of LR images. Image transformation includes image translation and rotation, fuzzy processing, down sampling, and image noise. An example with a size 640×512 and gray-scale level 256 image is as shown in Figure 2; we simulate four LR images with subpixel displacement. The sequence of LR images is created through the following steps. Firstly, original HR image is shifted with different motion vectors in vertical and horizontal directions to produce four images. Secondly, these images are converted to frequency domain for setting frequency range 0-0.1 to zero; we can get four blurred images. Thirdly, these images are downsampled by the factor of 2 in each direction to produce four LR images of a size of 320×256 . Finally, we add Gaussian noise to downsampled images, where the variance is 0.05 and the mean value is 0.

4.2. Image Registration. Image registration is to choose one LR image as reference frame, and the other LR images are aligned with reference frame on space. LR images registration is irregular sampling of HR grids. Registration models usually include translation model, affine transformation model, bilinear model, projection model, and rigorous model [26].

The scale invariant feature transform (SIFT) algorithm is adopted here to get subpixel precision in image registration. Image registration based on characteristics can be generally divided into the following three steps: feature extraction, feature description, and feature matching [27].

4.3. The Fuzzy Function and Noise Estimation. Fuzzy function describes image formation process affected by fuzzy degradation. The precision of the estimation of fuzzy function can directly affect the quality of SRIR. In these experiments, Gaussian fuzzy function is adopted. And Gaussian noise with mean 0 and variance 0.05 is added into LR image. Wiener filtering is used to deblur and denoise for LR images in the image preprocessing stage.

4.4. Image Reconstruction. A sequence of LR images are used to reconstruct the HR image with the same size of original image by IBP, POCS, and this algorithm. Reconstruction results are shown in Figure 3. We can see that the visual feeling of Figures 3(b) and 3(d) is better than that of Figure 3(c). For the detailed comparison, we can take a small part of the images and enlarge it in Figure 4. From Figure 4, we can

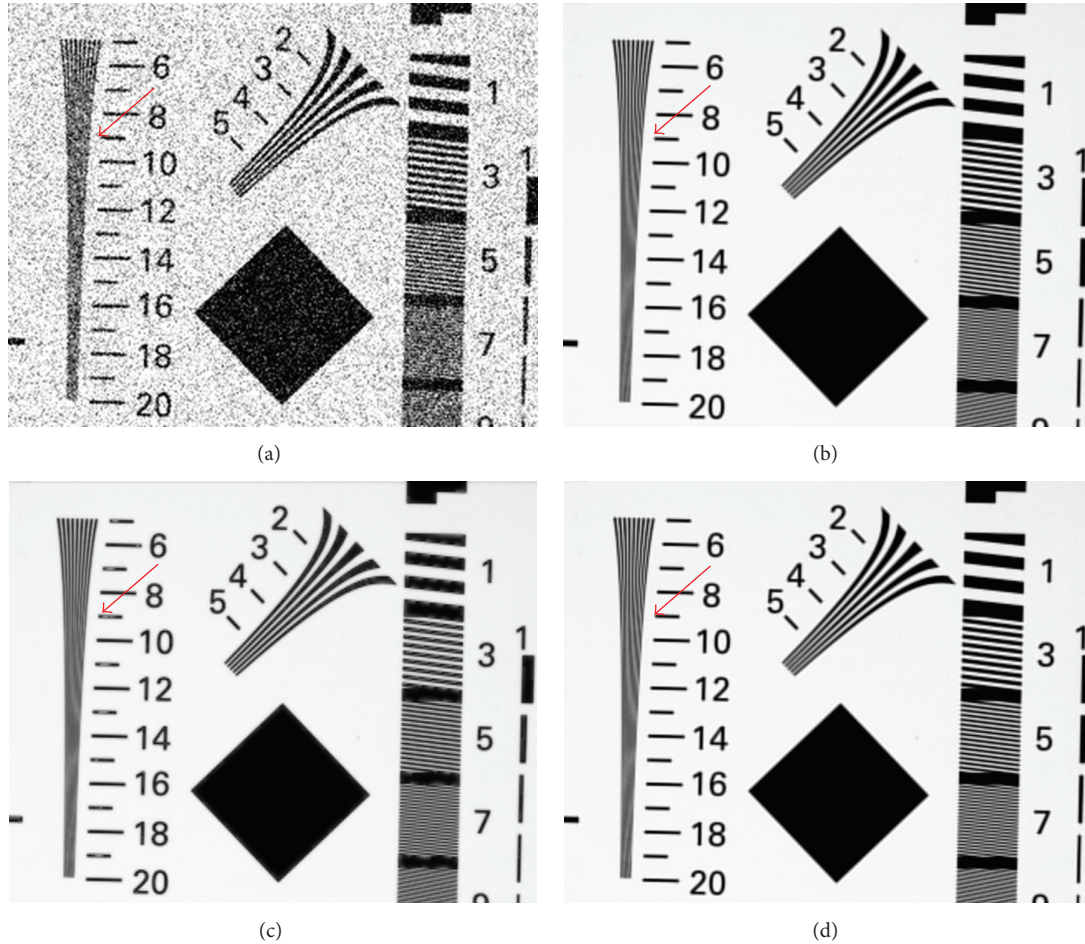


FIGURE 4: The results of intercepting part reconstruction image. (a) LR image, (b) image of IBP reconstruction, (c) image of POCS reconstruction, and (d) image of our algorithm reconstruction.

clearly see that the reconstruction images have richer details. Finally, the peak signal-to-noise ratio (PSNR) and structural similarity index (SSIM) are both used to evaluate the objective reconstruction. PSNR is a measure of gray similarity between two images. SSIM is a measure of structural similarity of two images. PSNR and SSIM can be simultaneously used to evaluate comprehensively reconstruction image from gray similarity and structural similarity [24]. The results are shown in Table 1. One can see that PSNR of the suggested method is nearly 1dB higher than that of the other two algorithms in Table 1. This means that reconstruction image by the suggested algorithm has higher gray level similarity with original image than the other two methods. From the value of SSIM, one can see that reconstruction image from the suggested algorithm in this paper has the same structural similarity with the other two algorithms.

5. Conclusions

The method proposed in this paper is based on surveying adjustment theory. Examples show that the method is feasible. The quadratic polynomial can be used as gray function

TABLE 1: Evaluation results of PSNR and SSIM.

Evaluation index	IBP	POCS	Our algorithm
PSNR/dB	68.6987	71.5415	72.3819
SSIM	0.8324	0.8016	0.8762

of object surface and the convergence speed of the methods is faster than that of POCS and IBP algorithm. Results also showed that the proposed method can obtain a good result of reconstruction image through the subjective and objective comprehensive evaluation.

Conflict of Interests

The authors declare that there is no conflict of interests regarding the publication of this paper.

Acknowledgments

The authors would like to thank the National Basic Research Program (no. 2013CC733303), the National Natural Science Foundation of China (nos. 41274010 and 40974007), the

National High Technology Research and Development Program of China (no. 2012AA121301), and the Fundamental Research Funds of Central South University for financial support.

References

- [1] J. L. Harris, "Diffraction and resolving power," *Journal of the Optical Society of America*, vol. 54, no. 7, pp. 931–933, 1964.
- [2] J. Goodman, *Introduction To Fourier Optics, McGraw-Hill Physical and Quantum Electronics Series*, McGraw-Hill, New York, NY, USA, 1968.
- [3] M. Elad and Y. Hel-Or, "A fast super-resolution reconstruction algorithm for pure translational motion and common space-invariant blur," *IEEE Transactions on Image Processing*, vol. 10, no. 8, pp. 1187–1193, 2001.
- [4] S. C. Park, M. K. Park, and M. G. Kang, "Super-resolution image reconstruction: a technical overview," *IEEE Signal Processing Magazine*, vol. 20, no. 3, pp. 21–36, 2003.
- [5] M.-G. Hu, J.-F. Wang, and Y. Ge, "Super-resolution reconstruction of remote sensing images using multifractal analysis," *Sensors*, vol. 9, no. 11, pp. 8669–8683, 2009.
- [6] L. Zhang, H. Zhang, H. Shen, and P. Li, "A super-resolution reconstruction algorithm for surveillance images," *Signal Processing*, vol. 90, no. 3, pp. 848–859, 2010.
- [7] X. Li, Y. Hu, X. Gao, D. Tao, and B. Ning, "A multi-frame image super-resolution method," *Signal Processing*, vol. 90, no. 2, pp. 405–414, 2010.
- [8] J. Tian and K.-K. Ma, "Stochastic super-resolution image reconstruction," *Journal of Visual Communication and Image Representation*, vol. 21, no. 3, pp. 232–244, 2010.
- [9] H. Nasir, V. Stanković, and S. Marshall, "Singular value decomposition based fusion for super-resolution image reconstruction," *Signal Processing: Image Communication*, vol. 27, no. 2, pp. 180–191, 2012.
- [10] N. Pinto, M. Simard, and R. Dubayah, "Using InSAR coherence to map stand age in a boreal forest," *Remote Sensing*, vol. 5, no. 1, pp. 42–56, 2013.
- [11] H. Zhang, L. Zhang, and H. Shen, "A super-resolution reconstruction algorithm for hyperspectral images," *Signal Processing*, vol. 92, no. 9, pp. 2082–2096, 2012.
- [12] M. Debella-Gilo and A. Käb, "Measurement of surface displacement and deformation of mass movements using least squares matching of repeat high resolution satellite and aerial images," *Remote Sensing*, vol. 4, no. 1, pp. 43–67, 2012.
- [13] M. Liu, J. Huang, M. Gao, and S. Qin, *High Performance Super-Resolution Reconstruction of Multiple Images Based on Fast Registration and Edge Enhancement*, Intelligence Science and Big Data Engineering, Springer, 2013.
- [14] A. G. Devi, T. Madhu, and K. L. Kishore, "An improved super resolution image reconstruction using SVD based fusion and blind deconvolution techniques," *International Journal of Signal Processing, Image Processing Pattern Recognition*, vol. 7, no. 1, p. 283, 2014.
- [15] H.-X. Wang, Z.-M. Lu, Y. Zhang, and Z. Diao, "Sub-dictionary based sparse representation for efficient super-resolution image reconstruction," *Information Technology Journal*, vol. 13, no. 1, pp. 94–101, 2014.
- [16] H. Zhang, Z. Yang, L. Zhang, and H. Shen, "Super-resolution reconstruction for multi-angle remote sensing images considering resolution differences," *Remote Sensing*, vol. 6, no. 1, pp. 637–657, 2014.
- [17] A. M. Tekalp, M. K. Ozkan, and M. I. Sezan, "High-resolution image reconstruction from lower-resolution image sequences and space-varying image restoration," in *Proceedings of the IEEE International Conference on Acoustics, Speech, and Signal Processing (ICASSP '92)*, pp. 169–172, 1992.
- [18] C. E. Davila, "Efficient recursive total least squares algorithm for FIR adaptive filtering," *IEEE Transactions on Signal Processing*, vol. 42, no. 2, pp. 268–280, 1994.
- [19] E. A. Kaltenbacher and R. C. Hardie, "High-resolution infrared image reconstruction using multiple low-resolution aliased frames," in *Proceedings of the IEEE Aerospace and Electronics Conference (NAECON '96)*, pp. 142–152, April 1996.
- [20] J. J. Clark, M. R. Palmer, and P. D. Lawrence, "A transformation method for the reconstruction of functions from nonuniformly spaced samples," *IEEE Transactions on Acoustics, Speech, and Signal Processing*, vol. 33, no. 5, pp. 1151–1165, 1985.
- [21] H. Stark and P. Oskoui, "High-resolution image recovery from image-plane arrays, using convex projections," *Journal of the Optical Society of America. A, Optics and image science*, vol. 6, no. 11, pp. 1715–1726, 1989.
- [22] M. Irani and S. Peleg, "Improving resolution by image registration," *Graphical Models and Image Processing*, vol. 53, no. 3, pp. 231–239, 1991.
- [23] R. R. Schultz and R. L. Stevenson, "Extraction of high-resolution frames from video sequences," *IEEE Transactions on Image Processing*, vol. 5, no. 6, pp. 996–1011, 1996.
- [24] M. Elad and A. Feuer, "Superresolution restoration of an image sequence: adaptive filtering approach," *IEEE Transactions on Image Processing*, vol. 8, no. 3, pp. 387–395, 1999.
- [25] Z. Xinming and S. Lansun, "The Development of Super-Resolution Restoration from Image Sequences," *Measurement & Control Technology*, vol. 21, no. 5, pp. 33–35, 2002.
- [26] A. G. Devi, T. Madhu, and K. L. Kishore, "An improved super resolution image reconstruction using SVD based fusion and blind deconvolution techniques," *International Journal of Signal Processing, Image Processing & Pattern Recognition*, vol. 7, no. 1, pp. 283–297, 2014.
- [27] Y.-N. Kang, H. Huang, Y.-Y. Zhu, and P.-J. Lai, "Super-resolution image registration based on SIFT and its realization with MATLAB," *Computer Knowledge and Technology*, vol. 5, no. 58, pp. 8031–8033, 2009.

Research Article

The Fabrication and Properties Characterization of Wood-Based Flame Retardant Composites

Xia He,¹ Xianjun Li,¹ Zhu Zhong,¹ Yongli Yan,¹ Qunying Mou,²
Chunhua Yao,¹ and Chun Wang¹

¹ Material Science and Engineering College, Central South University of Forestry and Technology, Changsha, Hunan 410004, China

² College of Science, Central South University of Forestry and Technology, Changsha, Hunan 410004, China

Correspondence should be addressed to Xianjun Li; lxjmu@163.com

Received 31 March 2014; Accepted 9 May 2014; Published 26 May 2014

Academic Editor: Sanqing Huang

Copyright © 2014 Xia He et al. This is an open access article distributed under the Creative Commons Attribution License, which permits unrestricted use, distribution, and reproduction in any medium, provided the original work is properly cited.

Wood-based flame retardant composites were fabricated based on vacuum-pressure impregnating method after high intensive microwave pretreatment. The effects of ammonium polyphosphate (APP) and modified nano-zinc borate (nZB) addition on flame-retardation and smoke-suppression properties of wood were investigated by cone calorimeter method (CONE) and thermogravimetric analysis (TGA). The results show that the heat release rate (HRR), peak heat release rate (pk-HRR), and total heat release (THR) of APP-treated woods decreased greatly with increasing concentration of APP. However, mean yield of CO (Mean COY) of APP-treated wood was much higher (3.5 times) than that of untreated wood. Compared with wood treated with APP at a concentration of 15%, the total smoke product (TSP), Mean COY, and pk-HRR decreased by 78.4%, 71.43%, and 31.23%, when wood was treated with APP and nZB (both concentrations were at 15%). APP and nZB have synergistic effects of flame-retardation and smoke-suppression. Nano-zinc borate combined with APP would be used in wood-based composites to efficiently retard flame, reduce fire intensity, and decrease noxious (CO)/smoke release.

1. Introduction

With the increase in living conditions and growing concerns about environmental protection for people, wood is attracting gradually more attention for its particular characteristics and excellent environmentally friendly properties. However, its marked combustibility may cause unexpected potential fire hazards. Flame-retardant treatment of a wood is one of the most effective ways to protect it from fire. Upon growing awareness of environmental protection and consumer safety, requirement standards to flame retardants have been raised accordingly. In addition to flame-retard capability, properties, such as being harmless to human, animals, and plants and less release of smoke and toxic gases when combusted, are important indices for people to choose a flame retardant. Inorganic flame retardants which have good thermal stability, less releases of smoke, and corrosive toxic gases are in line with requirements of our society for environment protections and have been widely used in flame retardation treatments of plastic, wood, and other materials [1].

Ammonium polyphosphate (APP), an inorganic fire-retardant, is a well-known phosphorus flame retardant due to its low cost and high flame-retard capacity, accounting for about 20% of flame retardants in the industry [2]. However, APP also catalytically generates a lot of smokes and poisonous gases during combustion [3]. Therefore, it is desirable to improve APP as a better flame retardant of wood which can reduce the smoke release from pyrolysis of wood, thus minimizing air pollution to the ecological environment. Adding some reagents into APP flame retardant is one of the methods for such purpose [4].

Zinc borate (ZB), a white or light yellow crystalline powder, is a new and efficient inorganic fire-retardant [5]. It has been widely used as a flame retardant in plastics, latex and painting materials due to its high thermal stability, fire-retardant, and smoke suppression properties. In addition, zinc borate has a good synergistic effect with aluminum hydroxide, magnesium hydroxide, and phosphorus flame retardant. Thus it can decrease the amounts of the flame retardants added in wood and reduce interference of the

flame retardants with processing capability of the wood. Nano-zinc borate (nZB) has a high ratio of surface area to weight; the smaller the particle size is, the bigger the ratio of surface area to weight is and the better flame retardant effect would be. In addition, nZB can adsorb more smoke and dust per unit weight than regular sizes during wood combustion, due to its good properties described above [6–8].

APP and ZB retard flame by producing a carbonaceous foam which can protect the underlying material from temperature raising. Kurt et al., separately, prepared flame retardant composites with ZB and APP as flame retardants [9, 10]. The mechanisms of char forming and smoke suppression of ZB and APP were also investigated [3]. However, few studies on fabricating flame retardant wood by impregnation method using APP and ZB as flame retardants were reported. The permeability of wood is a key factor to fabricate the high level wood-based flame retardant composites. Many attempts have been made to improve the permeability of wood. Wood microwave pretreatment is a new method to improve wood permeability and modify plantation wood. Microwave pretreatment for wood is executed by exposing green wood in a high intensive microwave electromagnetic field over a very short period of time. It causes that moisture inside wood to vaporize quickly and the generated water steam creates a high internal vapor pressure within wood cells cavity. Under such high internal vapor pressure, the weaker elements of wood structures, such as thin-walled cells and pit membranes, are ruptured to form many pathways for easy transportation of vapors and liquids within the wood, which can be used to increase permeability and drying quality of the wood, and provide favorable conditions for preparation of new wood-based composite materials [11]. Many studies indicate that microwave pretreatment for wood can significantly improve the permeability of the wood [12–15]. Researchers at Co-operative Research Center in Australia found that, after high intensive microwave pretreatment, timber volume and capacity of preservative uptake were increased by 13.4% and 10–14 folds, respectively, but modulus of elasticity (MOR) was reduced by 12–17% in comparison with untreated wood [16–20]. The overall goal of this work was to fabricate the wood-based flame retardant composites based on microwave pretreated wood and to evaluate some primary properties of the composites by CONE and TGA methods.

2. Materials and Methods

2.1. Materials. A green poplar wood of 7 years of age was selected from Yiyang, Hunan, China; ammonium polyphosphate (APP) used in this work was offered by Sichuang Changfeng Chemical Corporation; modified nano-zinc borate (nZB) was purchased from Weifang Fareast Rubber and Plastic Technology Corporation.

2.2. Microwave Pretreatment of Poplar Wood. The microwave pretreatment of poplar wood was carried out by a high intensive microwave pretreatment equipment (MDF-N40, Synotherm Corporation, China) with a microwave power of 12 kW for 80 s. Wood samples with dimensions of 100 mm

(length) \times 100 mm (width) \times 10 mm (thickness) and moisture content of 60–70% were placed on a belt moving through a microwave resonator that emits microwave on the sample surfaces uniformly.

2.3. Flame-Retarding Treatment of the Wood Samples. Solutions of APP and nZB were made with water, each at three different concentrations of 5%, 10%, and 15%, respectively. The flame retardant treatment of the microwave pretreated wood was carried out within a vacuum-pressure impregnating tank which contains either an APP or nZB solution: first, under a vacuum of -0.08 MPa for 30 minutes, then change to a pressure of 0.6 MPa for 1 hour. After being air-dried at ambient temperature for 2 days, the treated samples were oven-dried at $45 \pm 2^\circ\text{C}$ to 10% moisture content. All specimens were treated firstly in the impregnating tank as described above with three different concentrations (5%, 10%, and 15%) of APP, respectively; optimum concentration of APP was chosen based on CONE analysis of the APP-treated samples; then the sample treated with the optimum concentration of APP was retreated in the same way as described above with three different concentrations (5%, 10%, and 15%) of nZB, respectively, to prepare APP-nZB flame retardant wood composites.

2.4. Cone Calorimetric (CONE) and Thermogravimetric Analysis (TGA). The cone calorimetric tests for wood-based flame retardant composites were performed using a Stanton Redcroft (FTT, East Grinstead, U.K) cone calorimeter under a heat flux of 50 kW/m^2 and a gas flow rate of 24 L/s. The samples, with dimensions of 100 mm \times 100 mm \times 10 mm, were placed under the conical-shaped heater that provided uniform irradiance on the sample surface. Thermogravimetric analysis for wood samples was carried out by a Perkin-Elmer Pyris 6 Thermal Analyzer at a linear heating rate of $10^\circ\text{C}/\text{min}$ under pure nitrogen. The samples (5–10 mg) in powder form were placed in open vitreous silica pans. The measurement temperatures ranged from 30 to 800°C .

3. Results and Discussion

3.1. Effects of APP Addition on Flame Retardation and Smoke Suppression of Wood. Heat release rate (HRR, kw/m^2) of the woods treated with different concentrations of APP is shown in Figure 1. There were two peaks in HRR curve of untreated sample, which corresponded to the combustion of wood surface and the underlying wood, respectively. The first one appeared at 30 s, and the peak value was 190.7 kw/m^2 , while the second one was 288.5 kw/m^2 , appeared at 265 s. It indicates that there were two distinct rapid heat releases that occurred at the untreated wood during its entire combustion course. The profiles of the HRR curves of the APP-treated woods were similar to that of the untreated wood, but it is flatter with the lower pk-HRRs. The pk-HRRs of the APP-treated woods decreased significantly with increasing APP concentration. Compared with the untreated wood, the pk-HRR of the wood treated with 15% of APP decreased by 63.3%, and the peak time was also deferred by about

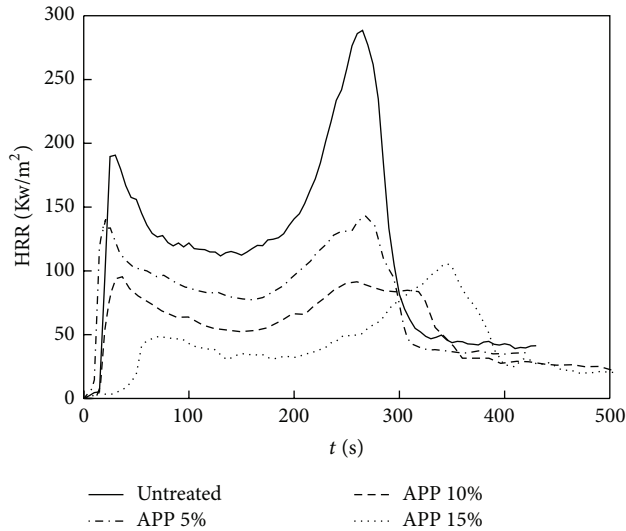


FIGURE 1: HRR curves of the poplar woods treated with different concentrations of APP.

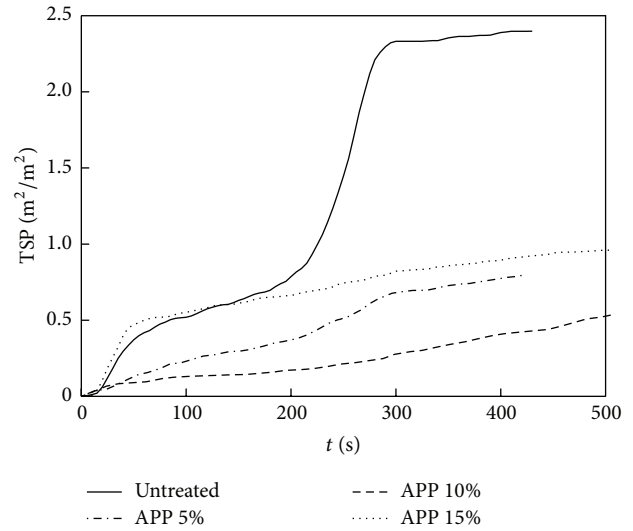


FIGURE 3: TSP curves of the poplar woods treated with different concentrations of APP.

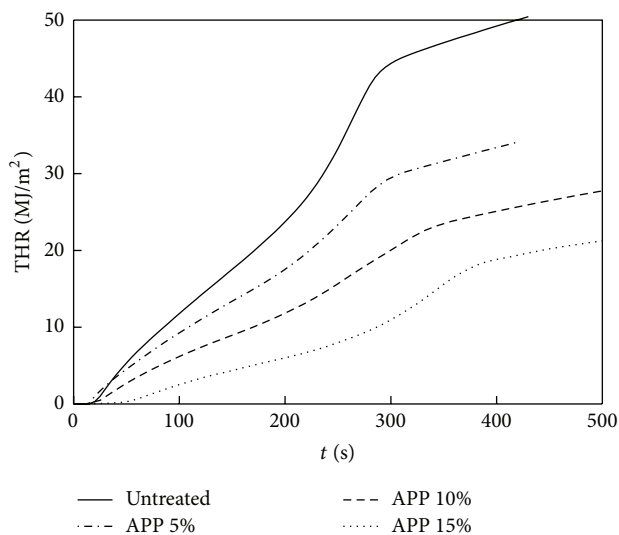


FIGURE 2: THR curves of the poplar woods treated with different concentrations of APP.

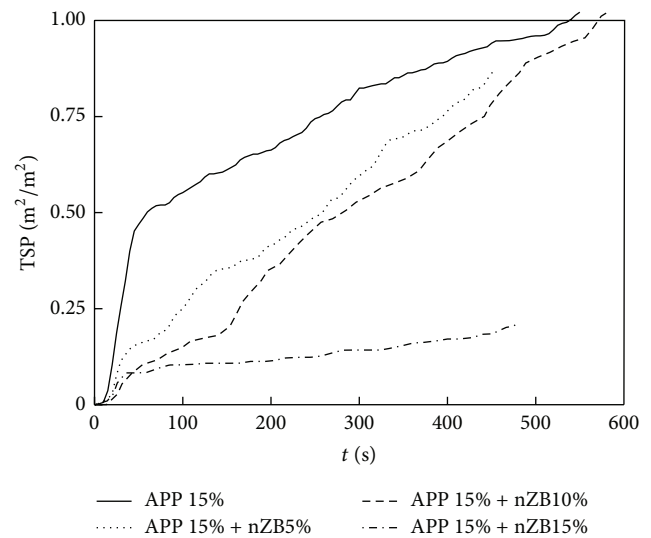


FIGURE 4: TSP curves of APP/nZB-treated woods.

78 seconds, which suggested that the pyrolysis process and heat release of wood were suppressed and delayed by APP.

Figure 2 shows the total heat release (THR, MJ/m^2) of woods treated with APP at three concentrations of 5%, 10%, and 15%, respectively. The THRs of the APP-treated woods decreased with increasing APP concentration, and the heat release process was also slightly delayed. Among the APP-treated wood samples, the one treated with 15% APP shows smallest THR as $22.32 \text{ MJ}/\text{m}^2$ whereas the THR for untreated sample as $50.45 \text{ MJ}/\text{m}^2$.

The total smoke product (TSP, m^2/m^2) of the woods treated with different concentrations of APP is illustrated in Figure 3. TSPs of APP-treated woods decreased significantly, suggesting that APP effectively suppresses smoke. In comparison with untreated sample, TSPs of the woods treated

at APP concentrations of 5% and 10% decreased by 56.83% and 69.40%, respectively. However, TSP of the wood treated at APP concentration of 15% increased rapidly to be higher than those of the wood treated at lower APP concentrations (5% and 10%), implicating that 15%-APP concentration would cause smoke problem.

In summary, from Figures 1, 2, and 3, it is shown that APP executes remarkable flame retardant effects, but unfortunately, at higher concentration (e.g., 15%), APP generates a relatively high level of smoke, and the mean carbon monoxide yield (Mean COY) increased by 250% compared with untreated wood, as shown in Table 1. This is because the fact that upon heating, APP generates a lot of noncombustible gases and moisture which dilute oxygen available to the wood, thus suppressing completion of combustion of the wood and consequently generating toxic gas (e.g., CO) and smoke.

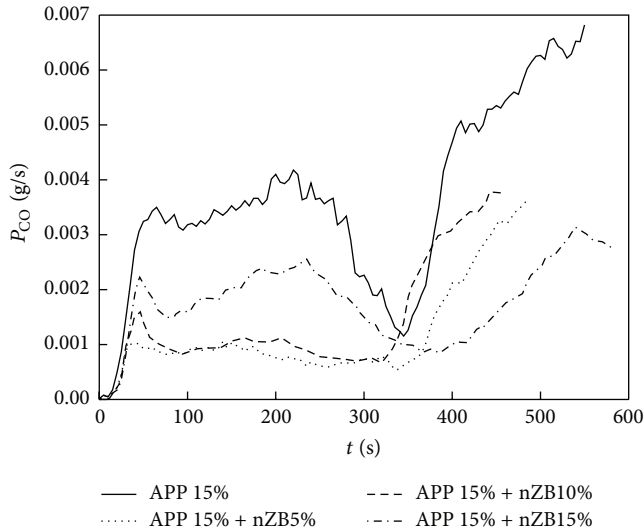


FIGURE 5: P_{CO} curves of APP/nZB-treated woods.

Therefore, for safety concern of APP application in wood-based composites, it is necessary to take effective methods to reduce smoke (CO, etc.) generated by APP. Because the wood treated with APP at the concentration of 15% exhibited wonderful flame retardant properties, and zinc borate has a good smoke suppression effect [6], 15% APP-treated woods were chosen as samples for smoke-suppression test of nano-zinc borate (nZB) in the following study.

3.2. Effects of nZB Addition on Smoke Suppression of APP-Treated Wood. Figure 4 shows the TSP curves of the APP-woods treated with nZB at three concentrations (5%, 10%, and 15%), respectively. The TSPs of APP and nZB- (APP/nZB-) treated woods significantly decreased with increasing concentration of nZB. At 15% concentration, nZB reduced TSP as much as 78.43% compared with that of APP-treated woods, and it reduced TSP to a much lower level than either 5%- or 10%-nZB did. It means that nZB efficiently reduces smoke generated from APP and can be used as an effective smoke-suppressing agent in APP-treated wood composites.

CO release rate (P_{CO} , g/s) of APP-woods treated with nZB at different concentrations is illustrated in Figure 5. For APP-treated wood sample, there was a peak valley at 350 seconds in its P_{CO} curve, corresponding to the second severe combustion that was from inside-wood burning, as shown in Figure 1. The P_{CO} s of APP/nZB-treated woods were significantly lower than that of APP-treated wood. It indicates that nZB inhibited CO release from APP-treated woods. Among P_{CO} curves of APP/nZB treated woods, there were two distinct stages around a turning point, the tip of the valley of the P_{CO} curve for untreated wood sample, which was corresponding to the combustion of underlying wood. At 1st stage ($t = 0$ to 350 s), P_{CO} of 15%-nZB, that is, APP(15%)/nZB(15%)-treated wood, was relatively higher than those of 5%- and 10%-nZBs, that is, APP(15%)/nZB(5%)- and APP(15%)/nZB(10%)-treated woods, but in second stage ($t = 360$ to 600 s), the situation was converted to be opposite to that of the 1st stage. Since the

2nd stage responding to the combustion of the bottom wood which causes major damages in a fire disaster, 15% would be a preferred concentration for nZB treatment of APP-treated wood.

nZB can form a glass-like barrier to block the transfer of the volatile combustibles and heat. When added to APP-treated wood, nZB, together with APP, forms a tighter barrier to further block the feedback between the volatile combustibles and heat to a higher extent, thus converting wood-burning into a more limited combustion and decreasing heat (THR) and smoke (TSP) release even more, as Figure 4 and Table 1 show. In addition, nZB can adsorb O_2 from air, and the absorbed O_2 can oxidize CO into CO_2 , resulting in decreasing Mean COY and increasing Mean CO_2Y in APP/nZB-treated wood, compared to those in the APP-treated. In comparison with regular sized zinc borate (ZB), nano-zinc borate (nZB) can adsorb more O_2 per unit weight, due to its very high ratio of surface area to weight and distribute more evenly in the wood due to its small size, thus exerting its function at a new optimal level.

3.3. Effects of APP and nZB Addition on Residual Carbon of Wood. Figure 6 shows the residues of the wood samples after CONE test. From the figure, it can be found that there were mostly only white ashes left for the untreated wood sample (a), which indicated that the combustion was carried out completely in untreated wood. Figure 6(b) shows that the residual carbon of APP-treated wood is black and relatively thick, indicating that APP promoted charcoal formation. The char layer also shows deep and broad cracks on the surface and bended upward which is a characteristic of intumescent fire-retardant treatments. The residual carbon of APP/nZB-treated wood sample (c) was darker and denser than that of APP-treated wood (b), and the char layer shows a dense texture with fewer crackers at surface, which implies more efficient blockage of transfer of the volatile combustibles and heat within the treated sample during combustion.

3.4. Effects of APP and nZB Addition on Thermogravimetric (TG) of Wood. Figure 7 shows the TG curves of different flame retardant systems. The carbon yield of APP-treated wood was much higher than that of untreated wood, and the APP/nZB-treated wood further improved the carbon yield. This shows that APP and nZB effectively promoted charcoal forming. In addition, APP and nZB have a good synergistic flame retardant effect, so that the carbon yield of APP/nZB-treated wood was the highest; the charring effect of the APP/nZB-treated wood was excellent. Meanwhile, there was a cross in curves of APP/nZB-treated wood and untreated wood at 350°C. Before 350°C, the curve of APP/nZB-treated wood was under the curve of untreated wood; however, the situation was opposite after 350°C. This shows that flame retardants catalyzed the pyrolysis of wood and made the decomposition process in advance, and the starting temperature of pyrolysis is decreasing, which lead to the mass loss rate of APP/nZB flame retardant wood becoming faster before 350°C. In addition, the direction of decomposition of wood was changed to generate a large amount of charcoal and water

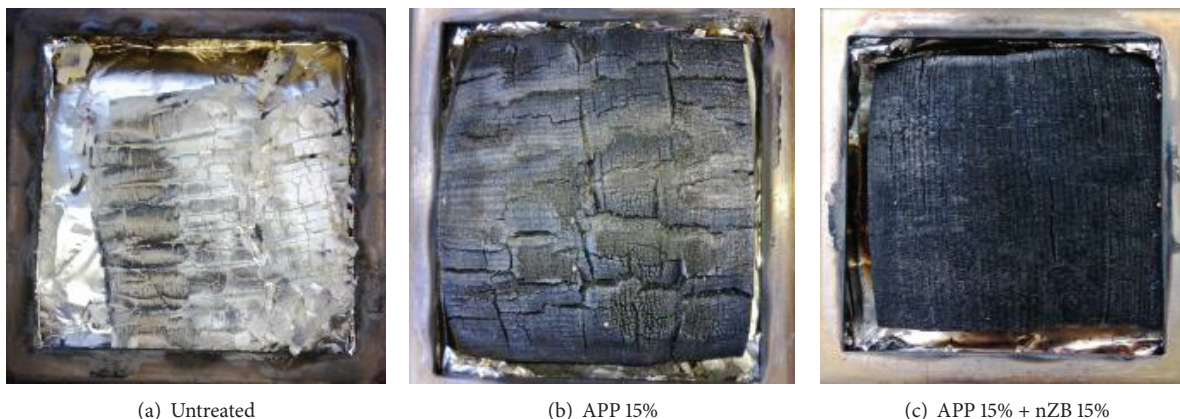


FIGURE 6: Photograph of residues of the wood samples with different flame retardant treatments after CONE.

TABLE 1: CONE data of different flame retardant systems.

Sample	m-HRR (kW/m ²)	pk-HRR (kW/m ²)	THR (MJ/m ²)	TSP (m ² /m ²)	Mean COY (kg/kg)	Mean CO ₂ Y (kg/kg)
Untreated	121.44	288.50	50.45	2.40	0.02	1.04
APP 15%	43.81	105.91	22.32	1.02	0.07	0.54
APP 15% + nZB 15%	37.11	72.83	20.51	0.22	0.02	0.70

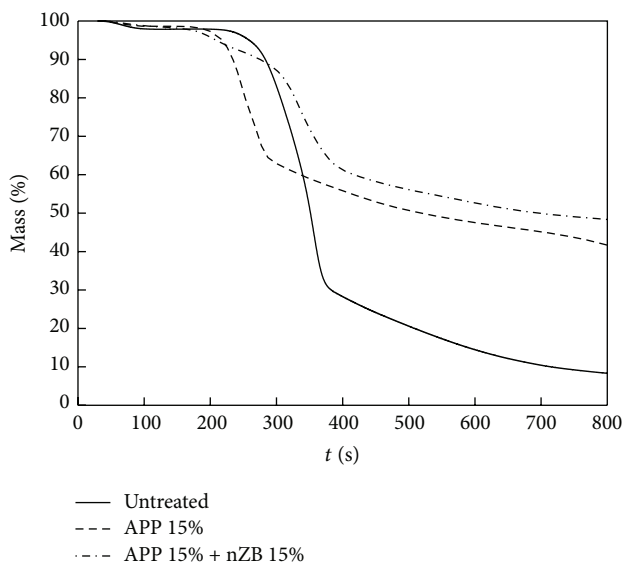


FIGURE 7: TG curves of the wood samples with different flame retardant treatments.

when APP and nZB were added. Therefore, APP/nZB-treated wood had greater residual masses and residual carbon after 350°C.

4. Conclusions

Based on vacuum-pressure impregnating method after high intensive microwave pretreatment, the wood-based flame retardant composites were fabricated, and the effects of

ammonium polyphosphate (APP) and modified nano-zinc borate (nZB) addition on flame-retardation and smoke-suppression properties of wood were investigated in this study. The results show that (1) APP suppresses combustion and markedly increases carbonization of the wood; (2) compared with untreated wood, the pk-HRR and THR of APP-treated wood sample were reduced by 63.3% and 55.76%, respectively, when the concentration of APP was at 15%; (3) the residual carbons increased to be 45% of the total mass in the APP-treated wood, comparing to 10% of the total mass in untreated wood. However, the CO's mean yield (Mean COY) of the APP-treated wood was much (3.5 times) higher than that of the untreated wood; (4) with the addition of nZB in APP-treated wood with a concentration of 15%, the TSP and Mean COY of APP/nZB treated wood decreased by 78.43 and 71.43%, compared with APP-treated wood, respectively; (5) nZB further suppresses combustion by reducing 31.23% of pk-HRR and 8.11% of THR, and increasing 11.11% of carbonization (residual carbons); compared with the APP-treated wood, APP and nZB have synergistic effects of flame-retardation and smoke-suppression.

Conflict of Interests

The authors declare that there is no conflict of interests regarding the publication of this paper.

Acknowledgments

Thanks for the support of the National Natural Science Foundation of China (no. 31370564), New-century Training

Program Foundation for the Talents by the Ministry of Education of China (NCET-11-0979), and the Graduate Science and Technology Innovation Fund of Central South University of Forestry and Technology (CX2014B09).

References

- [1] C. H. Yao, Y. Q. Wu, and Y. C. Hu, "Flame-retardation characteristics and mechanisms of three inorganic magnesium compounds as fire-retardant for wood," *Journal of Central South University of Forestry and Technology*, vol. 32, no. 1, pp. 18–23, 2012.
- [2] A. A. Klyosov, *Wood-Plastic Composites*, Wiley-Interscience, Hoboken, NJ, USA, 2007.
- [3] Y. C. Hu, *Char Forming and Smoke Suppression Function of Zinc Borate and Ammonium Polyphosphate on Wood During Combustion*, Central South University of Forestry and Technology, Changsha, China, 2006.
- [4] Y. Y. Xia, Y. C. Hu, and Y. Q. Wu, "Preparation of mesoporous SiO₂-APP composite flame retardant and effects of flame retardant and smoke suppression on wood," *Journal of Central South University of Forestry and Technology*, vol. 32, no. 1, pp. 9–13, 2012.
- [5] D. G. Su, C. H. Qu, M. F. Zhong, L. Li, and H. Y. Lin, "Study on preparation of nanometer zinc borate and its xylary flame-retardant properties," *Journal of Guizhou University of Technology*, vol. 37, no. 3, pp. 61–64, 2008.
- [6] G. H. Yuan, "Inflaming retarding mechanism and preparation methods of zinc borate nanoparticles," *Journal of Ankang University*, vol. 23, no. 5, pp. 97–99, 2011.
- [7] P. Wang, W. H. Chen, and L. F. Zhen, "Progress on the study of nanometer inorganic flame retardants in polymeric materials," *Journal of Materials Science and Engineering*, vol. 21, no. 1, pp. 122–125, 2003.
- [8] Z. P. Wu, Y. C. Hu, and W. G. Su, "Effect of ultrafine zinc borate on smoke suppression property of LDPE/IFR system," *Plastics Science and Technology*, vol. 36, no. 7, pp. 56–60, 2008.
- [9] R. Kurt and F. Mengeloğlu, "Utilization of boron compounds as synergists with ammonium polyphosphate for flame retardant wood-polymer composites," *Turkish Journal of Agriculture and Forestry*, vol. 35, no. 2, pp. 155–163, 2011.
- [10] N. M. Stark, R. H. White, S. A. Mueller, and T. A. Osswald, "Evaluation of various fire retardants for use in wood flour-polyethylene composites," *Polymer Degradation and Stability*, vol. 95, no. 9, pp. 1903–1910, 2010.
- [11] X.-J. Li, K.-Y. Lu, L.-Y. Lin, Y.-D. Zhou, Z.-Y. Cai, and F. Fu, "Fundamental characteristics of microwave explosion pretreatment of wood I. Properties of temperature development," *Forestry Studies in China*, vol. 12, no. 1, pp. 9–13, 2010.
- [12] Y. X. Lv, Z. H. Xue, and L. Z. Xue, "Observing ex-microcosmic structure of microwave modified wood," *Inner Mongolia Forestry Science & Technology*, vol. 4, pp. 31–33, 2001.
- [13] T. Jiang, Z. F. Zhou, and Q. W. Wang, "Effects of intensive microwave irradiation on the permeability of larch wood," *Scientia Silvae Sinicae*, vol. 42, no. 21, pp. 87–92, 2006.
- [14] Y.-D. Zhou, F. Fu, X.-J. Li, X.-M. Jiang, and Z.-L. Chen, "Effects of microwave treatment on residue growth stress and microstructure of Eucalyptus urophylla," *Journal of Beijing Forestry University*, vol. 31, no. 2, pp. 146–150, 2009.
- [15] X. J. Li, F. Fu, and Y. D. Zhou, "Effect of microwave pretreatment on permeability of Eucalyptus wood," *Journal of Central South University of Forestry and Technology*, vol. 31, no. 12, pp. 145–149, 2011.
- [16] M. A. Mekhtiev and G. I. Torgovnikov, "Method of check analysis of microwave-modified wood," *Wood Science and Technology*, vol. 38, no. 7, pp. 507–519, 2004.
- [17] G. A. Harris, G. Torgovnikov, P. Vinden, G. I. Brodie, and A. Shaginov, "Microwave pretreatment of backsawn messmate boards to improve drying quality: part 1," *Drying Technology*, vol. 26, no. 5, pp. 579–584, 2008.
- [18] G. Torgovnikov and P. Vinden, "New wood based materials TORGVIN and VINTORG," in *Proceedings of the 5th Pacific Rim Bio-Based Composite Symposium*, pp. 756–757, Canberra, Australia, 2000.
- [19] K. Sugiyanto, P. Vinden, G. Torgovnikov, and S. Przewloka, "Microwave surface modification of Pinus radiata peeler cores: technical and cost analyses," *Forest Products Journal*, vol. 60, no. 4, pp. 346–352, 2010.
- [20] P. Vinden, G. Torgovnikov, and J. Hann, "Microwave modification of Radiata pine railway sleepers for preservative treatment," *European Journal of Wood and Wood Products*, vol. 69, no. 2, pp. 271–279, 2011.

Research Article

Detection of Triphenylmethane Drugs in Fish Muscle by Surface-Enhanced Raman Spectroscopy Coupled with Au-Ag Core-Shell Nanoparticles

Lu Pei,¹ Yiqun Huang,^{1,2} Chunying Li,¹ Yuanyuan Zhang,¹
Barbara A. Rasco,² and Keqiang Lai¹

¹ College of Food Science and Technology, Shanghai Ocean University, No. 999 Hucheng Huan Road, LinGang New City, Shanghai 201306, China

² School of Food Science, Washington State University, Pullman, WA 99164, USA

Correspondence should be addressed to Keqiang Lai; kqlai@shou.edu.cn

Received 14 March 2014; Accepted 28 April 2014; Published 21 May 2014

Academic Editor: Yongfeng Luo

Copyright © 2014 Lu Pei et al. This is an open access article distributed under the Creative Commons Attribution License, which permits unrestricted use, distribution, and reproduction in any medium, provided the original work is properly cited.

Silver -coated gold bimetallic nanoparticles were synthesized and used as substrates for surface-enhanced Raman spectroscopy (SERS) in detecting prohibited triphenylmethane drugs (including crystal violet and malachite green) in fish muscle. The optical properties and physical properties of bimetallic nanospheres were characterized by UV-Vis spectroscopy and transmission electron microscopy. The optimal nanospheres selected had relatively uniform size (diameter: 33 ± 3 nm) with a silver layer coated on the surface of gold seed (diameter: 18 ± 2 nm). For both crystal violet and malachite green, characteristic SERS spectral features could be identified at concentration as low as $0.1 \mu\text{g/L}$ with these bimetallic nanospheres. Crystal violet and malachite green residues in fish muscle could also be detected at levels as low as 0.1 ng/g , which could meet the most restricted regulatory requirements for the limit of detection in terms of analytical methods for crystal violet or malachite green in fish muscle. This study provides a basis for applying SERS technology with bimetallic nanoparticles to the identification of trace amounts of prohibited substances in aquatic food products, and the methodology could be extended to analyses of other hazardous chemicals in complex food matrices like vegetables and meats.

1. Introduction

Surface-enhanced Raman spectroscopy or surface-enhanced Raman scattering (SERS) utilizes the tremendous enhancement effect of Raman scattering signals through adsorbing analytes onto the roughened surfaces of gold, silver, and other metallic materials [1, 2]. Chemical enhancement and electromagnetic enhancement are two accepted enhancement mechanisms, which contributed to the charge transfers between the adsorbed analyte molecule and metal substrate and the large local field enhancement in the vicinity of metal surfaces excited by the laser [3, 4]. SERS has shown great potential for analyses of trace amounts of chemicals at as low as single molecule level [5–7]. In recent years, SERS technology has been increasingly exploited in applications in various fields, such as material, physics, medicine, and

food science [8, 9]. It is well known that SERS effect is quite sensitive to the changes in substrate materials and surface morphology. One of the key factors for successful applications of SERS technology is preparation of highly active, stable, and reproducible SERS substrates [2, 10]. Au-Ag core-shell bimetallic nanoparticles (NPs) were synthesized by coating silver on the surface of gold seeds through chemical reduction. With appropriate particle sizes and thickness of silver shells, these bimetallic nanospheres could overcome problems, such as instability commonly tied to silver NPs and relatively low enhancement effects tied to gold NPs, and exhibit high enhancement effects similar to silver NPs with the advantages of high degree of homogeneity as gold NPs [8, 11–13]. However, similar to other SERS substrates with great potential as analytical tools, the application aspect of bimetallic nanospheres as SERS substrates is left far behind

the theory aspect of SERS related research and has become the bottleneck of the field.

Crystal violet (CV, 4-[bis(4-dimethylaminophenyl)methylidene]cyclohexa-2,5-dien-1-ylidene]-dimethylazanium chloride) and malachite green (MG, 4-[(4-dimethylamino-phenyl)-phenyl-methyl]-N,N-dimethyl-aniline), both triphenylmethane dyes, are remarkably effective against fungal infections and parasitosis in fish and had been worldwide used as biocide and fungicide in aquaculture for decades [14]. Since mid-1980s, efforts have been made to reduce the use of both CV and MG due to their links to genotoxicity and carcinogenicity [15]. Although the use of these drugs has been banned in the United States, the European Union, China, and many other countries [16], CV and MG are still used illegally in some parts of the world due to their low cost and high efficiency, resulting in frequent occurrence of aquatic products with safety issues and consequently leading to import bans and product recalls. Based upon the Rapid Alert System for Food and Feed online searchable database of the European Union, a total of 131 cases of various fish products (such as catfish, trout, tilapia, salmon, king prawn, and caviar) contaminated with CV or MG were reported from 2003 to 2012 [17]. Food safety incidents like these have brought huge barriers to import and export trades of global aquatic products, so it is particularly important to strengthen the monitoring system for CV and MG residues in aquatic products. High performance liquid chromatography (HPLC) is the most commonly used method for analyzing CV and MG drug residues in fish, but it has disadvantages such as high cost, time consuming, and too complicated sample preparation [18]. In addition, with the increasing tightened policy towards CV and MG, the sensitivity of HPLC method is unlikely to achieve the limit of detection at 1 ng/g level required by most of the countries that ban the drugs, and consequently not only more sensitive but also much costly liquid chromatography-mass spectrometry (LC-MS) is required for detecting CV or MG at such low level [19]. SERS technology has shown great potential for detecting trace amounts of analytes with a simpler sample extraction protocol and a shorter detection time, which makes it possible to rapidly screen and analyze the use of illegal drugs in aquatic products [20].

The objective of this study was to investigate the potential of applying Au-Ag core-shell bimetallic nanoparticles to the detection of banned triphenylmethane drugs in fish muscle. This study provides a basis for applying SERS technology to the identification of trace amounts of prohibited substances in aquatic food products, and the methodology could be extended to analyses of other hazardous chemicals in complex food matrices (such as fish and meat) with SERS technology.

2. Materials and Methods

2.1. Synthesis of Au-Ag Core-Shell Nanoparticles. Au-Ag core-shell NPs were synthesized in solution via a seed-growth method [21]. In brief, sodium citrate (0.74 mL, 1% w/w) was added to the boiling solution of chloroauric acid (50 mL, 2×10^{-4} mol/L), and the mixture was stirred and boiled until the color became wine red, indicating that Au NPs

were formed [22]. As-prepared Au colloids (3 mL) and L-ascorbic acid (0.4 mL, 0.1 mol/L) were added in a vial under continuous stirring. Then 0.3 mL, 0.6 mL, 0.9 mL, and 1.2 mL of silver nitrate (1×10^{-3} mol/L) were added dropwise (10 μ L per addition) to this mixture to prepare four different Au-Ag core-shell NPs varying in the thickness of silver coating, respectively. The formed Au-Ag core-shell NPs were transferred into a conical flask with stopper and kept in refrigerator at 4 °C before use.

2.2. Preparation of Standard Solutions. CV ($\geq 90\%$, Sigma-Aldrich, USA) and MG ($>99\%$, Sigma-Aldrich, USA) were dissolved in acetonitrile (HPLC reagent, Sigma, USA) aqueous solution (v/v = 1:1) to prepare a series of standard solutions (0.1, 1, 10, and 10^3 μ g/L). The pH of the CV and MG standard solutions ranged from 5.3 to 5.8, depending on the concentration of the drugs. The absorbance bands of CV and MG were at 590 nm and 620 nm, respectively, based upon UV-Vis spectroscopic analysis (UV3000PC, MAPADA Instruments Ltd., Shanghai, China).

2.3. Fish Sample Pretreatment. Tilapia filets (containing no CV or MG as confirmed with LC-MS) from Zhenye Aquatic and Cool Storage Ltd. (Guangdong, China) were used in this study. Tilapia filets were homogenized through blending frozen tilapia filets with dry ice in a laboratory blender (HGBTWTS3, Waring Commercial, Torrington, CT, USA) at high speed for 5 minutes to achieve uniform fish samples and therefore minimize spectral variation due to the disparity of nontargeted components in fish tissue. The extraction and purification protocol for CV and MG in fish muscle were based upon a conventional method adopted by the US Food and Drug Administration (FDA) with slight modifications [23]. In brief, homogenized tilapia filets spiked with CV or MG [0 (blank), 0.1, 1, and 10 ng/g] were blended with ammonium acetate buffer (Sinopharm Chemical Reagent Ltd., SCRC, Shanghai, China), hydroxylamine hydrochloride solution (ACS reagent, SCRC), and p-toluenesulfonic acid solution (ACS reagent, SCRC) and mixed well. Then, acetonitrile and alumina (chromatographic grade, SCRC) were added and the mixture was centrifuged, followed by the use of supernatants for liquid-liquid extraction with the addition of dichloromethane (ACS reagent, SCRC). The extract was evaporated to dry with a rotary evaporator (R206B, Shanghai Senco Technology Ltd., Shanghai, China), dissolved into acetonitrile, and mixed with 2,3-dichloro-5,6-dicyano-1,4-benzoquinone (DDQ) solution (98%; J&K SCIENTIFIC, Logan, UT, USA). The solution was further purified with solid phase extraction through alumina cartridge (1 g, 3 mL; Supelco, Bellefonte, PA, USA) positioned on top of a propylsulfonic acid cartridge (500 mg, 3 mL; ANPEL Scientific Instrument Co., Ltd., Shanghai, China). Unlike the FDA method, no vacuum pump was used to speed up the flow rate during the solid phase extraction. The final elute was reconstituted to 5 mL with ammonium acetate and acetonitrile (v/v = 1:1).

2.4. SERS Measurement. SERS spectra were collected by using a Nicolet DXR microscopy Raman spectrometer

(Thermo Fisher Scientific Inc., Waltham, MA, USA) with a 633 nm He-Ne laser source, 2 mW laser power, and 20x objective lens with a slit width of 50 μm .

To collect an SERS spectrum, 10 μL Au-Ag core-shell NPs were deposited onto a microscope glass slide, and after evaporation of solvent, one drop of sample solution or fish extract was pipetted onto the Au-Ag core-shell substrate. SERS spectra were immediately acquired after evaporation of the solvent. The exposure time was 20 s for each scan and each spectrum was the average of 5 scans. For each treatment of standard solutions (10^3 , 10, 1, and 0.1 $\mu\text{g/L}$) or fish fillets spiked with CV or MG [0 (blank), 0.1, 1, and 10 ng/g], 10 spectra from different locations of a substrate were collected, and triplicate analyses were conducted.

2.5. Characterizations of Nanoparticles. The optical properties of Au NPs used as seeds and Au-Ag core-shell NPs coated with different amounts of silver were analyzed with a UV-Vis absorbance spectroscopy (UV3000PC, MAPADA Instruments Ltd., Shanghai, China). General shapes of the Au and Au-Ag core-shell NPs were analyzed with a transmission electron microscopy (TEM; JEM-2100F, JEOL Ltd., Tokyo, Japan) and the core-shell structure of Au-Ag core-shell NPs was determined with a high-resolution TEM (HRTEM, JEM-2100F, JEOL Ltd., Tokyo, Japan). The average particle sizes of Au seeds and bimetallic NPs were calculated based upon TEM images of 50 particles.

CV standard solution (10 $\mu\text{g/L}$) was used as probe to understand the effect of the synthesized Au-Ag core-shell substrates on SERS enhancement. The SERS spectra of CV with the use of four different Au-Ag core-shell NPs as substrates were recorded, respectively, and the enhancement factors of these substrates were estimated and compared [24]. The substrate resulting in the highest enhancement for CV was selected for the further study on analysis of CV and MG standard solutions and fish fillets spiked with CV or MG.

To evaluate the stability of Au-Ag core-shell bimetallic nanosphere colloids, the selected Au-Ag core-shell NPs were stored at refrigerator temperature for up to 20 days. Sixteen spectra of CV standard solution (1 $\mu\text{g/L}$, 10 $\mu\text{g/L}$) with the use of the selected colloids as SERS substrates were acquired every other day. The Raman intensities at 1617 cm^{-1} (one of the primary characteristic peaks for CV) were compared among spectra collected from different days to see whether there was significant difference ($\alpha = 0.05$) with ANOVA analysis (Excel 2010; Microsoft Co., Redmond, WA, USA).

3. Results and Discussion

3.1. UV-Vis Spectra of Au-Ag Core-Shell NPs with Different Sizes. The surface plasmon resonance (SPR) peak of metal NPs can be detected with UV-Vis absorbance spectroscopy. It is well known that the position and shape of SPR peak depend upon the shape, size, and composition of NPs [25], and all these factors ultimately affect the enhancement effect of SERS substrates. The reported SPR peaks of Au NPs ranged from 517 nm to 575 nm (particle diameter: 9–99 nm), while the peaks of Ag NPs ranged from 390 nm to 438 nm (particle diameter: 10–80 nm), and the SPR peak tended to shift to

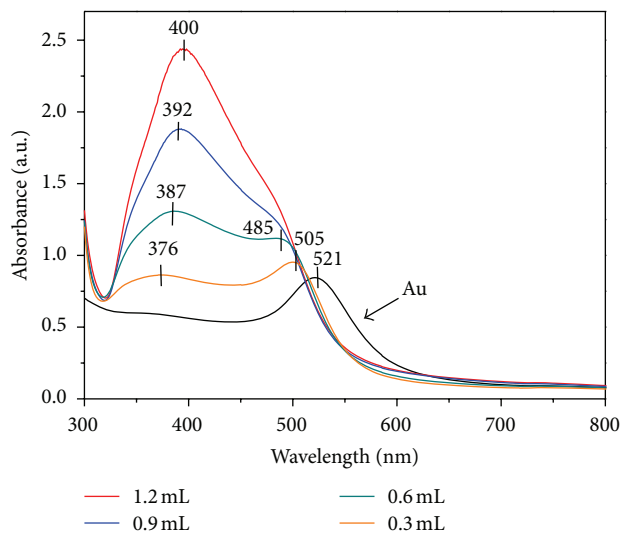


FIGURE 1: Changes of UV-Vis spectra of Au-Ag core-shell nanoparticles dispersion with the increased amounts of AgNO_3 used for synthesis.

higher wavelength (red shift) with an increase in particle sizes for Au or Ag NPs [26–28]. The optical properties of Au-Ag core-shell NPs are more complex than those of Au or Ag NPs because of an interaction between Au and Ag. As shown in Figure 1, the change in the plasmon resonance of Au-Ag core-shell NPs during the silver coating process was clearly affected by the ratio of Au to Ag and the thickness of Ag shell. Before adding AgNO_3 , Au NPs dispersion exhibited absorbance band at about 521 nm, and the shape of the SPR peak was symmetrical and narrow, indicating relatively good monodispersity of the Au NPs (diameter: 18 ± 2 nm). With the addition of AgNO_3 solution and ascorbic acid, Ag^0 was produced and gradually coated on the surface of Au seeds as indicated by the appearance of characteristic peak of silver shells (376–400 nm) as well as the shifts of SPR peaks for both Ag shells and Au seeds (Figure 1). As the amount of AgNO_3 solution increased from 0.3 mL to 1.2 mL, the SPR peak of Ag shells red-shifted from 376 nm to 400 nm and the peak intensity also strengthened due to increase in the thickness of silver layer deposited onto the Au seeds [29], while the SPR peak for Au seeds showed opposite trend and was barely discernible when the amount of AgNO_3 solution reached up to 0.9 mL (particle diameter: 33 ± 3 nm) and above. The overall SPR peaks of Ag shells for Au-Ag core-shell NPs appeared at relatively low wavelengths (376–400 nm) compared to those reported for Ag NPs (390–438 nm), which was mainly because the Ag shells (5–11 nm) were quite thin compared to the radii of the reported Ag NPs (5–40 nm) [27, 28].

3.2. Nanoparticles Size-Dependent SERS Enhancement Effect for CV. Figure 2 shows some representative SERS spectra of 10 $\mu\text{g/L}$ CV standard solution acquired by using four Au-Ag core-shell substrates synthesized with different amounts of AgNO_3 . The observed main characteristic peaks of CV at around 1617, 1367, 1173, 914, and 440 cm^{-1} are assigned to the

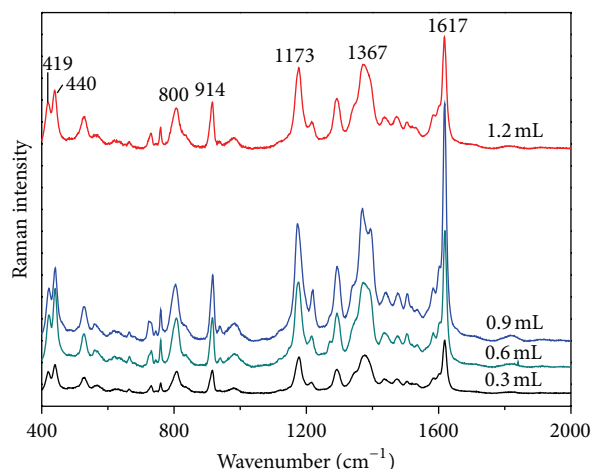


FIGURE 2: Representative SERS spectra of $10\ \mu\text{g/L}$ crystal violet solution by using Au-Ag core-shell substrates synthesized with different amounts of AgNO_3 .

in-plane stretching of the ring-C-C, N-phenyl stretching, in-plane bending of the ring-C-H, ring skeletal vibration of radical orientation, and out-of-plane deformation vibrations of the phenyl-C⁺-phenyl [30, 31]. As can be seen from the change in the intensity of CV characteristic peaks, an increasing enhancement effect was observed with the use of thicker silver-coated Au-Ag core-shell NPs when the amount of AgNO_3 used for silver coating was no more than 0.9 mL. The Au-Ag core-shell NPs could reach sufficiently intrinsic SERS activity of the growing Ag shells, which is much higher than Au NPs to generate strong electromagnetic enhancement for high SERS signals [32]. However, the enhancement effect decreased when the amount of AgNO_3 used for silver coating reached 1.2 mL. The enhancement factors for four Au-Ag core-shell substrates were calculated as 2.5×10^5 , 8.0×10^5 , 1.8×10^6 , and 6.1×10^5 , corresponding to 0.3, 0.6, 0.9, and 1.2 mL of AgNO_3 used for silver coating, respectively. Therefore, the Au-Ag core-shell NPs synthesized with 0.9 mL of AgNO_3 (particle diameter: $33 \pm 3\ \text{nm}$) were selected for further analysis of CV and MG in fish muscle.

Based on the calculation of the TEM images of 50 particles, the average particle size of Au seeds was $18 \pm 2\ \text{nm}$ in diameter, and the sizes of Au-Ag core-shell NPs were $28 \pm 4\ \text{nm}$, $30 \pm 4\ \text{nm}$, $33 \pm 3\ \text{nm}$, and $39 \pm 3\ \text{nm}$, corresponding to 0.3, 0.6, 0.9, and 1.2 mL of AgNO_3 used for silver coating, respectively. The TEM images of the Au seeds and the 33 nm Au-Ag core-shell NPs showed that both NPs were relatively uniform, nearly spherical with narrow size distribution (relative standard deviation: Au NPs, 11%; $33 \pm 3\ \text{nm}$ Au-Ag core-shell NPs, 9%) (Figures 3(a) and 3(b)). The average thickness of the Ag layer on the Au core is 7.5 nm for the selected Au-Ag core-shell NPs. In addition, no seed-size Au NPs or smaller Ag NPs were observed, suggesting that no other nucleation centers or separation from the Au-core layer occurred [6, 33]. The HRTEM image of Au-Ag core-shell NPs (Figure 3(c)) showed that some lateral moiré fringes were generated which indicated the selective growing of Ag [34–36].

During 20-day storage at refrigerator temperature, with the selected 33 nm Au-Ag core-shell NPs as substrates to acquire SERS spectra of CV standard solution ($1\ \mu\text{g/L}$, $10\ \mu\text{g/L}$), there was no significant change in the Raman intensities at $1617\ \text{cm}^{-1}$ for both $1\ \mu\text{g/L}$ and $10\ \mu\text{g/L}$ solutions, indicating that the colloids were stable and no obvious change occurred in 20 days.

3.3. Analysis of CV and MG with Au-Ag Core-Shell SERS Substrates. A series of CV and MG standard solution (0.1, 1, 10, and $10^3\ \mu\text{g/L}$) was used to evaluate the SERS activity of the selected 33 nm Au-Ag core-shell substrates. As can be seen from Figure 4, there was almost no SERS signal for blank substrates, whereas the intensity of the characteristic bands was drastically enhanced as the concentration of CV or MG solution increased from $0.1\ \mu\text{g/L}$ to $10\ \mu\text{g/L}$. Even at the concentration level as low as $0.1\ \mu\text{g/L}$, the major characteristic bands at around 440, 914, 1173, $1367\ \text{cm}^{-1}$, and $1617\ \text{cm}^{-1}$ could still be identified for both CV and MG. SERS spectra of MG were similar to those of CV because of their similar molecular structures, and only changes in the relative intensity among peaks were observed, such that the relative intensity of the peak at around $1217\ \text{cm}^{-1}$ for MG was stronger than that for CV [20, 37].

The optimal Au-Ag core-shell substrates were further used to detect CV and MG residues in fish samples with conventional sample preparation method. Figure 5 presents SERS spectra of CV and MG extracts [0 (blank), 0.1, 1, and 10 ng/g] adsorbed on Au-Ag core-shell substrates. There was no SERS signal detected for the blank extracts, which indicates that sample extract was relatively clean and the presence of some nontargeted compounds did not have obvious Raman scattering signals that may interfere with the analysis of CV or MG. The main spectral characteristic peaks of fish extracts with different levels of CV or MG were basically consistent with those of the standard solution, showing similar intensity and no obvious interference by other components from fish fillets. In addition, the major characteristic bands were discernable at a level as low as 0.1 ng/g for both CV and MG in contaminated fish samples, which were similar to the results for CV or MG standard solutions as discussed earlier. A high recovery rate (85.9–93.9%) was obtained by using the conventional methods for CV and MG extraction [38]. This high recovery rate of CV and MG together with little or no interference of other components in CV and MG extracts accounted for the similar SERS results for analysis of CV or MG in fish extracts and in standard solutions.

Obtaining reproducible spectra has been always a challenge for applying SERS technology as an analytical tool, since the intensities of SERS signals were greatly affected by the surface morphology of substrates, location, and direction of the targeted molecules adsorbed on a substrate and many other factors. To achieve reproducible results, ten spectra were acquired from different locations of a substrate each time during SERS collection, and the average of these ten spectra was used as the final spectra. Figure 6 exhibits the average spectra from triplicate analyses for CV and MG of both standard solutions ($1\ \mu\text{g/L}$) and fish extracts (1 ng/g),

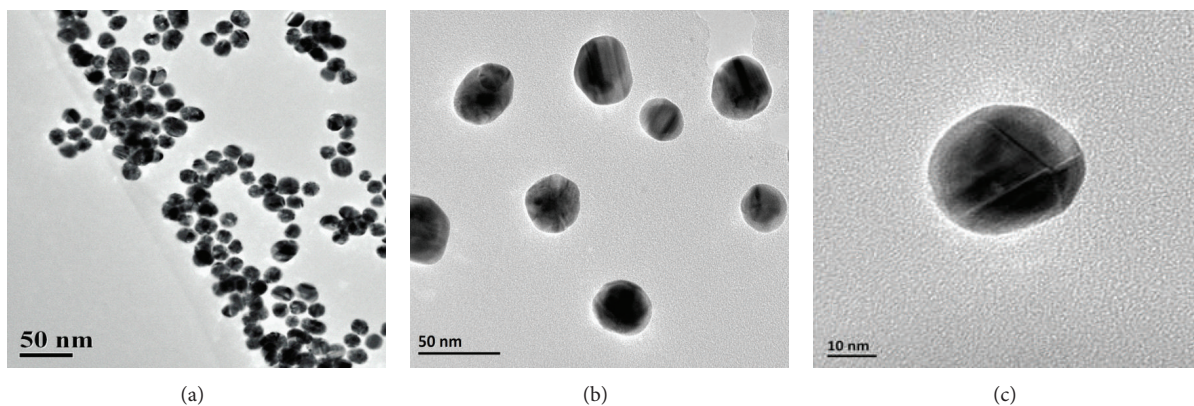


FIGURE 3: TEM images of (a) Au nanoparticles and (b) Au-Ag core-shell nanoparticles (0.9 mL AgNO_3 used) and (c) HRTEM image of Au-Ag core-shell nanoparticles (0.9 mL AgNO_3 used).

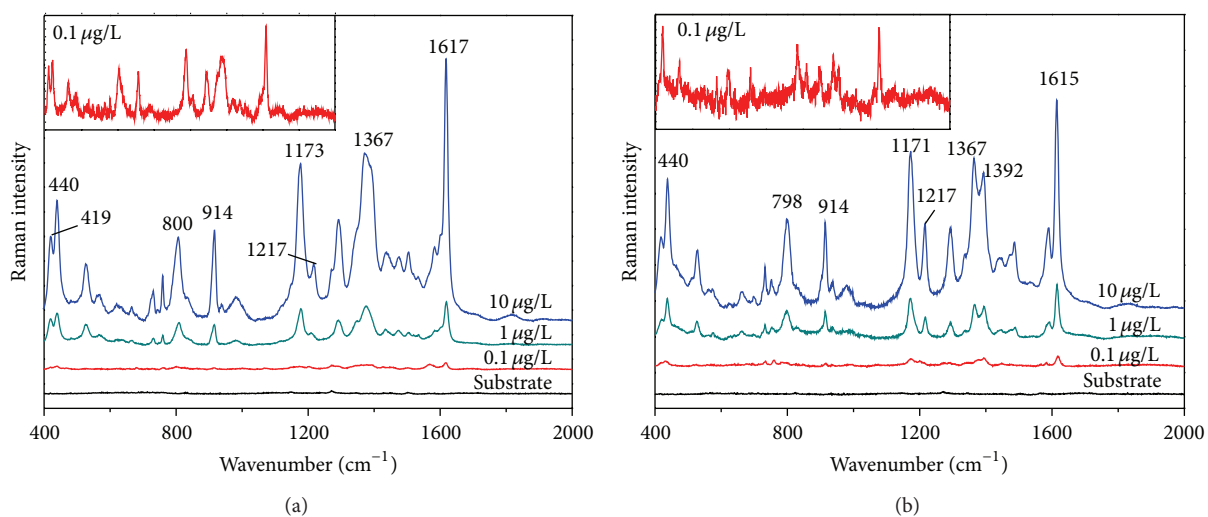


FIGURE 4: SERS spectra of (a) crystal violet standard solution and (b) malachite green standard solution deposited on Au-Ag core-shell nanoparticles.

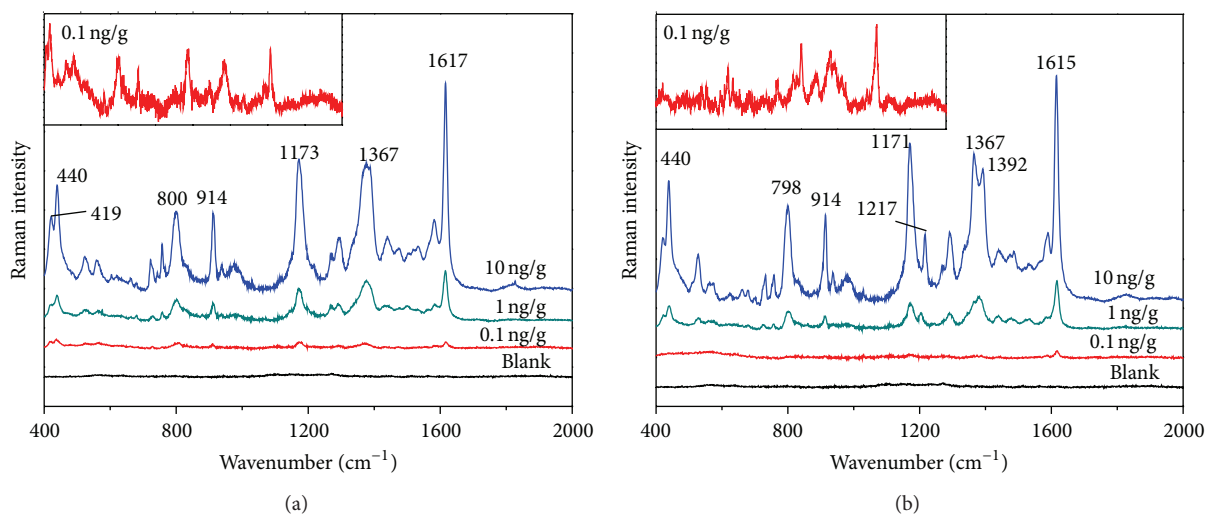


FIGURE 5: SERS spectra of (a) crystal violet extracts and (b) malachite green extracts from fish muscle.

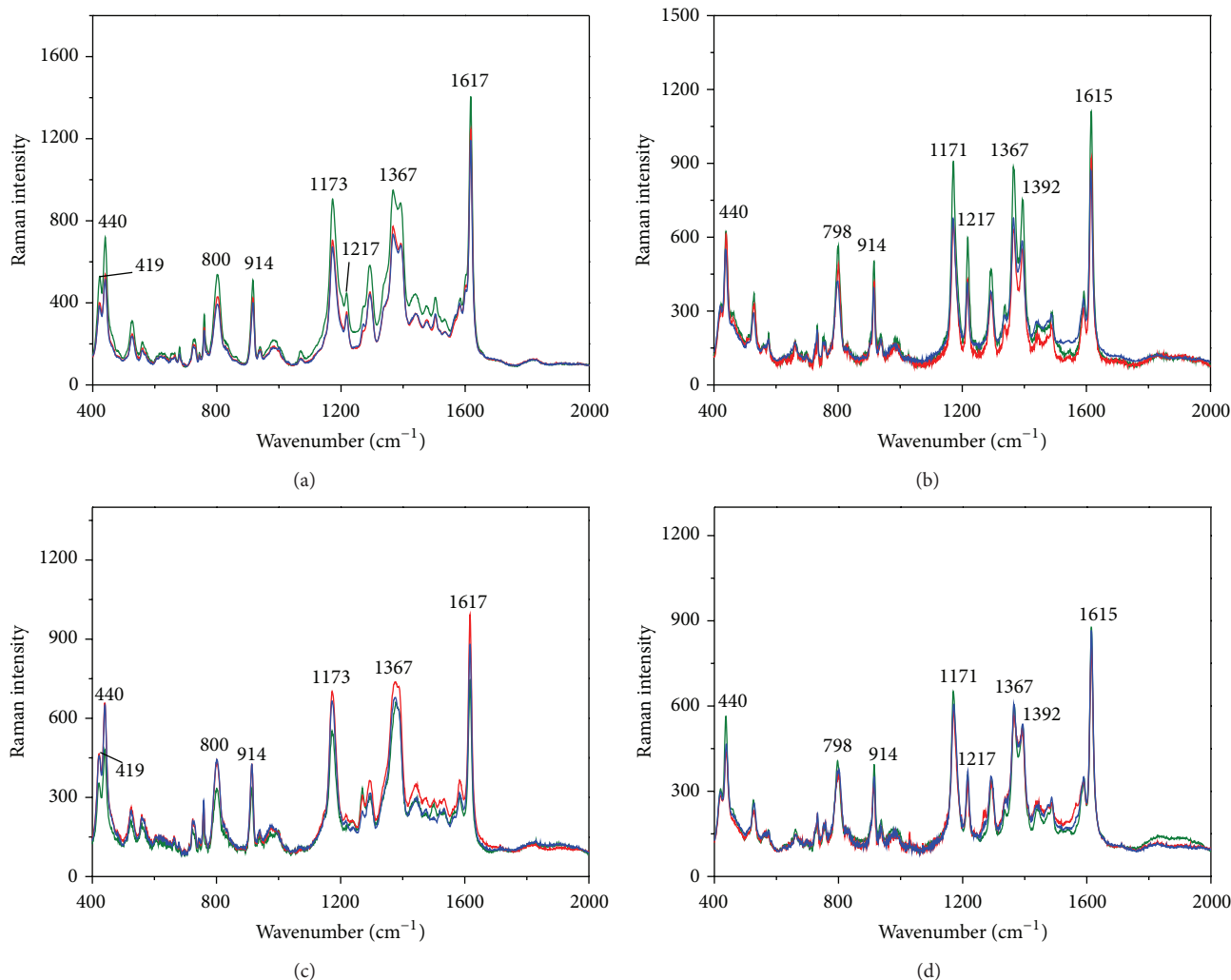


FIGURE 6: Average SERS spectra ($n = 10$) of (a) CV standard solutions ($1 \mu\text{g/L}$), (b) MG standard solutions ($1 \mu\text{g/L}$), (c) CV fish extract (1 ng/g), and (d) MG fish extract (1 ng/g) from triplicate analyses.

indicating that relatively repeatable SERS spectra could be achieved with the selected Au-Ag core-shell NPs as substrates.

Most of CV or MG dyes are metabolized to leucocrystal violet or leucomalachite green in fish [19]. The conventional sample preparation method applied in this study to extract CV or MG from fish fillet involved the use of DDQ to convert metabolites leucocrystal violet or leucomalachite green to CV or MG, and the final level of fish drug detected was actually the sum of CV (or MG) and its metabolite. Therefore, although only CV or MG was tested, the study results could be applied to analyze CV (or MG) and its metabolite in fish muscle.

4. Conclusions

Silver-coated gold bimetallic NPs were synthesized and successfully applied to detect as low as 0.1 ng/g of CV or MG in fish muscle, which made great improvement over our previous studies using commercial SERS substrates [20] and also could meet the most restricted regulatory requirements for the 1 ng/g limit of detection for crystal violet or malachite

green in fish muscle. This interdisciplinary study combined knowledge in SERS and analytical chemistry to solve a real world food safety problem, which helps to fill the gap between theory and application aspects of SERS-related research. Although there were reports on using SERS for nondestructive analyses of chemical hazards in food, such as pesticide in apples [35], since CV or MG residues are inside fish tissues, it is impossible to apply SERS technology to analyze these drugs without sample preparation involving extraction and purification. In this study, a general sample preparation method for chromatography-based analyses was adopted; the information gained from the study provides a basis for further explorations on simplifying sample preparation methods as well as for expanding SERS methods with bimetallic nanospheres for analysis of other harmful chemical substances, such as pesticides and antibiotics in food systems.

Conflict of Interests

The authors declare that there is no conflict of interests regarding the publication of this paper.

Acknowledgment

This research was supported by the National Natural Science Foundation of China (61250002 and 31250006).

References

- [1] D. L. Jeanmaire and R. P. van Duyne, "Surface Raman spectroelectrochemistry—part I: heterocyclic, aromatic, and aliphatic amines adsorbed on the anodized silver electrode," *Journal of Electroanalytical Chemistry and Interfacial Electrochemistry*, vol. 84, no. 1, pp. 1–20, 1977.
- [2] C. L. Haynes, A. D. McFarland, and R. P. van Duyne, "Surface-enhanced Raman spectroscopy," *Analytical Chemistry A*, vol. 77, no. 17, pp. 338–346, 2005.
- [3] E. Petryayeva and U. J. Krull, "Localized surface plasmon resonance: nanostructures, bioassays and biosensing—a review," *Analytica Chimica Acta*, vol. 706, no. 1, pp. 8–24, 2011.
- [4] D. Cialla, A. März, R. Böhme et al., "Surface-enhanced Raman spectroscopy (SERS): progress and trends," *Analytical and Bioanalytical Chemistry*, vol. 403, no. 1, pp. 27–54, 2012.
- [5] S. Nie, "Probing single molecules and single nanoparticles by surface-enhanced Raman scattering," *Science*, vol. 275, no. 5303, pp. 1102–1106, 1997.
- [6] M. Mandal, N. R. Jana, S. Kundu, S. K. Ghosh, M. Panigrahi, and T. Pal, "Synthesis of Au-core-Ag-shell type bimetallic nanoparticles for single molecule detection in solution by SERS method," *Journal of Nanoparticle Research*, vol. 6, no. 1, pp. 53–61, 2004.
- [7] M. V. Cañamares, C. Chenal, R. L. Birke, and J. R. Lombardi, "DFT, SERS, and single-molecule SERS of crystal violet," *The Journal of Physical Chemistry C*, vol. 112, no. 51, pp. 20295–20300, 2008.
- [8] L. Lu, H. Wang, Y. Zhou et al., "Seed-mediated growth of large, monodisperse core-shell gold-silver nanoparticles with Ag-like optical properties," *Chemical Communications*, no. 2, pp. 144–145, 2002.
- [9] F. Zhai, Y. Huang, C. Li, X. Wang, and K. Lai, "Rapid determination of ractopamine in swine urine using surface-enhanced Raman spectroscopy," *Journal of Agricultural and Food Chemistry*, vol. 59, no. 18, pp. 10023–10027, 2011.
- [10] Y. Li, H. Su, K. S. Wong, and X.-Y. Li, "Surface-enhanced Raman spectroscopy on two-dimensional networks of gold nanoparticle-nanocavity dual structures supported on dielectric nanosieves," *The Journal of Physical Chemistry C*, vol. 114, no. 23, pp. 10463–10477, 2010.
- [11] N. R. Jana, "Silver coated gold nanoparticles as new surface enhanced Raman substrate at low analyte concentration," *Analyst*, vol. 128, no. 7, pp. 954–956, 2003.
- [12] Y. Cui, B. Ren, J.-L. Yao, R.-A. Gu, and Z.-Q. Tian, "Synthesis of Ag-core-Au-shell bimetallic nanoparticles for immunoassay based on surface-enhanced Raman spectroscopy," *The Journal of Physical Chemistry B*, vol. 110, no. 9, pp. 4002–4006, 2006.
- [13] L. Guerrini, J. V. Garcia-Ramos, C. Domingo, and S. Sanchez-Cortes, "Ultrathin silver-coated gold nanoparticles as suitable substrate for surface-enhanced Raman scattering," *Journal of Raman Spectroscopy*, vol. 41, no. 5, pp. 508–515, 2010.
- [14] S. Srivastava, R. Sinha, and D. Roy, "Toxicological effects of malachite green," *Aquatic Toxicology*, vol. 66, no. 3, pp. 319–329, 2004.
- [15] N. A. Littlefield, B. N. Blackwell, C. C. Hewitt, and D. W. Gaylor, "A novel surface-enhanced Raman scattering sensor to detect prohibited colorants in food by graphene/silver nanocomposite," *Fundamental and Applied Toxicology*, vol. 5, pp. 902–912, 1985.
- [16] A. Stamatii, C. Nebbia, I. de Angelis et al., "Effects of malachite green (MG) and its major metabolite, leucomalachite green (LMG), in two human cell lines," *Toxicology in Vitro*, vol. 19, no. 7, pp. 853–858, 2005.
- [17] RAFFS, Subject: crystal violet or malachite green. Notification between 01/01/2003 to 31/12/2012, 2013, <https://webgate.ec.europa.eu/rasff-window/portal>.
- [18] A. A. Bergwerff and P. Scherpenisse, "Determination of residues of malachite green in aquatic animals," *Journal of Chromatography B: Analytical Technologies in the Biomedical and Life Sciences*, vol. 788, no. 2, pp. 351–359, 2003.
- [19] W. C. Andersen, S. B. Turnipseed, C. M. Karbiwnyk et al., "Multiresidue method for the triphenylmethane dyes in fish: malachite green, crystal (gentian) violet, and brilliant green," *Analytica Chimica Acta*, vol. 637, no. 1–2, pp. 279–289, 2009.
- [20] Y. Zhang, K. Lai, J. Zhou, X. Wang, B. A. Rasco, and Y. Huang, "A novel approach to determine leucomalachite green and malachite green in fish filets with surface-enhanced Raman spectroscopy (SERS) and multivariate analyses," *Journal of Raman Spectroscopy*, pp. 1208–1213, 2012.
- [21] T. Y. Olson, A. M. Schwartzberg, C. A. Orme, C. E. Talley, B. O'Connell, and J. Z. Zhang, "Hollow gold-silver double-shell nanospheres: structure, optical absorption, and surface-enhanced Raman scattering," *The Journal of Physical Chemistry C*, vol. 112, no. 16, pp. 6319–6329, 2008.
- [22] G. Frens, "Controlled nucleation for the regulation of the particle size in monodisperse gold suspensions," *Nature Physical Science*, vol. 241, pp. 20–22, 1973.
- [23] W. C. Andersen, S. B. Turnipseed, and J. E. Roybal, "FDA laboratory information Bulletin," LIB 4363, 2005, Laboratory Information Bulletin U.S. Food and Drug Administration, November 2005.
- [24] C. Ruan, W. Wang, and B. Gu, "Single-molecule detection of thionine on aggregated gold nanoparticles by surface enhanced Raman scattering," *Journal of Raman Spectroscopy*, vol. 38, no. 5, pp. 568–573, 2007.
- [25] S. He, J. Yao, P. Jiang et al., "Formation of silver nanoparticles and self-assembled two-dimensional ordered superlattice," *Langmuir*, vol. 17, no. 5, pp. 1571–1575, 2001.
- [26] S. Link and M. A. El-Sayed, "Size and temperature dependence of the plasmon absorption of colloidal gold nanoparticles," *The Journal of Physical Chemistry B*, vol. 103, no. 21, pp. 4212–4217, 1999.
- [27] S. D. Solomon, M. Bahadory, A. V. Jeyarajasingam, S. A. Rutkowsky, C. Boritz, and L. Mulfinger, "Synthesis and study of silver nanoparticles," *Journal of Chemical Education*, vol. 84, no. 2, pp. 322–325, 2007.
- [28] C. S. Seney, B. M. Gutzman, and R. H. Goddard, "Correlation of size and surface-enhanced Raman scattering activity of optical and spectroscopic properties for silver nanoparticles," *The Journal of Physical Chemistry C*, vol. 113, no. 1, pp. 74–80, 2009.
- [29] Y. Yang, J. Shi, G. Kawamura, and M. Nogami, "Preparation of Au-Ag, Ag-Au core-shell bimetallic nanoparticles for surface-enhanced Raman scattering," *Scripta Materialia*, vol. 58, no. 10, pp. 862–865, 2008.
- [30] E. J. Liang, X. L. Ye, and W. Kiefer, "Surface-enhanced Raman spectroscopy of crystal violet in the presence of halide and halate ions with near-infrared wavelength excitation," *The*

- Journal of Physical Chemistry A*, vol. 101, no. 40, pp. 7330–7335, 1997.
- [31] K. R. Strehle, D. Cialla, P. Rösch, T. Henkel, M. Köhler, and J. Popp, “A reproducible surface-enhanced Raman spectroscopy approach. Online SERS measurements in a segmented microfluidic system,” *Analytical Chemistry*, vol. 79, no. 4, pp. 1542–1547, 2007.
- [32] Z. Yi, X. Xu, X. Li et al., “Facile preparation of Au/Ag bimetallic hollow nanospheres and its application in surface-enhanced Raman scattering,” *Applied Surface Science*, vol. 258, no. 1, pp. 212–217, 2011.
- [33] F.-K. Liu, M.-H. Tsai, Y.-C. Hsu, and T.-C. Chu, “Analytical separation of Au/Ag core/shell nanoparticles by capillary electrophoresis,” *Journal of Chromatography A*, vol. 1133, no. 1-2, pp. 340–346, 2006.
- [34] C. Langlois, D. Alloeyau, Y. Le Bouar et al., “Growth and structural properties of CuAg and CoPt bimetallic nanoparticles,” *Faraday Discussions*, vol. 138, pp. 375–391, 2008.
- [35] B. Liu, G. Han, Z. Zhang et al., “Shell thickness-dependent Raman enhancement for rapid identification and detection of pesticide residues at fruit peels,” *Analytical Chemistry*, vol. 84, no. 1, pp. 255–261, 2012.
- [36] R. Juluri, A. Rath, A. Ghosh et al., “Coherently embedded Ag nanostructures in Si: 3D imaging and their application to SERS,” *Scientific Reports*, 2014.
- [37] L. He, N.-J. Kim, H. Li, Z. Hu, and M. Lin, “Use of a fractal-like gold nanostructure in surface-enhanced Raman spectroscopy for detection of selected food contaminants,” *Journal of Agricultural and Food Chemistry*, vol. 56, no. 21, pp. 9843–9847, 2008.
- [38] W. C. Andersen, S. B. Turnipseed, and J. E. Roybal, “Quantitative and confirmatory analyses of malachite green and leucomalachite green residues in fish and shrimp,” *Journal of Agricultural and Food Chemistry*, vol. 54, no. 13, pp. 4517–4523, 2006.